

Dissertation

**Making Real Time Measurements of Ice Nuclei
Concentrations at Upper Tropospheric Temperatures:
Extending the Capabilities of the Continuous Flow Diffusion
Chamber**

Submitted by
Mathews Richardson
Department of Atmospheric Science

In partial fulfillment of the requirements
For the degree of Doctor of Philosophy
Colorado State University
Fort Collins, Colorado
Spring 2009

UMI Number: 3374615

INFORMATION TO USERS

The quality of this reproduction is dependent upon the quality of the copy submitted. Broken or indistinct print, colored or poor quality illustrations and photographs, print bleed-through, substandard margins, and improper alignment can adversely affect reproduction.

In the unlikely event that the author did not send a complete manuscript and there are missing pages, these will be noted. Also, if unauthorized copyright material had to be removed, a note will indicate the deletion.

UMI[®]

UMI Microform 3374615
Copyright 2009 by ProQuest LLC
All rights reserved. This microform edition is protected against
unauthorized copying under Title 17, United States Code.

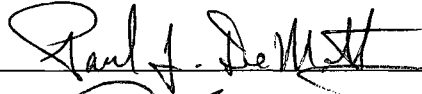
ProQuest LLC
789 East Eisenhower Parkway
P.O. Box 1346
Ann Arbor, MI 48106-1346

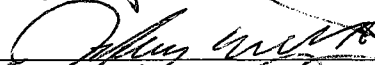
COLORADO STATE UNIVERSITY

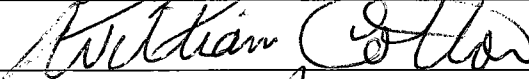
December 3, 2008

WE HEREBY RECOMMEND THAT THE DISSERTATION PREPARED UNDER OUR SUPERVISION BY MATHEWS RICHARDSON ENTITLED MAKING REAL TIME MEASUREMENTS OF ICE NUCLEI CONCENTRATIONS AT UPPER TROPOSPHERIC TEMPERATURES: EXTENDING THE CAPABILITIES OF THE CONTINUOUS FLOW DIFFUSION CHAMBER BE ACCEPTED AS FULFILLING IN PART REQUIREMENTS FOR THE DEGREE OF DOCTOR OF PHILOSOPHY.

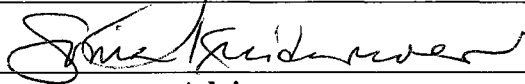
Committee on Graduate Work











Adviser



Department Head/Director

ABSTRACT OF DISSERTATION

MAKING REAL TIME MEASUREMENTS OF ICE NUCLEI CONCENTRATIONS AT UPPER TROPOSPHERIC TEMPERATURES: EXTENDING THE CAPABILITIES OF THE CONTINUOUS FLOW DIFFUSION CHAMBER

Due to their ubiquity, cirrus clouds are important drivers of climate.

Researchers have developed a parameterization that predicts the onset of freezing for a variety of particles with different chemical composition at cirrus temperatures. This parameterization is currently used in many parcel and climate models to predict the impact of changes in aerosol composition on cold cloud processes, but the applicability of this parameterization to real atmospheric aerosol has yet to be determined. The field-ready version of Colorado State University's (CSU) continuous-flow diffusion chamber (CFDC-1H) is one of the few instruments capable of measuring atmospheric ice nuclei (IN) concentrations in real time.

In this study, we examined the operational limits of the CFDC-1H at low temperature through a series of controlled laboratory studies using $(\text{NH}_4)_2\text{SO}_4$ particles at several different sets of operating conditions. Observed freezing onset conditions at 850 mb and 10 lpm deviated significantly from the predicted onset conditions. By operating the chamber over different flow rates and pressures, we found that residence time played a dominant role in the CFDC-1H's ability to detect the onset of freezing at conditions closer to those predicted. Numerical studies confirmed this and indicated that at warmer temperatures the inability of the CFDC-

1H to observe freezing onset conditions as predicted was attributable to the inability of particles to dilute rapidly enough while at colder temperatures the limited availability of water vapor in conjunction with limited residence times inhibited cloud particle growth.

The final portion of this study focused on measurements of the freezing onset conditions of an ambient aerosol. Using water uptake measurements, we found that the hygroscopicity (κ) of the ambient aerosol (0.1 to 0.2) was significantly lower than that of ammonium sulfate (0.6). However, as predicted by theory, there was no observably significant difference between the onset conditions of size-selected $(\text{NH}_4)_2\text{SO}_4$ and size-selected ambient aerosol. Freezing activation curves for the total ambient aerosol indicated that size plays an important role in the fraction freezing and should be considered when making conclusions regarding chemical composition as a function of fraction freezing. The chemical composition of ice crystal residuals was dominated by mineral type elements and carbon containing particles, contrary to expectations. Further work is necessary for any conclusive statement regarding the chemical composition of the freezing nuclei.

Mathews Sears Richardson
Department of Atmospheric Science
Colorado State University
Fort Collins, CO 80523
Spring 2009

ACKNOWLEDGEMENTS

None of the work presented in this dissertation without the support and encouragement of a considerable number of people. First and foremost, my advisor, Dr. Sonia Kreidenweis, provided ideas and direction, and, while giving me leeway to pursue work that I found interesting, made sure that I didn't get too far off track along the way. Dr. Paul DeMott made himself available to me on a (maybe too) regular basis, using his vast experience with regards to both the CFDC and atmospheric ice formation studies to provide insightful comments and ideas. In addition, my other committee members (Drs. Jeffrey Collet, Jr., William Cotton, and David Dandy) also maintained an open door policy that I more than willingly took advantage of and provided feedback that enriched this work.

Many within the Atmospheric Chemistry group here at CSU also provided direct support. Dr. Anthony Prenni developed the instrument studied in this dissertation and was able to provide not only material assistance, but invaluable insight into the workings of the instrument itself. Drs. Christian Carrico and Markus

Petters both supported the final portion of this study with their water uptake measurements and helped to interpret the final data. Ezra Levin also ran water uptake measurements when Dr. Carrico was not available and conducted measurements of the ambient aerosol size distribution which unfortunately did not work out.

Both Drs. Dave Rogers and Derek Straub assisted by sharing their experiences with modeling and operating this instrument.

And last but certainly not least, my family: Sasha, my wife and Noah, my son. Sasha has stood by me over my entire graduate school experience and has put up with my long days, working on weekends and my disappearance into the field for extended periods of time. Without her encouragement, none of this would be possible.

Finally, this work was funded by the National Science Foundation, grant no. ATM-0611936.

TABLE OF CONTENTS

Constants Used in this Work	xxxv
List of Acronyms.....	xxxvi
List of Symbols	xxxviii
1 Introduction	1
1.1 Initiation of Cold Cloud Formation.....	1
1.2 Laboratory Studies of Homogeneous Freezing.....	5
1.3 Homogeneous Freezing in the Atmosphere.....	6
1.4 Objectives and Overview	9
2 Theoretical Considerations.....	14
2.1 Relevant Properties of Water and Ammonium Sulfate Solutions	15
2.1.1 The Density of Water Substance	16

2.1.2	Water Vapor Diffusivity	17
2.1.3	Saturation Vapor Pressure	19
2.1.4	Surface Tension	24
2.1.5	Specific Heat Capacity and Latent Heating	25
2.1.6	Vapor Pressure over a Solution Surface	29
2.1.7	Vapor Pressure over a Curved, Solution Surface.....	32
2.2	The Path to Nucleation: From Dry Particle to Active Cloud	
	Condensation Nuclei	33
2.2.1	Deliquescence.....	34
2.2.2	Diffusional Drop Growth.....	36
	2.2.2.1 Diffusion Controlled (Maxwellian) Growth.....	37
	2.2.2.2 Growth in Transition: Inhibition of Mass Transfer	39
	2.2.2.3 Growth in Transition: Inhibition to Heat Transfer.....	43
	2.2.2.4 Growth in Transition: Bridging the Gap between Kinetic and	
	Diffusion Controlled Growth.....	45
2.3	Homogeneous Ice Nucleation	46
2.4	Diffusional Crystal Growth	51
3	Experimental Methodology.....	55

3.1	Overview of the CFDC	55
3.1.1	Early Development of the CFDC.....	55
3.1.2	Introduction of the CFDC-1H	57
3.1.3	Steady-State Flow Profile.....	60
3.1.4	Growth Region Thermodynamics.....	63
3.1.5	Uncertainty in the Growth Region Conditions.....	65
3.1.6	Optical Detection of Ice Nucleation.....	68
3.2	The Computational Study	72
3.2.1	Modeling the Continuous Phase	75
3.2.1.1	Mesh Generation.....	75
3.2.1.2	Properties of the Gas Phase	77
3.2.1.3	Initial and Boundary Conditions.....	81
3.2.1.4	Thermal Conduction in the CFDC Model Domain.....	96
3.2.2	Modeling the Particle Phase	98
3.2.3	Modeling the Microphysics	100
3.3	The Laboratory Study	102
3.3.1	Size Selected Ammonium Sulfate.....	103

3.3.1.1	Aerosol Generation	104
3.3.1.2	Size Selection by a Differential Mobility Analyzer.....	105
3.3.2	Ambient Aerosol	111
3.3.2.1	Analyzing Ambient Water Uptake Properties	113
3.3.2.2	Chemical Composition of Freezing Nuclei.....	120
3.3.3	Operation of the CFDC-1H	123
4	The Laboratory Study	129
4.1	High Flow Rate Results	132
4.1.1	Ambient Pressure	132
4.1.2	Low Pressure.....	136
4.2	Low Flow Rate Results	143
4.2.1	Ambient Pressure	143
4.2.2	Low Pressure.....	146
4.3	Summary of Size Selected Ammonium Sulfate Experiments	147
5	The Computational Study	149
5.1	Features of the Flow	150
5.1.1	Water Saturation	154

5.1.2	The Stream Function.....	157
5.2	Comparison of the CFD Trajectories with the Analytical Solution.	163
5.3	Ideal Operation	171
5.3.1	Standard Operation	175
5.3.2	The Effect of Water Vapor Diffusion: Operation at Low Pressure	180
5.3.3	Increasing Particle Residence Time	184
5.4	Examination of Instrumental Non-idealities.....	185
5.5	Summary of Results from the Computational Study	192
6	Measurement of the Freezing Behavior of an Ambient Aerosol	195
6.1	Measurements from 30 June 2008.....	199
6.2	Measurements from 1 July 2008	202
6.3	Measurements from 3 July 2008	204
6.4	Measurements from 9 July 2008	209
6.5	Discussion.....	214
7	Conclusions and Recommendations	222
7.1	Summary and Conclusions	222

7.2	Recommendations.....	229
Appendix A :	Simulated Crystal Size Distributions	233
A.1	The Base Case	233
A.2	Low Pressure	236
A.3	Low Flow Rate	238
A.4	Ice Crystal Distributions for the Perturbed Boundary Conditions..	241
A.4.1	Outer Wall Downward Gradient	241
A.4.2	Outer Wall Upward Gradient	243
A.4.3	Inner Wall Downward Gradient.....	246
A.4.4	Inner Wall Upward Gradient.....	248
A.4.5	Oscillating Growth Region Temperatures.....	251
Appendix B :	HTDMA Data	254
Appendix C :	CCN Data.....	256
C.1	Tabulated CCN Data	256
C.2	CCN Activation Curves	259
References	264

LIST OF FIGURES

- Figure 1.1. Results from the work of *Gierens* [2003] indicating that only for modest updrafts (given by the diagonals across this plot in and labeled on the right hand ordinate in m s^{-1}) will typical [IN] (left-hand ordinate; $1 - 10 \text{ l}^{-1}$) have an impact on cold cloud formation. At a pressure of 250 mb, the concentration of ice nuclei (N_c) required to significantly impact cirrus development increases with decreasing parcel temperature (abscissa)..... 4
- Figure 2.1. Diffusivity as a function of temperature and pressure as calculated from Equation 2.3. Contoured values are $Dv \times 10^5$ 19
- Figure 2.2. Saturation vapor pressure parameterizations for water (left) and ice (right) normalized to *Buck* [1981]. The solid line represents the parameterization of *Murphy and Koop* [2005] while the dashed represents the parameterization of *Goff and Gratch* [1946]. 22
- Figure 2.3. Variation in water vapor mixing ratio with saturation ratio and temperature at $p = 850 \text{ mb}$. Values are w_v (kg/kg) as calculated using Equations 2.4

to 2.6. Over 20°C, the variation of the mixing ratio is an order of magnitude, attributable to the exponential change in vapor pressure with temperature. 23

Figure 2.4. Latent heat of vaporization as used in this paper (blue) and a formulation based on the theory of a spinodal limit at -45°C from *Pruppacher and Klett* [1997]. The solid line shows the temperature limit of operation of the CFDC-1H as used for experiments described in the following section; the vertical dashed line shows the approximate limit of simulations described in this paper. 28

Figure 2.5. a) Water activity (***aw***) as a function of the weight percent of ammonium sulfate in a haze drop based on *Tang and Munkelwitz* [1994]. b) Deviations in the temperature dependent parameterization of *Clegg et al.*[1998] from that of *Tang and Munkelwitz's* parameterization ($\Delta aw = aw, Clegg - aw, Tang$) at two different temperatures. 31

Figure 2.6. Deliquescence relative humidity as a function of temperature [*Onasch et al.*, 1999]. 36

Figure 2.7. Contours of the estimated activation RH_w (%) for ammonium sulfate as a function of the initial dry diameter (***d0***) and the temperature (*T*) for a Δt of 3 seconds and a probability of nucleation of 0.1% ($f_{HF} = 0.001$). Droplets formed on particles with the initial dry diameter ***d0*** are assumed to be at equilibrium. 48

Figure 3.1. Overview of the CFDC. a) Mechanical drawings of (counter-clockwise from top) the inlet, inner wall and outer wall. b) Images of the disassembled chamber. 59

Figure 3.2. An example of the analytic solution to the steady state flow profile as given in [1988] for the same wall temperatures ($T_i = -49.5^\circ\text{C}$ and $T_o = -32^\circ\text{C}$) but different flow conditions. 60

Figure 3.3. Illustration of the conditions within the lamina for the four cases given in Figure 3.2. The lamina are shown as filled rectangles for the four flow cases in Figure 3.2. Red represents the 5 lpm case while the black indicates the 10 lpm case. Boxes enclosed by a dashed line indicate the 500 mb case while the solid indicate the 850 mb case. 64

Figure 3.4. Illustration of thermodynamic profile for values in the above figures. Total flow is 5 lpm and the pressure is 850 mb for the lamina position shown. 66

Figure 3.5. Results of calibration at 10 lpm in the OPC high gain. Although there are no results from 2 μm calibration, channel 180 (maximum channel being 191) is sufficient for distinguishing ice in high gain (as suggested from prior calibrations). This channel was used for discernment of ice in all experiments run at 10 lpm. ... 70

Figure 3.6. Results of medium gain calibration for a) 5 lpm and b) 10 lpm. The OPC was operated in medium gain for all experiments at 5 lpm. 71

Figure 3.7. Model domain for the CFDC simulations with close-ups of some critical regions showing contours of the stream function from simulations described below. The broken line shows the axis of symmetry..... 76

Figure 3.8. Laboratory setup for size selected ammonium sulfate studies..... 104

Figure 3.9. Generated size distribution from constant output atomizer and the resulting distribution of size selected particles for 100 nm (top) and 300 nm (bottom). For these plots, the pressure was assumed to be 842 mb, the temperature 293 K and the flows were balanced with 1 lpm sample flow rate and 10 lpm sheath flow rate. Insets focus on the distribution of particles emerging from the DMA. The input distribution is log-normal with a geometric mean diameter of 100 nm and a standard deviation of 2.2 (the generated distribution roughly estimated from the TSI 3076 manual for a 0.1% salt solution)..... 110

Figure 3.10. Experimental set up for ambient sampling. The CFDC-1H rack is described in Figure 3.8..... 112

Figure 3.11. Example calculation of cutpoint as a function of the air flow rate and the number of jets, N . Calculations were made for ambient pressure in Fort Collins (850 mb) as well as mid-atmospheric pressure (500 mb). This plot also shows calculations at two different temperatures for 500 mb. Results of calculations indicate that the cutpoint is relatively insensitive for small variations in pressure and temperature. 123

Figure 4.1. Ice nucleation (homogeneous freezing) curves for 100 nm particles at -45°C and various flow and pressure conditions..... 129

Figure 4.2. Laboratory data at $T_s \approx -42^\circ\text{C}$. A. Prenni measured these onset conditions using a version of the CFDC similar to that of the CFDC-1H. The data are represented by the box and whisker plot, where the red bar indicates the median SS_w , the box contains the extent of data from the lower quartile to the upper quartile and the whiskers extend to 1.5 times the inter-quartile range. The red crosses indicate outliers and most likely are associated with rapidly changing conditions. The dashed lines indicate the conditions predicted by *Koop et al.* [2000] for 0.1% and 1% of the population of particles at the given mobility diameters. 133

Figure 4.3. Freezing results from 27 May at -50°C using 300 nm ammonium sulfate particles. Data were recorded using the OPC's medium gain. Note the persistent residual of $\sim 10 \text{ scm}^{-3}$ at low supersaturations. The residual tails off as SS_w approaches -10%. 136

Figure 4.4. Measured IN concentrations versus SS_w on 15 May (a,b) and 21 May (c,d) for 100 nm ammonium sulfate particles. a) and c) show the measured [IN] with the MCA cut channel set to 180 ($> 2\mu\text{m}$) while b) and d) show the [IN] with the MCA cut channel set to 50 (600 to 700 nm)..... 140

Figure 4.5. Experimental results from two experiments showing anomalous behavior of homogeneous freezing at low pressure and -50°C . The series of figures on the left show an excerpt of the experimental time line from 27 May 2008 while those on the right show the same for a similar experiment on 15 May 2008. The top panel on each side shows the MCA counts as a function of time and channel number (the limits on the color axis are 0 and 30 for each plot), the middle shows SSw as a function of time and the bottom shows [IN] as a function of time using channel 180 as the channel for distinguishing ice crystals from drops and aerosol. In both cases, the size of the dry particle sampled is 100 nm..... 142

Figure 4.6. Summary of laboratory results with confidence intervals for a) 100 nm and b) 300 nm ammonium sulfate particles. Colors represent the different operating conditions: 10 lpm and 850 mb (blue), 10 lpm and 500 mb (red), 5 lpm and 850 mb (green) and 5 lpm and 500 mb (black). The dashed line represents predictions of the freezing onset point using the *Koop et al.* [2000] parameterization..... 147

Figure 5.1. Difference in warm wall temperature profiles for the two different configurations of the field CFDC. The “No flux” case represents the warm wall configurations discussed in *Rogers* [1988] and *Rogers et al.* [2001] while the “Fixed temperature” represents the configuration of the warm wall in the current field instrument. 152

Figure 5.2. A moist bubble exists throughout all of the simulations near the trailing edge of the collar (flow is downward in these figures). This plot shows an example of the moist bubble and associated properties in the region for the highest SS_w case at $P = 850$ mb, $Q_t = 10$ lpm and $T_{tar} = -45^\circ\text{C}$. a) Temperature profile ($^\circ\text{C}$). b) Water vapor mixing ratio wv (kg/kg). c) Super saturation with respect to water (SS_w) as calculated using (2.4), (2.5) and (2.6). The collar is recognizable as the region in the above plots for which there is a temperature profile but no water vapor or SS_w profile. These results are typical for *all* simulations..... 155

Figure 5.3. Plot of the stream function [kg/s] for several different sets of operating conditions. In each case, the conditions are for set for the highest target SS_w . a) -40 $^\circ\text{C}$, 10 lpm, 850 mb, b) -60 $^\circ\text{C}$, 10 lpm, 850 mb, c) -60 $^\circ\text{C}$, 10 lpm, 500 mb, d) -60 $^\circ\text{C}$, 10 lpm, 250 mb, e) -60 $^\circ\text{C}$, 5 lpm, 500 mb, f) -60 $^\circ\text{C}$, 5lpm, 250 mb. 159

Figure 5.4. Inlet temperatures for the $P = 850$ mb, $Q_t = 10$ lpm for target temperatures of a) -40 $^\circ\text{C}$ and b) -60 $^\circ\text{C}$. Both are set to the same temperature scale for comparison (the temperature of the inner wall in the -60 $^\circ\text{C}$ case is -65 $^\circ\text{C}$). 160

Figure 5.5. a) Contours of the stream function in the outlet region. b) Temperature profile in the same region. Both plots correspond to conditions for the final -40 $^\circ\text{C}$ case at 850 mb and $Q_t = 10$ lpm. 162

Figure 5.6. One micron particle trajectories (red) and pathlines (blue) in (a) the inlet region, (b) the transition to the evaporation region and c) the outlet. 164

Figure 5.7. Normalized thermodynamic trajectories for -40°C (a) and -50°C (b). Blue represents the normalized Ta whereas red represents the normalized SSw . The solid lines indicate a low saturation case while the dashed represents a case near water saturation and the dashed-dot line indicates a case where $SSw \approx 5\%$. These trajectories are representative of runs where the $Qt = 10$ lpm and $P = 850$ mb. The total residence times for the trajectories near water saturation are 8.78 s (-40°C) and 8.43 s (-50°C). 166

Figure 5.8. Velocity (upper), SSw (lower left) and T for several points in the chamber across the growth region as well as the conditions given by the analytic solution (Eqs. 3.1, 3.4 and 3.5). f represents the fractional distance from the cold wall. The distances given are referenced from the bottom of the chamber where 85 cm is near the top of the growth region and 35 cm is at the bottom of the growth region. These conditions are for the fifth set of conditions provided for $Ta = -40^{\circ}\text{C}$, $Qt = 10$ lpm and $P = 850$ mb given in Table 3.4. 168

Figure 5.9. Same as Figure 5.7, but for $P = 500$ mb at 10 lpm. 170

Figure 5.10. Same as Figure 5.7 for the $Qt = 5$ lpm and $P = 500$ mb. 171

Figure 5.11. 100 nm particle trajectory released from the center node in the sample inlet for $SSw = 1.64\%$ and $Ta \approx -40^{\circ}\text{C}$. Top panel shows the liquid drop and ice crystal growth while the bottom shows the temperature (left-hand ordinate) and

the saturation ratio as well as the drop water activity and the fraction nucleating
(right-hand ordinate). 175

Figure 5.12. Final predicted crystal sizes (in microns) based on simulations as
described above for $Qt = 10$ lpm and $P = 850$ mb. 178

Figure 5.13. Final predicted crystal sizes (in microns) based on simulations as
described above for $Qt = 10$ lpm and $P = 850$ mb. 182

Figure 5.14. Final predicted crystal sizes (in microns) based on simulations as
described above for $Qt = 5$ lpm and $P = 500$ mb. 184

Figure 5.15. a) Temperature and b) supersaturation with respect to water for target
conditions of $Ta = -45^{\circ}\text{C}$ and $SSw = 3.15\%$ ($Qt = 10$ lpm and $P = 850$ mb)
and for the ideal simulation (i.e. no wall temperature perturbations) and the five
perturbation cases simulated. In each case, the trajectory is that of the particle
released from the 5th (center) node of the modeled sample inlet. 186

Figure 5.16. Final crystal size for an initial dry diameter of 100 nm given wall
temperature perturbations at a) -40°C , b) -45°C , c) -50°C , and d) -60°C . ∇T refers
to the 2 K wall gradient for which subscript o refers to the outer wall while i refers
to the inner wall and subscript d refers to a downward pointing gradient
(temperatures increase down along the wall) and u refers to an upward pointing
gradient. 189

Figure 5.17. Same as in Figure 5.16 but for an initial dry diameter of 300 nm..... 190

Figure 6.1. Curves indicate the freezing onset S_w as a function of size and κ (0.6, 0.1, and 0.01) for three different temperatures (calculated for the equilibrium diameter at the given T , S_w pair, $fHF = 0.001$ and $\Delta t = 3$ s). Ammonium sulfate is assumed to have a $\kappa \approx 0.6$ [Petters and Kreidenweis, 2007], a value similar to that proposed for modeling marine aerosol ($\kappa = 0.7 \pm 0.2$) by Andreae and Rosenfeld [2008] based on a review of CCN activation studies. In the same review, Andreae and Rosenfeld have also proposed $\kappa = 0.3 \pm 0.1$ for modeling continental aerosol.
..... 197

Figure 6.2. Data collected from 30 June 2008 experiments. a) CCN derived κ as a function of time. Shaded areas indicate where HTDMA (light grey) and CFDC-1H (dark grey) measurements were made. The HTDMA derived κ values were 0.13 ± 0.02 for 100 nm particles and 0.1 ± 0.01 for 300 nm particles. The red filled circle with $\kappa \approx 0.6$ indicates an ammonium sulfate calibration point. b) Freezing activation curves for size-selected, ambient aerosol. Predicted freezing curves based on the Koop *et al.*[2000] parameterization are shown as solid lines (100 nm particles) and dashed lines (300 nm particles). Calculations were made for $\kappa \approx 0.15$ and $\Delta t = 3$ s. 200

Figure 6.3. Same as Figure 6.2 but for data collected on 1 July 2008. No HTDMA data are available for this day..... 202

Figure 6.4. Same as Figure 6.2 but for data collected on 3 July 2008. No valid [CN] data were collected that day, so only standard freezing nuclei ([IN]) concentrations are given. The HTDMA derived κ values are 0.16 and 0.26 for 100 nm and 300 nm particles respectively. No confidence intervals are given for the HTDMA measurements as there was only a single measurement at $S_w \geq 0.8$ for each diameter..... 204

Figure 6.5. Results from TEM analysis for 3 July 2008. a) Characterization of particle size as a function of the major axis length. b) Chemical analysis of the 100 nm particles analyzed. c) Chemical analysis of the 300 nm particles analyzed..... 207

Figure 6.6. Same as Figure 6.2 but for 9 July 2008. HTDMA measured κ 's are 0.23 ± 0.04 and 0.19 ± 0.04 for 100 nm and 300 nm particles respectively. 209

Figure 6.7. Results of homogeneous freezing experiments at the three different temperatures for 9 July 2008. The dashed black line in each panel shows the fraction freezing for a lognormally distributed aerosol with a count mean diameter of 150 nm and a geometric standard deviation of 2.0. The aerosol are assumed to have a κ of 0.1, a value near that measured on this day. 211

Figure 6.8. Results from analysis of two TEM grids collected on 9 July 2008. For these experiments, the whole ambient aerosol population was sampled. The samples were collected at two different processing temperatures (-40°C and -50°C). The SS_w 's for collection were -2% at -40°C and 3% at -50°C . a) Cumulative

distribution of the length of the major particle axis. b) Chemical composition of particles sampled at -40°C. c) Chemical composition of particles sampled at -50°C

..... 212

Figure 6.9. a) Size-selected ammonium sulfate onset SS_w plotted against size-selected ambient data for the three different T_a (-40°C, -45°C, and -50°C) and two different particles sizes. b) *Koop et al.* [2000] predicted onset SS_w for size-selected particles plotted against the measured SS_w at three different T_a (-40°C, -45°C and -50°C).

The predicted values are based on a $\Delta t = 3$ s, $fHF = 0.001$ and $\kappa \approx 0.15$.

Dashed (100 nm) and dotted (300 nm) lines show comparisons of the predicted SS_w using the freezing parameterization described in *DeMott et al.* [1997] for $\lambda = 2.0$ and 1.2 with that given by *Koop et al.* Bars on experimental data show the confidence interval for the measurement. Bars on *Koop et al.* values show

calculated $\Delta aw \pm 0.15$ 215

Figure C.1. CCN activation curves and size distributions of particles less than 400 nm measured by the CCNc's in-rack SMPS from 30 June 2008. The time of collection and the temperature gradient are given in the upper left hand corner of each plot.

..... 260

Figure C.2. CCN activation curves for 1 July 2008. 261

Figure C.3. CCN activation curves for 3 July 2008. 262

Figure C.4. CCN activation curves for 9 July 2008. 263

LIST OF TABLES

Table 2.1. Selected survey of proposed liquid water mass accommodation coefficients ($\alpha c, w$) used for drop growth.	42
Table 2.2. A survey of recent values of the thermal accommodation coefficient (αT) used for drop growth in the transition regime.	45
Table 3.1. CFDC-1H measurement uncertainties.	65
Table 3.2. Measurement uncertainty at the average lamina position for four different temperatures near water saturation. The three sets of uncertainty shown are for the lamina temperature (sT_a), supersaturation with respect to water (s_{sw}) and supersaturation with respect to ice (s_{si}).	68
Table 3.3. Inlet velocities for simulations at the given average temperature and pressure for the two different flow rate regimes. The inlet velocities are calculated assuming an inlet temperature of 293 K and the target flow rate is for the average conditions in the lamina.	82

Table 3.4. Cold (T_i) and warm (T_o) wall temperatures used in the simulations with a sheath flow of 9 lpm and a total flow of 10 lpm at 850 mb and a target lamina temperature of -40°C . The steady state conditions for the average lamina position are shown in the last three columns. The steady-state conditions are calculated as discussed in Chapter 3.1.3. 83

Table 3.5. Cold (T_i) and warm (T_o) wall temperatures used in the simulations with a sheath flow of 9 lpm and a total flow of 10 lpm at 850 mb and a target temperature of -45°C . The steady state conditions for the average lamina position are shown in the last three columns. The steady-state conditions are calculated as discussed in Chapter 3.1.3. 85

Table 3.6. Cold (T_i) and warm (T_o) wall temperatures used in the simulations with a sheath flow of 9 lpm and a total flow of 10 lpm at 850 mb and at target lamina temperature of -50°C . The steady state conditions for the average lamina position are shown in the last three columns. The steady-state conditions are calculated as discussed in Chapter 3.1.3. 87

Table 3.7. Cold (T_i) and warm (T_o) wall temperatures used in the simulations with a sheath flow of 9 lpm and a total flow of 10 lpm at 850 mb and a target temperature of -60°C . The steady state conditions for the average lamina position are shown in the last three columns. The steady-state conditions are calculated as discussed in Chapter 3.1.3. 88

Table 3.8. Cold (T_i) and warm (T_o) wall temperatures used in the simulations with a sheath flow of 9 lpm and a total flow of 10 lpm at 500 mb and a target temperature of -40°C . The steady state conditions for the average lamina position are shown in the last three columns. The steady-state conditions are calculated as discussed in Chapter 3.1.3. 89

Table 3.9. Cold (T_i) and warm (T_o) wall temperatures used in the simulations with a sheath flow of 9 lpm and a total flow of 10 lpm at 500 mb and a target temperature of -45°C . The steady state conditions for the average lamina position are shown in the last three columns. The steady-state conditions are calculated as discussed in Chapter 3.1.3. 90

Table 3.10. Cold (T_i) and warm (T_o) wall temperatures used in the simulations with a sheath flow of 9 lpm and a total flow of 10 lpm at 500 mb and a target temperature of -50°C . The steady state conditions for the average lamina position are shown in the last three columns. The steady-state conditions are calculated as discussed in Chapter 3.1.3. 91

Table 3.11. Cold (T_i) and warm (T_o) wall temperatures used in the simulations with a sheath flow of 9 lpm and a total flow of 10 lpm at 500 mb and a target temperature of -60°C . The steady state conditions for the average lamina position are shown in the last three columns. The steady-state conditions are calculated as discussed in Chapter 3.1.3. 91

Table 3.12. Cold (*T_i*) and warm (*T_o*) wall temperatures used in the simulations with a sheath flow of 4.5 lpm and a total flow of 5 lpm at 500 mb and a target temperature of -40°C. The steady state conditions for the average lamina position are shown in the last three columns. The steady-state conditions are calculated as discussed in Chapter 3.1.3. 92

Table 3.13. Cold (*T_i*) and warm (*T_o*) wall temperatures used in the simulations with a sheath flow of 4.5 lpm and a total flow of 5 lpm at 500 mb and a target temperature of -45°C. The steady state conditions for the average lamina position are shown in the last three columns. The steady-state conditions are calculated as discussed in Chapter 3.1.3. 93

Table 3.14. Cold (*T_i*) and warm (*T_o*) wall temperatures used in the simulations with a sheath flow of 4.5 lpm and a total flow of 5 lpm at 500 mb and a target temperature of -50°C. The steady state conditions for the average lamina position are shown in the last three columns. The steady-state conditions are calculated as discussed in Chapter 3.1.3. 94

Table 3.15. Cold (*T_i*) and warm (*T_o*) wall temperatures used in the simulations with a sheath flow of 4.5 lpm and a total flow of 5 lpm at 500 mb and a target temperature of -60°C. The steady state conditions for the average lamina position are shown in the last three columns. The steady-state conditions are calculated as discussed in Chapter 3.1.3. 95

Table 3.16. Material properties for the modeled solid portions of the chamber. SS316 refers to stainless steel 316. The temperatures given in the table below indicate the reference temperature for the measurement or the valid range of temperatures for the given property value. All properties are assumed constant through these simulations..... 97

Table 3.17. Expected size and transmission efficiency of multiply charged particles for 100 nm and 300 nm particles at laboratory pressure and temperature and a balanced, 10:1 sheath-to-sample flow ratio..... 108

Table 4.1. Homogeneous freezing onset conditions as given by *Koop et al.* [2000] for two different sizes of ammonium sulfate particles. Calculations were made using the equilibrium, haze drop diameter, a fraction freezing (f_{ht}) of 0.001 and a total time of 3 seconds..... 131

Table 4.2. Average onset conditions with 95% confidence intervals for ambient (≈ 850 mb) conditions and $Qt \approx 10$ lpm for experiments at different conditions. An estimate of the measurement uncertainty in the thermodynamic values ($sSSw$ and sTa) calculated as described in Chapter 3.1.5 is given to the right of the average measurement. 134

Table 4.3. Compiled Average onset conditions with standard deviations for $P \approx 500$ mb and $Qt \approx 10$ lpm for experiments at different temperatures. An estimate of

the measurement uncertainty in the thermodynamic values calculated as described in Chapter 3.1.5 is given to the right of the average measurement.	138
Table 4.4. Compiled Average onset conditions with standard deviations for $P \approx 850$ mb and $Qt \approx 5$ lpm for experiments at different temperatures. An estimate of the measurement uncertainty in the thermodynamic values calculated as described in Chapter 3.1.5 is given to the right of the average measurement.....	144
Table 4.5. Compiled Average onset conditions with standard deviations for $P \approx 500$ mb and $Qt \approx 5$ lpm for experiments at different temperatures. An estimate of the measurement uncertainty in the thermodynamic values calculated as described in Chapter 3.1.5 is given to the right of the average measurement.....	146
Table 6.1. Summary of data collected as described above. κ 's given for the HTDMA are provided with the 95% confidence interval for measurements at $S_w \geq 0.8$. No measurements are available on 1 July 2008. CCN derived κ 's are given as the median value (top) and the 25 th and 75 th percentiles (bottom in parentheses). CFDC sampling conditions and the sampled particles sizes in nm are given in the 6 th column while the sampling temperature and particle sizes collected for TEM analysis are given in the 7 th column. In both of these columns, all indicates a sample in which no size selection was made.....	214
Table 6.2. Freezing onset conditions from all ambient aerosol experiments	218
Table A.1. Results of base case simulations at $Ta = -40^\circ\text{C}$	234

Table A.2. Results of base case simulations at $Ta = -45^{\circ}\text{C}$	234
Table A.3. Results of base case simulations at $Ta = -50^{\circ}\text{C}$	235
Table A.4. Results of base case simulations at $Ta = -60^{\circ}\text{C}$	235
Table A.5. Results of low pressure simulations at $Ta = -40^{\circ}\text{C}$	236
Table A.6. Results of low pressure simulations at $Ta = -45^{\circ}\text{C}$	237
Table A.7. Results of low pressure simulations at $Ta = -50^{\circ}\text{C}$	237
Table A.8. Results of low pressure simulations at $Ta = -60^{\circ}\text{C}$	238
Table A.9. Results of low flow rate simulations at $Ta = -40^{\circ}\text{C}$	239
Table A.10. Results of low flow rate simulations at $Ta = -45^{\circ}\text{C}$	239
Table A.11. Results of low flow rate simulations at $Ta = -50^{\circ}\text{C}$	240
Table A.12. Results of low flow rate simulations at $Ta = -60^{\circ}\text{C}$	240
Table A.13. Results of the outer wall downward gradient simulations for $Ta = -40^{\circ}\text{C}$	241
Table A.14. Results of the outer wall downward gradient simulations for $Ta = -45^{\circ}\text{C}$	242
Table A.15. Results of the outer wall downward gradient simulations for $Ta = -50^{\circ}\text{C}$	242

Table A.16. Results of the outer wall downward gradient simulations for $Ta = -60^{\circ}\text{C}$	243
Table A.17. Results of the outer wall upward gradient simulations for $Ta = -40^{\circ}\text{C}$	244
Table A.18. Results of the outer wall upward gradient simulations for $Ta = -45^{\circ}\text{C}$	244
Table A.19. Results of the outer wall upward gradient simulations for $Ta = -50^{\circ}\text{C}$	245
Table A.20. Results of the outer wall upward gradient simulations for $Ta = -60^{\circ}\text{C}$	245
Table A.21. Results of the inner wall downward gradient simulations for $Ta = -40^{\circ}\text{C}$	246
Table A.22. Results of the inner wall downward gradient simulations for $Ta = -45^{\circ}\text{C}$	247
Table A.23. Results of the inner wall downward gradient simulations for $Ta = -50^{\circ}\text{C}$	247
Table A.24. Results of the inner wall downward gradient simulations for $Ta = -60^{\circ}\text{C}$	248

Table A.25. Results of the inner wall upward gradient simulations for $Ta = -40^{\circ}\text{C}$	249
Table A.26. Results of the inner wall upward gradient simulations for $Ta = -45^{\circ}\text{C}$	249
Table A.27. Results of the inner wall upward gradient simulations for $Ta = -50^{\circ}\text{C}$	250
Table A.28. Results of the inner wall upward gradient simulations for $Ta = -60^{\circ}\text{C}$	250
Table A.29. Results of the oscillating temperature profile simulations for $Ta = -40^{\circ}\text{C}$	251
Table A.30. Results of the oscillating temperature profile simulations for $Ta = -45^{\circ}\text{C}$	252
Table A.31. Results of the oscillating temperature profile simulations for $Ta = -50^{\circ}\text{C}$	252
Table A.32. Results of the oscillating temperature profile simulations for $Ta = -60^{\circ}\text{C}$	253
Table B.1. Measured HTDMA data for particles having a 100 nm mobility diameter.	254

Table B.2 Measured HTDMA data for particles having a 300 nm (30 June) or 250 nm mobility diameter.....	255
Table C.1. CCNc measurements from 30 June.	257
Table C.2. CCNc measurements from 1 July.	257
Table C.3. CCNc measurements from 3 July.	258
Table C.4. CCNc measurements from 9 July.	259

CONSTANTS USED IN THIS WORK

$c_{p,v}$	specific heat of water vapor at constant pressure	33.5 J/mol
$\mathcal{L}_{0e,w}$	latent heat of vaporization of water at the triple point	45051 J/mol
\mathcal{R}	universal gas constant	8.314 J K ⁻¹ mol ⁻¹
p_0	standard pressure	1013.25 mb
T_0	normal temperature	273.15 K
M_w	molecular weight of water	18.0152 kg/kmol
M_a	molecular weight of air	28.97 kg/kmol
ε	ratio of the molecular weight of water to that air	0.622
e	fundamental unit charge	1.602×10 ⁻¹⁹ C
λ_0	mean free path of air at $T_{s,0}$ and p_0	66×10 ⁻⁹ m
$T_{s,0}$	standard temperature	293.15 K
μ_r	reference viscosity of air at $T_{s,0}$	1.833×10 ⁻⁵ kg m ⁻¹ s ⁻¹
S_μ	Sutherland interpolation constant	110.4
g	gravitational acceleration	9.8 m/s ²
ρ_{AS}	ammonium sulfate density	1770 kg/m ³
M_{AS}	molecular weight of ammonium sulfate	132.14 kg/kmol
κ_T^0	isothermal compressibility of pure water at ambient pressure	1.6 GPa ⁻¹
d	CFDC chamber gap half width	0.0056 m

LIST OF ACRONYMS

AFT	Aerosol Flow Tube
APS	Aerodynamic Particle Sizer
CCN(c)	Cloud Condensation Nuclei (Counter)
CFD	Computational Fluid Dynamics
CFDC	Continuous Flow Diffusion Chamber
CFDC-1H	NCAR GV deployable CFDC
CRYSTAL-FACE	Cirrus Regional Study of Tropical Anvils and Cirrus Layers-Florida Area Cirrus Experiment
CSU	Colorado State University
CVI	Counter Flow Virtual Impactor
DAQ	Data Acquisition Program
DMA	Differential Mobility Analyzer
DMA	Differential Mobility Analyzer
DPM	Discrete Particle Model
DRH	Deliquescence Relative Humidity
EDS	Energy dispersive X-ray spectroscopy
FTIR	Fourier Transform Infrared Spectroscopy
GV	Gulfstream-V
IN	Ice Nuclei
INSPECT-I	The first Ice Nuclei and Spectroscopy Campaign
INSPECT-II	The second Ice Nuclei and Spectroscopy Campaign

LACIS	Leipzig Aerosol Cloud Interaction Simulator
MCA	Multi-channel Analyzer
MCm	Monte Carlo methods
NCAR	National Center for Atmospheric Research
OPC	Optical Particle Counter
PALMS	Particle Analysis by Laser Ablation Mass Spectrometry
PSL	Polystyrene Latex
RKF45	Runge-Kutta-Fehlberg method
SMPS	Scanning Mobility Particle Sizer
SUCCESS	SUBsonic aircraft: Contrail & Cloud Effects Special Study
TEM	Transmission electron microscopy
UDF	User Defined Function
(UF)CN(c)	(Ultrafine) Condensation Nuclei (Counter)
VOAG	Vibrating Orifice Aerosol Generator

LIST OF SYMBOLS

a_w	water activity
B	solute specific constant used in calculating solution surface tension
C_c	Cunningham correction factor
c_w	molar specific heat capacity of liquid water
d_0	initial diameter
d_{50}	50% cutpoint
d_d	drop diameter
D_d	dry diameter
d_e	volume equivalent diameter
d_m	mobility diameter
D_v	water vapor diffusivity
e_∞	ambient water vapor pressure
e_r	water vapor pressure at cloud particle surface
$e_{s,i}$	ice saturation vapor pressure
$e_{s,w}$	water saturation vapor pressure
f	rational activity coefficient
f_{HF}	fraction of particles freezing (probability of freezing)
F_{in}	vapor flux from walls
F_{out}	vapor flux onto particle surface
gf	growth factor

h	sensible enthalpy
I	identity tensor
J_{HF}	homogeneous freezing rate
k_a	thermal conductivity of air
Kn	Knudsen number
\mathcal{L}_e	latent heat of vaporization
\mathcal{L}_m	latent heat of fusion
\mathcal{L}_s	latent heat of sublimation
\mathcal{M}	molality
m_d	cloud particle mass
n	number of charges or real index of refraction
N	number of jets
p	pressure
Q	
Q_a	aerosol flow rate
Q_e	excess flow rate
Q_s	sample flow rate
Q_{sh}	sheath flow rate
Q_t	total flow rate
Ra	Rayleigh number
r_d	cloud particle radius
Re	Reynolds number
r_{flux}	ratio of flux of vapor from walls to the flux of vapor to the surface of the particles in the CFDC
RH_i	relative humidity with respect to ice ($S_i \times 100$)
RH_w	relative humidity with respect to water ($S_w \times 100$)
r_i	inner radius
r_o	outer radius
s_{50}	critical supersaturation

S_i	ice saturation ratio
s_i	ice supersaturation ratio ($S_w - 1$)
SS_i	ice supersaturation ($s_w \times 100$)
SS_w	water supersaturation ($s_w \times 100$)
Stk_{50}	Stokes number for particles at the impactor cutpoint
S_w	water saturation ratio
s_w	water supersaturation ratio ($S_w - 1$)
t	time
T_∞	ambient temperature
T_a	mean aerosol lamina temperature
T_{amb}	ambient temperature
T_{amb}	ambient temperature
T_c	cold wall temperature
T_i	inner wall temperature
T_o	outer wall temperature
T_r	temperature of cloud particle surface
T_{target}	target lamina temperature
T_w	warm wall temperature
\bar{T}	mean temperature
U	volume expansion coefficient
u_i	inner sheath velocity
u_o	outer sheath velocity
u_p	particle velocity
u_s	sample velocity
\bar{u}	mean velocity in growth region of CFDC
V_d	drop volume
v_i	molar volume of ice
V_s	solute volume
V_w	water volume

v_w	molar volume of water
w_v	water vapor mixing ratio
x	radial dimension across CFDC chamber gap
x_w	mass fraction of water
y	position on CFDC wall
y_l	lower coordinate on CFDC wall
Z	nominal mobility
$\alpha_{c,i}$	ice condensation coefficient
$\alpha_{c,w}$	liquid water condensation coefficient
γ	water vapor uptake coefficient
Δ_c	jump distance for water vapor condensation
δT	melting point depression
κ	hygroscopicity
λ	mean free path of air; coefficient for relation between melting point depression and freezing point depression
μ_a	viscosity of air
ρ_a	air density
ρ_i	ice density
ρ_p	particle density
ρ_p	particle density
ρ_v	water vapor density
ρ_w	water density
σ_{sol}	surface tension of solution
σ_w	surface tension of water
τ	period of temperature oscillation
χ	particle shape factor
D_v^*	modified diffusivity
k_a^*	modified thermal conductivity
ε_i	volume fraction of species i

1 INTRODUCTION

At any point in time, cirrus clouds cover an average of 30% of the Earth's surface and up to 70% of the tropical surface [*Wylie and Menzel, 1999*]. Due to their ubiquity, cold clouds are important drivers of climate. Cirrus clouds tend to be transparent to incoming UV radiation and trap outgoing long-wave radiation, therefore having a warming affect [*Hartmann, 1994*]. Changes in properties of these clouds (such as optical thickness and lifetime) due to changes in aerosol composition and concentration could have important implications for the Earth's radiative budget.

1.1 Initiation of Cold Cloud Formation

In recent years, with our growing understanding of the climatic importance of cold clouds, ice formation at low temperatures has undergone renewed scrutiny in the atmospheric science community. It is now well understood that, in contrast to formation of ice in a bulk sample, the formation of ice crystals on a particle surface or in droplets occurs with some degree of supercooling of water. The degree of supercooling required for ice formation depends on the mechanism under which the

nucleation of ice occurs. Ice may form on particles via two distinct pathways. First, ice may heterogeneously form on a foreign substrate. Although the mechanism of heterogeneous nucleation is poorly understood, it is apparent from extensive research that particles serving as heterogeneous nuclei must meet a set of requirements. In addition to being insoluble, these particles generally have diameters larger than 100 nm, a crystallographic structure at the surface similar to that of ice, hydrogen bonds available at the surface, and active sites for adsorption of water molecules [Pruppacher and Klett, 1997]. Particles that meet these requirements are rare and active under only very specific sets of conditions.

Below approximately 238 K, ice may form homogeneously in the liquid phase without the presence of an insoluble substrate [Schaefer, 1952]. In this case, nucleation occurs through spontaneous fluctuations in the liquid resulting in the molecular reorientation of water molecules and the formation of water-to-ice bonds. Depending on the thermodynamic conditions and the drop volume, a critical ice germ eventually forms thus resulting in the drop freezing. In cloud expansion chamber experiments, Hagen *et al.* [1981] found that pure water drops with a radius of ~ 100 nm nucleated in significant concentrations around 233 K. Research since the work of Hagen *et al.* has demonstrated that, as in bulk solutions, the presence of soluble material often has the effect of depressing this freezing temperature further (a colligative property of solutions [Pauling, 1970]).

The ability of cold clouds to affect the radiative and upper-tropospheric hydrologic budgets is driven by the crystal size distribution and number concentration. The size distribution and number concentration are in turn driven by (i) updraft velocities (i.e. cooling rates), (ii) parcel temperatures, (iii) ice crystal growth rates, and (iv) the physical and chemical nature of the aerosol. At low temperatures, the two different freezing mechanisms come into direct competition [Haag *et al.*, 2003]. In cirrus, the presence of heterogeneous ice nuclei (IN) may result in optically thinner, shorter lived clouds. However, the impact of IN is dependent on the number concentration of these nuclei, the onset saturation ratio at a given temperature and the local atmospheric dynamics [DeMott *et al.*, 1994; DeMott *et al.*, 1997; Gierens, 2003; Kärcher, 2004; Ren and MacKenzie, 2005].

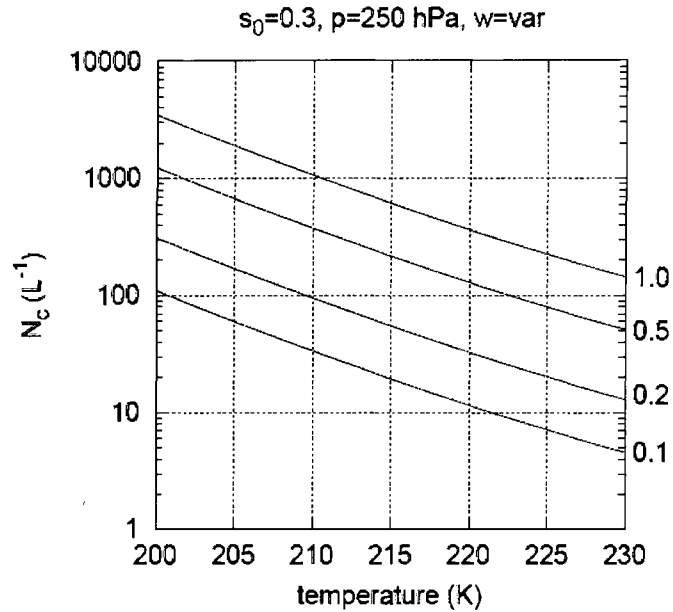


Figure 1.1. Results from the work of *Gierens* [2003] indicating that only for modest updrafts (given by the diagonals across this plot in and labeled on the right hand ordinate in m s^{-1}) will typical [IN] (left-hand ordinate; $1 - 10 \text{ l}^{-1}$) have an impact on cold cloud formation. At a pressure of 250 mb, the concentration of ice nuclei (N_c) required to significantly impact cirrus development increases with decreasing parcel temperature (abscissa).¹

In a box-model study of cold cloud formation, *Gierens* [2003] suggested that cirrus formation is susceptible to the impact of moderately potent IN (activating at an ice saturation ratio of 1.3) in low concentrations ($1 - 10 \text{ l}^{-1}$) only at the most modest updrafts (those on the order of synoptic scale motions; Figure 1.1). These results are in line with the findings of both *Karcher* [2004] as well as *Ren and MacKenzie* [2005] and suggest that, given the relatively small numbers of IN [cf. *DeMott et al.*, 2003;

¹ This figure was reproduced from *Gierens* [2003] under the Creative Commons Attribution 3.0 License.

Prenni et al., 2007a; Richardson et al., 2007; Rogers et al., 1998], homogeneous freezing is likely to be the dominant mechanism for cold cloud formation at temperatures below approximately 235 K.

1.2 Laboratory Studies of Homogeneous Freezing

One important thread amongst recent studies modeling cold cloud formation is the parameterization of homogeneous freezing. In each case, researchers use the parameterization developed in *Koop et al.* [2000], a parameterization developed using a wide array of laboratory data. The studies forming the basis of this parameterization were conducted on a variety of solutions using several different techniques. *Koop et al.* found that they could collapse all of the data such that homogeneous freezing was strictly a function of the solution water activity (a_w) and the ambient temperature. This parameterization is discussed in greater detail in the following chapter.

Although most laboratory studies are in broad agreement with the results of this parameterization [e.g. *Chen et al., 2000; Prenni et al., 2001b; Sassen and Dodd, 1988*], others suggest that salts such as ammonium sulfate may be active to some extent as heterogeneous ice nuclei [*Abbatt et al., 2006; Cziczo and Abbatt, 1999; Mangold et al., 2005; Wise et al., 2004*]. The most divergent results seem to be attributable to studies conducted using aerosol flow tubes [*Cziczo and Abbatt, 1999; Wise et al., 2004*]. The discrepancy in onset conditions led *Hung and Martin* [2001]

to study the instrumental limitations of several techniques. *Hung and Martin* investigated the feasibility of a common nucleation rate coefficient (J) for these instruments with potentially different operational artifacts and found that there was no common J that could explain discrepancies in the measurements from the different techniques.

1.3 Homogeneous Freezing in the Atmosphere

Researchers from various groups have conducted a significant amount of both laboratory and field work to constrain these uncertainties associated with predicting the onset and effects of nucleation on cirrus properties. However, *in-situ* studies of homogeneous freezing nuclei are lacking and the parameterization of homogeneous freezing suggested by *Koop et al.* [2000], though widely accepted as a reasonable approximation of the homogeneous nucleation rate, has yet to be validated for a real population of ambient aerosol. This is primarily due to the lack of instrumentation available for examining aerosol freezing in this temperature range. Typically, inferences concerning homogeneous freezing in clouds are made using measurements of cloud particle residuals [*Lin et al.*, 1998; *Noone et al.*, 1993; *Seifert et al.*, 2003; *Twohy and Poellot*, 2005] or via remote sensing techniques [*Sassen and Dodd*, 1988; 1989]. Further, while early lab studies (the basis of the *Koop et al.* parameterization) focused on the freezing properties of inorganic salts, it is clear that atmospheric aerosol tend to be a complex mixture of both organic and inorganic material that

covers a broad range of hygroscopicity. *Twohy and Poellot* [2005] measured the composition of anvil cirrus ice crystal residuals during the Cirrus Regional Study of Tropical Anvils and Cirrus Layers-Florida Area Cirrus Experiment (CRYSTAL-FACE) captured using a counter-flow virtual impactor (CVI), a device which selects activated cloud particles while rejecting cloud inactive aerosol from the sample stream. Using electron microscopy, they found that the composition of ice crystal residuals tended to correlate with cloud temperature and that soluble material such as salts and sulfates tended to dominate at low temperatures. *Cziczo et al.* [2004b] coupled a CVI with the particle analysis by laser ablation mass spectrometer (PALMS) to measure the elemental composition of ice crystal residuals from anvil cirrus during the same campaign. *Cziczo et al.* found that the composition of the residual aerosol differed from that of the interstitial aerosol even though homogeneous freezing was likely the dominant mechanism for cloud formation. This conclusion implied that the parameterization of *Koop et al.* [2000] might not be sufficient to model the chemically diverse nature of the atmospheric aerosol and its impact on homogeneous freezing.

Presently, one of the few currently operational instruments for measuring the ice nucleating properties of an ambient aerosol *in-situ* is the Colorado State University (CSU) continuous flow diffusion chamber (CFDC) [*Rogers, 1988*]. Initially developed for laboratory work at warm temperatures, the CFDC was redesigned for operation on an aircraft platform [*Rogers et al., 2001*]. The field unit developed by

Rogers et al. has been used successfully in a variety of aircraft based field campaigns [DeMott et al., 2001; Kristovich et al., 2000; Prenni et al., 2007a; Rogers et al., 1998] as well as some ground based campaigns [DeMott et al., 2003; Richardson et al., 2007]. Researchers at CSU have also operated the field unit under homogeneous freezing conditions in several campaigns including SUCCESS [Rogers et al., 1998], CRYSTAL-FACE [Prenni et al., 2007a] and INSPECT-I [Cziczo et al., 2004a; DeMott et al., 2003] as well as others for which the data are as yet unpublished (such as INSPECT-II [Richardson et al., 2004]). Cziczo et al. [2004a] used data from INSPECT-I regarding the composition of homogeneous ice nuclei to support their theory that organic material “preferentially remains unfrozen”.

Though potentially a powerful tool for studying homogeneous freezing *in-situ*, the field version of the CFDC has been plagued by operational uncertainties at low temperature. During CRYSTAL-FACE, corrections applied to the sampling condition data based on work presented in Richardson et al. [2007] indicated that homogeneous freezing conditions were not actually reached though the data system indicated otherwise. Water saturation ratios (S_w) well in excess of 1 were required for activation as homogeneous freezing nuclei in INSPECT-II, findings not consistent with the predictions of Koop et al. [2000]. The high onset S_w was correlated with large temperature gradients on the inner wall (as high as 5 K across the length of the cylinder). In laboratory tests following this campaign, the CFDC measured a similar

response to size-selected ammonium sulfate particles. Clearly, these observations were contrary to prior work conducted with the laboratory CFDC [*Chen et al.*, 2000], results of which were in reasonable agreement with the work of *Koop et al.* [2000]. These results suggest two possible explanations: 1) the parameterization of *Koop et al.* is not applicable to the complex mixtures of aerosol found in the atmosphere, or 2) the CFDC has limited operating capability at low temperatures. The consistency between the findings of the laboratory study following and the field measurements from INSPECT-II suggest the latter.

1.4 Objectives and Overview

In 2006, researchers in Colorado State University's Atmospheric Chemistry group redeveloped the field unit for operation on the National Center for Atmospheric Research (NCAR) Gulfstream V (GV). In this new version, the measurements of the chamber were refined and several portions were redesigned based on results from computational fluid dynamic (CFD) simulations of the previous design [*Rogers et al.*, 2004; *Straub et al.*, 2004]. Following the initial construction of the new chamber, anomalous results at low temperatures and simplified calculations indicated that the crystals were evaporating in the bottom third of the chamber and the CFDC was further reconfigured such that the lower section of the chamber is now actively cooled to the inner wall temperature. The most recent iteration of the field CFDC is hereafter referred to as the CFDC-1H.

As the concept of the CFDC has been successfully utilized in various configurations for studies of heterogeneous nucleation as well as homogeneous freezing, the CFDC-1H is ideal for extending atmospheric measurements to low temperatures. Extending the capability of the instrument to low temperatures provides the ability to test the widely used parameterization of *Koop et al.* [2000], a parameterization that has never been validated for real atmospheric aerosol. However, since the initial development of the field instrument, no study has been undertaken to determine the operational characteristics of the field CFDC at low temperature. The study described below is an attempt to determine the capabilities and limitations of the CFDC-1H through a mixture of laboratory work and CFD simulations coupled with microphysical modeling.

There are three distinct parts to this study. The first two are concerned with the homogeneous freezing characteristics of size selected ammonium sulfate particles, an aerosol considered well characterized in terms of its water uptake and freezing properties. Using laboratory based experiments, this study seeks to determine under what set of operating conditions the CFDC-1H can accurately capture the onset of homogeneous freezing for a well characterized, lab generated aerosol at several different temperatures. The CFD simulations complement the laboratory work in several ways. First, output from the simulations is used to examine the fluid dynamics and thermodynamics in the chamber, aiding in identification of any anomalous or

unexpected behavior. Through the use of particle trajectories, this study determines whether the analytical solution of the steady state heat/mass transfer and flow equations [Rogers, 1988] accurately describes conditions within the growth region. Second, coupling the CFD simulations with a microphysical model allows us to probe a wider set of particle sizes than is experimentally feasible as well as simulate those conditions currently unobtainable in the laboratory. Finally, for those conditions under which the instrument is not able to capture the onset of homogeneous freezing accurately, the simulations will provide insight into what is inhibiting that ability, hopefully providing guidance for future redevelopment of the field CFDC.

The final portion of this study measures the freezing characteristics of an ambient aerosol in an attempt to determine the applicability of the homogeneous freezing parameterization of *Koop et al* [2000] to a non-ideal, atmospheric aerosol. This portion of the study involves sampling of ambient aerosol outside of the Department of Atmospheric Science at CSU. While not necessarily representative of upper-tropospheric aerosol, an ambient sample represents an internally and externally mixed aerosol for which the composition is not known *a priori*. Examination of the water-uptake properties coincident with the CFDC measurement of the freezing properties provides insight into the mixing state of the aerosol. Chemical analysis of the residual freezing nuclei will provide direct indication of the type of particle that is serving as an ice nucleus.

The following chapters provide a path to further our understanding of the operation of the CFDC at low temperature and to thereby further fundamental understanding of low temperature ice nucleation processes. Chapter 2 lays the theoretical foundation for processes relevant to cloud particle formation and growth in the CFDC-1H. The quantitative aspects of these processes are discussed in some detail as the various equations provided are utilized in both the CFD simulations and the microphysical model. Chapter 3 starts with a discussion of the development of the CFDC including the equations used to describe conditions in the growth region of the chamber. This chapter describes the process of modeling the chamber as well as the actual operation of the CFDC and the other instruments used in the laboratory portion of this study. Chapter 4 discusses the results from the laboratory experiments of homogeneous freezing for a size selected aerosol of known composition. The freezing onset conditions are measured under a variety of operating conditions. Chapter 5 discusses the results of the CFD-microphysical model simulations, starting with a detailed discussion of the fluid mechanics of flow in the chamber, and identifying interesting aspects of the flow that are not available from the solution of the analytical equations. Following this, the thermodynamic variables along the trajectory are compared to the solution of the analytical equations. The chapter finishes with a discussion of the final crystal size distributions produced by the microphysical model in both the ideal and non-ideal simulations. Chapter 6 reports and discusses the measurements of the water-uptake properties of the ambient aerosol

measured near the Atmospheric Chemistry laboratory as well as the onset conditions for freezing. Results from the chemical analysis of the freezing nuclei are also presented and discussed. The final chapter summarizes and brings the results of the preceding experiments together, putting them in the context of the requirements for effectively measuring the low temperature nucleation using this technique. This chapter finishes by providing recommendations for future work.

2 THEORETICAL CONSIDERATIONS

This chapter presents some of the theoretical aspects of homogeneous freezing that are relevant to understanding this process. As discussed below, many of the properties of water and water-based solutions at low temperatures are not particularly well understood. While there are parameterizations of homogeneous freezing that appear to capture the onset conditions of nucleation of some supercooled solutions, attempts to apply nucleation theory to the process of homogeneous freezing have been relatively unsuccessful; however, *Khvorostyanov and Curry* [2004] suggested that, with proper constraint of the important physical parameters, classical nucleation theory can indeed be applied to the problem of homogeneous freezing. With this in mind, it is apparent that there are a variety of sometimes irreconcilable theories governing the properties and processes related to the path toward homogeneous freezing in the CFDC. The following sections discuss some of the theoretical aspects of drop and crystal growth and outline the theories used in the modeling portion of this study. The theories related to these processes are important in understanding

how homogeneous freezing proceeds in the CFDC and what might be the fundamentally important variables that govern our ability to measure homogeneous freezing at low temperatures.

2.1 Relevant Properties of Water and Ammonium Sulfate Solutions

Our understanding of water in the supercooled regime carries a considerable amount of uncertainty. Indeed, in the case of deep supercooling (as in droplet cooling in the absence of heterogeneous nuclei) there is a divergence in the theory concerning the properties of water substance. This divergence in the theory found in the literature is attributable to experimental issues which often make it difficult to measure the properties of water drops as temperatures approach 235 K simply because it is difficult to prevent ice nucleation of water substance at these temperatures. On the one hand, some researchers propose a spinodal instability in supercooled water occurring somewhere around 228 K [*Pruppacher, 1995; Pruppacher and Klett, 1997*]. In this theory, certain properties of water begin to change in an exponential manner near the spinodal limit [viscosity, density, etc.; see *Pruppacher and Klett, 1997*] and ice will form spontaneously with no chance of liquid water below this temperature. Others have criticized this theory [*Bartell, 1997*]. *Bartell* [1997] put forth a theory of a two state model in which it is possible for liquid water to exist beyond this singularity. *Murphy and Koop* [2005] supported this singularity-free hypothesis with a review of literature that indicated liquid water exhibits structural changes that

mimic those of amorphous ice when cooled at ambient pressure. In their work, *Murphy and Koop* use the measured properties of amorphous ice to constrain thermodynamic properties of supercooled water between 235 K and 155 K, where no measurements exist.

The following section describes those properties of water that are required to formulate a model of nucleation. It is not intended to be an exhaustive survey of the literature, but to provide some insight into the modeling portion of the study described in the following chapters. Due to a lack of evidence supporting the singularity hypothesis, when the two theories do diverge in their description of a certain property of water, a formulation has been selected that allows for deeper supercooling without discontinuities in the property.

2.1.1 The Density of Water Substance

The density of ice and water both vary as functions of temperature. For ice, *Pruppacher and Klett* [1997] suggest the use of the following

$$(\rho_i / \text{kg m}^{-3}) = 916.7 - 0.175(T / ^\circ\text{C}) - 5.0 \times 10^{-7}(T / ^\circ\text{C})^2 \quad 2.1$$

where T is the temperature. According to the authors, this fit is valid from 273.15 to 93.15 K.

The density of supercooled water is more complicated to express. Given the current lack of understanding in this area and the apparent divergence of

thermodynamic properties of water in this range, the microphysical model below uses the equation for supercooled water density given in *Pruppacher and Klett* [1997] for the given range (273.15 to 240.15 K) and limits the lower end of water density to that found at 240 K. This equation is

$$\begin{aligned}
 (\rho_w/\text{kg m}^{-3}) = & 999.86 + 6.69 \times 10^{-2}(T/^\circ\text{C}) - 8.486 \\
 & \times 10^{-3}(T/^\circ\text{C})^2 + 1.518 \times 10^{-4}(T/^\circ\text{C})^3 \\
 & - 6.9984 \times 10^{-6}(T/^\circ\text{C})^4 - 3.6449 \\
 & \times 10^{-7}(T/^\circ\text{C})^5 - 7.497 \times 10^{-12}(T/^\circ\text{C})^6
 \end{aligned} \tag{2.2}$$

Extrapolating this fit to lower temperatures results in a calculated density of supercooled water approaching that of ice around 228 K; the calculated density rapidly decreases below this temperature. In contrast, the two-state model suggests that the density will exhibit a minimum somewhere around 228 K and increase slowly at temperatures below this value. Since there are neither measurements nor available parameterizations of the density of supercooled water below 240 K, the error in making the assumption that the density does not change beyond this temperature is not calculable. However, relative to the measurement capabilities of the CFDC, it is likely that the difference is not resolvable.

2.1.2 Water Vapor Diffusivity

In the study of cloud drop and crystal growth rates, Fick's second law of diffusion is often called upon to model growth as a function of time. Diffusion

describes the transport of molecules in the presence of a concentration gradient. In Fick's model, a binary diffusion coefficient, or diffusivity, describes the rate at which one minor component of a gaseous mixture moves through another component. In these studies, water vapor diffuses through air. Although there are measurements of the diffusivity of water vapor in air above 273 K, there is a noticeable lack of measurement in the literature for lower temperatures. Based on an extrapolation of reasonable measurements, *Hall and Pruppacher* [1976] developed the following formulation which they suggested was applicable between 233 K and 313 K:

$$(D_v/\text{cm}^2\text{s}^{-1}) = 0.211 \left(\frac{[T/\text{K}]}{T_0} \right)^{1.94} \left(\frac{p_0}{[p/\text{mb}]} \right) \quad 2.3$$

where T_0 is 273.15 K and p_0 is 1013.25 mb. For the purposes of this study and due to the lack of other measurements, this parameterization is extrapolated to considerably lower temperatures. Diffusivity as a function of temperature and pressure is shown in Figure 2.1. From this plot, it is apparent that, although a stronger function of temperature than pressure ($D_v \propto T^2/P$), the diffusivity varies less than a factor of 3 over typical range of pressures and temperatures relevant to this study (an important consideration with regards to drop and crystal growth).

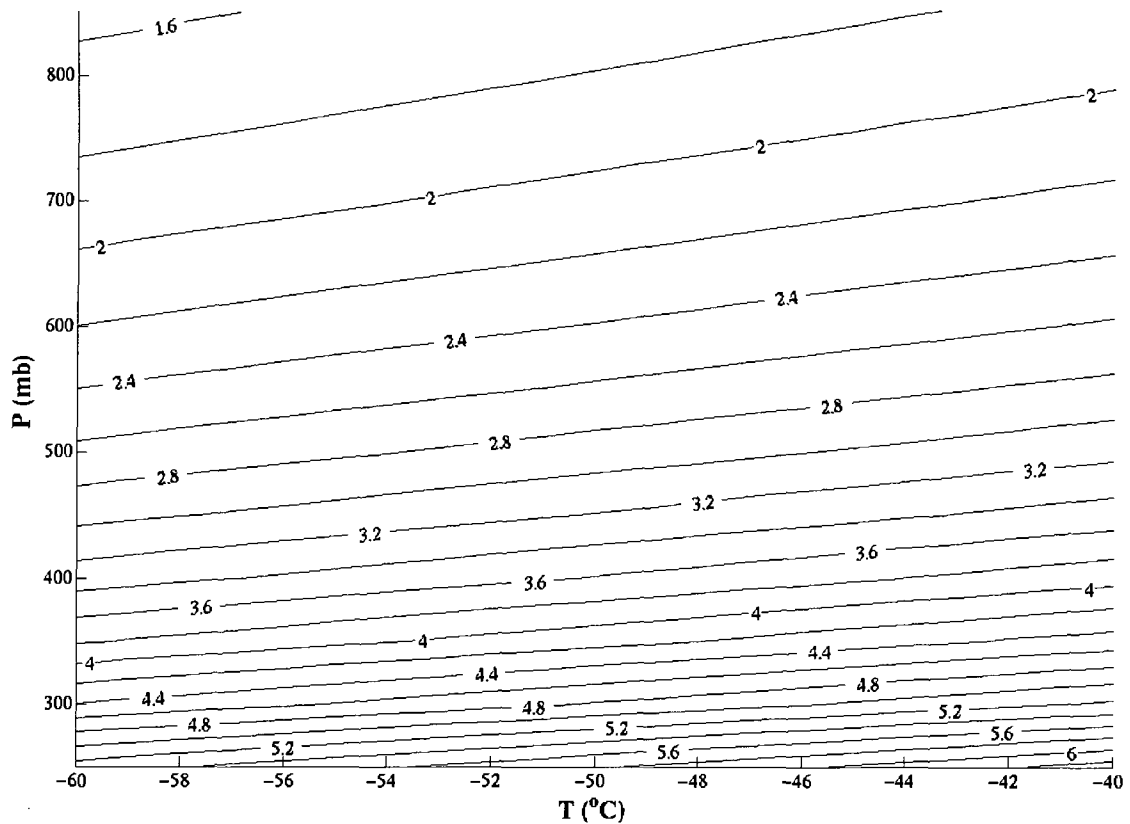


Figure 2.1. Diffusivity as a function of temperature and pressure as calculated from Equation 2.3. Contoured values are $D_v \times 10^5$.

2.1.3 Saturation Vapor Pressure

The saturation vapor pressure of water over liquid or ice is fundamental to the calculation of growth rates. The saturation vapor pressure and the actual vapor pressure determine the saturation ratio with respect to the phase of interest. The saturation ratio in turn will drive the growth or evaporation of cloud particles. From *Pruppacher and Klett* [1997], water vapor partial pressure (e) may be calculated from the water vapor mixing ratio (w_v) as

$$e \approx \frac{w_v p}{\varepsilon} \quad 2.4$$

where p is the total pressure and ε is the ratio of the molecular weight of water to that of air ($M_w/M_a \approx 0.622$). The mixing ratio is significant as it is a measurement that is readily accessible and does not require extensive knowledge of the thermodynamics of water. In this study, as described below, w_v is the variable retrieved from CFD simulations of the CFDC (see equation 3.12 in the following chapter). From this calculation of e , the saturation ratio over a water surface of phase n may then be calculated as

$$S_n = \frac{e}{e_{s,n}} \quad 2.5$$

where n is either w or i representing liquid water or ice respectively and $e_{s,n}$ corresponds to the saturation with respect to liquid water or ice. The supersaturation ratio with respect to the phase is $s_n = S_n - 1$ while the relative humidity is simply $RH_n = s_n \times 100\%$. In some cases, the supersaturation is given as a percentage. In these cases, $SS_n = s_n \times 100\% = (S_n - 1) \times 100\%$.

To calculate the saturation vapor pressure of water vapor over liquid water ($e_{s,w}$), the model uses the parameterization given in *Buck* [1981]:

$$[e_{s,w}/\text{mb}] = 6.1121 \exp\left(\frac{(18.729 - [T/^\circ\text{C}]/227.3)[T/^\circ\text{C}]}{[T/^\circ\text{C}] + 257.87}\right) \quad 2.6$$

This equation corresponds to that given in (4a) in *Buck* [1981] which gives a better fit to the data set than the other formulations of the liquid water saturation vapor pressure given in the same paper at the expense of greater complexity. Similarly, the model uses the parameterization of the saturation vapor pressure over ice ($e_{s,i}$) as a function of temperature given in *Buck* [1981]

$$[e_{s,i}/\text{mb}] = 6.1115 \exp\left(\frac{(23.036 - [T/^\circ\text{C}]/333.7)[T/^\circ\text{C}]}{[T/^\circ\text{C}] + 279.82}\right) \quad 2.7$$

Both of these formulations are based on data collected over the temperature range of 298 K to 373 K and at the triple point. These parameterizations are comparable to the parameterizations given in *Wexler* [1976] and *Wexler* [1977] but are intended to be computationally more efficient. These formulations are consistent with the saturation vapor pressure formulations used in the CFDC data acquisition software (DAQ).

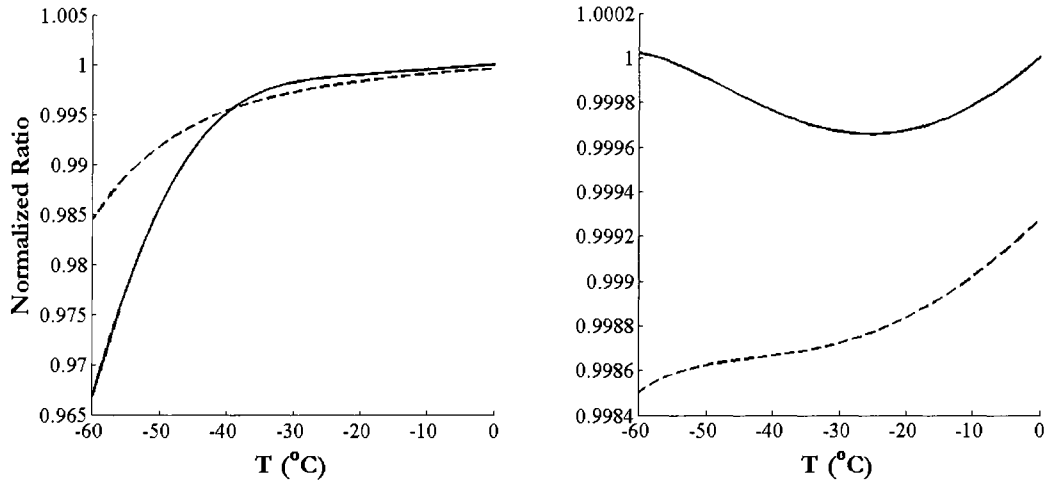


Figure 2.2. Saturation vapor pressure parameterizations for water (left) and ice (right) normalized to *Buck* [1981]. The solid line represents the parameterization of *Murphy and Koop* [2005] while the dashed represents the parameterization of *Goff and Gratch* [1946].

Calculation of the saturation vapor pressure is an ultimately more confounding exercise. As *Murphy and Koop* [2005] point out, none of the formulations of saturation vapor pressure over liquid water currently used in the literature were intended for the supercooled regime. *Murphy and Koop* [2005] reviewed work on vapor pressure over liquid water and ice and developed parameterizations for saturation vapor pressures in both instances. In the more recent work reviewed, data on molar heat capacity were collected to ~ 236 K with experimental limitations preventing the extension of these studies to lower temperatures. Therefore, the thermodynamics of water vapor below this point is highly uncertain. Normalized ratios of both the *Murphy and Koop* [2005] and *Goff and Gratch* [1946] parameterizations (the latter being an oft used parameterization of the saturation vapor pressure and previously used by the CFDC) are shown in Figure 2.2. While the

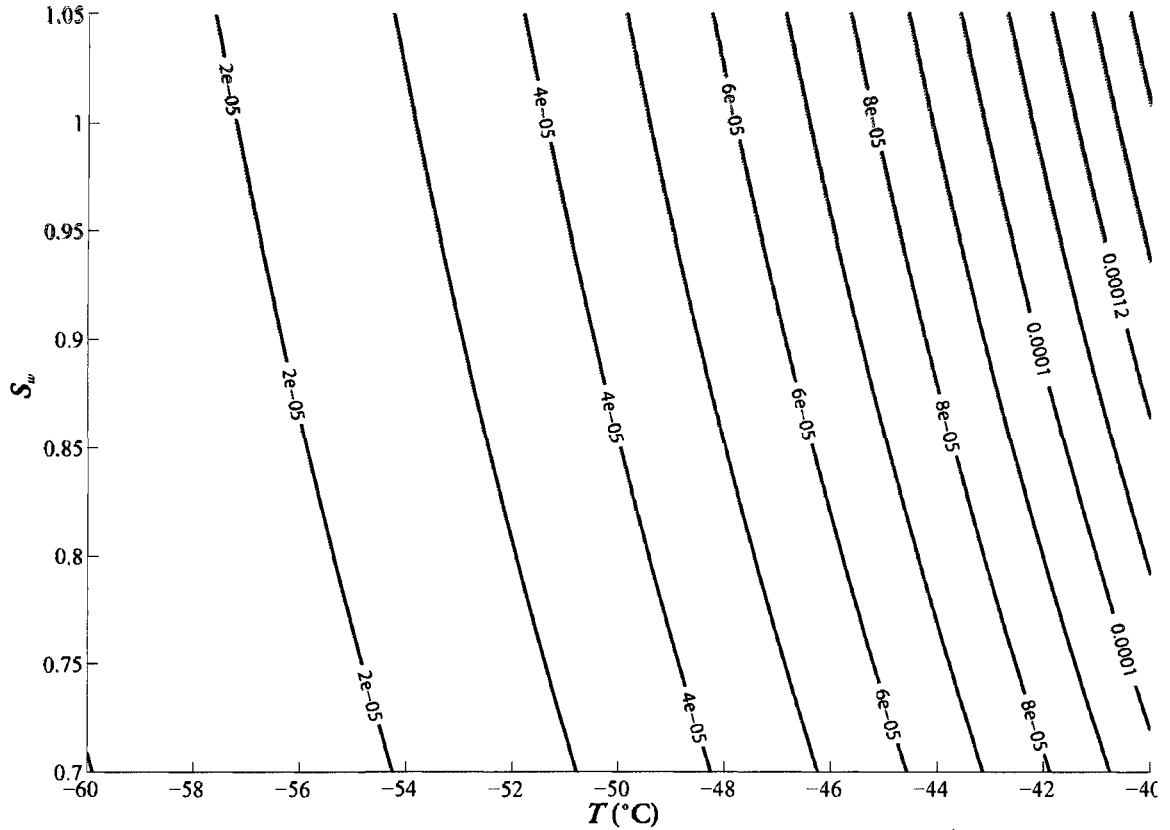


Figure 2.3. Variation in water vapor mixing ratio with saturation ratio and temperature at $p = 850$ mb. Values are w_v (kg/kg) as calculated using Equations 2.4 to 2.6. Over 20°C , the variation of the mixing ratio is an order of magnitude, attributable to the exponential change in vapor pressure with temperature.

parameterizations for $e_{s,i}$ (right) show little deviation from that of *Buck* [1981], the parameterizations of both *Goff and Gratch* [1946] and *Murphy and Koop* [2005] indicate $e_{s,w}$ significantly lower than that of *Buck* [1981] at temperatures below 235 K. Given the uncertainties in measurements below this point and to retain consistency with the CFDC DAQ, the simulations described below retain the *Buck* [1981] parameterization of $e_{s,w}$ for modeling purposes.

An important factor to consider for low temperature operation is the expected exponential change in vapor pressure with temperature. While the water mass available for growth increases with increasing S_w at fixed T , the variation with T is considerably more dramatic. In fact, over the temperature range of interest for instrument operation, the mass available varies by over an order of magnitude (Figure 2.3). This has significant implications for cloud particle growth at low temperatures.

2.1.4 Surface Tension

The surface tension of pure water (σ_w) varies inversely with temperature.

Seinfeld and Pandis [1998] give this relation as

$$[\sigma_w/\text{J m}^{-2}] = 0.0761 - 1.55 \times 10^{-4}[T/^\circ\text{C}] \quad 2.8$$

According to *Seinfeld and Pandis*, this parameterization is valid for the temperature range 233 to 313 K. Given the lack of data below 233 K, the model extrapolates this parameterization to lower temperatures. An alternative formulation for pure water surface tension is given in *Pruppacher and Klett* [1997]. In this formulation, the surface tension of water is a 6th order polynomial with respect to temperature. As with the formulation above, the surface tension increases with decreasing temperature; however, as the temperature approaches 228 K, the increase in surface tension accelerates almost exponentially. This parameterization is based on the theory of a spinodal limit of supercooled water and is therefore not used here.

The presence of a solute has the potential to affect the surface tension of a drop. Some organics decrease surface tension while inorganic salts such as ammonium sulfate increase the surface tension of the solution. The change in surface tension due to the presence of an inorganic salt tends to be monotonic with the salt molality. In this case, the solution surface tension can be computed from

$$[\sigma_{sol}/\text{J m}^{-2}] = [\sigma_w/\text{J m}^{-2}] + B[\mathfrak{M}/\text{mol kg}^{-1}] \quad 2.9$$

where B is a solute specific constant (2.17×10^{-3} in the case of ammonium sulfate) and \mathfrak{M} is the molality [*Seinfeld and Pandis, 1998*].

2.1.5 Specific Heat Capacity and Latent Heating

In the presence of a phase change, energy will be removed or added to the surrounding environment; this change in energy results in a decrease or increase in the temperature of the surrounding environment. Within the CFDC, there are two phase changes of interest: evaporation (or condensation) associated with growing drops and sublimation associated with the growth or evaporation of ice crystals via vapor deposition. The third phase change, melting, is not considered significant in the CFDC as temperatures within the instrument domain remain well below 273.15 K. However, melting is important in the sense that the latent heat of sublimation is the sum of the latent heats of evaporation and melting.

Kirchoff's equations [*Pruppacher and Klett, 1997*] provide a reasonable, temperature dependent approximation of the latent heat terms. For the latent heat of evaporation,

$$\frac{d\mathcal{L}_e}{dT} \approx c_{p,v} - c_w \quad 2.10$$

where $c_{p,v}$ is the specific heat of water vapor at constant pressure and c_w is the specific heat of liquid water. Using a similar relation, the latent heat of melting is written as

$$\frac{d\mathcal{L}_m}{dT} = c_w - c_i \quad 2.11$$

where c_i is the specific heat capacity of ice. In both cases, the differences in heat capacity are integrated with respect to temperature to determine the appropriate value for latent heat. For the latent heat of sublimation (\mathcal{L}_s), the value is equal to the sum of the latent heat of melting and the latent heat of evaporation.

For \mathcal{L}_e associated with supercooled drop growth, *Murphy and Koop* [2005] provide a parameterization based on heat capacity from other works that is valid from 273.15 to 235 K. This parameterization is

$$\begin{aligned} [\mathcal{L}_e/\text{J mol}^{-1}] \approx & 56579 - 42.212[T/\text{K}] \\ & + \exp[0.1149(281.6 - [T/\text{K}])] \end{aligned} \quad 2.12$$

As stated in the introduction to this section, the properties of supercooled water at temperatures beyond the lower bound of this range are uncertain, making the

integration of Eq. 2.10 more complicated. In the work of *Starr et al.* [2003], the investigators used the thermodynamic properties of water at the glassy transition point and those at the lower limit of measurable supercooling to provide an estimate of the properties of water below 235 K. *Murphy and Koop* [2005] follow the example of these researchers to estimate c_w at low temperatures. This exercise results in the following 7th order polynomial, the coefficients of which are given in the footnotes of Table C1 of *Murphy and Koop* [2005]

$$\begin{aligned}
[c_w/J \text{ mol}^{-1}] = & 38565.2 - 635.6299 [T/K] \\
& + 0.964911 [T/K]^2 + 3.646245 \times 10^{-2} [T/K]^3 \\
& - 2.189861 \times 10^{-4} [T/K]^4 + 4.197441 \\
& \times 10^{-8} [T/K]^5 + 2.456321 \times 10^{-9} [T/K]^6 \\
& - 4.839049 \times 10^{-12} [T/K]^7
\end{aligned} \tag{2.13}$$

In the interest of consistency, the computational work described herein uses this approach and solves Eq. 2.10 in a piece-wise fashion such that

$$\mathcal{L}_e = \mathcal{L}_{0e,w} + \int_{273.15}^{231} \Delta c \, dT + \int_{231}^{T'} \Delta c \, dT \tag{2.14}$$

where $\mathcal{L}_{0e,w}$ is the latent heat of evaporation of liquid water at the triple point [45051 J/mol; *Murphy and Koop*, 2005] and Δc is the difference in heat capacity between liquid water and vapor. The second integral on the right hand side of Eq. 2.14 is

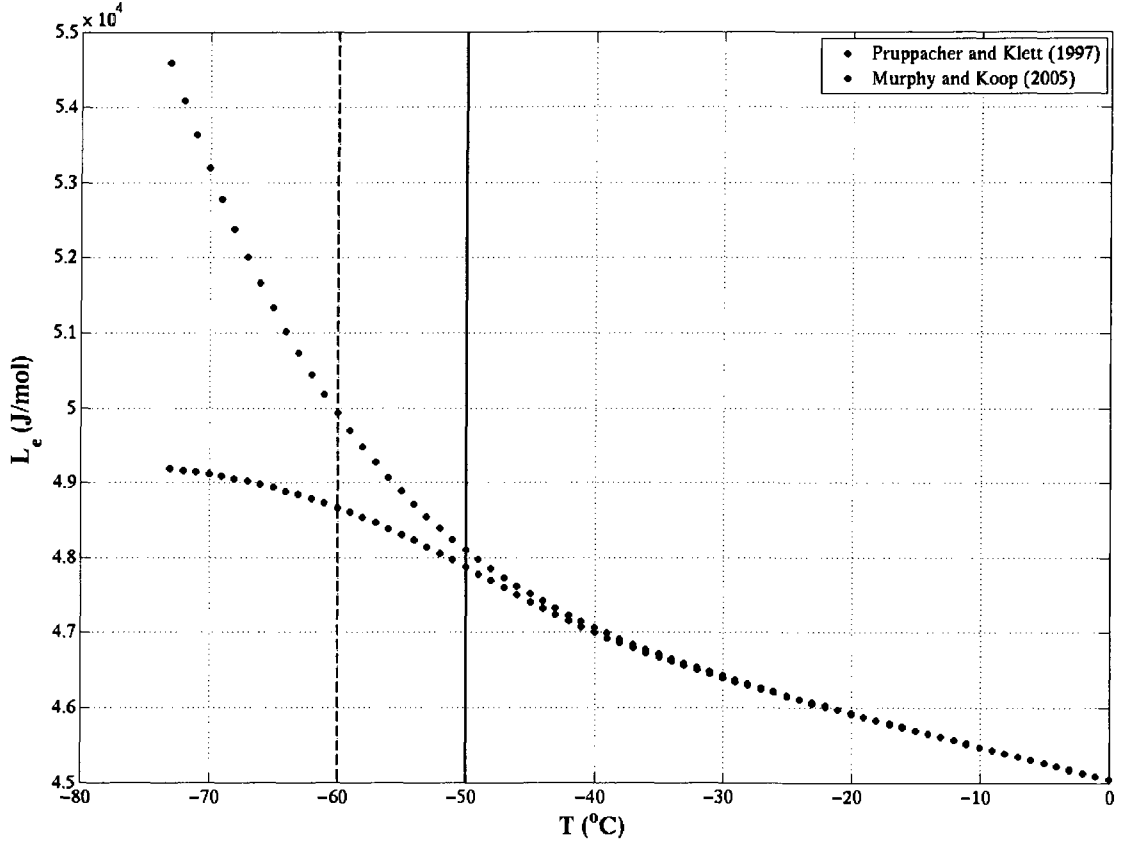


Figure 2.4. Latent heat of vaporization as used in this paper (blue) and a formulation based on the theory of a spinodal limit at -45°C from *Pruppacher and Klett* [1997]. The solid line shows the temperature limit of operation of the CFDC-1H as used for experiments described in the following section; the vertical dashed line shows the approximate limit of simulations described in this paper.

given by the integration of Eq. 2.13. The solution of the first integral on the right

hand side of (2.14), \mathcal{L}_e'' , is given as

$$\mathcal{L}_e'' = \mathcal{L}_e' - \mathcal{L}_{0e,w} - \int_{231}^{T'} c_{v,p} dT \quad 2.15$$

Here, \mathcal{L}_e' is given by Eq. 2.12 with $T = 231$ K. The specific heat of water vapor at constant pressure is approximately constant with temperature. For the purposes of solution, this value is estimated as $33.5 \text{ J mol}^{-1}\text{K}^{-1}$ from *Murphy and Koop* [2005].

Figure 2.4 shows a comparison of the latent heat of vaporization of supercooled water as calculated using the above method and that using *Pruppacher and Klett's* parameterization of c_w [Eq. 3-16; *Pruppacher and Klett, 1997*]. The parameterizations are in reasonable agreement to 233 K, as expected. Beyond this lower limit, the two parameterizations diverge as the specific heat of water increases in an exponential manner in *Pruppacher and Klett's* parameterization in accordance with the theory of a spinodal limit of stability of water.

The solution for \mathcal{L}_s is considerably more straight-forward than the solution of \mathcal{L}_e as there is no dependence on c_w . *Murphy and Koop* [2005] integrated the sum of Eqs. 2.10 and 2.11, including the terms related to the difference between the molar volume of ice and water as well as non-ideal gas effects (although these terms tend to be small). The parameterization to this solution is used here and is given as

$$[\mathcal{L}_s/\text{J mol}^{-1}] = 46782.5 + 35.8925[T/\text{K}] - 0.7414[T/\text{K}]^2 + 541.5 \exp\left[-\left(\frac{[T/\text{K}]}{123.75}\right)^2\right] \quad 2.16$$

According to *Murphy and Koop*, this parameterization is valid to 30 K.

2.1.6 Vapor Pressure over a Solution Surface

Water activity plays an important role in cloud and haze drop growth. For an ideal solution, the ratio of the water vapor partial pressure over the saturation vapor pressure at temperature T is given by Raoult's Law, which defines the mole fraction of water in solution, or

$$\frac{e}{e_{s,w}(T)} = x_w \quad 2.17$$

is the saturation vapor pressure with respect to liquid water (as given in This relation will hold for sufficiently dilute solutions in which there is no interaction between solute and solvent. However, small cloud particles deviate significantly from ideal behavior due to both long range and short range interactions between ions. To account for non-idealities in solutions, the mole fraction in Raoult's Law is replaced by the product of the mole fraction and the rational activity coefficient f [Pruppacher and Klett, 1997] such that

$$\frac{e}{e_{s,w}(T)} = a_w = f x_w \quad 2.18$$

This equation provides a more generalized form of Raoult's Law where $a_w \rightarrow x_w$ as $a_w \rightarrow 1$.

Water activity is a function of the solute composition, concentration and the temperature. There are various ways to parameterize water activity for different inorganic salts [Clegg *et al.*, 1998; Petters and Kreidenweis, 2007; Pitzer and Mayorga, 1973; Tang and Munkelwitz, 1994], all of which are in reasonable agreement for the solute weight fractions relevant to haze drop growth. Pitzer and Mayorga [1973] provide a model of the osmotic coefficient that may be used to calculate the water activity. Petters and Kreidenweis [2007] introduce a single parameter that represents the hygroscopicity of the substance. The single parameter may represent a single

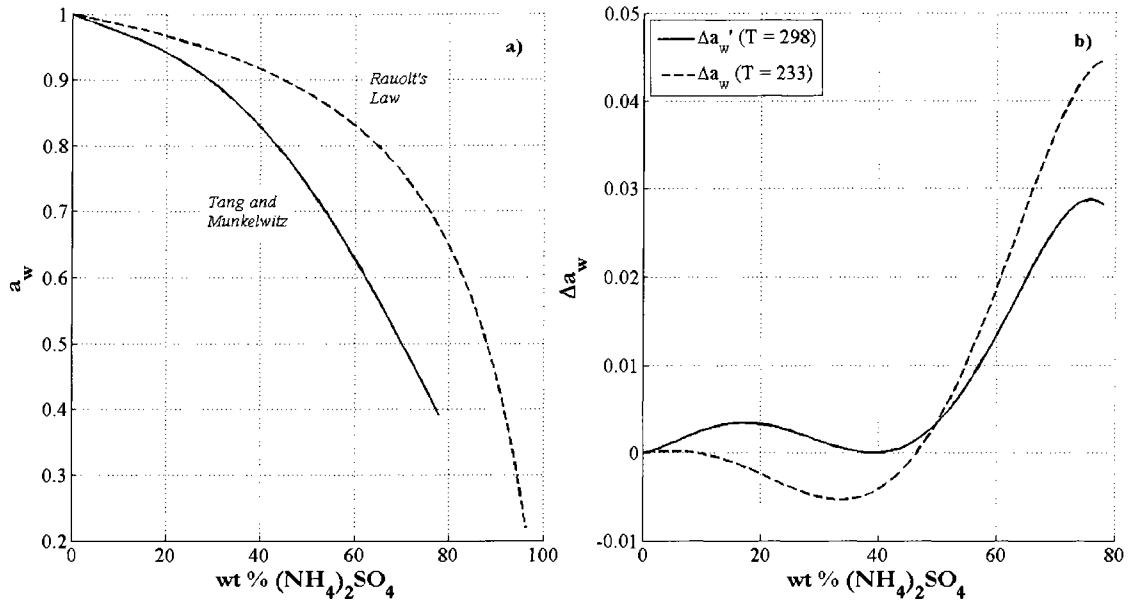


Figure 2.5. a) Water activity (a_w) as a function of the weight percent of ammonium sulfate in a haze drop based on *Tang and Munkelwitz* [1994]. b) Deviations in the temperature dependent parameterization of *Clegg et al.*[1998] from that of *Tang and Munkelwitz's* parameterization ($\Delta a_w = a_{w,Clegg} - a_{w,Tang}$) at two different temperatures.

known substance such as ammonium sulfate or an internal mixture of different chemical species for which the value can be derived from water uptake measurements. *Tang and Munkelwitz* [1994] provide a parameterization based on measurements of a_w as a function of solute weight percent using an electrodynamic trap at 298 K for several atmospherically relevant salts.

The a_w formulation used in the microphysical simulations described below is that of *Clegg et al.* [1998] which uses extensive thermodynamic data for the different water-salt systems in the literature to develop descriptions of the mole fraction activity coefficients from this data. According to *Clegg et al.*, the results are mildly

temperature dependent and valid for relevant tropospheric temperatures (328 K to 200 K). Figure 2.5 shows the water activity of ammonium sulfate calculated using *Tang and Munkelwitz* [1994] (a widely used model of water activity) alongside the water activity calculated using Raoult's Law and a comparison of the *Clegg et al.* model with the *Tang and Munkelwitz* parameterization at two different temperatures. The two parameterizations compare favorably at the two different temperatures (with the temperature varying only in the *Clegg et al.* model) above the deliquescence point (approximately 43% (NH₄)₂SO₄ by mass) but deviate at higher weight fractions (lower a_w). However, the deviations are still small and will have no impact on the ice crystal distributions produced by the microphysical simulations. The *Clegg et al.* model is readily available on the web (AIM; <http://www.aim.env.uea.ac.uk-/aim/aim.php>).

2.1.7 Vapor Pressure over a Curved, Solution Surface

As measurements within the CFDC are typically made for small particles, the effect of droplet curvature must be considered when discussing equilibrium vapor pressure for haze drops. The vapor pressure over a curved surface will generally always exceed that over the flat surface and the vapor pressure over a curved solution surface [*Seinfeld and Pandis, 1998*] may be written as

$$e = e_{s,w} \times a_w Ke \tag{2.19}$$

Ke is the Kelvin term which describes the elevation of the vapor pressure over a drop surface. This term may be written as

$$Ke = \exp\left(\frac{4M_w\sigma_{sol}}{\mathcal{R}T\rho_w d_d}\right) \quad 2.20$$

Here, σ_{sol} is the solution surface tension, \mathcal{R} is the universal gas constant, T is the temperature, and d_d is the diameter of the deliquesced drop. The partial molar volume of water in solution is approximated by the molar volume of water ($\frac{\rho_w}{M_w}$, where M_w is the molecular weight of water and ρ_w is the density of bulk water); this assumption is equivalent to the assumption of volume additivity which, according to *Brechtel and Kreidenweis* [2000], leads to minimal errors in equilibrium values of the S_w . The impact of the Kelvin effect becomes more significant at lower drop diameters, but is included in all equations of drop growth.

2.2 The Path to Nucleation: From Dry Particle to Active Cloud Condensation Nuclei

In the CFDC, water vapor is actively removed from the sample stream so as to prevent spuriously high saturations as the stream is cooled from ambient conditions (often at temperatures greater than 273.15 K) to conditions within the chamber. Dry salt particles must first deliquesce before growing by condensation in the chamber. This is the thermodynamic process by which a dry particle transforms into a saturated solution consisting of water and the salt [*Martin*, 2000]. For freezing to occur, these

haze drops subsequently grow to a size such that the probability of nucleation is significant. The timescales for growth within the CFDC are quite short (on the order of a few seconds), and growth modeled assuming that particles are in equilibrium with the vapor at all times may deviate significantly from kinetic growth with corresponding differences in the predicted fractions freezing. The following sections describe the interaction of a dry, salt particle with water vapor as a function of saturation ratio and temperature.

2.2.1 Deliquescence

Deliquescence of ammonium sulfate particles in the microphysical model is temperature dependent and is based on a parameterization by *Onasch et al.* [1999]. Deliquescence is assumed to have no kinetic barrier that would significantly impact the results of the simulations described below [*Onasch et al.*, 1999; *Xu et al.*, 1998]. *Onasch et al.* conducted water uptake experiments using a flow tube system coupled with Fourier transform infrared spectroscopy (FTIR). In this study, the authors were unable to conduct measurements in the ice equilibrium region of the phase diagram and therefore measurements extend only to approximately 256 K where the deliquescence curve crossed the ice saturation line. In this parameterization, the deliquescence data were fit to yield the following equation (Figure 2.6):

$$\log(DRH) = 4.9015 - \frac{6.1612 \times 10^2}{[T/K]} + \frac{2.0656 \times 10^5}{[T/K]^2} - \frac{2.0716 \times 10^7}{[T/K]^3} \quad 2.21$$

Onasch et al. conducted these experiments on a polydisperse distribution of sub-micron particles. The results of this work compare favorably with other theoretical and laboratory studies to temperatures near the eutectic temperature. Both *Braban et al.* [2001] and *Fortin et al.* [2002] have examined the water uptake behavior of ammonium sulfate below the eutectic point and there is little evidence for the overturning behavior observed in the *Onasch et al.* [1999] fit to the data below the eutectic. The data of both *Braban et al.* and *Fortin et al.* exhibit behavior similar to the theoretical data developed by *Clegg et al.* [1998] and *Tabazadeh and Toon* [1998] indicating a monotonic rise in the DRH as temperature decreases. However, the fit shown in Figure 2.6 is within the uncertainty of both measurements down to 213 K. Use of the theoretical fit described in *Tabazadeh and Toon* [1998] for a simulated CFDC trajectory indicates that there is no difference in the final outcome from that given in *Onasch et al.* [1999].

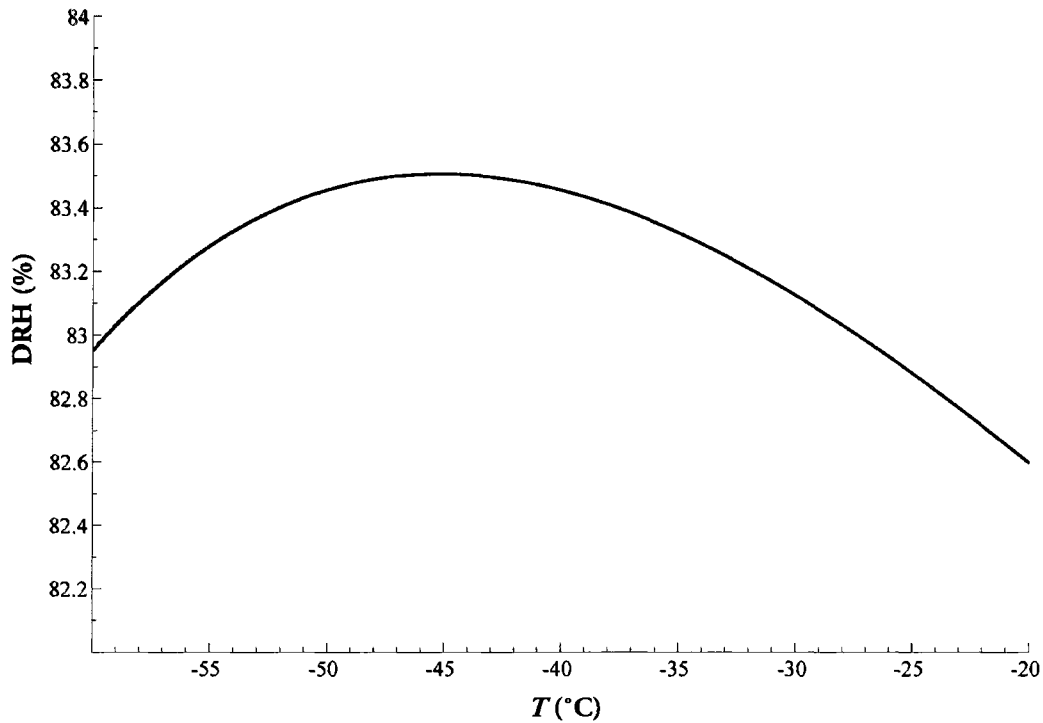


Figure 2.6. Deliquescence relative humidity as a function of temperature [Onasch *et al.*, 1999].

2.2.2 Diffusional Drop Growth

Upon deliquescence, droplets will grow via diffusion. Given a sufficient amount of time, a droplet containing a soluble substance and exposed to an environmental water saturation ratio less than 1 will grow to an equilibrium size. One can determine this size using Eq. 2.19. In cases where droplets are exposed to supersaturated environments or when there is insufficient time for them to come to equilibrium, the particle size as a function of time is determined by the rate of diffusional water uptake.

2.2.2.1 Diffusion Controlled (Maxwellian) Growth

A first step to determining the rate of droplet growth is provided by Maxwellian model [*Fukuta and Walter, 1970*]. This model assumes that the vapor field is at a steady-state and utilizes Fick's first law of diffusion,

$$-J_v = D_v \nabla \rho_v \quad 2.22$$

where ρ_v is the water vapor density, J_v is the water vapor flux and D_v is the water vapor diffusivity as given in Eq. 2.3. The Maxwellian description of drop growth is found by integrating over the spherical drop surface,

$$\frac{dm_d}{dt} = 4\pi r_d D_v (\rho_{v,\infty} - \rho_{v,r}) \quad 2.23$$

where m_d is the mass of the drop, r_d is the radius of the drop and $\rho_{v,\infty}$ and $\rho_{v,r}$ are the ambient vapor density and the vapor density at the droplet surface respectively. This can be written in terms of vapor pressure using the ideal gas law as

$$\frac{dm_d}{dt} = \frac{4\pi r_d D_v M_w}{\mathcal{R}} \left(\frac{e_\infty}{T_\infty} - \frac{e_{s,w}(T_r)}{T_r} \right) \quad 2.24$$

A further requirement for drop growth in an undisturbed, gaseous environment is that the release of latent heat attributable to drop growth must balance the heat conduction from the droplet surface, or $\nabla^2 T = 0$. In this case,

$$\mathcal{L}_e \frac{dm_d}{dt} = -\frac{dQ}{dt} \quad 2.25$$

where Q is the amount of heat that must be dissipated by conduction from the drop,

or

$$\frac{dQ}{dt} = 4\pi r_d k_a (T_r - T_\infty) \quad 2.26$$

Here, k_a represents the thermal conductivity of air and T_r and T_∞ are the temperatures at the drop surface and the ambient field respectively. In this case, it is assumed that we may neglect the amount of heat flowing into the drop, a reasonable assumption given that the heat capacity of the growing drop is small compared with the latent heat released and heat conduction in the drop itself is fast [*Fukuta and Walter, 1970*]. The thermal conductivity of air as a function of temperature is given as in *Pruppacher and Klett* [1997]

$$[k_a/\text{cal cm}^{-1}\text{°C}^{-1}] = [5.69 + 0.17 \times [T/\text{°C}]] \times 10^{-5} \quad 2.27$$

Following the argument given in *Pruppacher and Klett*, the contribution of water vapor to the conductivity may be neglected as the mole fraction of water vapor is typically small in these systems (several orders of magnitude smaller than air).

Assuming that the difference between the far-field temperature and the temperature at the surface is small, Eq. 2.24 can be manipulated such that

$$\frac{dm_d}{dt} = \frac{4\pi r_d S_w}{\frac{\mathcal{L}_e^2 M_w}{k_a \mathcal{R} T_\infty^2} - \frac{\mathcal{L}_e}{k_a T_\infty \rho_w} + \frac{\mathcal{R} T_\infty}{D_v M_w e_{s,w}(T_\infty)}} \quad 2.28$$

Eq. 2.28 describes growth/evaporation in an environment super/sub-saturated with respect to water and can be written with respect to the growth of the radius r_d as

$$r_d \frac{dr_d}{dt} = \frac{D_v M_w}{\mathcal{R} \rho_w} \left(\frac{e_\infty}{T_\infty} - \frac{e_r}{T_r} \right) = \frac{s_w}{\frac{\mathcal{L}_e^2 M_w \rho_w}{k_a \mathcal{R} T_\infty^2} + \frac{\mathcal{R} T_\infty \rho_w}{D_v M_w e_{s,w}(T_\infty)}} \quad 2.29$$

This equation is often referred to as the Maxwell equation.

2.2.2.2 Growth in Transition: Inhibition of Mass Transfer

Growth of droplets is considered a two step process: first, water vapor must diffuse to the surface of the drop then the vapor must be accommodated by or incorporated into the drop. If the process were strictly controlled by diffusion, then the mass growth rate of the particle would be proportional to the drop radius as in Eq. 2.28. For particles considerably larger than the vapor mean free path, growth is indeed a diffusion-limited process [*Pruppacher and Klett, 1997*]. On the other end of the spectrum, kinetic theory governs the growth of particles much smaller than the mean free path of the vapor phase. In this kinetic regime, the gas phase may be considered uniform and the rate of molecular collision multiplied by its accommodation coefficient (or α , the probability that a molecule will stick upon collision) controls the rate of condensation.

The growth of atmospheric particles relevant to cloud formation is generally in the transition regime as the particle diameters are of the same order of the mean free path of vapor phase water. Transition regime theory assumes that kinetic theory will

govern the flux of vapor near the surface and diffusion theory will govern in the far field. At some distance from the drop (Δ_c) the two fluxes will match [*Fukuta and Walter, 1970*]. In this model, the effects of particle size on condensation are accounted for in a modified diffusivity. This modified diffusivity may be calculated as

$$D_v^* = \frac{D_v}{\left[\frac{r_d}{r_d + \Delta_c} + \frac{D_v}{r_d \alpha_{c,w}} \left(\frac{2\pi M_w}{\mathcal{R}T_r} \right)^{\frac{1}{2}} \right]} \quad 2.30$$

This form of the diffusivity introduces the new term $\alpha_{c,w}$, the liquid water mass accommodation coefficient. This term describes the fraction of molecules colliding with a surface that are subsequently incorporated into the condensed phase without causing a similar molecule to be ejected [*Kulmala and Wagner, 2001*]. This coefficient is also referred to as the sticking probability or the condensation coefficient.

The mass accommodation coefficient is an important parameter for drop growth in the atmosphere [*Chuang et al., 1997*] as well as in the CFDC. Even below water saturation, small $\alpha_{c,w}$ can impede haze drop growth and in turn the onset of homogeneous freezing. Over the past 100 years, researchers have expended a considerable amount of effort studying model growth of liquid droplets. Kulmala and Wagner have argued vigorously for a value close to unity [*Kulmala and Wagner, 2001; Laaksonen et al., 2005; Winkler et al., 2004*]. The results of *Shaw and Lamb* [1999] are on the low end of the spectrum of suggested values, below 0.1. The work

of *Li et al.* [2001] suggests a negative temperature dependence for the mass accommodation coefficient. *Davidovits et al.* [2006] provide a brief review and discussion of recent measurements while *Mozurkewich* [1986] reviewed measurements prior to 1986. Table 2.1 lists several recent studies and the range of accommodation coefficients observed therein. For the most part, recent work suggests that $\alpha_{c,w}$ is greater than 0.1. *Jakubczyk et al.* [2007] initially found temperature dependent values with a minimum of 0.036 coinciding with the maximum water density; however, these values were revised upward as described in *Zientara et al.* [2008] to > 0.1 .

Table 2.1. Selected survey of proposed liquid water mass accommodation coefficients ($\alpha_{c,w}$) used for drop growth.

Reference	Method	Value
<i>Shaw and Lamb</i> [1999]	Homogeneous freezing of drops in an electrodynamic trap	0.04→0.1
<i>Li et al.</i> [2001]	Uptake of ^{17}O -labeled water vapor in a droplet train flow reactor	0.17 (280 K), 0.32 (258 K)
<i>Voigtlander et al.</i> [2007]	Droplet growth in the Leipzig Aerosol Cloud Interaction Simulator (LACIS), a laminar flow diffusion tube	> 0.3
<i>Winkler et al.</i> [2004]	Droplet growth in an expansion cloud chamber	> 0.4 (1.0 likely)
<i>Gershenzon et al.</i> [2004]	Uptake of ^{17}O -labeled water vapor on H_2SO_4 solution drops in a droplet train flow reactor	0.54 (295 K), 0.69 (252 K) - increases with increasing solute concentration
<i>Vieceli et al.</i> [2004]	Molecular dynamics simulations	1.0
<i>Fukuta and Myers</i> [2007]	Drop growth in a horizontal diffusion chamber	0.043±0.016
<i>Zientara et al.</i> [2008]	Evaporation of drop in electrodynamic trap	0.18-0.13 (negative T dependence)

Fukuta and Meyers [2007] claim to have found a link between these disparate values of $\alpha_{c,w}$ using a theory that accounts for the boundary separating the kinetic-controlled (inner) region from the diffusion-controlled region (outer). In their work, the correction results in a decrease of <20% in the mass accommodation coefficients measured in previous studies and cannot explain the difference between these measured coefficients in this study and those closer to unity. *Fukuta and Myers* do

make the reasonable argument that experiments such as those conducted by *Winkler et al.* [2004], where the value of $\alpha_{c,w}$ was measured closer to unity, were conducted under a set of conditions in which growth may be less sensitive to the condensation coefficient.

It is beyond the scope of this work to make a rigorous determination of $\alpha_{c,w}$, but an estimate of this value is necessary for modeling cloud drop growth. The purpose of the above discussion and Table 2.1 is to highlight the wide range of measured values in the literature. An estimate of $\alpha_{c,w}$ for modeling purposes herein is based on comparisons of modeled growth in the CFDC-1H with that of measurements at cold temperatures and is constrained by the range of values given in Table 2.1. It is likely that no one accommodation coefficient will exactly match the laboratory results at all sets of conditions given the measurement uncertainties associated the CFDC. However, a single value representing the mass accommodation coefficient is used throughout all simulations for modeling drop growth.

2.2.2.3 Growth in Transition: Inhibition to Heat Transfer

As with water vapor diffusivity, there exists a kinetic barrier to molecular heat transfer. To represent this kinetic barrier, there is an equation analogous to Eq. 2.30 for the thermal conductivity. This modified thermal conductivity is given in *Pruppacher and Klett* [1997] as

$$k_a^* = \frac{k_a}{\frac{r_d}{r_d + \Delta_T} + \frac{k_a}{r_d \alpha_T \rho_a c_{p,a}} \left(\frac{2\pi M_a}{\mathcal{R}T_r} \right)^{\frac{1}{2}}} \quad 2.31$$

Note the similarities between Eqs. 2.29 and 2.30: here D_v is replaced by the thermal conductivity, k_a , in the numerator, Δ_T and α_T represent the thermal jump distance and accommodation coefficient respectively, and $\frac{k_a}{\rho_a c_{p,a}}$ is the thermal diffusivity of air. Although research on the thermal accommodation coefficient is considerably sparser than that on the mass accommodation coefficient (*Pruppacher and Klett* cite one reference prior to 1997), the literature values from recent works are in line with each other and close to unity. It is interesting to note that *Mozurkewich* [1986] suggests that there is no reason to believe that the thermal accommodation coefficient is greater than the mass accommodation coefficient; that is, it is not likely that a molecule will come into thermal equilibrium without being accommodated by the drop thus suggesting that, based on the consensus that α_T is greater than 0.1, the mass accommodation coefficient must be closer to one than suggested by others such as *Shaw and Lamb* [1999]. Some values of α_T from recent works are given in Table 2.2.

Table 2.2. A survey of recent values of the thermal accommodation coefficient (α_T) used for drop growth in the transition regime.

Reference	Method	Value
<i>Shaw and Lamb</i> [1999]	Homogeneous freezing of drops in an electrodynamic trap	0.1→1.0
<i>Li et al.</i> [2001]	Uptake of ^{17}O -labeled water vapor in a droplet train flow reactor	1 (280 -258 K)
<i>Winkler et al.</i> [2004]	Droplet growth in an expansion cloud chamber	1.0 (250 – 290 K)
<i>Vieceli et al.</i> [2004]	Molecular dynamics simulations	0.99
<i>Fukuta and Myers</i> [2007]	Drop growth in a horizontal diffusion chamber	0.81±0.07
<i>Jakubczyk et al.</i> [2007]	Evaporation of drop in electrodynamic trap	0.7±0.2 (277 – 298 K)

2.2.2.4 Growth in Transition: Bridging the Gap between Kinetic and Diffusion

Controlled Growth

Recognizing the effects of solute and the drop curvature on the equilibrium vapor pressure, assuming that the drop temperature is approximately that of the ambient temperature, and substituting the modified diffusivity and conductivities from Eqs. 2.30 and 2.31 into Eq. 2.29, the final form of the drop growth equation used in the following simulations is

$$r_d \frac{dr_d}{dt} = \frac{S_w - a_w \text{Ke}}{\frac{\rho_s \mathcal{R} T_\infty}{e_{s,w}(T_\infty) D_v^* M_w} + \frac{\mathcal{L}_e \rho_w}{k_a^* T_\infty} \left(\frac{\mathcal{L}_e M_w}{T_\infty \mathcal{R}} - 1 \right)} \quad 2.32$$

Here, ρ_s is the aqueous solution density and is determined via volume additivity

[*Brechtel and Kreidenweis*, 2000]. According to *Pruppacher and Klett* [1997]. When

compared with the fully implicit set of equations, Eq. 2.32 agrees within a few percent, a reasonable error given the uncertainty found in the kinetic parameters and the CFDC measurement technique. In the simulations that follow, the mass and thermal jump distances are assumed to contribute negligibly to the estimate of the accommodation coefficients as in *Fukuta and Walter* [1970] and are set to 0. Given the limited effect of the thermal accommodation coefficient on drop growth under the conditions simulated and the small range of literature values, the thermal accommodation coefficient is assumed to have a value of one in this work.

2.3 Homogeneous Ice Nucleation

Homogeneous freezing of concentrated solution drops proceeds at measurable rates at temperatures below 235 K. Many researchers have carried out extensive studies of the freezing behavior of salt solutions. Typically, the common basis for quantifying the homogeneous freezing process is classical nucleation theory. The use of classical nucleation theory is limited by the applicability of macroscopic properties such as surface tension and solution density to a microscopic process. Nevertheless, researchers have applied this theory to explain observed rates of nucleation as a function of temperature and time. The fundamental parameter which describes the nucleation process is the nucleation rate J_{HF} . Recognizing that nucleation is a stochastic process, one can calculate the fraction of particles freezing over a given time (Δt) for a given drop volume (V_d) using the following equation

$$f_{HF} = 1 - \exp(-J_{HF}(T)V_d\Delta t) \quad 2.33$$

For inorganic salts, two widely used formulations of J_{HF} have arisen. The first was put forth by *Sassen and Dodd* [1988]. In this parameterization of homogeneous freezing, the authors use a combination of theoretical and experimental rate parameterizations for pure water drops. However, rather than using the ambient temperature T to determine the rate of nucleation in solution drops, *Sassen and Dodd* used an effective temperature which related the freezing point depression resulting from the introduction of the solute to the melting point depression. This effective temperature was calculated as

$$T^* = T + \lambda\delta T \quad 2.34$$

where δT is the melting point depression and λ is the parameter that relates the melting point depression to the freezing point depression. In their work, *Sassen and Dodd* took the average value of a variety of solutes from *Rasmussen* [1982] ($\lambda \approx 1.7$), indicating that the presence of a solute depresses the onset of homogeneous freezing from that of pure water. For a variety of solutes, previous researchers have found values of λ ranging from 1.4 to 2.2 [*DeMott*, 2002]. However, the studies of *Cziczo and Abbatt* [1999] and *Wise et al.* [2004] both indicated $\lambda < 1$ for ammonium sulfate; *Wise et al.* hypothesized that this was attributable to the stochastic nature of nucleation. On the other hand, the work of *Bertram et al.* [2000] suggest $\lambda \leq 1.7$

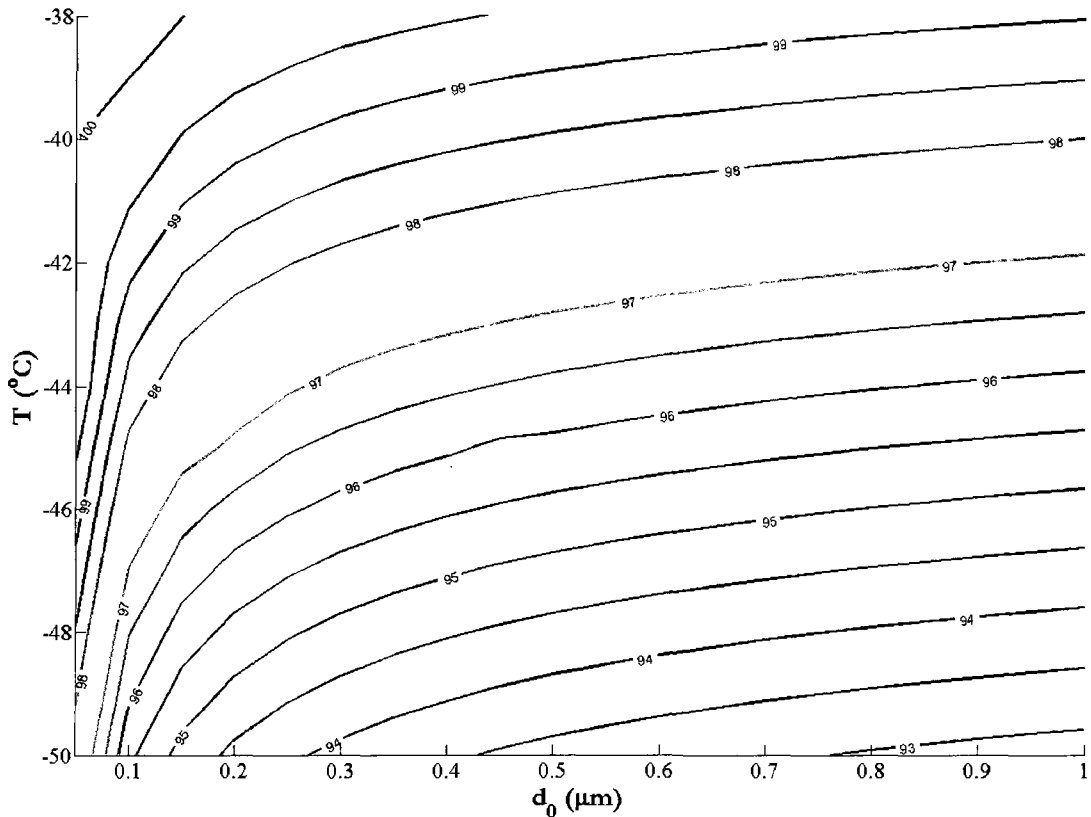


Figure 2.7. Contours of the estimated activation RH_w (%) for ammonium sulfate as a function of the initial dry diameter (d_0) and the temperature (T) for a Δt of 3 seconds and a probability of nucleation of 0.1% ($f_{HF} = 0.001$). Droplets formed on particles with the initial dry diameter d_0 are assumed to be at equilibrium.

while that of *Chen et al.* [2000] suggests a slightly larger λ ; both, however, are well within the range given in *DeMott* [2002].

The other widely used parameterization of homogeneous freezing of solutions was put forth by *Koop et al.* [2000]. In that study, *Koop et al.* hypothesized that freezing behavior of supercooled solutions is not a function of the nature of the solute; rather, it is a function of a_w . Their results indicate that the kinetic process of nucleation is driven entirely by the thermodynamic quantity $\Delta a_w = a_w - a_w^i$ which

they term the water activity criterion. The quantity a_w^i is the ice water activity which is the saturation vapor pressure of ice at temperature T (Eq. 2.7) over the saturation vapor pressure over water at temperature T (Eq. 2.6). Given the general acceptance of *Koop et al.*'s parameterization of homogeneous freezing by the atmospheric science community, it is used in this work to model this process. It is important to note that the parameterization is based on freezing onset conditions for a variety of solutions. Although the authors suggest that the nature of the solute does not play a role in the freezing behavior, there is a considerable amount of scatter about the ice line in the parameterization resulting in an uncertainty in the water activity on the order of ± 0.025 . While this may be attributable to measurement uncertainties, this may also arise due to small contributions from compositional differences.

From Table 1 in *Koop et al.*, the homogeneous freezing rate is given as

$$\begin{aligned} \log[J_{HF}/cm^{-3}s^{-1}] \\ &= -906.7 + 8502\Delta a_w - 26924 (\Delta a_w)^2 \\ &\quad + 29180(\Delta a_w)^3 \end{aligned} \tag{2.35}$$

According to *Koop et al.*, the valid range of Δa_w is 0.26 to 0.34. Since the thermodynamic criterion is a function not only of the solution concentration but also of the mechanical pressure

$$\Delta a_w = a_w(c^{eff}, T, 0) \exp\left(\int [v_w(C, T, p) - v_i(C, T, p)] dp / RT\right) - a_w^i(T, 0) \quad 2.36$$

where v_w and v_i are the partial molar volume of water and ice respectively. From Table 1 in *Koop et al*, the value of the integral is given as

$$\begin{aligned} \int (v_w - v_i) dp = & [-230.76 - 0.1478 T + 4.099.2 T^{-1} \\ & + 48.83 \ln(T)] \\ & \times \left[p - \frac{1}{2} \kappa_T^0(T, p) p^2 - \frac{1}{6} \left(\frac{\partial \kappa_T^0}{\partial p} \right) p^3 \right] \\ & - [19.43 - 2.2 \times 10^{-3} T + 1.08 \times 10^{-5} T^2] \\ & \times \left[p - \frac{1}{2} \kappa_T^i p^2 - \frac{1}{6} \left(\frac{\partial \kappa_T^i}{\partial p} \right) p^3 \right] \end{aligned} \quad 2.37$$

where p is the internal drop pressure, κ_T^0 is isothermal compressibility of pure water at ambient pressure (1.6 GPa^{-1}), $\partial \kappa_T^0 / \partial p$ is the pressure dependence of this parameter (-8.8 GPa^{-2}), κ_T^i is the isothermal compressibility of hexagonal ice at ambient pressure and $\partial \kappa_T^i / \partial p$ is the pressure dependence of this parameter (-0.17 GPa^{-2}). In Eq. 2.37, the internal drop pressure p is

$$p = \left(\frac{2\sigma_{sol}}{r_d} + e_{s,w} \right) \quad 2.38$$

Onset conditions as a function of the dry diameter are shown in Figure 2.7 for ammonium sulfate. The onset RH_w is calculated for a drop in equilibrium with the

environment at $f_{HF} = 0.001$. Note the strong size dependence of the onset RH_w for droplets with initial dry diameters smaller than 200 nm, particularly at lower temperatures.

2.4 Diffusional Crystal Growth

As in *Pruppacher and Klett* [1997], growth of crystals is treated similarly to the growth of drops (Chapter 2.2.2.4) by making use of an analogy between the governing equation and boundary conditions in electrostatic and diffusion problems. Using this analogy, we can assign a capacitance C to the growing crystal (for a more complete discussion, see *Pruppacher and Klett*) such that

$$\frac{dm}{dt} = -4\pi D_v C (\rho_{v,r} - \rho_{v,\infty}) \quad 2.39$$

Under the assumption that ice crystals in the CFDC are essentially spherical ($C = 1$) and noting the similarity between Eqs. 2.23 and 2.39, the diffusional crystal growth equation may be written as

$$r_d \frac{dr_d}{dt} = \frac{s_i}{\frac{\rho_s \mathcal{R} T_\infty}{e_{s,i}(T_\infty) D_v^* M_w} + \frac{\mathcal{L}_s \rho_w}{k_a^* T_\infty} \left(\frac{\mathcal{L}_s M_w}{T_\infty \mathcal{R}} - 1 \right)} \quad 2.40$$

Here, the effects of the solute and curvature are assumed to be negligible.

As with drop growth, water vapor molecules must be accommodated by the ice crystal lattice and once again the kinetic effects must be taken into account through the thermal and mass accommodation coefficients (α_T and $\alpha_{c,i}$ respectively),

utilizing the modified diffusivity and conductivity in Eq. 2.30 and 2.31. As there are no studies available on the thermal accommodation coefficient with respect to ice, we must assume that the value is similar to that of liquid water (that is unity).

In contrast, there has been extensive research on $\alpha_{c,i}$, particularly at low temperatures (< 200 K). In typical experiments, researchers measure the rate of adsorption or desorption of water vapor from an ice surface [*Brown et al.*, 1996; *Haynes et al.*, 1992; *Libbrecht*, 2003; *Sadtchenko et al.*, 2004]. The value that is actually measured in these experiments is the uptake coefficient, γ . As *Kulmala and Wagner* [2001] discuss, γ differs from $\alpha_{c,i}$ in that it measures the actual probability of a vapor molecule sticking rather than the probability associated with kinetic inhibition. According to *Kulmala and Wagner*, for Knudsen numbers (Kn; the mean free path of the gas divided by a characteristic length scale, such as particle diameter) much greater than 1, $\gamma \rightarrow \alpha_{c,i}$. For smaller Kn, the measurement of the uptake coefficient will tend to under-estimate the value of the condensation coefficient. In most cases, this larger Kn criterion is satisfied. In at least one recent paper, this does not seem to be the case [*Libbrecht*, 2003]. The values of $\alpha_{c,i}$ are fairly wide ranging from these experiments (0.1 to 1.0) with some showing a temperature dependence [*Haynes et al.*, 1992; *Pratte et al.*, 2006] (though the two differ as to the sign of that dependence).

Magee et al. [2006] approached the problem of finding $\alpha_{c,i}$ using an electrodynamic balance to measure the rate of mass addition and modeled the growth of crystals using a cloud particle model. Using this technique, they estimated $\alpha_{c,i}$ between 0.0045 and 0.0075. Their measurements, made close to ice saturation, indicated that the condensation coefficient was also dependent on the saturation ratio. *Gierens et al.* [2003] produced a similar value by comparing simulations with results from the INCA campaign. Finding the value difficult to reconcile with experimental data, the authors suggested that the discrepancy lay in the fact that $\alpha_{c,i}$ depends on the size of the crystal, citing the fact that previous research was primarily performed on larger crystals.

Using observations of ice saturation ratios near the tropical tropopause, *Jensen et al.* [2005] suggest that, barring uncertainties in water vapor partial pressure, $\alpha_{c,i}$ lower than 0.0001 are required to simulate the observed values of ice supersaturation occasionally observed in the tropical troposphere. *Kay and Wood* [2008] conducted parcel model studies to infer a lower bound of 0.1 on the value of $\alpha_{c,i}$ at high S_i . *Ström et al.* [2003] also constrained $\alpha_{c,i}$ to values greater than 0.1 using measurements from INCA. However, the authors note that the low number of ice crystals observed in some studies (such as *Jensen et al.*) might be confounding to their model results but could possibly be explained by very low updrafts or if small crystals fall below the limit of detection for the measurement.

As with $\alpha_{c,w}$, $\alpha_{c,i}$ in this study is determined via comparison of simulations with experimental work. Although there is evidence of temperature and vapor concentration dependencies for this value, the uncertainties in the measurement technique (CFDC) within the limited temperature range examined inhibit observation of these variations. Therefore, the value in this study will be constant and constrained by the broad range of values found in the literature.

3 EXPERIMENTAL METHODOLOGY

3.1 Overview of the CFDC

3.1.1 Early Development of the CFDC

The concept of the CFDC was developed in the early 80's and the original design is discussed in [*Rogers, 1988*]. The original instrument differed significantly from the current field implementation. It consisted of two concentric cylinders 0.46 m in length (with the last 0.1 m of the inner wall encased in 0.0025 m thick closed cell foam serving as a thermally insulating vapor barrier) and 0.08 and 0.1 m in diameter. The chamber was initially designed to operate at temperatures ranging from 263 to 253 K and saturations ranging from 0.9 to 1.1. *Rogers* operated the original CFDC at total flow rates ranging from 4 to 10 lpm. One important operational difference between the original instrument and the current instrument is the arrangement of the walls: in the original instrument the outer wall served as the cold wall while the inner wall served as the warm wall. In contrast, as the temperature range was extended to considerably lower temperatures, the walls are

now reversed in the current version of the field instrument such that the chamber is operated with the cold wall on the inside. The whole chamber in the original version was wrapped in rigid foam 0.05 m thick and enclosed in an 8" PVC pipe.

In further studies, *Rogers* [1994] recommended three changes to the chamber to improve the performance: (1) inclusion of a refrigeration system that allowed temperatures below the homogeneous freezing limit to be probed, (2) increasing the chamber length and (3) splitting the insulating sleeve on the warm wall with refrigeration coils allowing the study of nucleation through droplet evaporation. These recommendations led to the next iteration of the CFDC – the first aircraft version of this instrument [*Rogers et al.*, 2001]. The development of this version was shaped by requirements for aircraft operation which put limitations instrument size, weight and power consumed. Limitations on size are equivalent to limitations on particle residence time whereas the weight and power consumed would have important implications for the type of refrigeration system used and therefore the temperatures the instrument could reach.

Rogers [1988] studied the performance of the chamber using both mathematical models and laboratory experiments. In his modeling studies, *Rogers* determined that for particle concentrations less than 3000 cm^{-3} , the presence of the aerosol had no significant effect on the vapor field. By analyzing the response of the optical particle counter (OPC) to a pulse of lab generated aerosol, *Rogers* [1988] found

the flow to be laminar at smaller wall temperature differences while potentially turbulent at larger gradients, assuming that the dispersion in the pulse was attributable to the recirculation region protruding into the lamina; these results were corroborated in *Rogers* [1994].

3.1.2 Introduction of the CFDC-1H

In 2006, researchers at CSU developed a modified design of the first field version of the CFDC for operation on the NCAR Gulfstream (CFDC-1H). While much of the previous design was retained, CSU researchers made several minor changes based on CFD analysis of the first version of the field CFDC [*Rogers et al.*, 2004; *Straub et al.*, 2004]. However, the primary difference between the CFDC-1H and the previous field instrument lay in how the evaporation system is operated. In the *Rogers et al.* [2001] design, the evaporation region consisted of PVC on the lower third of the outer wall. The PVC was intended to act as a hydrophobic surface with low thermal conductivity such that the temperature of the wall would relax to that of the inner wall thus resulting in a region of ice saturation. However, laboratory tests indicated that the PVC did not relax to the cold wall temperature and ice crystals were evaporating in this region. In the CFDC-1H, the evaporation portion of the outer-wall is constructed of copper and actively cooled to the inner wall temperature.

The field version of the CFDC-1H (Figure 3.1) can be conceptually divided into four different sections. In the first section, the sample flow is introduced

through a thin annular gap (0.010") at the top of the chamber. The purpose of the small gap width is to create a large pressure drop which should ensure even distribution of the flow through the annulus. In the current field version, the annular gap is created by two 'blades' constructed of stainless steel. The inner portions of these blades are flat. At the outer tip of the inlet blades, the blades are chamfered with an angle of 45°. The sample flow is confined to a narrow portion of the chamber via a particle free sheath flow. The sheath flow enters the chamber through two rings of 72 holes arranged about the inlet blades. The holes are approximately 0.043" in diameter.

The next section of the chamber consists of the region in which the walls are constructed of copper and are coated with ice. This region is 31.75" in length. While the inner wall is a continuous piece of copper maintained at a single temperature, the outer wall is divided into two separate pieces of copper separated by a Delrin (DuPont; Wilmington, DE) collar. The gap created by the collar between the two walls is 0.5". On the outer portion of the two copper cylinders the collar extends 1.5" in both directions.

The cylinders comprising the outer wall are maintained at two distinct temperatures. In the current configuration, the upper portion of the outer wall is maintained at a temperature warmer than that of the inner wall. The lower portion is maintained at the same temperature as the cold (inner) wall. This generates a region

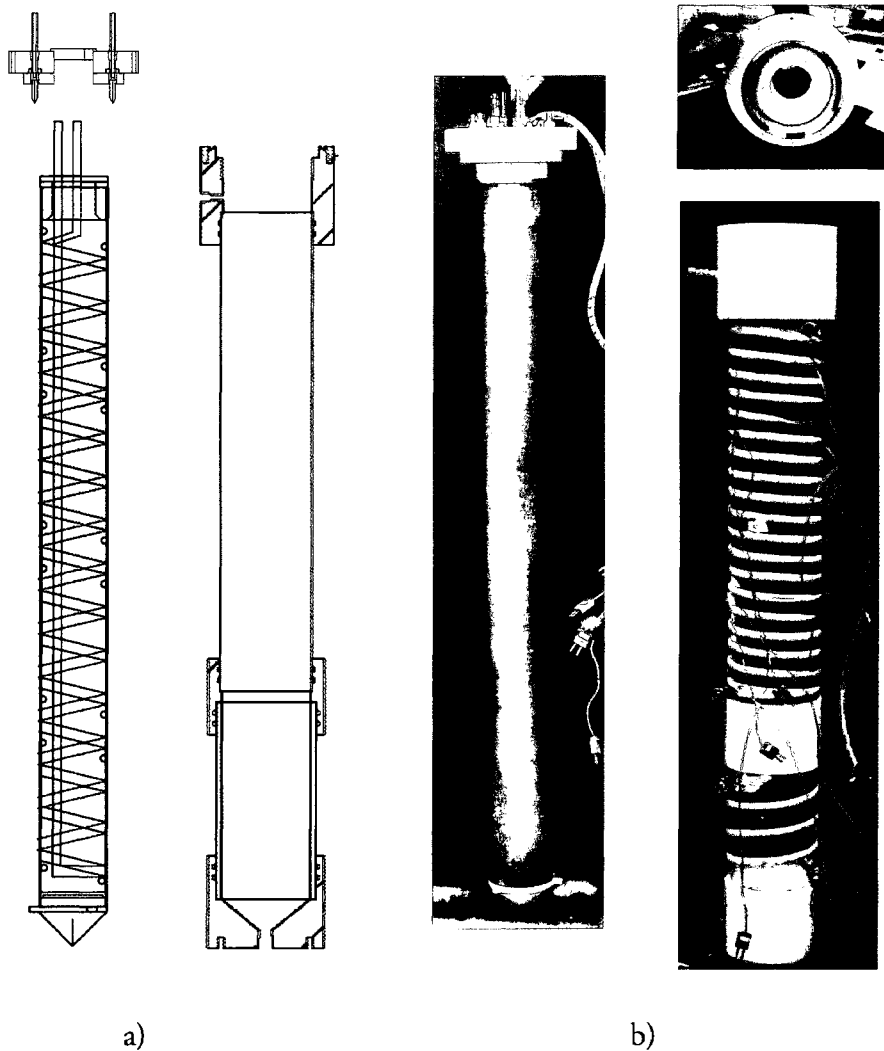


Figure 3.1. Overview of the CFDC. a) Mechanical drawings of (counter-clockwise from top) the inlet, inner wall and outer wall. b) Images of the disassembled chamber.

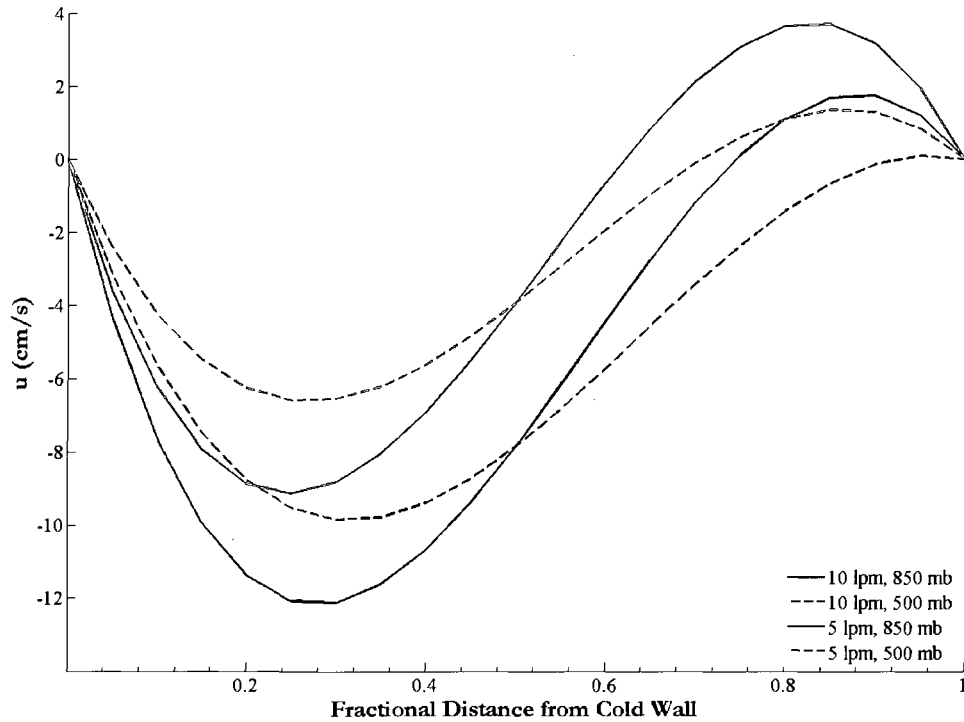


Figure 3.2. An example of the analytic solution to the steady state flow profile as given in [1988] for the same wall temperatures ($T_i = -49.5^\circ\text{C}$ and $T_o = -32^\circ\text{C}$) but different flow conditions.

which is saturated with respect to ice and subsaturated with respect to water (by up to $\sim 45\%$, depending on the temperature), a region in which ice crystals maintain their final size while drops evaporate thereby creating a difference in size between drops and crystals which can be detected by an OPC.

3.1.3 Steady-State Flow Profile

In a domain bounded by differentially heated, vertically-oriented plates as in the CFDC, flow is characterized by a superposition of a buoyant circulation and a viscous (Poiseuille) flow. This superposition of free and forced convection results in a flow profile for which the maximum downward velocity is skewed toward the cold

wall. The steady-state velocity profile as a function of the gap width may be calculated as in *Rogers* [1988]

$$u(x, \Delta T) = \frac{3}{2} \bar{u} \left(1 - \left(\frac{x}{d} \right)^2 \right) + \frac{\rho_a U g d^2 \Delta T}{12\mu} \left[\left(\frac{x}{d} \right)^3 - \frac{x}{d} \right] \quad 3.1$$

where \bar{u} is the average velocity in the gap (Q_t/A_c , where Q_t is the total flow rate and A_c is the cross sectional area of the annular region of the chamber), x is the distance from the center line, d is the gap half-width, g is gravity, U is the volume expansion coefficient of air ($1/\bar{T}$) and ΔT is the temperature differential between the two walls. Several velocity profiles predicted by Eq. 3.1 are shown in Figure 3.2. A similar solution for the velocity profile given between vertically-oriented plates maintained at two different temperatures is given in a nondimensional form by *Boulama and Galanis* [2004].

As shown in Figure 3.2, for a given flow rate and pressure, large temperature gradients result in flow profiles in which the motion along the warm wall is upward. Given that the Reynolds number of the flow throughout the chamber is small ($Re < 100$), one might expect that the flow is laminar. If the flow is laminar, then the sample is confined to a narrow region centered near the velocity maximum, the width of which will be a function of the temperature difference between the inner and outer walls as well as the ratio of the total flow to the sample flow and the fluid density. From *Rogers* [1988], the lamina position may be located (assuming that the

sample flow is bounded by half of the sheath flow on either side) by integrating Eq.

3.1 across the lamina width

$$(1 - q) \frac{Q_t}{2} = \frac{Q_t}{2\bar{u}d} \int_b^d u dx = \frac{Q_t}{2\bar{u}d} \int_{-d}^a u dx \quad 3.2$$

where a and b are the distances of the lamina sample boundaries from the geometric center line and q is the fraction of flow represented by the aerosol sample.

However, at large enough temperature gradients the flow will be unstable to perturbations and transitions to turbulence may occur despite the low Reynolds number. This transition is highly dependent on the orientation and geometry of the domain studied and is characterized by the Rayleigh number (Ra), a non-dimensional parameter that is the product of two other non-dimensional numbers: the Grashof number and the Prandtl number. The Grashof number is the ratio of the buoyancy force in a free convective flow to the shear force. The Prandtl number is the ratio of momentum diffusivity to thermal diffusivity. In convective flows, this number will control the relation between the velocity and thermal profiles. The Rayleigh number may be written for the CFDC as

$$Ra = \frac{c_{p,a} g \rho_a^2 \Delta T (2d)^3}{\mu_a k_a \bar{T}} \quad 3.3$$

Here, $c_{p,a}$ is the specific heat of air at constant pressure and \bar{T} is the average temperature between the two plates. For operations between 223 and 213 K (as in the work presented in this research), Ra is on the order of 10^8 .

High Ra flow stability is a source of ongoing research and is complicated by dependencies on the flow geometry. In some cases, high Ra such as this can result in flow unstable to perturbations. In these instances, flow exposed to perturbations will transition from the laminar regime to a turbulent one. The mixing associated with turbulence will result in dispersion of the aerosol. This in turn should result in a nucleation signal containing a considerable amount of dispersion as the aerosol is exposed to a wide range of saturations. As discussed in the experimental results, this dispersion in the nucleation signal was generally never observed.

3.1.4 Growth Region Thermodynamics

As with previous analyses of diffusion chambers, *Rogers* [1988] assumed that the convective portion of the flow had little influence on the thermodynamic profile established in the growth region of the chamber. By solving the equations for heat and water vapor flux across a static air gap, *Rogers* developed a linear relation for the water vapor partial pressure and temperature profiles. For the water vapor partial pressure, *Rogers* assumed that the partial pressure at the walls was that of ice saturation at the measured wall temperature. By solving the equation describing Fick's second law of diffusion and truncating the higher order terms, he found that the water vapor partial pressure as a function of the distance from the cold wall x in the growth region could be written as

$$e = e_{s,i}(T_c) + \frac{e_{s,i}(T_w) - e_{s,i}(T_c)}{\Delta x} x \quad 3.4$$

where T_w and T_c are the warm and cold wall temperatures and Δx is the gap width (1.1 cm). Similarly, the temperature profile is found by solving Fourier's law of heat conduction. This results in an equation analogous to that of Eq. 3.4 for temperature:

$$T = T_c + \frac{T_w - T_c}{\Delta x} x \quad 3.5$$

The resulting T and SS_w profiles along with the corresponding lamina positions for

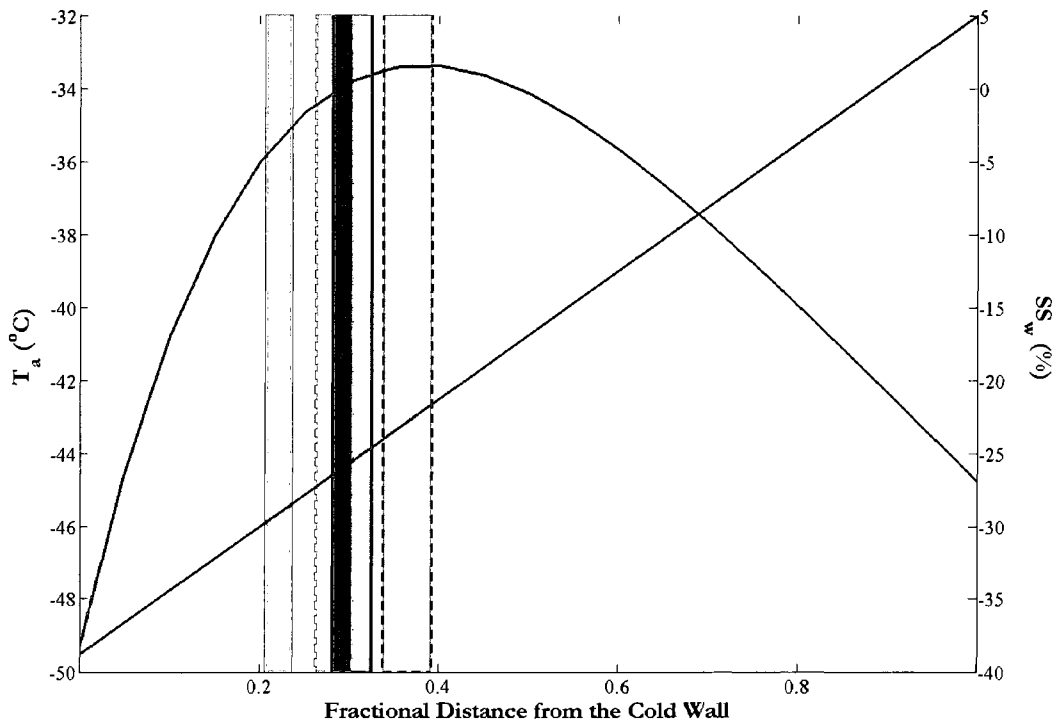


Figure 3.3. Illustration of the conditions within the lamina for the four cases given in Figure 3.2. The lamina are shown as filled rectangles for the four flow cases in Figure 3.2. Red represents the 5 lpm case while the black indicates the 10 lpm case. Boxes enclosed by a dashed line indicate the 500 mb case while the solid indicate the 850 mb case.

the conditions given in Figure 3.2 is shown in Figure 3.3.

3.1.5 Uncertainty in the Growth Region Conditions

As discussed above, the thermodynamic conditions within the chamber are inferred based on measurements of chamber pressure, wall temperatures and flow rates. The growth region thermodynamic conditions generally reported are those calculated at the average lamina position. The solution for the lamina position is not straightforward and requires the use of numerical routines thus making the calculation of uncertainty in the conditions more complex than propagation of error. A simple way to overcome this is to employ Monte-Carlo methods (MCm) in the solution of the analytic equations. These methods rely on random sampling to estimate an inferred value for which an exact result is difficult to measure and have been used in other studies to compute uncertainty [*Doser et al.*, 1998].

Table 3.1. CFDC-1H measurement uncertainties.

Measurement	Uncertainty	Units
Total and sheath flow rates	±0.17	slpm
Temperature	±max(1° or 0.4% of the absolute value of the reading)	°C
Pressure	±12.18	Mb

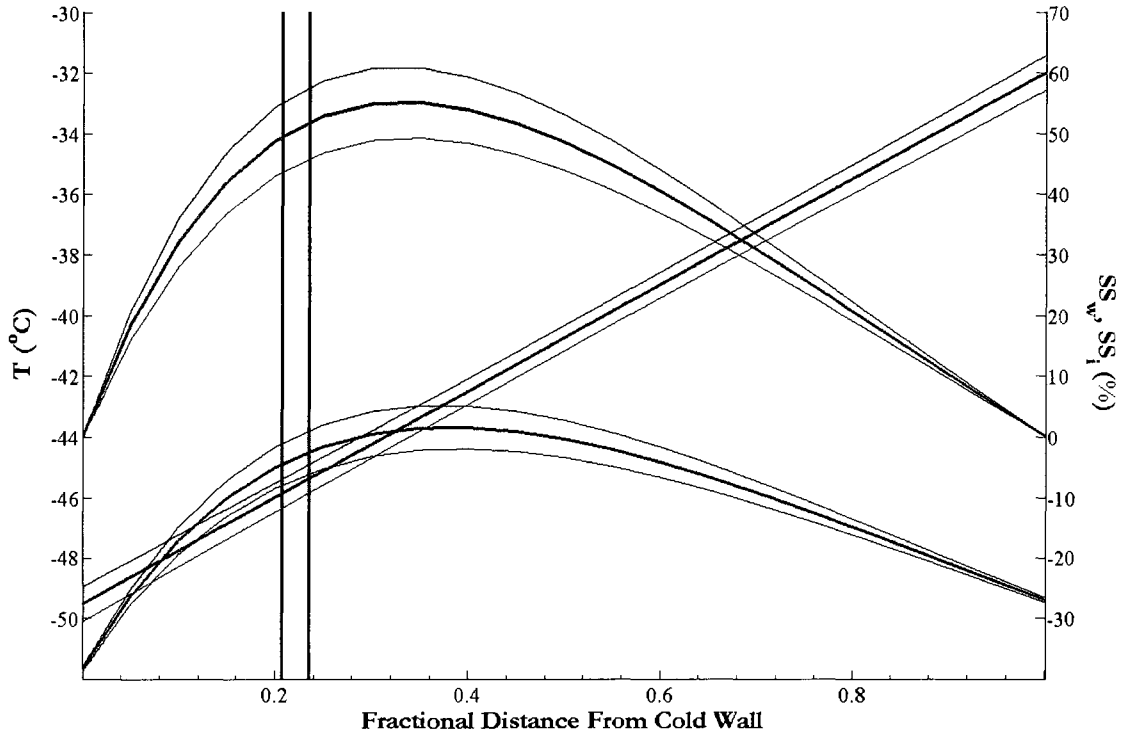


Figure 3.4. Illustration of thermodynamic profile for values in the above figures. Total flow is 5 lpm and the pressure is 850 mb for the lamina position shown.

In the MCm simulations conducted here, Gaussian noise was applied to the values of the measurements over the ranges of the uncertainties of the measurements for N trials (Table 3.1). The simulation was run with $N=1000$ to gather reasonable statistics for the final estimation of uncertainty; however, repeated MCm simulations indicate that the results are relatively insensitive to the number of trials beyond 100. As in the discussion of the MCm by *Doser et al.* [1998], the final uncertainty of the measurement is then determined from

$$s_x = \sqrt{\frac{1}{N} \sum_{i=1}^N (x_i - \bar{x})^2} \quad 3.6$$

where x_i is the estimate of the inferred thermodynamic condition with applied measurement noise and \bar{x} is the mean value of that measurement. Here, x is SS_w , SS_i or T_a . Uncertainties for one set of conditions given in Figure 3.3 are shown in Figure 3.4.

The MCM indicates that the uncertainties in the values of saturation are a function of the operational temperature and the temperature gradient across the sample gap (or SS_w). The value of the uncertainty of the average lamina temperature is insensitive to the wall temperatures and operational conditions and is approximately ± 0.5 K. Values of the uncertainties associated with the other variables are shown in Table 3.2 for average lamina temperatures relevant to this study and near water saturation. From Table 3.2, it is apparent that the uncertainty in the values of the supersaturations to which the aerosol is exposed is quite large. However, measurements of the onset conditions for homogeneous freezing using a well characterized aerosol (such as ammonium sulfate) should provide a reference with which to constrain measurements using this instrument.

Table 3.2. Measurement uncertainty at the average lamina position for four different temperatures near water saturation. The three sets of uncertainty shown are for the lamina temperature (s_{Ta}), supersaturation with respect to water (s_{ssw}) and supersaturation with respect to ice (s_{ssi}).

	T_a				
	233 K	228 K	223 K	218 K	213 K
s_{Ta} (K)	0.50	0.49	0.52	0.51	0.50
s_{ssw} (%)	3.24	3.76	4.1	4.42	4.9
s_{ssi} (%)	5.15	6.22	7.12	8.0	9.20

3.1.6 Optical Detection of Ice Nucleation

Observation of ice nucleation is based on the final particle size. Given that the CFDC-1H consists of a growth region *followed* by an evaporation region, there should be a considerable difference in size between ice crystals and those particles that did not nucleate ice (interstitial aerosol and haze drops). The CFDC OPC detects particles larger than about 300 nm exiting the chamber. The OPC in the CFDC-1H is a Climet 3100 (Climet Instruments Co.; Redlands, CA). The OPC uses a laser diode with a peak power of 50 mW at 655 nm and is configured to operate at 10 mW. The optics consist of an elliptical light collecting mirror. The intensity of the scattered light will be proportional to the size of the particle which in turn produces a voltage pulse in a silicon photo diode. A multi-channel analyzer card (MCA, Ortec; Oak Ridge, TN) collects the voltage pulses from the OPC and in turn classifies the pulses into discrete ranges. In the CFDC-1H, the pulses are discretized over approximately 190 channels and delivered to the CFDC-1H data acquisition software (DAQ).

The response of the OPC is sensitive to a variety of particle parameters besides size: refractive index, shape, and surface characteristics being chief among these. In addition, the response is sensitive to the flow rate at which the OPC is operated at; lower flow rates will increase the residence time in the sensing volume and therefore decrease the range of sensitivity for a given operational gain. For the CFDC-1H, the OPC may operate in three separate ranges or gains, referred to here as high, medium and low; however, only the high and medium gains were utilized in this study. The OPC is most sensitive to particle size in high gain. Here, the range of sizes accurately detected is limited to at most 300 nm to 2 μm at 10 lpm. In medium gain, the discernable particle size range is limited to approximately 2 μm to 5 μm at 10 lpm. In each case, particles larger than the upper size limit will be counted but their size will be unresolved.

Prior to operation, the OPC was calibrated using monodisperse aerosol for both high and medium gain. The calibration determined the response of the OPC as a function of particle size and flow rate. For particles smaller than 2 μm , a nebulizer was used to generate polystyrene latex particles (PSL; Duke Scientific Corp.; Palo Alto, CA). PSL have a refractive index (n) of 1.59 at a wavelength of 589 nm and a density (ρ_{PSL}) of 1.05 g/cm³. For larger sizes, a vibrating orifice aerosol generator [VOAG; *Berglund and Liu*, 1973] was used to produce larger particles of oleic acid ($n = 1.46$ at 589 nm, $\rho_{OA} = 0.89$ g cm⁻³). Particles sizes generated by the VOAG were

monitored by an aerodynamic particle sizer (APS; TSI 3321). During calibration, the OPC sampled a monodisperse aerosol for 30 to 60 seconds. The spectra shown below from the calibrations are averages over the sampling periods.

Results from the calibration are shown below for 10 lpm in high gain (Figure 3.5) and 10 lpm and 5 lpm in medium gain (Figure 3.6). From these plots it is apparent that the response of the OPC is broad for a monodisperse sample. Particle sizes are generally associated with the channel that resides near the peak. However, in practice, the broad peak can make it difficult to associate a single size with a single

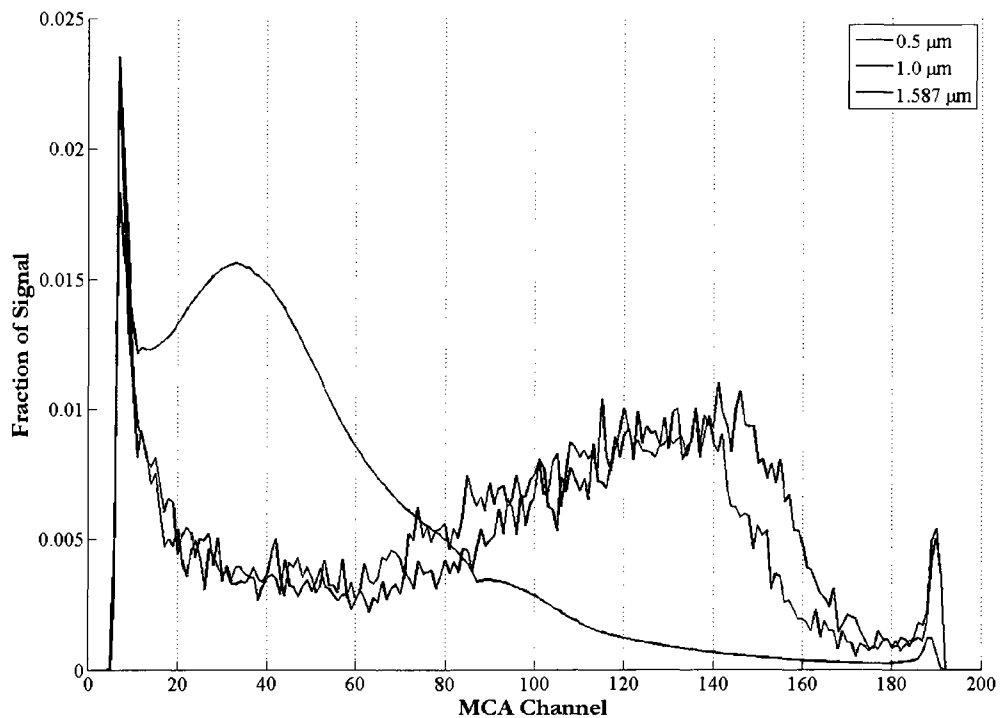


Figure 3.5. Results of calibration at 10 lpm in the OPC high gain. Although there are no results from 2 μm calibration, channel 180 (maximum channel being 191) is sufficient for distinguishing ice in high gain (as suggested from prior calibrations). This channel was used for discernment of ice in all experiments run at 10 lpm.

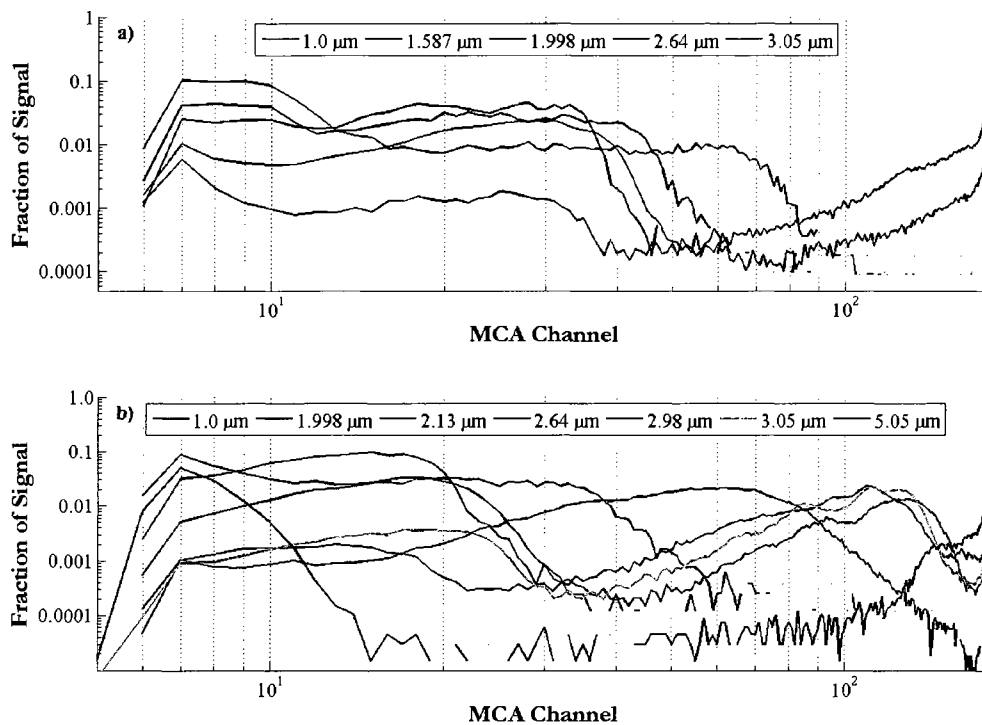


Figure 3.6. Results of medium gain calibration for a) 5 lpm and b) 10 lpm. The OPC was operated in medium gain for all experiments at 5 lpm.

channel; so, for the purposes of this study, only those channels for distinguishing ice are identified. As it is desirable to be able to size not just the crystals larger than 2 μm , but perhaps early onset, all experiments run at 10 lpm were conducted with the OPC set to high gain. This allows the observation of the aerosol signal as well as small shifts that may be attributable to the early onset of ice nucleation. The results of the current calibration and comparison with previous calibrations suggest that MCA channel 180 is sufficient to delineate unactivated from activated particles.

At 5 lpm, most particles produced via atomization appear in the upper channels in high gain. Therefore, only medium gain was used for these experiments

and no results are shown for a high gain calibration at 5 lpm. Figure 3.6 suggests that the range of sensitivity is just below a micron to approximately 2.5 μm . Beyond 2.5 μm , the signals start bleeding into the upper channels and it becomes difficult to differentiate between the different particle sizes. Based on Figure 3.6(a), channel 90 should be sufficient though for distinguishing particles greater than 2 μm from smaller particles.

3.2 The Computational Study

Researchers have used CFD in the past to model a variety of different instruments relevant to the study of cloud particle development. *Roberts and Nenes* [2005] constructed a simple grid to numerically solve the conservative equations of fluid dynamics coupled with a cloud particle growth model to assess the performance of a new streamwise thermal gradient CCN counter (CCNc). *Stratmann et al.* [2004] used FLUENT (Ansys, Inc.; Lebanon, NH) and developed a new cloud particle growth package utilizing the power of user defined function (UDF) within the CFD package to model flow dynamics and drop growth in LACIS, a flow tube. *Stratmann et al.* found that particle growth in the model was within the experimental uncertainty of the measurement. *Khalizov et al.* [2006b] modeled the flow dynamics using CFX (Ansys, Inc.; Lebanon, NH) in several different design configurations for aerosol flow tubes (AFT) and found that under operation conditions used in other AFT studies, the residence time of the particles is poorly defined due to zones of recirculation. In this

study, the researchers also found that wall effects can have a profound impact on the aerosol composition. Using the results from this study, the researchers developed a new AFT which was designed to eliminate any turbulent mixing as well as buoyancy driven convection cells [*Khalizov et al.*, 2006a].

Thus far, CFD has been employed successfully within a limited setting to model flow in the field version of the CFDC. *Rogers et al.* [2004] and *Straub et al.* [2004] modeled conditions relevant to heterogeneous nucleation ($T_a > 248$ K) using standard laboratory operating conditions ($Q_t = 10$ lpm and $P = 850$ mb). They found that, for laminar flow, the conditions relaxed approximately to the analytical solution for the conditions in the growth region [*Rogers*, 1988] within 2 seconds along the particle path. *Straub et al.* also modeled turbulent flow using the Reynold's stress model in FLUENT and found that, as expected, particles released from the sample inlet would be well dispersed and the particle residence time (as well as the conditions they are exposed to) would not be well defined.

The computational portion of this study extends the work of *Rogers et al.* [2004] and *Straub et al.* [2004] by first extending the CFD simulations to conditions relevant to homogeneous freezing and then processing the trajectories produced from the CFD simulation using a microphysical model to study cloud particle growth. As in the previous studies, the gas phase is modeled using FLUENT. These simulations model the fluid dynamic and thermodynamic fields as a function of position within

the CFDC-1H. Variables predicted by these simulations include the water vapor mixing ratio, temperature and fluid velocity. This portion of the study allows identification of key features of the flow as well as thermodynamic information required for the second portion of the study.

Information retrieved from the CFD simulations is used to model particle growth along a predicted path. The particle path within the CFDC model is determined using the FLUENT discrete phase model (DPM). Information along these particle trajectories is fed into a microphysical model which solves a set of equations for cloud drop and crystal growth. This model produces a final size distribution of ice crystals. Feeding the trajectories produced via CFD into the microphysical model allows us to evaluate instrument performance.

In some cases, operating conditions modeled in the simulations are not accessible in the current experimental configuration but may be encountered in the field (as is the case for low pressure operation in the upper troposphere); in these instances, the models provide a basis for expectations regarding the performance and motivate further study for developing techniques which allow researchers to fully take advantage of these techniques.

3.2.1 Modeling the Continuous Phase

3.2.1.1 Mesh Generation

The model domain was constructed using FLUENT's geometry and mesh generation software, Gambit (Ansys, Inc.; Lebanon, NH). The geometry of the domain is based on the dimensions of the CFDC-1H. The initial grid was based on a grid topology developed by *Straub et al.* [2004] for operation at warm temperatures. However, at more extreme conditions (i.e. low flow rates and a target temperature of 213 K), the solution exhibited unsteady behavior. In an attempt to determine whether this unsteady behavior was real, the development of the grid went through five different iterations in which the density was increased in what were considered critical regions. As it turned out, the most critical area needing refinement was not the sample inlet, but rather the growth region. This is not totally unexpected as the Rayleigh number in this region is often $> 10^8$, a number that could result in unstable flows as described in Chapter 3.1.3. As the density of the grid was increased, the unsteady behavior of the flow disappeared. The density was considered sufficient when there was no noticeable change in the solution at the more extreme operating conditions.

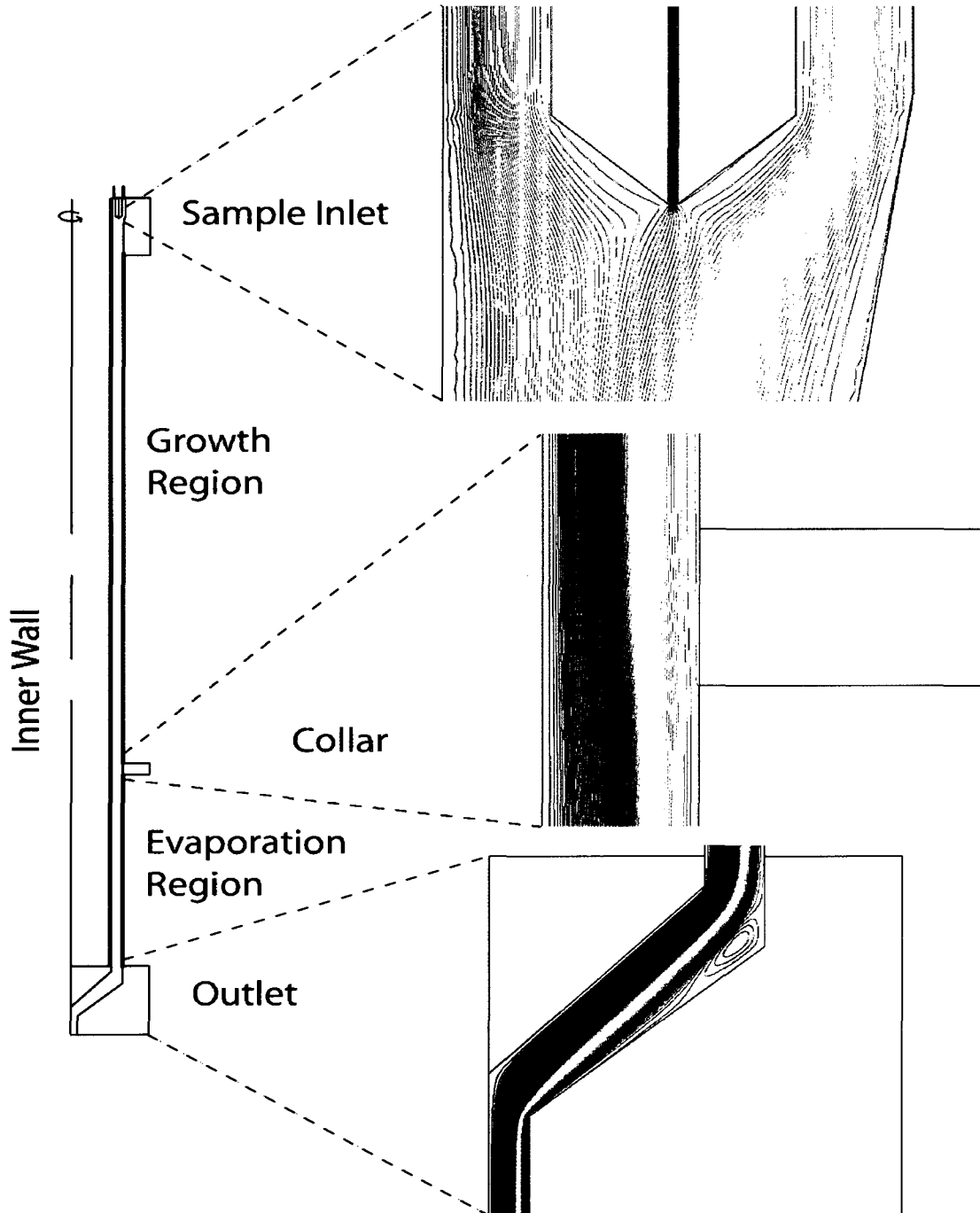


Figure 3.7. Model domain for the CFDC simulations with close-ups of some critical regions showing contours of the stream function from simulations described below. The broken line shows the axis of symmetry.

The final domain, shown in Figure 3.7, is 2D and axisymmetric. The grid consists of a mixture of 2×10^5 quadrilateral and triangular cells. The grid density is greatest in regions of transition such as the sample inlet and the outlet. In the simulations, the region of primary interest is the one that contains the fluid. However, as in *Stetzer et al.* [2008], the solid portions of the chamber are also modeled. Modeling of the solid portions of the chamber allows us to determine the effects of conduction on the thermodynamic and flow profiles, an aspect of heat transfer that was neglected in previous studies. Four of the solid regions are constructed of Delrin (DuPont; Wilmington, DE) and are therefore collected in a single computational zone. These regions are: the outer inlet portion which slides on the outside of the outer wall, the collar which separates the growth region from the evaporation region on the outer wall, the outer portion of the outlet and the outlet cone. The final solid region is the inlet which is constructed of stainless steel. The solid regions are important only in the manner in which they impact the fluid dynamics and mass transfer aspects of the simulations.

3.2.1.2 Properties of the Gas Phase

The gas phase consists of a mixture of water vapor and air. For the set of simulations described in the following sections, the full set of viscous equations (i.e., the Navier-Stokes equations) is solved. The flow in these simulations is assumed to be steady, laminar, and axisymmetric. The conservative form of the continuity,

momentum and energy equations in vector notation are given as [*Anderson Jr.*, 1995; *FLUENT*, 2003]

$$\frac{\partial \rho}{\partial t} + \nabla \cdot (\rho \vec{v}) = 0 \quad 3.7$$

$$\left(\frac{\partial \rho \vec{v}}{\partial t} + \nabla \cdot \rho \vec{v} \vec{v} \right) = -\nabla p + \nabla \cdot \bar{\bar{\tau}} + \rho \vec{f} \quad 3.8$$

$$\frac{\partial}{\partial t} (\rho E) + \nabla \cdot (\vec{v} (\rho E + p)) = \nabla \cdot (k \nabla T - h \vec{j} + (\bar{\bar{\tau}} \cdot \vec{v})) \quad 3.9$$

Here, \vec{v} is the velocity, $\bar{\bar{\tau}}$ represents the viscous stress tensor, \vec{f} is an external body force acting on the fluid and E is the total energy, or the sum of the sensible enthalpies of the different species in the flow and the kinetic energy. In these simulations, the only body force represented by \vec{f} is gravity, which acts parallel to the CFDC axis. The viscous stress tensor may be rewritten in terms of the velocity and the bulk viscosity of the medium

$$\bar{\bar{\tau}} = \mu \left[(\nabla \vec{v} + \nabla \vec{v}^T) - \frac{2}{3} \nabla \cdot \vec{v} I \right] \quad 3.10$$

where I is the identity tensor and μ is the viscosity. The simulations for these experiments use a temperature dependent viscosity described by Sutherland's law [*Sutherland*, 1893],

$$\mu = \mu_r \left[\left(\frac{T}{T_{S,0}} \right)^{3/2} \left(\frac{T_{S,0} + S_\mu}{T + S_\mu} \right) \right] \quad 3.11$$

where μ_r is a reference viscosity ($1.833 \times 10^{-5} \text{ kg m}^{-1}\text{s}^{-1}$) at the reference temperature $T_{S,0} = 293.15 \text{ K}$ and $S_\mu = 110.4$ is the Sutherland interpolation constant. For steady-flow, as in these simulations, the time dependent portion of any of the equations solved will disappear.

The right hand side of the energy Eq. 3.9 contains the heat transfer term related to diffusion of water vapor, $h\vec{j}$. Here, h is the sensible enthalpy of water vapor and \vec{j} is the diffusion flux of water vapor. The first term on the right hand side of the energy equation is the heat transfer associated with conduction. For this set of simulations, the contribution of the thermal conductivity of water vapor is negligible and the temperature dependent conductivity of dry air is used (Eq. 2.27).

When solving the conservation equations for water vapor, FLUENT uses the convective-diffusion equation,

$$\frac{\partial}{\partial t}(\rho Y) + \nabla \cdot (\rho \vec{v} Y) = -\nabla \cdot \vec{j} \quad 3.12$$

Y represents the mass fraction of water vapor (equivalent to w_v , the mixing ratio in Eq. 2.4). The diffusive flux \vec{j} for water vapor is solved using the following formulation:

$$\vec{j} = -\rho D_v \nabla Y \quad 3.13$$

Here, D_v is the binary coefficient of diffusion of water vapor in air given as in Eq. 2.3 and ρ is the total density. The concentration of particles at which growth may be limited can be determined by comparing the flux of vapor from the walls to the flux

of vapor to the surface of a particle for an infinitesimal volume. The total mass per unit time entering the element is

$$F_{in} = D_v \frac{\partial \rho_v}{\partial x} \Delta y \Delta z \quad 3.14$$

where Δy and Δz represent dimensions normal to the flow of water vapor from the walls. An upper limit on the total mass per unit time accommodated by the particles within the element may be defined as

$$F_{part} = \frac{dm}{dt} [N] \Delta x \Delta y \Delta z \quad 3.15$$

where dm/dt is given by the solution to the diffusion limited drop growth (Eq. 2.23) and $[N]$ is the particle number concentration. The ratio of the two provides an indication of significance of the sink relative to the source and is given by

$$r_{Flux} = \frac{\partial e / \partial x}{[N] 2\pi d_p (e(T) - e_{s,i}(T)) \Delta x} \quad 3.16$$

Here, Δx represents the width of the lamina and the water vapor partial pressure is substituted for the water vapor density using the ideal gas law. The cloud particle is assumed to be ice and at the same temperature as the surroundings (T) and is growing in a diffusion controlled manner. This ratio provides a conservative, order of magnitude estimate of the maximum concentration of ice crystals with diameter d_p that can be present without significantly perturbing the water vapor field.

Calculations using Eq. 3.16 indicate that, for temperatures warmer than -60°C and

cloud particle diameters less than 5 μm , crystal concentrations on the order of 10^3 cm^{-3} should have no significant impact on the availability of water vapor. This finding is in agreement with *Rogers* [1988] who provided an estimate based on crystal and drop growth modeled with feedback. In the corresponding calculations of the heat flux from the walls and that associated with the growth of crystals, *Rogers* [1988] found that the flux from the walls was over 8 orders of magnitude greater than that of 1000 cm^{-3} particles growing and therefore the latent heat release of growing particles has no significant impact on the temperature fields within the lamina.

3.2.1.3 Initial and Boundary Conditions

Each simulation is started with a specific set of initial and boundary conditions. At both the sheath and the sample inlets, dry air ($w_v = 0$) enters the chamber at 293 K, similar to the lab ambient temperature. On the portions of the chamber exposed to the laboratory and not actively cooled (such as the collar and the outer portions of the inlet and base), the outer boundary is set to 273.15 K. Although these portions are insulated, there is no reason to believe that the temperature of the ambient air (on the outer portion of the chamber) does not heavily influence this outer boundary. However, there is no temperature measurement located on any of these exposed portions of the chamber and therefore there is no record of these temperatures

Table 3.3. Inlet velocities for simulations at the given average temperature and pressure for the two different flow rate regimes. The inlet velocities are calculated assuming an inlet temperature of 293 K and the target flow rate is for the average conditions in the lamina.

T_{tar} (°C)	$Q_{sh,tar}$ (lpm)	$Q_{t,tar}$ (lpm)	u_i (cm/s)	u_o (cm/s)	u_s (cm/s)
-40	10	9	33.17	27.21	28.61
	5	4.5	16.58	13.60	14.30
-45	10	9	33.89	27.80	29.24
	5	4.5	16.95	13.90	14.62
-50	10	9	34.65	28.42	29.81
	5	4.5	17.33	14.21	14.94
-60	10	9	36.282	29.759	31.293
	5	4.5	18.14	14.88	15.64

Each temperature and flow rate determines the velocity at the sample and sheath inlets. As the sheath inlets are not made up of individual holes (as in the real instrument) but rather a narrow slit having the width of the diameter of a single sheath hole, the initial velocity differs for the inner and outer sheath entry points. The velocity of each inlet is calculated based on a mass balance as

$$u = \frac{Q}{\pi(r_o^2 - r_i^2)} \frac{T_{amb}}{T_{tar}} \quad 3.17$$

Here, Q is the total flow rate or half the sheath flow rate, r_o and r_i are the distances of the outer and inner points of the inlet from the axis of symmetry, T_{amb} is the ambient temperature (293.15 K) and T_{tar} is the target operational temperature in the chamber.

The inlet velocities are not affected by the operational pressure as the pressure is

assumed to be approximately constant through the system. The inlet velocities for the inner sheath (u_i), the outer sheath (u_o) and the sample inlet velocity (u_s) are given in Table 3.3 as a function of the target temperature and the flow rates.

Along the boundaries in the growth and evaporation regions, the water vapor mixing ratio is set to that of ice saturation (using Eq. 2.4) to calculate the water vapor mixing ratio with the water vapor pressure calculated using Buck's formulation of ice saturation, Eq. 2.7) at the boundary temperature. Simulation boundary temperatures were calculated based on target conditions. The target conditions were calculated solving Eq. 3.2 for the lamina position in the steady state region and Eqs. 3.4 and 3.5 for the saturation and temperature at the average lamina position. The wall

Table 3.4. Cold (T_i) and warm (T_o) wall temperatures used in the simulations with a sheath flow of 9 lpm and a total flow of 10 lpm at 850 mb and a target lamina temperature of -40°C . The steady state conditions for the average lamina position are shown in the last three columns. The steady-state conditions are calculated as discussed in Chapter 3.1.3.

T_i ($^\circ\text{C}$)	T_o ($^\circ\text{C}$)	T_a ($^\circ\text{C}$)	SS_w (%)	SS_i (%)
-45	-30	-40.11	-8.17	35.97
-	-29.5	-40.01	-6.33	38.55
-45.5	-	-40.41	-4.61	41.65
-	-29	-40.31	-2.61	44.49
-	-28.5	-40.21	-0.52	47.44
-	-28	-40.11	1.64	50.50
-	-27.5	-40.01	3.90	53.70
-45.75	-	-40.22	4.99	55.62

temperatures used are unique to the pressure, flow rate and the target conditions as these latter values impact the position of the lamina. The following tables (Table 3.4 through Table 3.9) give the wall temperatures used in the simulations described later as well as the steady state conditions in the growth region at the average lamina position. In the simulations, the evaporation region temperature on the outer wall is always maintained at the inner wall temperature. In contrast, limited refrigeration capacity in the actual instrument results in the outer wall in the evaporation region being slightly warmer (~ 1 K) than the inner wall. This results in an evaporation region that is still significantly subsaturated with respect to water but slightly supersaturated with respect to ice.

The base cases describe an ideal situation in which spatial or temporal deviations from the average wall temperature are insignificant. In this study, three sets of perturbed conditions are examined for the ambient pressure, high flow rate case ($p = 850$ mb and $Q_t = 10$ lpm): an upward pointing linear temperature gradient, a downward pointing linear temperature gradient, and an oscillating temperature profile. In each case, the average temperature for the perturbation profile is given by the tables previously described. The linear temperature gradient describes conditions

Table 3.5. Cold (T_i) and warm (T_o) wall temperatures used in the simulations with a sheath flow of 9 lpm and a total flow of 10 lpm at 850 mb and a target temperature of -45°C . The steady state conditions for the average lamina position are shown in the last three columns. The steady-state conditions are calculated as discussed in Chapter 3.1.3.

T_i ($^\circ\text{C}$)	T_o ($^\circ\text{C}$)	T_a ($^\circ\text{C}$)	SS_w (%)	SS_i (%)
-50	-35	-45.22	-10.17	39.68
-	-34.5	-45.11	-8.23	42.56
-	-34	-45.01	-6.20	45.56
-50.5	-	-45.42	-4.24	49.19
-	-33.75	-45.38	-3.15	50.82
-	-33.5	-45.33	-2.03	52.49
-	-33.25	-45.28	-0.89	54.19
-	-33	-45.23	0.26	55.93
-	-32.75	-45.18	1.44	57.70
-	-32.5	-45.13	2.65	59.51
-	-32.25	-45.09	3.892	61.35
-	-32	-45.04	5.150	63.23

which, to some degree, have been observed in previous experiments. For the purpose of this study, the linear temperature gradient is applied to a single wall for a simulation and the total gradient is 2 K over the length of the wall. The wall temperature is calculated as

$$T(y) = \frac{\Delta T}{\Delta y} (y - y_l) + \bar{T} + \frac{\Delta T}{2} \quad 3.18$$

where ΔT is ± 2 K (+ if the gradient points upward and – if downward), y is the position along the wall of that the gradient resides on, y_l is the lower coordinate of the wall, Δy is the length of that wall segment and \bar{T} is the average wall temperature.

The oscillatory boundary condition describes the case in which the temperature of the wall is elevated slightly above that of the point where the coil is in contact with the wall. Given the high conductivity of copper and the small spacing between the coils (1”), the maximum temperature perturbation is assumed to be 1 K at the center of the distance between coils. This is calculated in the model as

$$T(y) = \bar{T} + \Delta T + \frac{\Delta T}{2} \sin\left(2\pi \frac{y - y_l}{\tau}\right) \quad 3.19$$

where τ is the period of oscillation, 0.05 m (2”).

Table 3.6. Cold (T_i) and warm (T_o) wall temperatures used in the simulations with a sheath flow of 9 lpm and a total flow of 10 lpm at 850 mb and at target lamina temperature of -50°C . The steady state conditions for the average lamina position are shown in the last three columns. The steady-state conditions are calculated as discussed in Chapter 3.1.3.

T_i ($^{\circ}\text{C}$)	T_o ($^{\circ}\text{C}$)	T_a ($^{\circ}\text{C}$)	SS_w (%)	SS_i (%)
-55	-40	-50.33	-11.80	43.91
-	-39.5	-50.23	-9.75	47.12
-	-39	-50.13	-7.60	50.49
-	-38.5	-50.03	-5.36	54.00
-55.5	-	-50.45	-3.11	58.28
-	-38	-50.36	-0.65	62.15
-	-37.5	-50.27	1.90	66.18
-	-37.25	-50.22	3.22	68.26
-	-37	-50.18	4.56	70.38

Table 3.7. Cold (T_i) and warm (T_o) wall temperatures used in the simulations with a sheath flow of 9 lpm and a total flow of 10 lpm at 850 mb and a target temperature of -60°C . The steady state conditions for the average lamina position are shown in the last three columns. The steady-state conditions are calculated as discussed in Chapter 3.1.3.

T_i ($^\circ\text{C}$)	T_o ($^\circ\text{C}$)	T_a ($^\circ\text{C}$)	SS_w (%)	SS_i (%)
-64.5	-49.5	-60.04	-13.77	53.70
-	-49	-59.95	-11.43	57.74
-65	-	-60.37	-9.01	62.66
-	-48.5	-60.28	-6.43	67.14
-	-48	-60.20	-3.73	71.83
-	-47.5	-60.11	-0.90	76.74
-	-47	-60.02	2.05	81.88
-	-46.5	-59.94	5.14	87.25

Table 3.8. Cold (T_i) and warm (T_o) wall temperatures used in the simulations with a sheath flow of 9 lpm and a total flow of 10 lpm at 500 mb and a target temperature of -40°C . The steady state conditions for the average lamina position are shown in the last three columns. The steady-state conditions are calculated as discussed in Chapter 3.1.3.

T_i ($^\circ\text{C}$)	T_o ($^\circ\text{C}$)	T_a ($^\circ\text{C}$)	SS_w (%)	SS_i (%)
-45	-30	-39.24	-7.35	36.03
-45	-29.5	-39.09	-5.47	38.60
-45.5	-29.5	-39.46	-3.70	41.68
-45.5	-29	-39.31	-1.66	44.50
-45.5	-28.5	-39.17	0.46	47.42
-45.5	-28	-39.04	2.67	50.46
-45.5	-27.5	-38.90	4.96	53.61
-45.75	-27.5	-39.09	6.07	55.52

Table 3.9. Cold (T_i) and warm (T_o) wall temperatures used in the simulations with a sheath flow of 9 lpm and a total flow of 10 lpm at 500 mb and a target temperature of -45°C . The steady state conditions for the average lamina position are shown in the last three columns. The steady-state conditions are calculated as discussed in Chapter 3.1.3.

T_i ($^\circ\text{C}$)	T_o ($^\circ\text{C}$)	T_a ($^\circ\text{C}$)	SS_w (%)	SS_i (%)
-51.25	-35.50	-45.39	-6.74	45.26
-51.25	-35.25	-45.32	-5.68	46.81
-51.25	-35.00	-45.26	-4.60	48.39
-51.25	-34.75	-45.19	-3.50	50.01
-51.25	-34.50	-45.12	-2.38	51.65
-51.25	-34.25	-45.05	-1.23	53.33
-51.25	-34.00	-44.98	-0.07	55.05
-51.50	-34.00	-45.17	1.07	57.09
-51.5	-33.75	-45.108	2.28	58.88
-51.5	-33.5	-45.043	3.52	60.71
-51.75	-33.5	-45.23	4.75	62.91

Table 3.10. Cold (T_i) and warm (T_o) wall temperatures used in the simulations with a sheath flow of 9 lpm and a total flow of 10 lpm at 500 mb and a target temperature of -50°C . The steady state conditions for the average lamina position are shown in the last three columns. The steady-state conditions are calculated as discussed in Chapter 3.1.3.

T_i ($^{\circ}\text{C}$)	T_o ($^{\circ}\text{C}$)	T_a ($^{\circ}\text{C}$)	SS_w (%)	SS_i (%)
-55	-40	-49.42	-10.96	44.05
-55	-39.5	-49.28	-8.86	47.25
-55	-39	-49.15	-6.68	50.60
-55	-38.5	-49.01	-4.40	54.08
-55.5	-38.5	-49.39	-2.11	58.33
-55.5	-38	-49.26	0.37	62.16
-55.5	-37.5	-49.13	2.96	66.14
-55.5	-37.25	-49.07	4.29	68.19
-55.5	-37	-49.01	5.65	70.29

Table 3.11. Cold (T_i) and warm (T_o) wall temperatures used in the simulations with a sheath flow of 9 lpm and a total flow of 10 lpm at 500 mb and a target temperature of -60°C . The steady state conditions for the average lamina position are shown in the last three columns. The steady-state conditions are calculated as discussed in Chapter 3.1.3.

T_i ($^{\circ}\text{C}$)	T_o ($^{\circ}\text{C}$)	T_a ($^{\circ}\text{C}$)	SS_w (%)	SS_i (%)
-64.50	-49.50	-59.11	-12.91	53.97
-64.50	-49.00	-58.99	-10.53	57.98
-65.00	-49.00	-59.37	-8.07	62.89
-65.00	-48.50	-59.24	-5.46	67.33
-65.00	-48.00	-59.12	-2.73	71.98
-65.00	-47.50	-59.00	0.13	76.83
-65.00	-47.00	-58.88	3.10	81.90
-65.00	-46.50	-58.76	6.21	87.19

Table 3.12. Cold (T_i) and warm (T_o) wall temperatures used in the simulations with a sheath flow of 4.5 lpm and a total flow of 5 lpm at 500 mb and a target temperature of -40°C . The steady state conditions for the average lamina position are shown in the last three columns. The steady-state conditions are calculated as discussed in Chapter 3.1.3.

T_i ($^{\circ}\text{C}$)	T_o ($^{\circ}\text{C}$)	T_a ($^{\circ}\text{C}$)	SS_w (%)	SS_i (%)
-45.25	-28.25	-40.28	-1.03	46.78
-45.25	-28	-40.24	0.01	48.27
-45.25	-27.75	-40.19	1.08	49.80
-45.25	-27.5	-40.15	2.18	51.36
-45.25	-27.25	-40.10	3.30	52.95
-45.25	-27	-40.06	4.44	54.57

Table 3.13. Cold (T_i) and warm (T_o) wall temperatures used in the simulations with a sheath flow of 4.5 lpm and a total flow of 5 lpm at 500 mb and a target temperature of -45°C . The steady state conditions for the average lamina position are shown in the last three columns. The steady-state conditions are calculated as discussed in Chapter 3.1.3.

T_i ($^{\circ}\text{C}$)	T_o ($^{\circ}\text{C}$)	T_a ($^{\circ}\text{C}$)	SS_w (%)	SS_i (%)
-50.25	-34.25	-45.59	-6.84	45.36
-50.25	-34	-45.544	-5.81	46.90
-50.25	-33.75	-45.5	-4.76	48.47
-50.25	-33.5	-45.455	-3.69	50.08
-50.25	-33.25	-45.41	-2.60	51.73
-50.25	-33	-45.36	-1.48	53.40
-50.25	-32.75	-45.32	-0.34	55.11
-50.25	-32.5	-45.28	0.82	56.86
-50.25	-32.25	-45.23	2.00	58.64
-50.25	-32	-45.19	3.21	60.46
-50.25	-31.75	-45.15	4.45	62.32
-50.25	-31.5	-45.11	5.71	64.21

Table 3.14. Cold (T_i) and warm (T_o) wall temperatures used in the simulations with a sheath flow of 4.5 lpm and a total flow of 5 lpm at 500 mb and a target temperature of -50°C . The steady state conditions for the average lamina position are shown in the last three columns. The steady-state conditions are calculated as discussed in Chapter 3.1.3.

T_i ($^\circ\text{C}$)	T_o ($^\circ\text{C}$)	T_a ($^\circ\text{C}$)	SS_w (%)	SS_i (%)
-55	-38.75	-50.40	-7.09	51.70
-55	-38.5	-50.36	-5.98	53.46
-55	-38.25	-50.32	-4.84	55.25
-55	-38	-50.27	-3.68	57.09
-55	-37.75	-50.23	-2.49	58.96
-55	-37.5	-50.19	-1.28	60.87
-55	-37.25	-50.15	-0.04	62.83
-55	-37	-50.11	1.22	64.83
-55	-36.75	-50.07	2.51	66.86
-55.25	-36.75	-50.28	3.81	69.32
-55.25	-36.5	-50.24	5.16	71.46

Table 3.15. Cold (T_i) and warm (T_o) wall temperatures used in the simulations with a sheath flow of 4.5 lpm and a total flow of 5 lpm at 500 mb and a target temperature of -60°C . The steady state conditions for the average lamina position are shown in the last three columns. The steady-state conditions are calculated as discussed in Chapter 3.1.3.

T_i ($^\circ\text{C}$)	T_o ($^\circ\text{C}$)	T_a ($^\circ\text{C}$)	SS_w (%)	SS_i (%)
-64.5	-48.75	-60.22	-10.85	59.15
-64.5	-48.5	-60.18	-9.63	61.27
-64.5	-48.25	-60.13	-8.38	63.43
-64.5	-48	-60.09	-7.11	65.65
-64.5	-47.75	-60.06	-5.80	67.92
-64.5	-47.5	-60.02	-4.47	70.24
-64.75	-47.5	-60.23	-3.09	73.03
-64.75	-47.25	-60.199	-1.69	75.47
-64.75	-47	-60.16	-0.25	77.97
-64.75	-46.75	-60.12	1.21	80.53
-64.75	-46.5	-60.08	2.71	83.15
-64.75	-46.25	-60.04	4.24	85.82

3.2.1.4 Thermal Conduction in the CFDC Model Domain

As discussed briefly in Chapter 3.2.1.1, several of the meshed sections of the CFD domain correspond to solid material. Including these solid regions in the CFD calculations allows for modeling of heat transfer through these regions. In previous simulations, *Straub et al.* [2004] as well as *Rogers et al.* [2004] model these boundaries of the chamber (the inlet and outlet regions as well as the collar) as zero heat flux boundaries. A zero heat flux boundary is unaffected by the outer boundary which may be in contact with warmer air; this means that the boundary will equilibrate to the inner wall temperature. Heat transfer through these regions may have significant impacts on the flow profile in the fluid domain as well as the water vapor structure within the annular region. The outer wall inlet region, the collar, the outlet cone and the outer wall outlet region are all constructed of Delrin (Figure 3.7). Delrin is hydrophobic and is therefore assumed to not maintain an ice surface in the model. It should be noted here that, upon disassembly at low temperatures, a patchy growth of ice has been observed on the surface. However, the extent of vapor deposition is most likely not sufficient to significantly perturb the vapor profiles in the chamber during operation and the assumption of a no vapor flux boundary is reasonable for modeling purposes.

For each of the regions not actively cooled, and exposed to laboratory conditions, it is assumed that insulation is sufficient to maintain a temperature of

273.15 K. No attempt has been made to measure the temperature on these portions of the outer wall, but condensation has been observed on the surface, indicating that 273.15 K may underestimate the temperature at this boundary. The temperature at the boundaries of the inlet blade as well as the inner portions of the outlet, collar and inlet are governed by heat transfer. The heat transfer equation for solid regions with no specified translation or rotation and no volumetric heat source is

$$\frac{\partial}{\partial t}(\rho h) = \nabla \cdot (k \nabla T) \quad 3.20$$

where ρ is the density of the material, k is the thermal conductivity and h is the specific enthalpy, given by

$$h = \int_{T_{ref}}^T c_p dT \quad 3.21$$

The properties of the materials for which heat transfer was modeled are given in Table 3.16. The properties of stainless steel (SS316) shown were taken from the

Table 3.16. Material properties for the modeled solid portions of the chamber. SS316 refers to stainless steel 316. The temperatures given in the table below indicate the reference temperature for the measurement or the valid range of temperatures for the given property value. All properties are assumed constant through these simulations.

Property	Materials	
	SS316	Delrin
Density (kg/m ³)	8000	1420
k (W m ⁻¹ K ⁻¹)	16.2 (373 K)	0.33
C (J kg ⁻¹ K ⁻¹)	500 (273-373 K)	1465

Australian Stainless Steel Development Association (<http://www.assda.asn.au/asp/-index.asp>). Although the thermal properties of SS316 are temperature dependent, measurements of these properties for stainless steel 304 (a material with similar properties to that of SS316) indicate that the conductivity and heat capacity do not vary enough over a broad range of temperatures to significantly affect the results of the numerical simulations [Sweet *et al.*, 1987]. Delrin is a product of DuPont and the properties of this material may be found in the DuPont Product and Properties guide (http://plastics.dupont.com/plastics/pdflit/americas/delrin/H76836.pdf?GXHC_locale=en_US).

3.2.2 Modeling the Particle Phase

Particle trajectories are run from the model using FLUENT's discrete phase model (DPM). The DPM tracks particles in the Lagrangian reference frame. In this reference frame the force balance on a particle may be written as

$$\frac{du_p}{dt} = F_D(u - u_p) + \frac{g(\rho_p - \rho)}{\rho_p} + F \quad 3.22$$

where the first term on the right hand side represents the drag force per unit mass, the second term represents the gravitational force per unit mass acting on the particle and the final term represents additional forces acting on the particle. These additional forces include the pressure gradient force (not applicable in this case), the virtual mass force as well as forces attributable to phortetic effects.

In these simulations, particles are assumed to have the density of bulk ammonium sulfate (1740 kg m^{-3}). The diameter of all particles is a constant one micron. This should be sufficient for tracking particle paths through the gas phase. The contribution of the particle settling velocity to the final velocity is negligible given that the fluid velocity u is several orders of magnitude greater than the settling velocity [Hinds, 1999]. The influence of thermophoretic and diffusiophoretic forces which will act to push the particles toward the cold wall are also considered negligible given that the velocities imparted by the forces are both on the order of $10 \text{ }\mu\text{m/s}$ at most [Prodi et al., 2002; Pruppacher and Klett, 1997]. .

A form of Stoke's law available through FLUENT is used to model particle drag, F_D . In this case, the drag force per unit mass is

$$F_D = \frac{18\mu}{D_p^2 \rho_p C_c} \quad 3.23$$

Here, ρ_p is the particle density and C_c is the Cunningham-Stokes correction factor.

While the continuous phase always impacts the physics of the discrete phase, the impact of the discrete phase on the continuous phase in the simulations is assumed negligible; this means that these particles will not act as a vapor source/sink in the CFD simulations and remain a constant size. As discussed in the chapter outlining the properties of the continuous phase, for particle concentrations on the order of 1000 cm^{-3} the impact of particle growth on the vapor field is negligible.

In these simulations, particles are released from ten points along the sample inlet surface. These particles are tracked through the entire domain.

Thermodynamic variables pertinent to drop/crystal growth (i.e. temperature and saturation) are extracted from grid points (generally 7000 to 8000 points with time steps on the order of milliseconds) along these trajectories generating a profile of those variables as a function of space in the CFDC. The ten trajectories which span the width of the “lamina” through the domain are then run through a microphysical model (described below).

3.2.3 Modeling the Microphysics

For this study, a microphysical model was developed for calculating particle growth along a given thermodynamic trajectory. The microphysical model was constructed in the object-oriented language, Java (<http://java.sun.com>). For each simulation, 100, discrete ammonium sulfate particles were run along a single trajectory for a fixed, initial dry size. Each particle entered the simulation dry and deliquesced according to Eq. 2.19. Upon deliquescence, particles begin to grow diffusively via Eq. 2.32. The diffusional growth equation is solved iteratively using the Runge-Kutta-Fehlberg method [RKF45; *Shampine*, 1986]. For each of these simulations, the water activity of drops is calculated as a function of temperature and solute molality. The water activity parameterization is based on the AIM model as described in Chapter 2.1.6 [*Clegg et al.*, 1998].

While the process of diffusional growth is deterministic, nucleation is stochastic. Therefore, at each time step the probability of nucleation is calculated using the parameterization of *Koop et al.* [2000] as described in Chapter 2.3. The nucleation rate is deemed significant for a time step when the probability of nucleation (Eq. 2.33) multiplied by the number of particles is greater than 1 (i.e. $f_{HF} \times N_{tot} > 1$, where N_{tot} is the total number of discrete particles available for nucleation and f_{HF} is the probability given in Eq. 2.33). As the diffusional growth of ice is deterministic, each ice crystal nucleating from a particular point will grow at the same rate. The number nucleating and the growth of the crystal as a function of time are tracked for each step where nucleation is significant. As with drop growth, the diffusional growth equation for ice crystals (Eq. 2.40) is solved using the same RKF45 routine.

Droplets readily evaporate in the lower portion of the chamber. The rate of evaporation is solved as for growth described above. However, as described in *Seinfeld and Pandis* [1998], water will remain associated with the particles well below the DRH. As for growth, the water activity during evaporation is also modeled using the data from AIM. When conditions reach $S_w = 0.35$, the haze drop is assumed to lose its water and crystallize to the initial dry diameter of the particle. The point and method of crystallization is not necessarily important to the simulations as haze drops

exiting the chamber tend to be near the dry diameter and easily differentiated from crystals. Crystallization is modeled only to prevent instances in which $d_d < d_0$.

3.3 The Laboratory Study

The CFDC has successfully measured both heterogeneous nucleation of ice and homogeneous freezing in different configurations. However, attempts to measure homogeneous freezing in the field have yet to be successful. The laboratory portion of this study is conducted with two objectives in mind. The first objective is to determine whether the CFDC-1H can accurately capture the onset of homogeneous freezing of a well characterized aerosol. For this portion of the study, the freezing properties of ammonium sulfate as measured by the CFDC-1H over a range of pressures and flow rates are compared with those predicted by the *Koop et al.* [2000] parameterization. This will provide operational guidelines for future operation of the CFDC-1H in the field at low temperatures. In addition, it provides important data for comparison of simulated cloud particle growth and allows predictions of the performance of the instrument at conditions not currently accessible in the current instrumental setup. And, finally it provides a data set for comparison with onset freezing conditions of an ambient aerosol.

3.3.1 Size Selected Ammonium Sulfate

Figure 3.8 shows the laboratory setup for studies conducted using size selected ammonium sulfate. In these studies, laboratory air was used to generate and dilute the aerosol as well as to re-pressurize the CFDC. Two packed bed desiccant driers containing silica gel dried the laboratory air (the relative humidity of the lab air was generally greater than 10% at 293 K) to dewpoints below 253 K, the lowest measureable dewpoint by a single-stage, chilled mirror dewpoint hygrometer (GE1111H-SR, General Eastern; Willmington, MA). The dried air was subsequently filtered using a HEPA capsule filter (PALL Gelman Laboratory; Ann Arbor, MI) prior to flow splitting. The generation and size selection portion of these experiments is discussed in the following two sections while the CFDC is discussed in the final section of this chapter as it is used in a similar manner through both the ambient tests and the lab-generated aerosol tests.

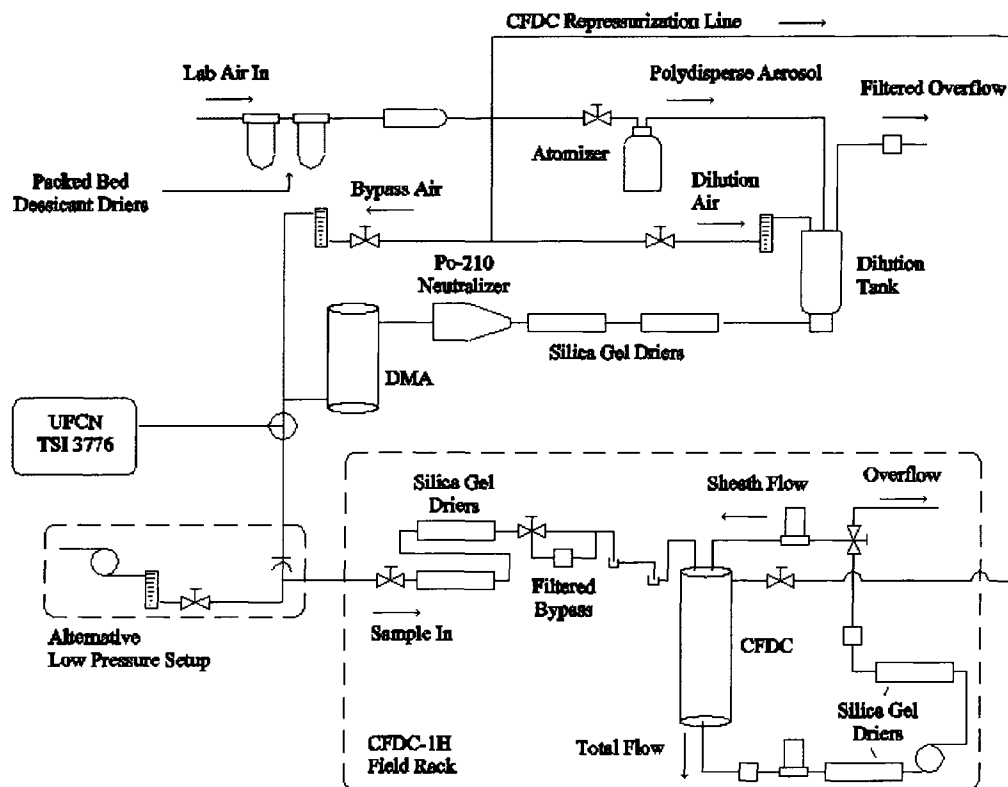


Figure 3.8. Laboratory setup for size selected ammonium sulfate studies.

3.3.1.1 Aerosol Generation

A constant output atomizer (Model 3076, TSI, Inc.; Shoreview, MN) generated a polydisperse distribution of ammonium sulfate from a 0.1-1% by mass solution of ammonium sulfate and deionized water. The generated aerosol then entered a tank where it was diluted and dried. The diluted aerosol was then further dried using two flow-through silica gel desiccant driers. The polydisperse aerosol was then neutralized by a ^{210}Po source [Liu and Pui, 1974], thus obtaining an equilibrium charge distribution. The distribution of charges obtained by the aerosol is known and

given by *Wiedensohler* [1988] for charges up to ± 2 and *Gunn* [1956] for particles obtaining more ions.

3.3.1.2 Size Selection by a Differential Mobility Analyzer

A TSI differential mobility analyzer (DMA; TSI 3080) produced an approximately monodisperse size distribution from the generated aerosol [*Knutson and Whitby*, 1975]. The DMA consists of two concentric cylinders with two inlets (for the polydisperse flow and the sheath flow) and two outlets (for the excess flow and the monodisperse sample flow). A particle free sheath flow enters the annular region created by the two cylinders near the inner wall. The polydisperse aerosol enters the outer region of the annular gap through two diametrically opposed holes. The sheath flow confines the aerosol flow to a thin region near the outer wall, the width of which is defined by the ratio of the two flows.

The center cylinder consists of a rod which is maintained at a fixed voltage resulting in an electric field in the analyzer region. This field causes the charged particles to migrate through the clean sheath flow toward the rod as they are carried down the length of the DMA. Particles within a narrow range of mobility will penetrate a sampling slit located near the inner wall in the outlet region of the DMA. Those with higher mobilities will impact upstream of the slit while those with lower mobilities will be carried out with the excess flow.

Particle mobility is a measure of a particle's ability to move within an electrical field. The mobility for a particle (in $\text{m}^2\text{V}^{-1}\text{s}^{-1}$) with diameter d_p carrying n discrete charges (positive or negative) is given in *Hinds* [1999] as

$$Z^* = \frac{neC_c}{3\pi\mu d_p} \quad 3.24$$

where e is the charge of a single electron (1.6×10^{-19} C). This formulation assumes that the particle Re is within the Stokes region ($\text{Re} \ll 1$). As d_p decreases, the fluid through which they travel may no longer appear continuous to them. In this case, the slip correction factor (C_c) describes the tendency of particles to 'slip' between collisions with fluid molecules. This factor becomes significant and must be accounted for as particle sizes approach $1 \mu\text{m}$. *Hinds* [1999] gives this correction factor as

$$C_c = 1 + \frac{\lambda}{d_p} \left[2.34 + 1.05 \exp\left(-0.39 \frac{d_p}{\lambda}\right) \right] \quad 3.25$$

where λ is the mean free path of the gas. The mean free path of air can be calculated from the mean free path at reference conditions and the assumption that air acts as an ideal gas,

$$\lambda = \lambda_0 \frac{p_0}{p} \frac{T}{T_{S,0}} \quad 3.26$$

At the reference conditions, the mean free path of air at the reference conditions (λ_0) is 66×10^{-9} m.

Due to the finite width of the aerosol lamina entering the analyzer region, there is a range of mobilities that have a probability of penetrating the slit and entering the sampled, “monodisperse” flow. This range of mobilities is given by

$$Z = Z^* \pm \frac{Q_a + Q_s}{Q_e + Q_{sh}} Z^* \quad 3.27$$

where Z^* is the nominal mobility, Q_a is the aerosol flow, Q_s is the sample flow, Q_e is the excess flow and Q_{sh} is the sheath flow. The probability of penetration as a function of mobility is given by the transfer function Ω (Eq. 12 in *Knutson and Whitby* [1975]).

In addition to the range of mobilities, the charging efficiency as discussed above must be accounted for. A certain percentage of larger particles having the same mobility as the singly charged particles, but carrying more than one charge will penetrate into the sampling slit. Figure 3.9 shows an example of a size distribution produced by a constant output atomizer from a 0.1% solution of ammonium sulfate by mass as well as the calculated distribution of particles with DMA voltage set to produce 100 nm particles (top panel) and 300 nm particles (bottom panel). The insets show a close up view of the particle concentrations produced for up to +4 charges. From this plot, it is evident that the charging efficiency of the neutralizer has a profound effect on the population of particles produced in the 300 nm case. While the +2 charged particles are ~150 nm in the 100 nm case, the +2 charges are almost 500 nm in the 300 nm case and have a higher charging efficiency associated with

Table 3.17. Expected size and transmission efficiency of multiply charged particles for 100 nm and 300 nm particles at laboratory pressure and temperature and a balanced, 10:1 sheath-to-sample flow ratio.

Charge	Size		Charging Efficiency	
+1	100	300	21.38%	17.83%
+2	149.2	495	5.5%	8.92%
+3	191	682	3.63%	4.79%
+4	229	866	1.49%	3.1%

them than the doubly charged 100 nm particles (Table 3.17). However, for freezing studies, it is important to understand that the onset conditions for the +2 charged particles are not significantly different from those of the singly charged particles (Figure 2.7).

The DMA sheath flow throughout all experiments was 10 lpm. Downstream of the DMA, the flow was split between the particle condensation nucleus counter (UFCNc; TSI 3776) and the CFDC. The UFCNc flow rate was 1.5 lpm at laboratory conditions for all experiments while the CFDC flow rate varied with the conditions. A bypass flow downstream of the DMA maintained the sample flow rate below 2 lpm thereby limiting the maximum flow ratio to 1:5. In most cases, the bypass flow limited this ratio to 1:10. A higher sample-to-sheath flow ratio has the effect of broadening (but not changing the shape of) the range of mobilities transmitted through the DMA. But, as discussed above, the small increases expected by changing the flow ratio have a limited effect on the set of onset conditions measured by the CFDC. The dilution and bypass flows were adjusted such that CN concentrations

([CN]) were less than approximately 1000 scm^{-3} for all experiments, regardless of particle size. [CN] were checked periodically throughout experimental periods to verify that concentrations were not significantly fluctuating. Concentrations were logged manually, but not recorded electronically.

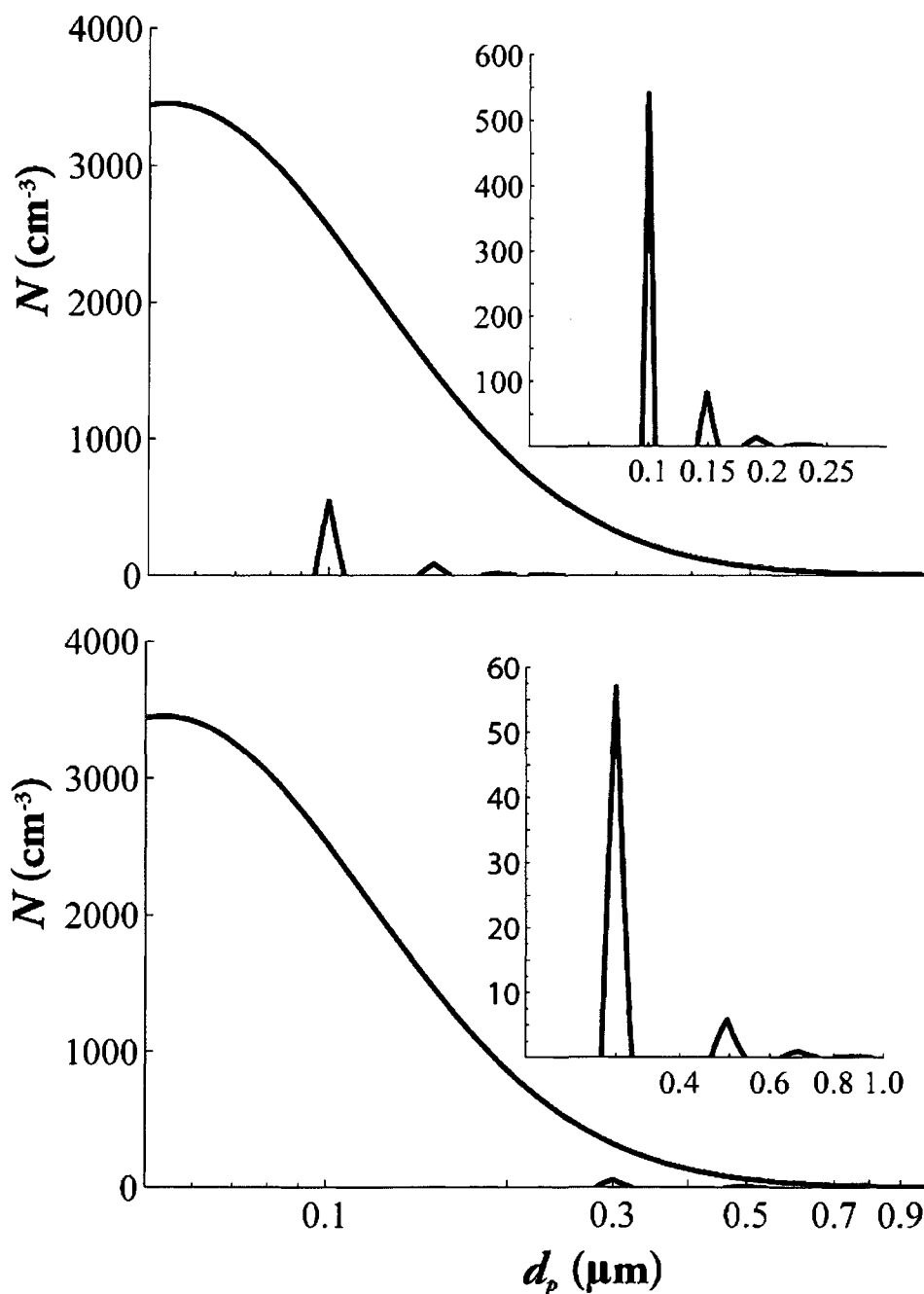


Figure 3.9. Generated size distribution from constant output atomizer and the resulting distribution of size selected particles for 100 nm (top) and 300 nm (bottom). For these plots, the pressure was assumed to be 842 mb, the temperature 293 K and the flows were balanced with 1 lpm sample flow rate and 10 lpm sheath flow rate. Insets focus on the distribution of particles emerging from the DMA. The input distribution is log-normal with a geometric mean diameter of 100 nm and a standard deviation of 2.2 (the generated distribution roughly estimated from the TSI 3076 manual for a 0.1% salt solution).

3.3.2 Ambient Aerosol

In late June and early July of 2008, the CFDC-1H sampled ambient aerosol from an inlet located immediately outside of the CSU Atmospheric Chemistry building. The purpose of this set of experiments was to determine 1) how the onset freezing conditions of an ambient, size-selected aerosol compared to that of a lab generated aerosol and 2) whether the parameterization of *Koop et al.* [2000] might adequately capture the onset conditions for homogeneous freezing of a population of ambient particles with no predetermined chemical composition. Two instruments running parallel to the CFDC-1H measured the water uptake properties of the ambient aerosol: a hygroscopic, tandem differential mobility analyzer (HTDMA) and a cloud condensation nuclei counter (CCNc). The CCNc instrument rack contained a scanning mobility particle sizer (SMPS; TSI) which provided information on the size distribution of particles ranging from 3 nm to 397 nm. In addition, particles acting as freezing nuclei were collected by impaction on grids located immediately downstream of the CFDC-1H and subsequently analyzed by collaborators at RJ LeeGroup, Inc. using standard electron-microscopy techniques.

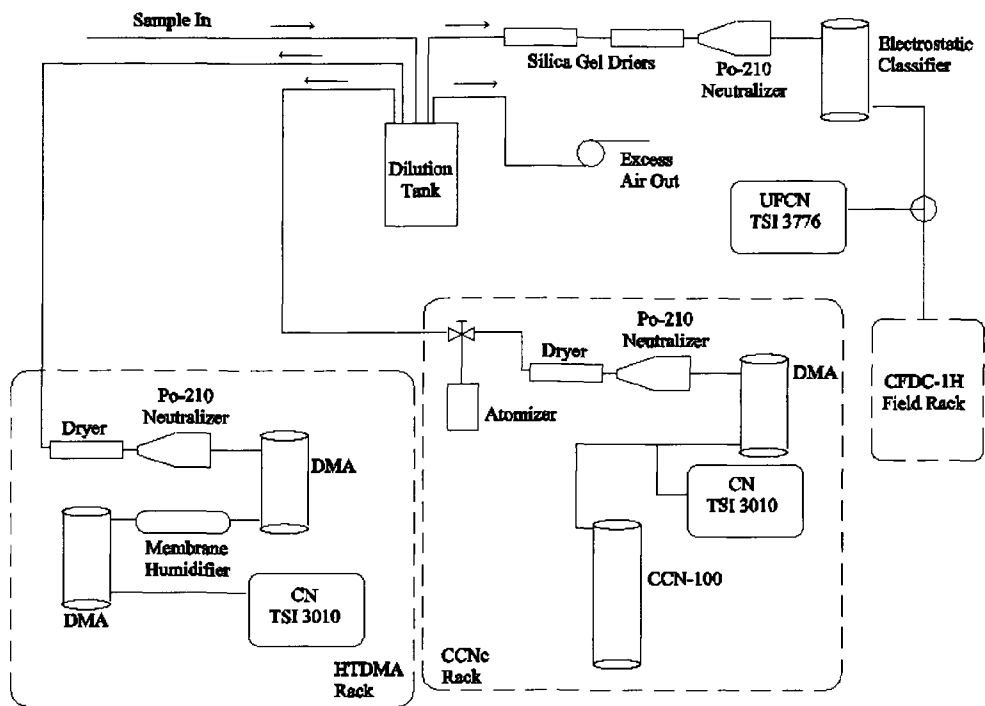


Figure 3.10. Experimental set up for ambient sampling. The CFDC-1H rack is described in Figure 3.8.

Figure 3.10 shows the ambient sampling setup. The sample inlet was located on the east side of the Atmospheric Chemistry building and just northwest of the main Department of Atmospheric Science building. The inlet was elevated approximately 1.5 meters off of the surface. The sample aerosol was pulled through approximately 9 meters of 3/8" (9.52 mm) inner diameter conductive tubing to a reservoir tank. From the reservoir, the HTDMA pulled 3 lpm, the CCNc pulled 0.5 lpm and the UFCNc/CFDC-1H pulled approximately 2 lpm. To reduce the residence time in the sample tubing, a Gast pump (Benton Harbor, MI) pulled an excess flow of 1.5 lpm.

The configuration of the CFDC-1H was similar to that described in the previous section. However, for each of these experiments, the total flow rate was approximately 5 lpm at chamber conditions. To maximize transmitted particle concentrations, the orifice located upstream for the low pressure measurements was not utilized. Pressure drops through the sampling system resulted in an operating pressure of approximately 820 mb for all experiments.

3.3.2.1 Analyzing Ambient Water Uptake Properties

The water uptake properties, or hygroscopicity, of particles may be quantified by two key parameters: the growth factor (gf) and the critical supersaturation (s_{crit}). The growth factor describes the equilibrium size of a haze drop relative to the initial dry size as a function of the water saturation ratio under sub-saturated conditions. The critical saturation describes the saturation at which a drop is no longer in equilibrium with its environment and growth at higher saturation ratios is therefore unrestrained.

The HTDMA captured the water uptake properties of size selected aerosol below water saturation ($S_w \approx 0.2 \rightarrow 0.9$) and the CCNc (Droplet Measurement Technologies, Boulder, CO) measured the CCN activity above water saturation. *Rader and McMurry* [1986] applied the concept of the TDMA to droplet growth studies and the guiding principles have not changed significantly since the initial

development. The setup used in these studies is described extensively in *Carrico et al.* [2008] and briefly below.

The flow path in the HTDMA consists primarily of two DMAs connected via a short section of tubing for particle conditioning (humidification). The sample stream entering the first DMA is dried via a single tube membrane drier and neutralized using a ^{210}Po aerosol neutralizer. Size selected particles exiting this DMA then travel through a short section of tubing consisting of a membrane humidifier. The second DMA is set up to scan voltages and, in conjunction with a CCNc, measures the humidified size distribution. Growth was measured as a function of S_w at two different dry sizes, which took approximately 2.75 h. The final drop diameter at each S_w was then obtained by fitting the size distribution using the TDMAFIT instrument transfer model [*Zhou et al.*, 2002]. Both DMAs in the HTDMA rack operated at a sample to total flow ratio of 5:1.

Roberts and Nenes [2005] developed the prototype of the CCNc used in these studies. The CCNc is a simple cylinder in which the walls are wetted. Heaters along the wall maintain a downward pointing temperature gradient. As water diffuses faster than heat, the temperature gradient along the wetted walls generates a supersaturation with respect to water along the centerline of the cylinder. The sample flow is confined to the centerline using a particle-free sheath flow. CCN are

detected based on size using an OPC at the outlet; particles larger than $\sim 1\mu\text{m}$ are assumed to be CCN.

The CCNc sample flow was diverted at known intervals between a calibration aerosol (ammonium sulfate) and the ambient aerosol. A DMA selected specific sizes from the aerosol stream to produce an approximately monodisperse aerosol. A CNc measured aerosol concentrations upstream of the CCNc. Data retrieved from the system were inverted according to the method described in *Petters et al.* [2007]. The inversion accounts for multiply charged particles emanating from the DMA upstream of the CCNc. These multiply charged particles can significantly skew CCN activation curves, particularly for critical diameters greater than 100 nm and smaller than the mode of the size distribution.

Droplet activation is described as a function of s_w using the ratio of [CCN] to [CN] ratio. The supersaturation in the CCNc is a function of the streamwise thermal gradient. During this set of experiments, particle mobility diameters from approximately 3 nm to 397 nm were scanned for a single temperature gradient. After the full range of diameters was scanned, the gradient was adjusted upward toward a greater supersaturation. Each scan took approximately 16 minutes. Four different gradients were chosen: 5.71 K, 8.49 K, 10.57 K, and 12.66 K over the length of the CCNc cylinder. After each supersaturation cycle, the gradient would then be adjusted to the smallest one. Every sixth cycle, the gradient was maintained and the

calibration aerosol consisting of ammonium sulfate was sampled in a similar manner. Supersaturations were calculated based on the results of these calibrations as discussed in *Prenni et al.* [2007b]. The activation curves were fit using sigmoidal function

$$f = \frac{1}{2} \operatorname{erfc} \left[\frac{(s_w - s_{50})}{\sigma_s \sqrt{2}} \right] \quad 3.28$$

where s_{50} is the supersaturation at which 50% of the particles activate and σ_s describes the dispersion of the curve.

For a soluble particle, the water activity of the haze drop may be determined using Eqs. 2.19 and 2.20. From these two equations the saturation is

$$S_w = a_w \exp \left(\frac{4M_w \sigma_{sol}}{\mathcal{R}T \rho_w g f d_d} \right) \quad 3.29$$

where d_d is the drop size size. Since a particle of known size is exposed to an environment of known relative humidity, the water activity may be determined by dividing the relative humidity by the Kelvin portion of the Kohler equation.

Petters and Kreidenweis [2007] proposed a simple model (the κ -Kohler model) that compares favorably with previously proposed models and allows us to take into account a mixture of components with different water uptake properties. In this parameterization, the water activity is related to the ratio of the dry volume to the volume of water in the drop by

$$\frac{1}{a_w} = 1 + \kappa \frac{V_s}{V_w} \quad 3.30$$

where κ is the new parameter proposed by *Petters and Kreidenweis* and V_s and V_w are the dry volume of the solute and the volume of water in the drop. κ describes the mass of water associated with the mass of dry particle. Eq. 2.19 may then be written using the relation in Eq. 3.30 as

$$S_w = \frac{d_d^3 - d_0^3}{d_d^3 - d_0^3(1 - \kappa)} \exp\left(\frac{4M_w\sigma_{sol}}{\mathcal{R}T\rho_w g f d_d}\right) \quad 3.31$$

where d_0 is the initial dry diameter. For a particle consisting of various chemical components (i.e. one that is internally mixed), κ is described by a simple mixing rule:

$$\kappa = \sum_i \varepsilon_i \kappa_i \quad 3.32$$

where ε_i is the volume fraction of component i . κ generally ranges from wettable but insoluble ($\kappa = 0$) to very hygroscopic ($\kappa \approx 1.4$ for NaCl). From the above relations, it is apparent that the presence of an insoluble component will have the effect of increasing the bulk water activity as given by Eq. 3.30 relative to the apparent water activity determined by assuming that the particle is completely soluble.

Measurements of hygroscopicity (HTDMA) and critical saturations (CCNc) can be related using Eq. 3.31. According to Kohler theory [*Pruppacher and Klett, 1997*], the critical saturation (s_{50} from the CCNc measurements; Eq. 3.28) for cloud drop activation for a given particle will be the maximum of Eq. 3.31. κ can be discerned

from the HTDMA measurements by manipulating the water activity term in Eq. 3.31 such that

$$a_w = \frac{gf^3 - 1}{gf^3 + \kappa - 1} \quad 3.33$$

Information regarding the heterogeneity of the aerosol can also be deduced from the CCNc measurements of critical saturation ratio. Heterogeneity of the sample has two possible sources: shape and composition. In Eq. 3.31, d_0 is a volume equivalent diameter. However, size selection by the DMA produces a mobility diameter. For approximately spherical particles such as ammonium sulfate, the volume equivalent diameter is roughly equivalent to the mobility diameter. However, for more complicated particle shapes such as those found in ambient aerosol, the aerosol may contain particles consisting of various shapes. The irregularity of shape may be captured by the shape factor, χ , and the volume equivalent diameter is given in *Hinds* [1999] as

$$d_e = \frac{d_m}{\sqrt{\chi}} \quad 3.34$$

For a cubic particle such as NaCl, the shape factor is given as 1.08 and the mobility diameter is converted to the volume equivalent diameter by multiplying by a factor of ≈ 0.96 . However, in an ambient aerosol, it is likely that the aerosol itself is externally mixed and the aerosol may be composed of a variety of shapes of particles.

Heterogeneity may also result from a chemical diversity, either internally or

externally, in the aerosol. In this case, the aerosol can be represented by a range of hygroscopicities.

In either case, it is not possible to discern the source of heterogeneity.

However, the extent of the heterogeneity may be quantified using a parameter that ratios the width of the activation curve to the critical diameter, or

$$\beta = \frac{\sigma_s}{D_{50}} \quad 3.35$$

Using this definition of heterogeneity, activation curves defined by Eq. 3.28 can be grouped into four different categories. In the first group (Type-I), the activation curve resembles a step function with a β of ~ 0.1 . This group represents a homogeneous aerosol such as ammonium sulfate. The second group (Type-II), $\beta \approx 0.2$ and the activation curves tend to be smooth. These curves exhibit heterogeneity but the steps in s_w are too coarse to determine multiple activation points. The third group (Type-III) exhibit activation behavior that is distinct such that multiple activation points may be determined. The fourth group (Type-IV) represents complex mixtures for which there is no dominant response mode. The complexity of the mixture for the final group prevents the extraction of any further information regarding the aerosol hygroscopicity.

3.3.2.2 Chemical Composition of Freezing Nuclei

During selected experiments, active freezing nuclei were collected on electron microscopy grids immediately downstream of the CFDC-1H OPC. *Rogers et al.* [2001] describe the setup for collecting freezing residuals while *Kreidenweis et al.* [1998] demonstrate the ability of the CFDC to separate active from non-active nuclei. Researchers have used this technique in prior field campaigns to study both heterogeneous IN residuals (MPACE, INSPECT-I, CRYSTAL-FACE, INSPECT-II) as well as homogeneous freezing residuals (INSPECT-I, INSPCET-II). The technique and setup are described briefly below.

An impactor located immediately downstream of the OPC collected particles larger than the impactor cutpoint on an appropriate substrate. The impactor is a 1 cm, replaceable cartridge consisting of five jets 0.075" (0.2 cm) in diameter. There is one central jet with the four remaining jets arranged symmetrically about the central jet. The collection surface on this impactor is located on a post centered 3 to 5 jet diameters below this central jet. The collection surface consisted of carbon coated, Formvar films supported by Au transmission electron microscopy (TEM) grids. The grids were affixed to the post using double sided tape.

The aerodynamic cut-point for the impactor (d_{50}) is a function of the flow rate, air density, and viscosity. The cut-point for a circular jet impactor can be defined using the Stokes number (Stk_{50}) [*Hinds*, 1999]. From Table 5.4 in *Hinds*

[1999], $Stk_{50} = 0.24$ for Re ranging from 500 to 3000. Using this parameter, the following equation gives the cutpoint as

$$d_{50}\sqrt{C_c} = \sqrt{\frac{9\mu N_j \pi d_j^3 Stk_{50}}{4\rho_p Q}} \quad 3.36$$

where d_j is the diameter of the jet and N_j is the number of jets.

The impactor for collecting ice crystal residuals was designed such that the cutpoint might be adjusted by plugging individual holes with small ball bearings. To determine the number of holes to plug, Eq. 3.36 may be solved for a given d_{50} . Given that, for the portion of the study in which the impactor was utilized, ambient air was sampled at low flow rates (as discussed later), a reasonable cutpoint for extracting ice crystals containing homogeneous freezing nuclei while not collecting interstitial aerosol or activated drops is 2 μm , a size which is considerably larger than the majority of ambient particles and crystals sizes should exceed. Since the cutpoint of the impactor is dependent on C_c which in turn is dependent on particle diameter, Eq. 3.36 must be solved numerically. Solutions to Eq. 3.36 are given in Figure 3.11 for two different temperatures and two different pressures. Figure 3.11 indicates that filling all but two jets is appropriate for capturing particles greater than 2 μm at approximately 5 lpm.

RJLeeGroup, Inc. (Monroeville, PA) performed the TEM analyses using a JEOL Model 2000FX equipped with an Advanced Analysis Technologies light element

energy dispersive spectrometer. Particles collected via impaction on the TEM grids were examined directly in the microscope. The TEM focuses the electron beam transmitted through the specimen creating an image at an increased magnification onto a fluorescent screen. Grids were initially evaluated by scanning from one end of the grid to another in multiple directions at a low magnification of $\sim 1000\times$ to identify regions of particle impact. TEM analysis was then conducted at higher magnifications (ranging from $20k\times$ to $85k\times$) to provide information on individual particle morphology and elemental composition, concentrating on significant impaction areas, if detected. Micrographs of each particle were recorded to illustrate morphological characteristics. Particles were measured for the major dimensions using an image analysis program (AnalySIS). For each particle, an energy dispersive spectrum was acquired and in some cases for separate features within particles. Background spectra acquired from particle-free areas indicate the presence of carbon and oxygen (from the support film), copper and gold (from the TEM grid), and silicon (from an unknown source within the TEM). Due to the presence of the elements in the background, identification of these elements in particles can be problematic in some cases; however, minerals were distinguished on the basis of significantly higher levels of silicon compared to background spectra, and particles generating only spectral peaks comparable to the background spectra were classified as carbonaceous. In addition to background analysis, blanks on which filtered air was run were also

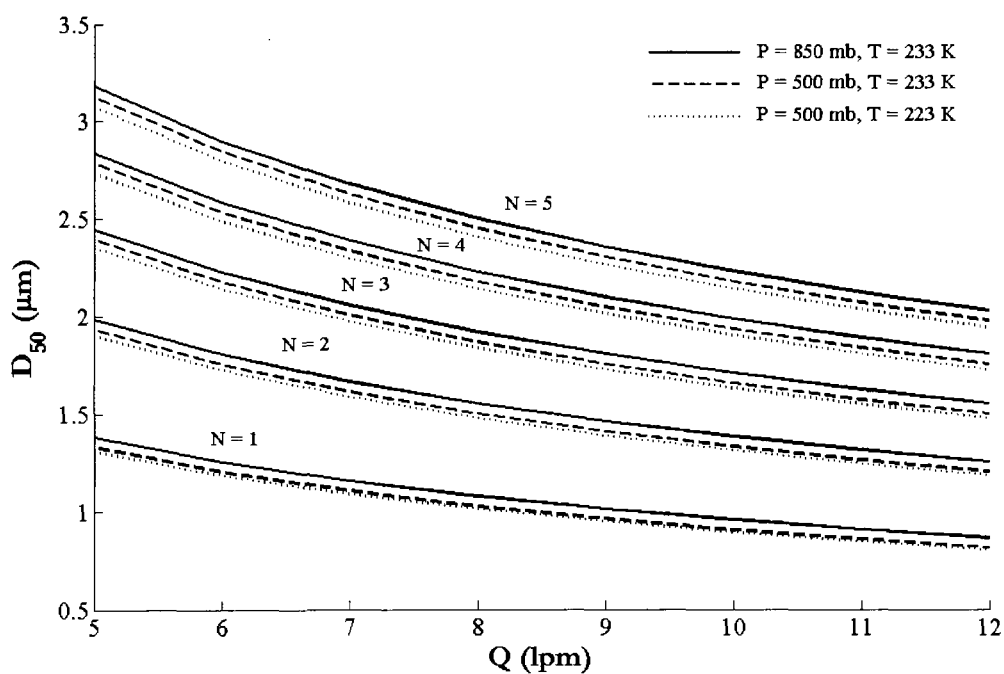


Figure 3.11. Example calculation of cutpoint as a function of the air flow rate and the number of jets, N . Calculations were made for ambient pressure in Fort Collins (850 mb) as well as mid-atmospheric pressure (500 mb). This plot also shows calculations at two different temperatures for 500 mb. Results of calculations indicate that the cutpoint is relatively insensitive for small variations in pressure and temperature.

collected and analyzed. Analysis of these blanks indicated that contamination was minimal using this technique.

3.3.3 Operation of the CFDC-1H

With the exception of the low temperature condensing unit, the CFDC-1H is a self contained unit intended for measurements on an aircraft platform. In the CFDC rack, two flow-through, silica-gel desiccant driers removed more water vapor. After the driers, the sample flow passes through a valve that allows the operator to measure background by changing the path of the flow such that it travels through a HEPA-

CAP filter (Whatman, Inc; Florham Park, NJ). Switching to the filter allows the operator to determine particle concentrations attributable to leaks, frost, or electronic noise. Because the concentrations of homogeneously freezing particles were large relative to the background, few evaluations of the background were conducted. For low pressure experiments, a #12 metal orifice (O'Keefe Controls Co.; Trumbull, CT) was located immediately upstream of the instrument. This orifice was sufficient to drop the pressure from laboratory pressure (~840 to 850 mb) to ~500 mb using a 10 lpm flow rate at chamber conditions. To operate at a combination of lower pressure and a lower flow rate, a pump was added just downstream of the orifice to skim the flow and provide a further pressure drop. A rotameter upstream of the pump measured the flow. Depending on the conditions within the chamber, flow rates were typically less than 1 lpm at 500 mb.

In each set of experiments, the CFDC-1H was operated using a single set of standard protocols for conducting experiments in a consistent manner. Prior to operation, the walls were cooled to approximately -30°C in preparation for icing. While the walls cooled, a vacuum pump brought the chamber to low pressure (on the order of 10 mb). As the temperature approached icing conditions, the vacuum pump was shut off and the change in pressure was monitored. For operational purposes, leak rates of less than 5 mb/min were deemed acceptable while higher leak rates required identifying and eliminating the source of the leak (typically by tightening of

lines). Typical leak rates during this set of experiments were below 1 mb/min at icing temperatures.

It should be noted here that, during these experiments, a leak associated with low temperature operation ($T_c \leq 216$ K) was identified. This temperature is in a range of conditions under which leak rates are not normally determined. These leaks (on the order of 100 mb/min) occurred at temperatures coincident with the operational limit of the o-ring material used to seal the cold portions of the chamber. Upon determination of the source of the leak, o-rings in contact with the cold surfaces were replaced with o-rings constructed of fluorosilicone (Parker Hannifin, Corp; Cleveland, OH). Results presented herein are from experiments in which the chamber was run with these new o-rings. No significant leak rate was observed at low temperatures upon replacement of these o-rings.

After leak tests indicated that there was no significant leak rate, the chamber was re-pressurized using filtered and dried lab air (Figure 3.8). The chamber was then flooded with ultrapure, de-ionized (18.3 M Ω -cm) water thereby creating a thin ice surface as described in *Rogers et al.* [2001]. As the lowest points along the outer wall rose to temperatures greater than 273 K during the initial icing, the chamber was rapidly iced a second time.

In the midst of these experiments, the chamber was disassembled several times. During several of these disassemblies, the inner wall was removed after icing

and while still at low temperature. While the coat on the upper portion of the inner wall and all along the outer wall was relatively level and consistent (i.e. not patchy), a bulge on the lower portion of the inner surface was noted. This bulge was associated with increased water residence time in the lower portion of the chamber due to resistance to draining after the water pump was shut off. This was observable in the residence time of the water - while the pumping time was approximately 45 seconds, the time to drain was almost twice as long. To circumvent this problem, a bypass valve that dumped water directly into the top of the tank was added thereby decreasing the drain time to approximately one minute or less. This had the effect of noticeably decreasing the thickness of the bulge on the lower portion of the inner wall (although the bulge was still evident, as might be expected). There was no noticeable effect on the outcome of the experiments.

After the icing process was complete, the chamber was evacuated once again and the wall temperatures were adjusted to the desired operational conditions. The purpose of evacuating the chamber upon icing is to inhibit the formation of frost that might occur during the icing process. Frost may form on surfaces in the chamber during the initial icing, after extended periods of sampling or if the chamber is exposed to unusually moist air. Frost is observable in the OPC signal while the CFDC-1H samples filtered air. The frost signal can inhibit the ability to detect heterogeneous [IN] in the atmosphere but generally does not have a significant

impact on the ability of the instrument to detect the onset of freezing. However, the chamber was still evacuated for a maximum of ten minutes so as to limit any depletion of the ice surface.

Once the conditions were reached, the chamber was once again re-pressurized, the OPC was moved into position, the sheath and total flows were set appropriately and the air pump was started. After the pump was turned on, experiments might continue for up to 6 hours after icing with no apparent impact on the results. For each temperature and particle size selected, water saturation ratios were scanned from those below observed activation to $S_w > 1.05$.

For each unique set of temperature, particle diameter, operation pressure and flow rate, experiments were run on at least three separate occasions providing a statistically relevant dataset and ensuring that results were consistent from day to day. The onset of homogeneous freezing was deemed the point at which a significant change in particles above a certain size threshold occurred. There is little or no difference between the two methods for identifying the onset of homogeneous freezing in this study as the changes in activating concentrations are sufficiently steep in the region of nucleation. It is important to note that in all cases, observed variations in the onset conditions for replicate homogeneous freezing experiments were well within the instrumental uncertainty.

The CFDC-1H DAQ uses a Newton-Raphson zero finding routine to determine the steady state position of the aerosol lamina and therefore the conditions within the lamina. Under more extreme cases where buoyant effects significantly limit the extent of the aerosol lamina (deemed critical flow; as in low temperature or low flow rate operation), this numerical method is unable to resolve the boundaries of the lamina and will report conditions significantly different than those expected. In these cases, the appropriate conditions were determined using a set of tools developed in Matlab (The Mathworks, Inc.; Nantucket, MA). The flow profile routine in this toolbox utilizes Matlab's zero finding function, `fzero`, which uses a combination of bisection, secant and inverse quadratic interpolation methods to find zeros. Results from this routine compare favorably with those calculated in the CFDC-1H data acquisition system for non-critical flow.

4 THE LABORATORY STUDY

In this study, homogeneous freezing was detected as a step-like increase in the concentration of particles larger than $2\ \mu\text{m}$. In previous CFDC studies, researchers

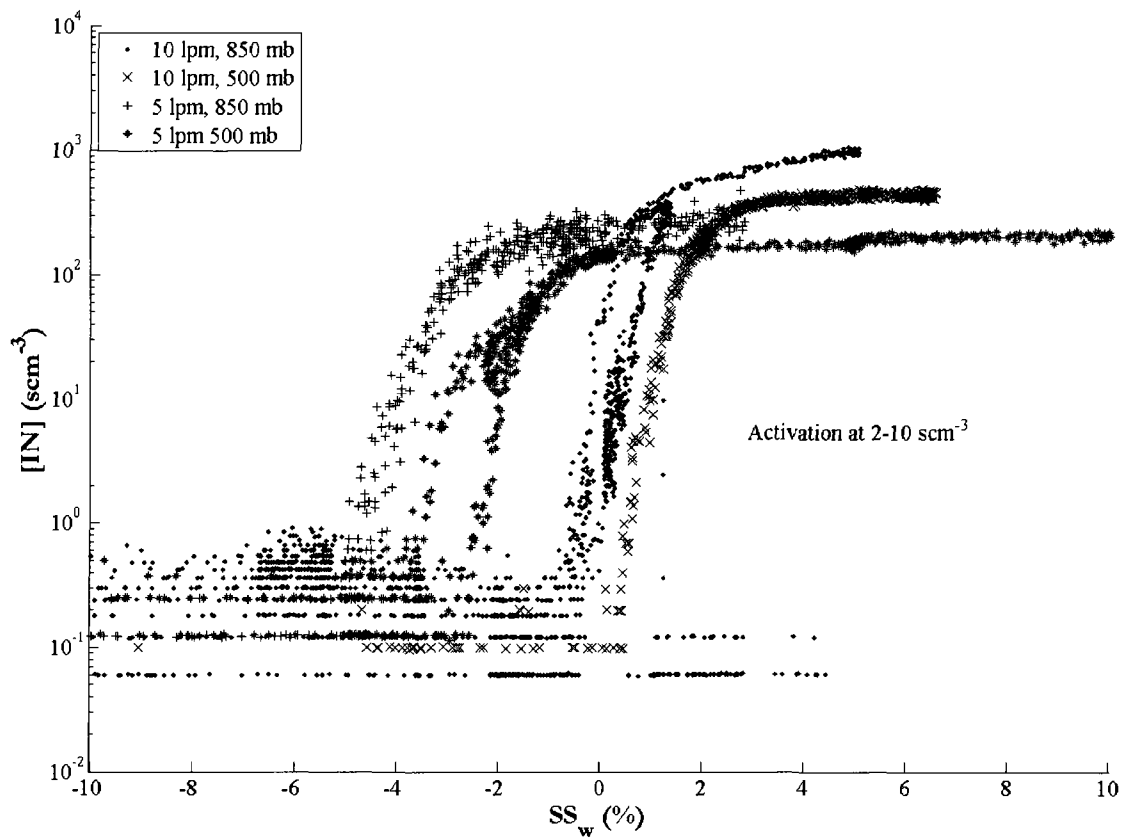


Figure 4.1. Ice nucleation (homogeneous freezing) curves for 100 nm particles at -45°C and various flow and pressure conditions.

utilized a threshold which indicates the onset of ice formation, often 0.1% or 1% of the input [CN] for both heterogeneous nucleation and homogeneous freezing studies [Archuleta *et al.*, 2005; Chen *et al.*, 2000; Prenni *et al.*, 2001a]. From 0.1% to 10% activation, there should be little change in the onset conditions. And, as demonstrated in the following sections, this is often the case. With this in mind, the onset conditions reported below are based on the change in the shape of the nucleation curve. In most cases, the nucleation curves are indeed steep. Figure 4.1 shows results from four different experiments at -45°C – notice that the conditions where the activated concentration increases rapidly do not change significantly from the first point to the point where the curve begins to flatten, at least a couple orders of magnitude in concentration. The shaded region indicates a region where the activated concentration ranges from 2 to 10 scm^{-3} ; in a typical experiment, this is the region from which conditions are generally reported.

It should be kept in mind that what are quoted as ‘onset conditions’ do not necessarily indicate where nucleation is occurring. As this study is focused on the measurement capabilities of the current system, an optical diameter of $2\text{ }\mu\text{m}$ was used as the threshold for detection. In most cases, crystals grew rapidly enough such that the observable onset was the same as the onset determined by the threshold. In others, such as in the 500 mb case, nucleation was observed in the lower channels of

the MCA spectrum prior to meeting the detection threshold. These cases are discussed individually below.

The initial portion of this study focuses on the freezing onset conditions for size –selected ammonium sulfate. Research indicates that ammonium sulfate is well characterized with regards to water uptake and homogeneous freezing as solution drops thus making this an ideal candidate for exploratory laboratory tests of the low temperature measurement capabilities of the CFDC-1H. For each of these tests, 100 nm and 300 nm particles are selected as described in Chapter 3.3.1.2 from a polydisperse population of ammonium sulfate particles. The expected onset conditions relevant to these experiments as predicted using the *Koop et al.* [2000] parameterization are given in Table 4.1. An important point to reiterate is that the population of particles produced by the size selection using a DMA is not truly monodisperse. In fact, depending on the mean diameter of the polydisperse population produced via atomization, the presence of multiply charged particles can

Table 4.1. Homogeneous freezing onset conditions as given by *Koop et al.* [2000] for two different sizes of ammonium sulfate particles. Calculations were made using the equilibrium, haze drop diameter, a fraction freezing (f_{HF}) of 0.001 and a total time of 3 seconds.

T _a (°C)	D _p	
	100nm	300 nm
-40	99.9	98.8
-45	97.87	96.35
-50	95.62	93.87

be significant (Table 3.17). However, as indicated in Figure 2.7, the presence of multiply charged particles are likely to have little impact on our observation of the onset of homogeneous freezing relative to the uncertainty in the measured value (Table 3.2); the difference between the calculated onset condition of a +3 charged particle for the 300 nm case results in a difference in the SS_w of at most about 1% at the given temperature, a difference that is not resolvable using this measurement technique.

4.1 High Flow Rate Results

4.1.1 Ambient Pressure

The first set of experiments consisted of measurements of the onset conditions of homogeneous freezing for size-selected ammonium sulfate under typical operating conditions in the laboratory. Current standard operating procedures dictate the use of higher flow rates (≥ 10 lpm) to avoid reverse flow at low temperatures and higher atmospheric pressures. Previous laboratory experiments (shown in Figure 4.2) indicate that at the lowest temperatures achievable with the unit in flight-ready configuration ($\approx -42^\circ\text{C}$), the onset SS_w of homogeneous freezing as a function of temperature and particle size is elevated above that predicted by theory. In addition, the lack of a clear size dependence across an almost order of magnitude change in the initial dry diameter suggests that the particles must be activated cloud drops prior to the onset of freezing.

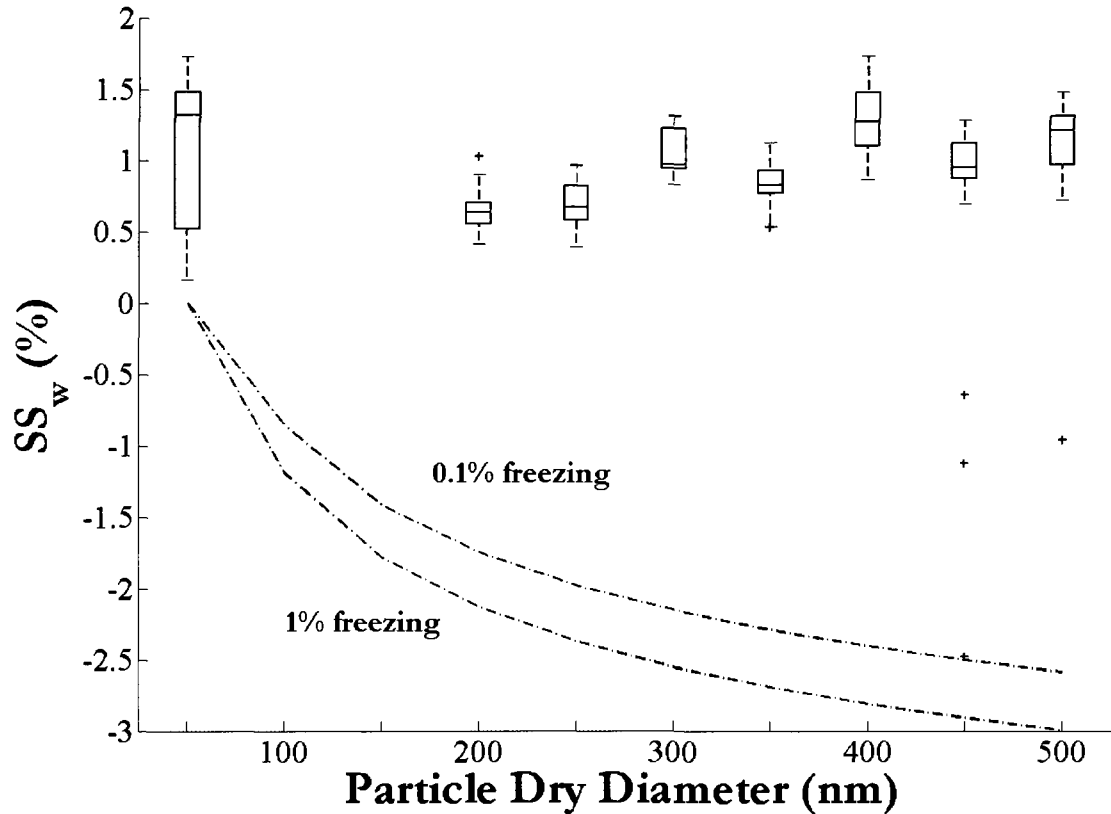


Figure 4.2. Laboratory data at $T_a = -42^\circ\text{C}$. A. Prenni measured these onset conditions using a version of the CFDC similar to that of the CFDC-1H. The data are represented by the box and whisker plot, where the red bar indicates the median SS_w , the box contains the extent of data from the lower quartile to the upper quartile and the whiskers extend to 1.5 times the inter-quartile range. The red crosses indicate outliers and most likely are associated with rapidly changing conditions. The dashed lines indicate the conditions predicted by *Koop et al.* [2000] for 0.1% and 1% of the population of particles at the given mobility diameters.

Higher SS_w 's than those predicted by *Koop et al.* were observed in the current experiments also. Results from several compiled experiments are shown in Table 4.2.

Onset conditions are calculated by averaging the conditions over the initial steep increase in large particle concentrations (as described in Figure 4.1). In Table 4.2 we see that the measured onset conditions trend as expected – with the onset SS_w

decreasing with temperature. However, despite the prediction by *Koop et al.* [2000], there appears to be no significant difference between the 100 nm and 300 nm onset conditions, a difference which should be evident at lower temperatures. The deviation of the measured onset conditions from theory becomes progressively larger with decreasing temperature.

Before moving on to the low pressure results, it should be noted that

Table 4.2. Average onset conditions with 95% confidence intervals for ambient (≈ 850 mb) conditions and $Q_t \approx 10$ lpm for experiments at different conditions. An estimate of the measurement uncertainty in the thermodynamic values (s_{SS_w} and s_{T_a}) calculated as described in Chapter 3.1.5 is given to the right of the average measurement.

D_p (nm)	T_{target} (°C)	T_a (°C)	SS_w (%)	$\overline{SS_w}$	s_{SS_w}	$\overline{T_a}$	s_{T_a}	
100	-40	-40.42	0.95	0.82 ± 0.14	3.41	-40.48 ± 0.28	0.49	
		-40.75	0.70					
		-40.27	0.80					
	-45	-45.60	-0.29	-0.33 ± 0.37	3.57	-45.37 ± 0.22	0.5	
		-45.35	-0.50					
		-45.46	-0.71					
		-45.08	0.17					
	-50	-50.33	-2.09	-1.83 ± 0.29	4.02	-50.29 ± 0.13	0.49	
		-50.38	-1.81					
		-50.16	-1.59					
	300	-40	-40.40	1.60	1.53 ± 0.3	3.51	-40.37 ± 0.13	0.51
			-40.43	1.29				
-40.47			1.30					
-40.18			1.94					
-45		-45.94	-0.05	-0.02 ± 0.22	3.74	-45.5 ± 0.43	0.5	
		-45.30	-0.20					
		-45.26	0.19					
-50		-50.66	-2.49	-2.07 ± 0.72	3.98	-50.53 ± 0.23	0.49	
		-50.63	-2.38					
		-50.30	-1.33					

anomalous freezing behavior was observed at the lowest temperatures during this portion of the study. The anomalous behavior motivated the dismantling of the chamber and prompted the experiments uncovering the leaking o-rings (Chapter 3.3.3). Figure 4.3 shows an example of this behavior; from this plot, it is apparent that residual concentrations at low SS_w are significant ($\approx 10 \text{ scm}^{-3}$). In initial experiments, these residuals were occasionally observed down to near ice saturation (i.e. where the two wall temperatures in the growth region converge) and were hypothesized to be associated with the leaking o-rings. However, as in Figure 4.3, persistent residuals still appeared to be an occasional issue; decreasing the sample flow rate decreased the occurrence of these episodes and so all measurements at these operating conditions were taken using a sample flow rate of 0.5 lpm. Still, this behavior never completely disappeared. The source of the residual counts is not apparent, but this behavior has been occasionally observed in other studies with the laboratory instrument at low temperatures. The inconsistent reproducibility of these observations suggests that the problem may lie with the seal on the OPC plate which must be adjusted for each experimental run due to the need for evacuation and icing.

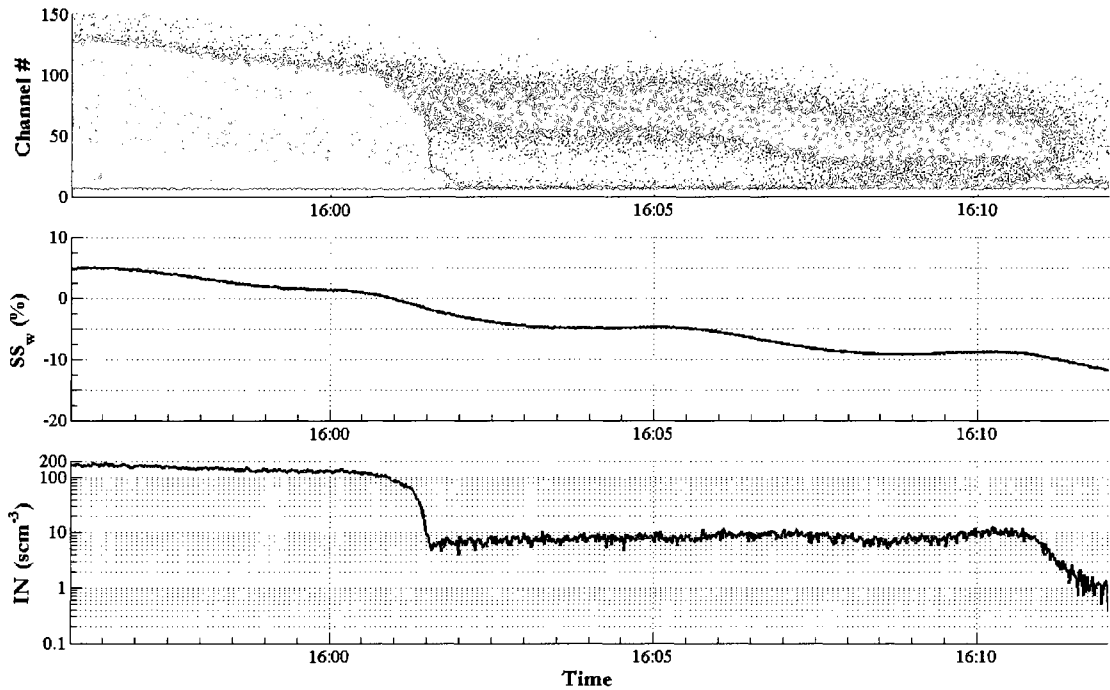


Figure 4.3. Freezing results from 27 May at -50°C using 300 nm ammonium sulfate particles. Data were recorded using the OPC's medium gain. Note the persistent residual of $\sim 10 \text{ scm}^{-3}$ at low supersaturations. The residual tails off as SS_w approaches -10% .

4.1.2 Low Pressure

With decreased pressure, two effects impacting particle trajectories are anticipated: the influence of the buoyant force will decrease due to decreasing air density and the diffusivity will increase (Eq. 2.3). With the influence of buoyancy more limited, the velocity profile will flatten and particle residence time in the growth region will increase. Increased diffusivity will result in faster relaxation times to the growth region water vapor profile as well as more rapid transport of water vapor to the particle surface. Given these two effects and the poor performance of the

CFDC-1H at ambient pressure, it is reasonable to expect experimental results at low pressure to demonstrate better agreement with the *Koop et al.* parameterization (Table 4.1). However, Table 4.3 indicates that *higher* SS_w were consistently required for observation of freezing; results were not even in agreement with theory within the measurement uncertainty at lower temperatures ($\pm 4-4.25\%$ at water saturation and $T = -50^\circ\text{C}$).

It is unclear why higher SS_w are required at the lower temperatures to grow crystals to observable size at the lower pressure, but it is apparent upon closer examination that nucleation is occurring earlier in the low pressure case. Figure 4.4

Table 4.3. Compiled Average onset conditions with standard deviations for $P \approx 500$ mb and $Q_t \approx 10$ lpm for experiments at different temperatures. An estimate of the measurement uncertainty in the thermodynamic values calculated as described in Chapter 3.1.5 is given to the right of the average measurement.

D_p (mm)	T_{target} (°C)	T_c (°C)	SS_w (%)	$\overline{SS_w}$	S_{SS_w}	$\overline{T_a}$	S_{T_a}	
100	-40	-40.22	1.34	1.31 ± 0.11	3.54	-40.23 ± 0.13	0.47	
		-40.13	1.20					
		-40.36	1.38					
	-45	-45.37	0.38	-0.21 ± 1.23	3.74	-45.27 ± 0.1	0.47	
		-45.41	0.72					
		-45.28	0.80					
		-45.12	-2.57					
		-45.20	-0.37					
	-50	-50.89	0.03	-0.46 ± 0.63	4.07	-50.41 ± 0.24	0.47	
		-50.24	0.47					
		-50.31	-1.13					
		-50.61	0.07					
		-50.40	-0.61					
	300	-40	-40.00	1.68	1.73 ± 0.05	3.61	-40.33 ± 0.38	0.45
			-40.31	1.74				
-40.67			1.77					
-45		-45.15	0.16	0.07 ± 0.32	3.85	-45.41 ± 0.2	0.46	
		-45.66	-0.38					
		-45.41	0.10					
		-45.41	0.40					
-50		-50.36	-0.42	-0.07 ± 0.64	4.23	-50.24 ± 0.12	0.46	
		-50.14	0.96					
		-50.39	0.34					
		-50.21	-0.35					
		-50.09	-0.89					

shows results expressed as [IN] versus SS_w for two different days. While on 15 May measurements were close to those predicted by the *Koop et al.* [2000] parameterization at -45°C , it is apparent that the -50°C results are off significantly (closer to water saturation). By adjusting the MCA channel used for discerning ice from 180 ($> 2\mu\text{m}$) to 50 ($> 500\text{ nm}$), the onset SS_w clearly separate such that the -50°C onset is at lower SS_w than at -45°C which in turn is lower than that at -40°C . Similar results were obtained on 21 May (bottom two panels) with the exception that onset SS_w were measured at all temperatures near water saturation for the data collected with the MCA cut channel set to 180.

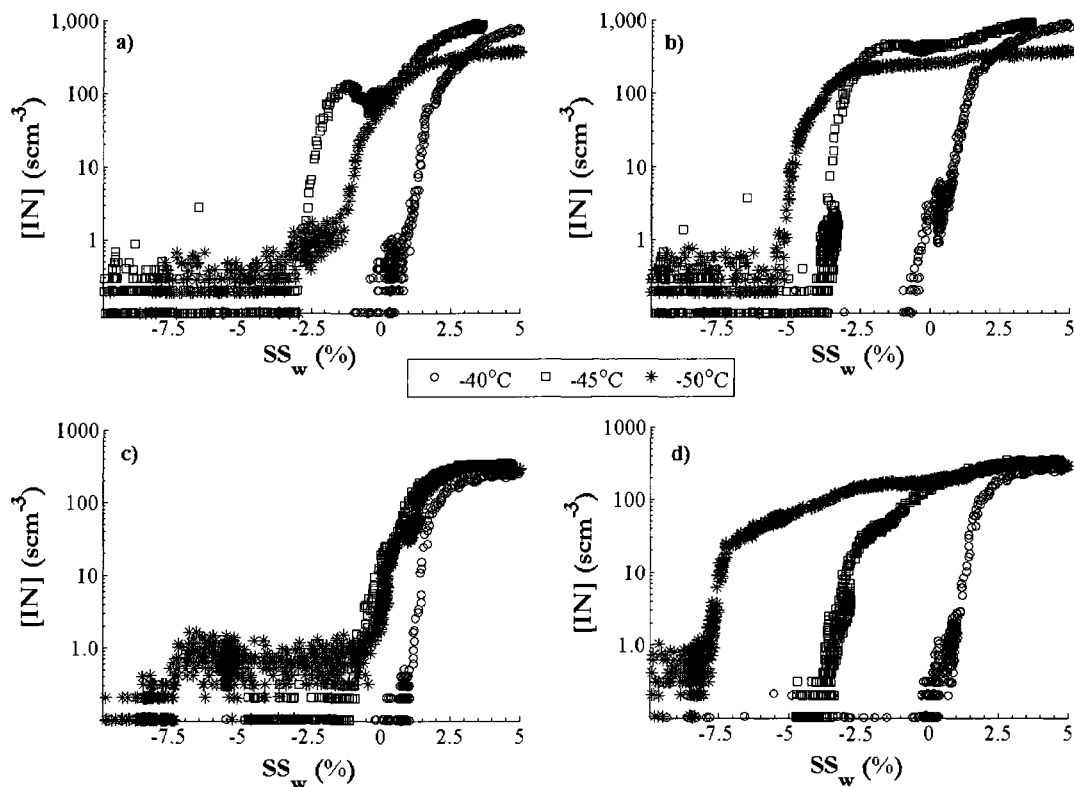


Figure 4.4. Measured IN concentrations versus SS_w on 15 May (a,b) and 21 May (c,d) for 100 nm ammonium sulfate particles. a) and c) show the measured $[IN]$ with the MCA cut channel set to 180 ($> 2\mu\text{m}$) while b) and d) show the $[IN]$ with the MCA cut channel set to 50 (600 to 700 nm).

Figure 4.4(d) shows a considerable amount of dispersion in the nucleation signal; that is, while the rise from background concentrations to those on the order of 10 cm^{-3} is steep, full activation occurs over a broad range of SS_w at each temperature. A look at several MCA spectra provides insight. Figure 4.5 plots MCA spectra for two different days taken during experiments conducted at -50°C with 100 nm particles. Although it is not apparent why, the response of the OPC to crystals at these conditions resembles distributions retrieved for monodisperse aerosol using a non-

ideal OPC inlet. In that case, the particles are not well contained in the sensing volume of the OPC and the monodisperse aerosol shows up as two peaks (as is shown in Figure 4.5). Although these distributions never happen at -40°C and only occasionally at -45°C , this suggests that these conditions may result in divergent flow as the sample exits the OPC inlet nozzle. Light scattered from particles of a similar size in the OPC is collected over a wide range of channels by the MCA (Figure 3.5). At onset the freezing particles appear so small that the signal generated by some of these crystals is binned into the lowest MCA channels (i.e. those below channel 50). It is only after SS_w increases and the crystals have grown to a size greater than that represented by channel 50 that the full concentration of frozen aerosol is directly observable.

The formation of crystals smaller than $2\ \mu\text{m}$ at the onset was observed only under this specific set of operating conditions ($P \approx 500\ \text{mb}$ and $Q_t \approx 10\ \text{lpm}$). Under other operating conditions, changing the MCA cutoff channel from 180 to 50 in the ambient pressure case resulted in less than a 1% change in the onset SS_w , a change that was generally within the confidence limit and well within the uncertainty of the measurement.

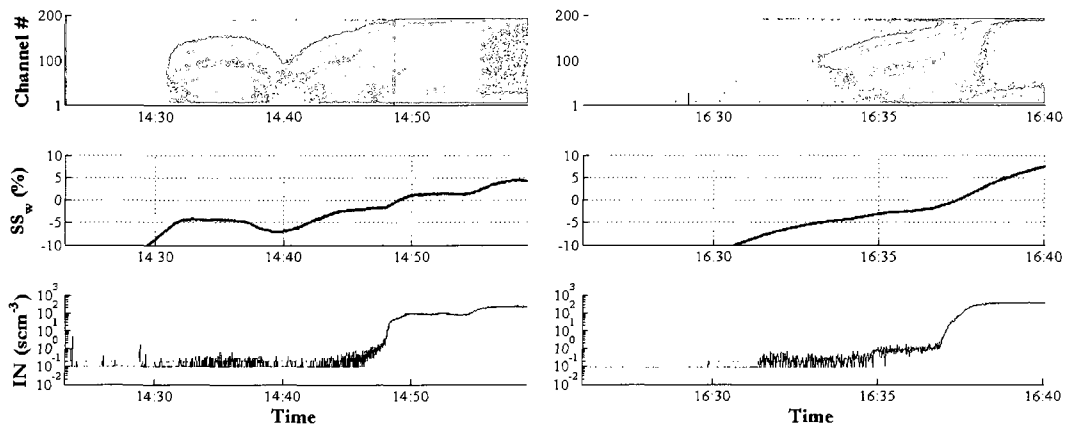


Figure 4.5. Experimental results from two experiments showing anomalous behavior of homogeneous freezing at low pressure and -50°C . The series of figures on the left show an excerpt of the experimental time line from 27 May 2008 while those on the right show the same for a similar experiment on 15 May 2008. The top panel on each side shows the MCA counts as a function of time and channel number (the limits on the color axis are 0 and 30 for each plot), the middle shows SS_w as a function of time and the bottom shows $[IN]$ as a function of time using channel 180 as the channel for distinguishing ice crystals from drops and aerosol. In both cases, the size of the dry particle sampled is $100\ \text{nm}$.

4.2 Low Flow Rate Results

4.2.1 Ambient Pressure

To increase the residence time, a second set of experiments was run at the same three temperatures and two pressures using a total flow rate of approximately 5 lpm (referenced to the average steady state conditions in the aerosol lamina) with 10% attributable to the sample flow. As with the low pressure case discussed in the previous section, decreasing the flow rate does not result in a proportional increase in the residence time. Closer examination of Figure 3.2 shows that as the flow rate decreases, the influence of the buoyant portion of the flow increases if the temperature gradient and pressure are maintained. This causes the downward portion of the flow to shift toward the cold wall and develop a more distinct maximum. For the case in Figure 3.2, the residence time for the 5 lpm case at 850 mb resembles that of the 10 lpm case at 500 mb.

It is reasonable to expect that the increased residence time associated with a smaller flow rate will result in onset conditions that more closely resemble those given by the *Koop et al.* [2000]. Table 4.4 indicates that the decrease in flow rate results in significantly lower freezing onset SS_w 's at each temperature than those observed at the higher flow rate. In fact, at 850 mb, the measured onset conditions for the 100 nm particles are comparable to those defined by *Koop et al.* (Table 4.1). These observed onset conditions at ambient pressure (Table 4.4) are slightly lower

Table 4.4. Compiled Average onset conditions with standard deviations for $P \approx 850$ mb and $Q_t \approx 5$ lpm for experiments at different temperatures. An estimate of the measurement uncertainty in the thermodynamic values calculated as described in Chapter 3.1.5 is given to the right of the average measurement.

D_p (nm)	T_{target} (°C)	T_a (°C)	SS_w (%)	$\overline{SS_w}$	S_{SS_w}	$\overline{T_a}$	S_{T_a}
100	-40	-40.31	-2.14	-2.38 ± 0.24	3.04	-40.39 ± 0.23	0.52
		-40.24	-2.52				
		-40.62	-2.49				
	-45	-45.20	-4.21	-3.80 ± 0.46	3.36	-45.35 ± 0.39	0.52
		-45.11	-3.78				
		-45.74	-3.40				
-50	-50.52	-5.10	-5.02 ± 0.37	3.52	-50.62 ± 0.21	0.52	
	-50.84	-4.66					
	-50.51	-5.29					
300	-40	-40.26	-1.27	-1.68 ± 0.41	3.08	-40.32 ± 0.1	0.53
		-40.27	-1.86				
		-40.42	-1.93				
	-45	-45.56	-3.92	-3.95 ± 0.22	3.34	-45.67 ± 0.23	0.51
		-45.90	-3.78				
		-45.54	-4.16				
-50	-50.31	-4.86	-4.28 ± 0.62	3.56	-50.21 ± 0.28	0.52	
	-50.40	-4.22					
	-49.93	-3.77					

than those predicted by *Koop et al* [2000], but they agree within the uncertainty of the measurement.

The mean onset conditions for the 300 nm particles, though still agreeing within the uncertainty of the measurement, begin to deviate more significantly from those conditions predicted by *Koop et al*. In fact, the observed onset conditions closely resemble (and are slightly depressed from) the observed conditions for onset ice formation by the 100 nm particles given in Table 4.4. These results may be indicative of a kinetic inhibition related to dilution: the larger, 300 nm particles require more water mass than the 100 nm particles for dilution to achieve the water activity required for the onset of homogeneous freezing. Inability to dilute rapidly enough will require higher SS_w than those predicted by *Koop et al*, possibly to the extent that 300 nm particles appear to freeze near the same point as the 100 nm particles. This effect would be exaggerated at lower temperatures given that the available mass of water is significantly smaller. The data are consistent with such an impact (Table 4.4).

4.2.2 Low Pressure

Although on average, the freezing onset SS_w for a given temperature is slightly higher at low pressure, in general the low pressure results at lower flow rates shown in Table 4.5 agree within the confidence limits with those at low flow rate and ambient pressure. At ambient pressure, the freezing onset conditions approach those predicted by *Koop et al.* [2000]. Given that the parameterization of *Koop et al.* provides a lower bound on the onset SS_w at freezing and that lower pressure provides

Table 4.5. Compiled Average onset conditions with standard deviations for $P \approx 500$ mb and $Q_t \approx 5$ lpm for experiments at different temperatures. An estimate of the measurement uncertainty in the thermodynamic values calculated as described in Chapter 3.1.5 is given to the right of the average measurement.

D_p (mm)	T_{target} (°C)	T_o (°C)	SS_w (%)	$\overline{SS_w}$	S_{SS_w}	$\overline{T_a}$	S_{T_a}
100	-40	-40.52	-1.098	-1.07 ± 0.18	3.21	-40.42 ± 0.24	0.5
		-40.18	-0.90				
		-40.58	-1.22				
	-45	-45.85	-2.70	-2.84 ± 0.45	3.51	-45.79 ± 0.22	0.52
		-45.58	-2.54				
		-45.95	-3.30				
	-50	-50.71	-4.77	-4.76 ± 1.45	3.73	-50.53 ± 0.18	0.52
		-50.39	-3.48				
		-50.50	-6.04				
300	-40	-40.48	-0.94	-1.11 ± 0.20	3.18	-40.82 ± 0.33	0.51
		-40.99	-1.29				
		-40.97	-1.11				
	-45	-45.69	-2.82	-2.72 ± 0.11	3.39	-45.73 ± 0.05	0.5
		-45.77	-2.71				
		-45.728	-2.63				
	-50	-50.85	-3.19	-3.65 ± 0.55	3.87	-50.71 ± 0.14	0.49
		-50.66	-3.61				
		-50.62	-4.16				

a more favorable environment for nucleation and crystal growth, these results are not surprising. However, it is interesting to note that the results from the 300 nm particle experiments at low pressure still show the same inhibition to freezing as those at the higher pressure.

4.3 Summary of Size Selected Ammonium Sulfate Experiments

Figure 4.6 shows all of the data collected for these experiments along with the 95% confidence interval (bars). It is apparent that at 5 lpm, both the 100 nm and 300 nm results trend as predicted by the *Koop et al.* [2000] parameterization down to

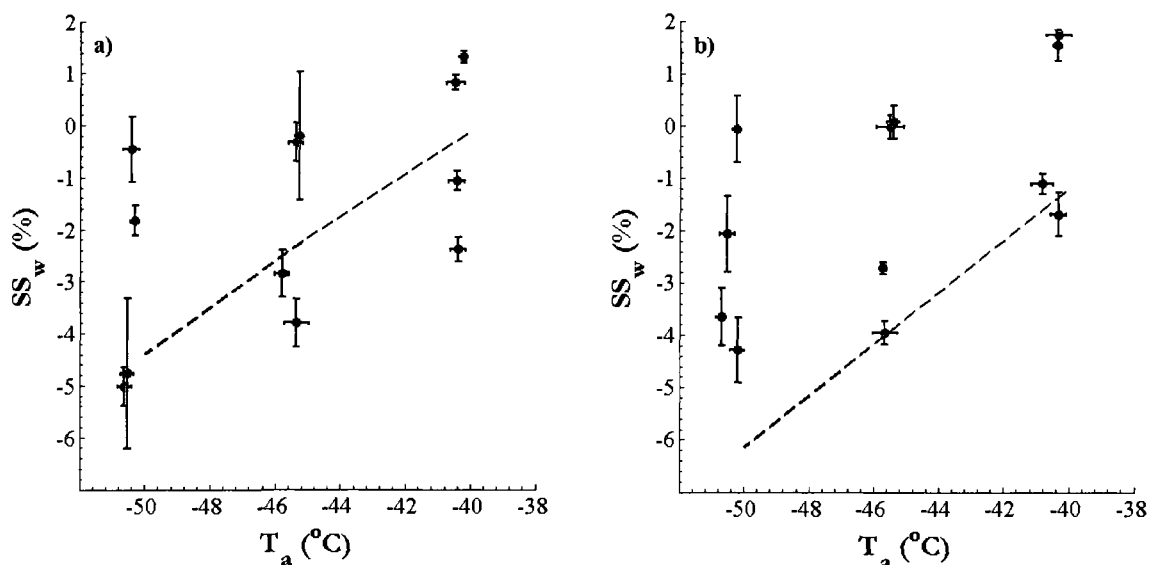


Figure 4.6. Summary of laboratory results with confidence intervals for a) 100 nm and b) 300 nm ammonium sulfate particles. Colors represent the different operating conditions: 10 lpm and 850 mb (blue), 10 lpm and 500 mb (red), 5 lpm and 850 mb (green) and 5 lpm and 500 mb (black). The dashed line represents predictions of the freezing onset point using the *Koop et al.* [2000] parameterization.

-45°C. Below this, the 100 nm particles maintain a similar onset SS_w compared to that predicted by the parameterization. However, the onset SS_w 's for the 300 nm particles seems to be deviating from the parameterization although they still agree within the uncertainty of the measurement (not shown to maintain clarity; see Table 4.2 through Table 4.5 for estimates of uncertainty at the different operating conditions).

The surprising result is the inability of the CFDC-1H to observe freezing below water saturation in the 10 lpm, 500 mb experiments. However, the presence of freezing was detected in lower channels for most of these experiments and the onset conditions for smaller crystals would be in-line with those predicted by the parameterization. The small initial size of the crystals suggests that drops are freezing near the end of the growth region, thus inhibiting crystal growth such that freezing is not observed using the typical OPC size threshold.

5 THE COMPUTATIONAL STUDY

The CFD/microphysical simulations are designed to estimate particle response to the thermodynamic fields to which they are exposed. For the most part, the conditions studied in the laboratory corresponded to those studied in the computational domain. For each pair of pressure and flow rate, the three experimental target temperatures were simulated (-40°C, -45°C and -50°C) and an additional simulation with a target temperature of -60°C is included, which extends the study of freezing further into the lower temperature bounds of cirrus in the mid-latitude upper troposphere. Due to instabilities in the solution most likely associated with the complexities of modeling a mixed convection problem, simulation of a low flow rate (5 lpm) at higher pressure (850 mb) was not possible without further refinement of the grid. Therefore, no results are shown for this regime (although both sets of conditions were used in the laboratory). CFD simulations were also run at a lower pressure (250 mb) at both flow rates across the entire temperature spectrum. For the most part, the results of these simulations are not discussed below

as they provide no further insight into the ability of the CFDC to measure homogeneous freezing.

5.1 Features of the Flow

In the initial paper describing the CFDC, *Rogers* [1988] developed a mathematical model to predict conditions within the chamber as a function of time (or vertical position). This model predicted that flow entering the chamber dry and warm rapidly and smoothly equilibrates to the target conditions in the growth region. At the exit of the growth region where the evaporation region begins, the conditions within the chamber once again change in a smooth fashion as the water vapor profile relaxes toward that of ice saturation at the cold wall temperature as it proceeds to the chamber exit and the OPC. In these simulations, the conditions in the chamber only fully relax to the final temperature and water vapor profile at the end of the evaporation region. The numerical work of *Straub et al.* [2004] and *Rogers et al.* [2004] show similar results.

While the previous numerical studies provide an excellent starting point, there is reason to believe that transitions may not be as smooth in the current design of the CFDC-1H. There are several possible scenarios as to how the transition from the growth to the evaporation region may proceed. In both the original instrument [*Rogers*, 1988] and the first field unit [*Rogers et al.*, 2001], the evaporation region consisted of a hydrophobic surface of low thermal conductivity that was not actively

cooled. In these instruments, the thermodynamic transitions marking the change in boundary conditions are expected to be smooth as the evaporation region surface gently relaxes to the cold wall temperature. The water vapor profile has time to diffuse and relax toward ice saturation before the temperatures reach this cold wall temperature. The downside of the design of the field unit described in *Rogers et al.* [2001] is that the location of the warm wall (on the outside) exposes the evaporation region which is not actively cooled to the heat of the ambient environment. This may prevent the temperature in this region from fully relaxing to the cold wall temperature (as previously discussed) and result in crystal evaporation.

In the CFDC-1H, the growth and evaporation regions are separated by a 1.25 cm Delrin, collar. The collar material (Delrin) is hydrophobic and has a relatively low thermal conductivity. In this design, the boundaries of the collar are maintained at the warm wall (upper) and cold wall (lower) temperatures respectively, therefore forcing a more rapid adjustment to the cold wall temperature. The issues associated with this design are discussed in the following section. A final possible transition from the growth to the evaporation region is a warm wall constructed of a single piece with the upper and lower portions maintained at two different temperatures. This is a design currently under consideration in the laboratory unit and is not discussed here. The two differences between the warm wall configuration in the first

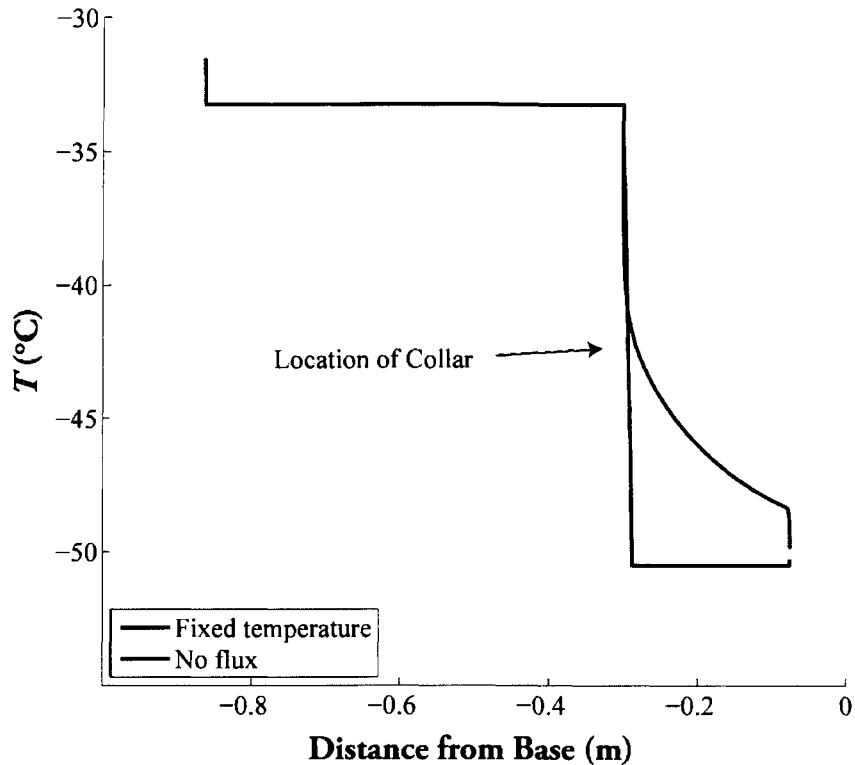


Figure 5.1. Difference in warm wall temperature profiles for the two different configurations of the field CFDC. The “No flux” case represents the warm wall configurations discussed in *Rogers* [1988] and *Rogers et al.* [2001] while the “Fixed temperature” represents the configuration of the warm wall in the current field instrument.

field unit and the current is illustrated by the wall temperature profiles shown in Figure 5.1.

Another transition not explicitly resolved in previous modeling efforts is that of the transition from the evaporation region to the outlet. In this region, conduction has the potential to alter the thermodynamic and fluid dynamic profiles because no portion of this region is actively cooled. Previous studies assume that the outer wall boundary in the outlet region is a perfect insulator and therefore does not conduct

heat. This assumption maintains the water vapor and temperature profile of the evaporation region. Simulations in this study account for the heat transfer through the base material.

Several interesting features of the flow dynamics and thermodynamics associated primarily with the transitions discussed above were observed throughout the simulations. These features have the potential to alter the observation of freezing either directly by altering the water vapor or temperature profile to which aerosol are exposed or indirectly by altering the position of the lamina or the distribution of aerosol throughout the chamber. Although these features may depend on the choice of how to model the chamber (such as specification of boundary conditions which are not well constrained by direct observation), these features tend to be consistent across all of the simulations and exhibit consistent behavior as conditions change within the chamber.

Before proceeding, it is important to define some terminology used below. Two different terms are used to describe different simulations. “Operating conditions” refer to a unique flow rate-pressure (Q_t, P) combination. “Target conditions” on the other hand define the target thermodynamic conditions (T_a, SS_w) in the aerosol lamina.

5.1.1 Water Saturation

The first prominent feature observed in the calculated supersaturation field is a moist bubble near the trailing edge of the collar on the outer wall separating the growth region from the evaporation region. In the region of the collar, the outer wall temperature is transitioning from the warm wall temperature to the cold wall temperature (Figure 5.2). The surface of the collar itself is hydrophobic and is therefore modeled as a zero water vapor flux boundary condition. Near the trailing edge of the collar, SS_w can reach as high as 80 to 90%. Water vapor from the trailing edge of the growth region diffuses into the rapidly cooling evaporation entry region. Because the bubble is created primarily through the diffusion of water vapor into this region, the extent and strength of the bubble is greater at warmer operating temperatures, higher temperature gradients (i.e. higher lamina SS_w 's) and lower pressures. According to Eq. 2.3, diffusivity is greater at both higher temperatures and lower pressures, thus enhancing the larger bubble at these conditions. The larger bubble at greater temperature gradients is a result of a larger change in temperature across the collar, therefore more water vapor is being added to a colder region. In addition to the diffusive nature of the problem, there is also a convective aspect to the transport of water vapor Eq. 3.12. As a result, a decrease in the flow rate decreases the influence of the moist bubble in the domain.

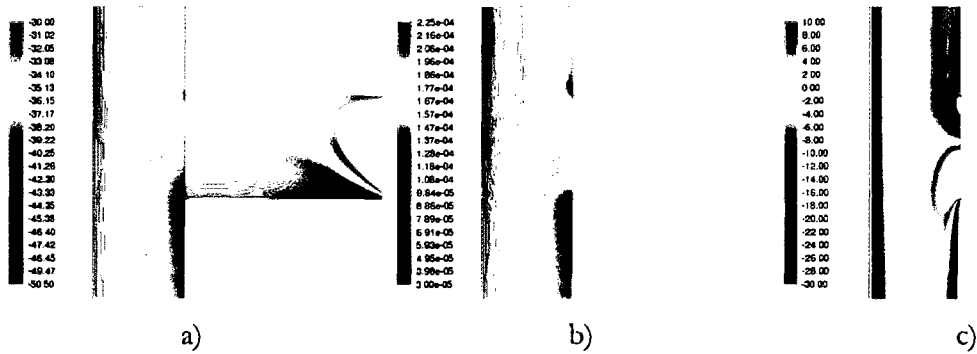


Figure 5.2. A moist bubble exists throughout all of the simulations near the trailing edge of the collar (flow is downward in these figures). This plot shows an example of the moist bubble and associated properties in the region for the highest SS_w case at $P = 850$ mb, $Q_t = 10$ lpm and $T_{tar} = -45^\circ\text{C}$. a) Temperature profile ($^\circ\text{C}$). b) Water vapor mixing ratio w_v (kg/kg). c) Super saturation with respect to water (SS_w) as calculated using (2.4), (2.5) and (2.6). The collar is recognizable as the region in the above plots for which there is a temperature profile but no water vapor or SS_w profile. These results are typical for *all* simulations.

The temperature profile along the collar strongly influences the extent of the moist bubble and is in turn influenced by 1) the boundary conditions at the leading and trailing edges of the collar (assumed to be the warm and cold temperatures respectively), 2) the temperature on the outer portion of the collar (assumed to be 273.15 K in all simulations) and 3) the width of the collar. The distance between the inner and outer portions of the collar is approximately twice the width of the gap between the inner and outer walls; therefore, the influence of the outer-most boundary is significant only in cases where the outer boundary temperature approached that of the cold wall. Instead, the cold and warm boundaries above and below the collar have the most significant impact on this bubble. The length of the collar will control how rapidly the temperature profile adjusts to the evaporation

region temperature. A longer collar will result in a more gradual shift in the temperature and more time for water vapor to diffuse, thus inhibiting the development of the supersaturation bubble. A short collar may result in a more abrupt change in the outer wall temperature, and, therefore result in a larger supersaturation bubble. The model neglects the Delrin portions into which the walls slide. This may result in significantly different water vapor profiles than those shown in Figure 5.2.

In fact, although not shown here, the overlap of the copper on the Delrin was modeled for the region in which the outer wall slides into the outlet cone. The overlap between the copper and Delrin in this region is 3.81 cm. The outer boundary was maintained at 273.15 K and, in the model, the copper is assumed to be thin enough such that conduction is one dimensional; this resulted in a warming of the ice coated copper surface which in turn generated spuriously high saturations that extended well into the sample lamina entering the outlet region. The water saturations were high enough to result in drop growth and possible nucleation that was not observed in prior experiments. Since there is no way to verify these results through direct measurement (i.e., the assumption of 1-D conduction through the copper carries a considerable amount of uncertainty), the ice coated region in contact with the Delrin in the outlet region (as in the region surrounding the collar) was neglected in these simulations. One fundamental difference between the overlapping

copper in the outlet region and the overlapping copper in the region of the collar is that the inner wall is actively cooled in the region of the collar whereas it is not in the outlet region. In the region of the collar, the cold wall will drive the temperature of the overlapping portion of the outer wall most likely resulting in a smoother temperature transition between the growth and evaporation regions.

5.1.2 The Stream Function

A line that is tangent everywhere to the velocity u at time t is termed a streamline [*Batchelor*, 1967]. For a steady, two dimensional flow (as is the case here), the family of streamlines is given by

$$\frac{dx}{u(x)} = \frac{dy}{v(y)} \quad 5.1$$

For consistency, we define u as the axial component of the velocity in the CFDC and v as the radial component. As the flow is steady, path lines, or a trajectory traced out by a moving fluid particle, are coincident with stream lines. So, in the case of CFDC simulations, streamlines in the CFDC indicate the path that a fluid particle released from some point may take. Along streamlines, the stream function ψ is constant. The stream function is given as

$$u = \frac{\partial\psi}{\partial y} \text{ or } v = -\frac{\partial\psi}{\partial x} \quad 5.2$$

Using Eqs. 5.1 and 5.2 and realizing that ψ is constant along a stream line, this can be rewritten as

$$\psi = \int u dy - v dx$$

5.3

The volume flow rate between two stream lines may be written as the difference between the values of the stream function along the two different lines.

With this in mind, plots of the stream function indicate features of the flow that may be unexpected. In *Straub et al.* [2004], the authors identified an area of recirculation in the outer sheath inlet region where the flow encountered a physical step along the outer wall boundary. This analysis guided researchers at CSU in the re-design of the chamber and the step in this region was removed in order to prevent potential perturbations to the flow immediately downstream.

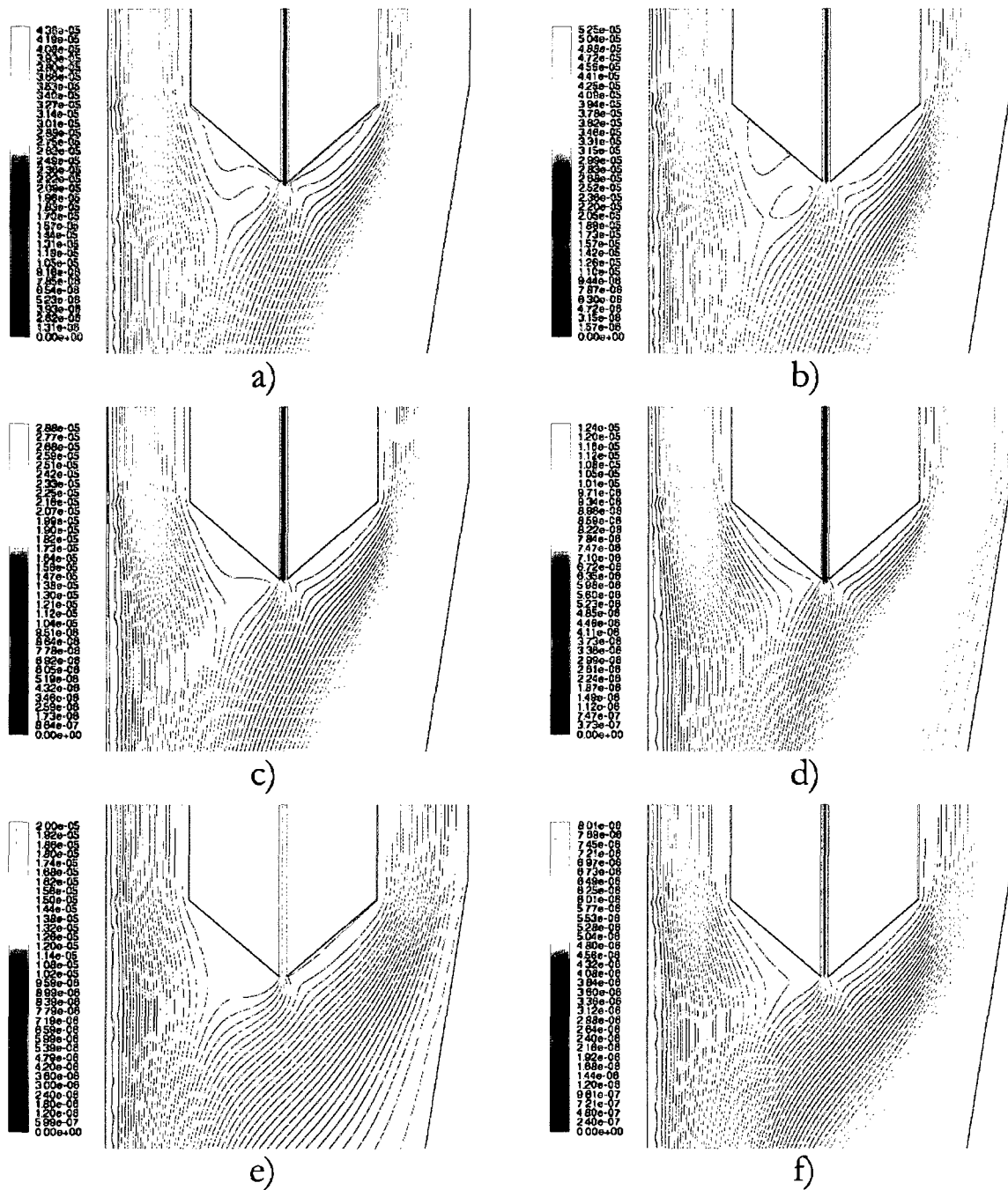


Figure 5.3. Plot of the stream function [kg/s] for several different sets of operating conditions. In each case, the conditions are for set for the highest target SS_w . a) - 40°C, 10 lpm, 850 mb, b) -60°C, 10 lpm, 850 mb, c) -60°C, 10 lpm, 500 mb, d) -60°C, 10 lpm, 250 mb, e) -60°C, 5 lpm, 500 mb, f) -60°C, 5lpm, 250 mb.

In the current analysis, plots of Ψ show several non-ideal flow features. First, as expected analysis in *Rogers* [1988], the recirculation in the growth region is readily apparent when operating at lower temperatures and larger temperature gradients (not shown). This vortex is weakened by lowering the pressure or increasing the flow rate as predicted by Eq. 3.1. The presence of the vortex is apparent in both plots of the stream function as well as in the position of the lamina (not shown). As discussed below, results of the steady-state analysis compare favorably (with minor deviations) with the approximately steady portion of the flow profile in the CFD simulations.

Being confined to a narrow region, the sample stream enters the chamber at a considerably higher velocity than the surrounding fluid. The region in which the sheath and sample flows converge represents a region of free shear; a region in which

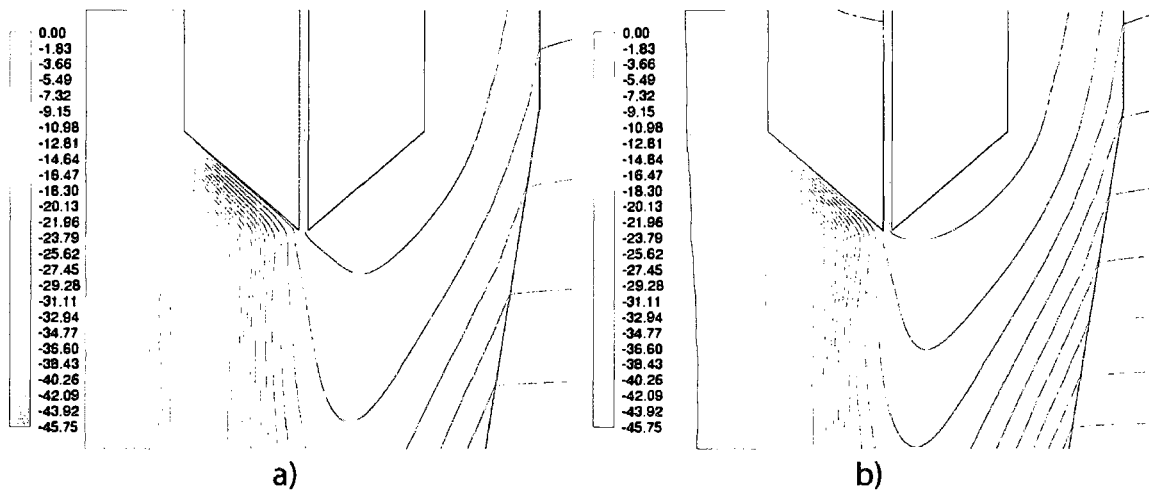


Figure 5.4. Inlet temperatures for the $P = 850$ mb, $Q_t = 10$ lpm for target temperatures of a) -40°C and b) -60°C . Both are set to the same temperature scale for comparison (the temperature of the inner wall in the -60°C case is -65°C).

the interacting flow velocities are very disparate, the sample flow velocity being considerably higher than the other two. In this region, plots of Ψ indicate boundary layer separation as the sample flow comes into contact with the sheath flows. This separation is evident along the outer portion of the inner-most inlet blade (Figure 5.3). As shown in Figure 5.3, the distortion of the flow caused by the velocity mismatch is sensitive to the operating pressure, the target operating temperature and the operating flow rate. In Figure 5.3 a) and b), it is evident that by decreasing the operating temperature from -40°C to -60°C , the stream lines become more distorted in the outer region near the inner inlet blade such that a region of significant recirculation exists. Decreasing the pressure in the -60°C case (Figure 5.3 c) and d)) results in more ideal (i.e. smoother) flow. Decreases in the flow rate, Figure 5.3 e) and f), result in further distortion of the flow field in this region.

As with the vortex in the growth region, these distortions of the flow field are manifestations of density gradients near the inlet as well as the interaction between the rapidly decelerating sample fluid and the converging sheath flows. As expected, the effect of the density has the same impact here as in the growth region. Figure 5.4 shows the temperature variations in the inlet region with position for the cases shown in Figure 5.3 a) and b). The gradients in this region are driven primarily by the temperature of the cold wall, the only wall that, in this region, is actively cooled. The colder temperature of the cold wall creates slightly larger gradients in the region near

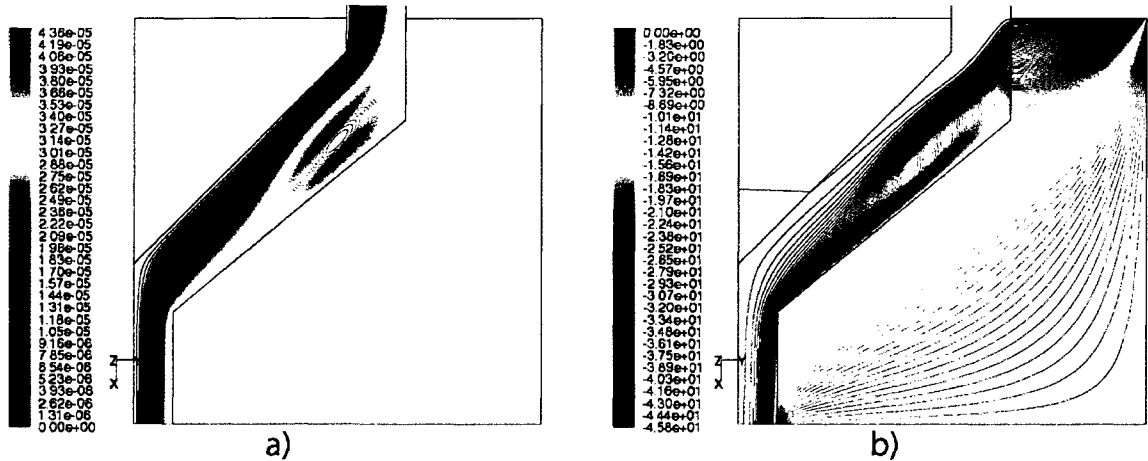


Figure 5.5. a) Contours of the stream function in the outlet region. b) Temperature profile in the same region. Both plots correspond to conditions for the final -40°C case at 850 mb and $Q_t = 10$ lpm.

the outer portion of the inlet blade. This in turn creates observable changes in the flow field in this region. These distortions of the flow field can be ameliorated as with the vortex in the growth region by operating at lower pressure.

Finally, another vortex appears consistently in the outlet region (Figure 5.5). This vortex is the result of density changes induced by conduction through the outer portion of the Delrin in the outlet region. Here, neither the bottom nor the top of the outlet is actively cooled. As the outer boundary is assumed to be 273 K and the conductivity of the Delrin is finite (though small), heat is transferred through the outer portion of the outlet via conduction such that the air in the outlet begins to warm. The large temperature gradient generated by the cold flow interacting with the warmer wall results in a vortex that is present throughout all simulations. The intensity is governed by the cold wall temperature as well as the flow rate. The

presence of the vortex pushes the sample lamina closer to the outlet cone and results in a higher peak velocity than would be generated if the boundary was assumed to be a no heat flux boundary

The features described above have the potential to perturb both the particle path and thermodynamics of the particle trajectory. It is not apparent that these features are having any impact on the final experimental results. Unstable flow resulting from any of the flow features would result in dispersion of the nucleation signal as the particles are spread throughout the chamber, a feature not directly observed in the current set of experiments described in Chapter 4. Nevertheless, it is also not apparent from the above experiments that the particles are interacting with any pockets of anomalously high water vapor content. However, these features are important to keep in mind; simple design changes in future iterations of this instrument may be sufficient to eliminate even the potential that these features could impact the particle trajectory in the CFDC-1H.

5.2 Comparison of the CFD Trajectories with the Analytical Solution

Particles released from the inlet region in the simulations take a well defined path through the instrument. Given that gradients are small in the narrow inlet region, the velocity in the lamina rapidly relaxes to a parabolic profile between the inlet blades. As the sample lamina (the red lines in Figure 5.6) exits the inlet region, the flow rapidly decelerates and is driven toward the cold wall due to the temperature

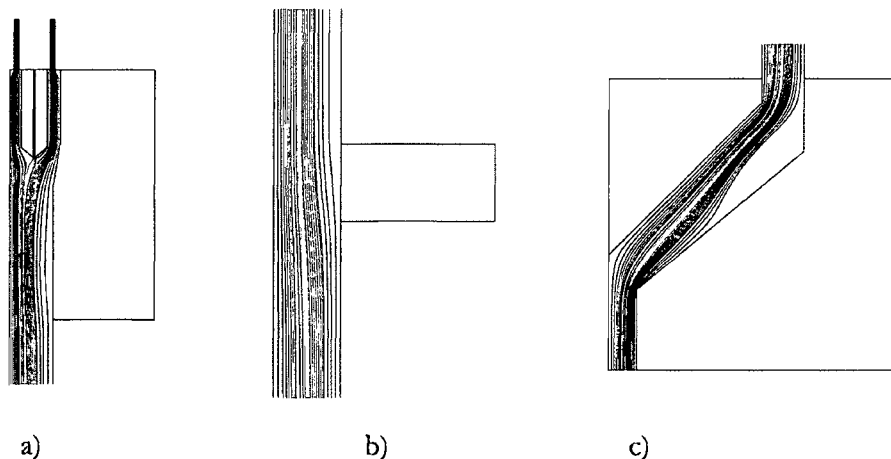


Figure 5.6. One micron particle trajectories (red) and pathlines (blue) in (a) the inlet region, (b) the transition to the evaporation region and c) the outlet.

gradient in the chamber above the evaporation region (Figure 5.6(a)). As the flow enters the growth region of the chamber, the temperature profile, and therefore the velocity profile, rapidly relaxes toward the growth region target profile. Upon reaching the region near the collar which separates the growth and evaporation regions on the outer wall, the temperature begins to rapidly decrease toward the cold wall temperature and the sample lamina begins to shift toward the center of the chamber (Figure 5.6(b)). In this region, the peak velocity drops and the flow becomes essentially parabolic. In the outlet region, the flow becomes more narrowly confined, resulting in considerably higher peak velocities (Figure 5.6(c)). In addition, the vortex on the outer portion of the flow further confines the exiting flow thus resulting in even higher velocities. The acceleration of the lamina in this region limits particle residence times such that the impacts of increasing temperature and decreasing saturation have a limited impact on the final crystal size.

It's important to acknowledge that, as stated in previous sections, the lamina is of finite width in which the conditions can vary significantly (*Chen et al.*[2000] suggest that, for a 1:10 sample to total flow ratio, the variation in temperature can be as much as 1.5 K and 3% in the lamina water saturation ratio). In the CFD simulations, the width of the lamina is modeled by releasing 10 particles from the 10 grid points at the sample inlet (100 particles total for a single simulation). In addition, conditions typically quoted in previous studies refer to those of the average position of the lamina from the solution of the analytical, steady-state equations in *Rogers* [1988]. Therefore, in the following analysis, only the trajectory released from the center node (the 5th trajectory) is compared with the conditions given by the analytical solution. For comparison, all variables are normalized. In the case of saturation with respect to water (SS'_w), the relative humidity ($RH_w; SS_w + 100$) has been normalized to the calculated steady-state RH_w . For the temperature, the trajectory value is normalized as

$$T'_a = \frac{293 - [T_{traj}/K]}{293 - [T_{tar}/K]} \quad 5.4$$

where T_{traj} is the temperature along the trajectory at t' and T_{tar} is the target sampling temperature. The reference temperature, 293 K, was chosen as this is the initial temperature of the sample for each simulation. The time is normalized by the maximum time along the trajectory (the time at which the trajectory exits the domain). Normalization of the time allows direct comparison of the trajectories, but

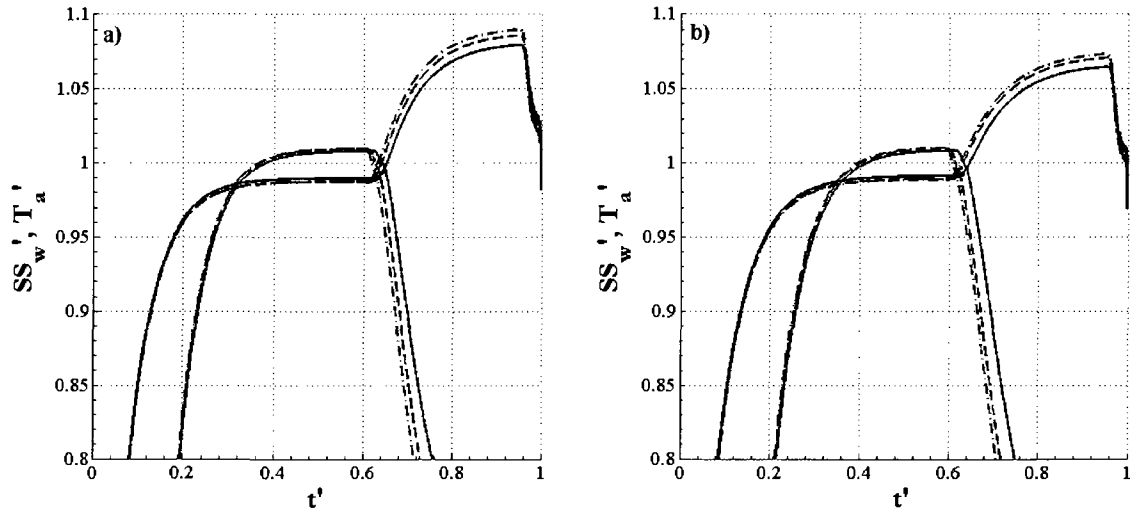


Figure 5.7. Normalized thermodynamic trajectories for -40°C (a) and -50°C (b). Blue represents the normalized T_a whereas red represents the normalized SS_w . The solid lines indicate a low saturation case while the dashed represents a case near water saturation and the dashed-dot line indicates a case where $SS_w \approx 5\%$. These trajectories are representative of runs where the $Q_t = 10$ lpm and $P = 850$ mb. The total residence times for the trajectories near water saturation are 8.78 s (-40°C) and 8.43 s (-50°C).

it should be noted that increasing the difference in the wall temperatures decreases the particle residence time (as does increasing the SS_w or decreasing T_a).

Figure 5.7 shows normalized trajectories for the ambient case (850 mb) in which the total flow rate at the estimated steady-state temperature is 10 lpm. The figure shows normalized trajectories of SS_w and T_a in the -40°C and -50°C simulations at three different steady state SS_w 's – the low SS_w for the individual set of conditions, a simulation run near water saturation and one in which the SS_w is a maximum for the individual set of operational conditions (for actual values see Table 3.4 and Table 3.6). First, note that the trends are similar for both sets of target conditions and is

consistent throughout all simulations for this set of operating conditions. For these operating conditions, the simulations are warmer and more moist than those conditions given by the analytic solution.

Figure 5.8 provides some insight as to why this occurs at these different sets of operating conditions. Shown in Figure 5.8 are the evolution of the velocity, SS_w and T across the annular gap starting near the top of the growth region (85 cm) and proceeding to near the end (35 cm) for the -40°C case near water saturation. The velocity profile relaxes rapidly (by 75 cm) to the profile found near the end of the growth region and differs only slightly from the estimate provided by the analytic solution (Eq. 3.1). The temperature has relaxed to near the final profile by 65 cm and the supersaturation is the last to adjust with relaxation by 55 cm. From Figure 5.8, it becomes apparent where the deviations from the analytical solution observed in Figure 5.7 arise. The slight bow in the final temperature profile suggests that the convection term in the energy equation (Eq. 3.9) plays a significant role in the final profile; significant enough to perturb the profile such that conditions within the lamina are ~ 1 K higher than those predicted by the analytic solution to the steady-state temperature (Eq. 3.5). Indeed, this bowing is also evident in the water vapor partial pressure profile (not shown).

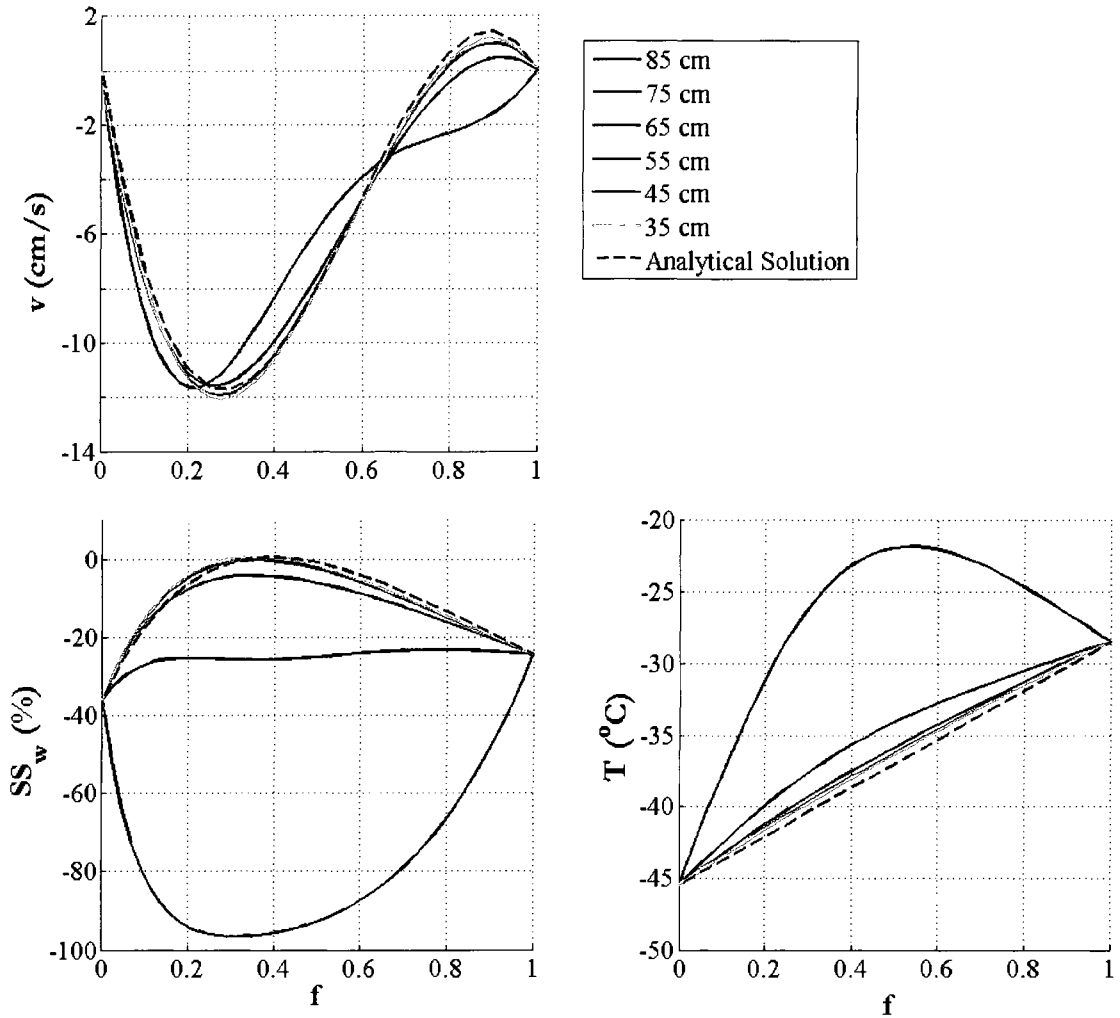


Figure 5.8. Velocity (upper), SS_w (lower left) and T for several points in the chamber across the growth region as well as the conditions given by the analytic solution (Eqs. 3.1, 3.4 and 3.5). f represents the fractional distance from the cold wall. The distances given are referenced from the bottom of the chamber where 85 cm is near the top of the growth region and 35 cm is at the bottom of the growth region. These conditions are for the fifth set of conditions provided for $T_a = -40^\circ\text{C}$, $Q_t = 10$ lpm and $P = 850$ mb given in Table 3.4.

The profiles computed for different target conditions also indicate that the structure of the temperature and water vapor profiles are affected by the same convective component. This results in warmer temperatures and higher water vapor

contents at the lamina centerline in the growth region than those predicted by the analytical equation (Eq. 3.5). However, despite the higher water vapor mass, the SS_w is not considerably higher ($\Delta SS_w \leq 1\%$) because the saturation vapor pressure also increases with increasing T (Eqs. 2.6 and 2.7).

Figure 5.9 and Figure 5.10 show the same normalized variables as Figure 5.7, but for the operating conditions of 10 lpm and 5 lpm at 500 mb respectively. Close examination of Figure 5.9, shows that, although the temperature deviates as in the 850 mb case, the SS_w seems to align with the actual steady-state state estimate in the growth region. However, at low flow rates (Figure 5.10) deviations in the SS_w are similar to those found in the base case (Figure 5.7).

Figure 5.7, Figure 5.9, and Figure 5.10 demonstrate how the operating as well as the target conditions impact both the relaxation of the thermodynamic conditions toward steady-state and the relative time (t) spent in the growth region. In each case, increasing the target SS_w has the effect of decreasing the relative residence time in the growth region but has no significant impact on the relaxation time. The decrease in residence time is expected as increasing the SS_w is occurs through imposing a larger temperature gradient which creates larger density gradients thus generating higher peak velocities. In the 10 lpm at 850 mb case, the total residence time of the particles near steady-state conditions is very sensitive to the target conditions – as the target temperature is lowered, the lamina has increasing difficulty relaxing to that

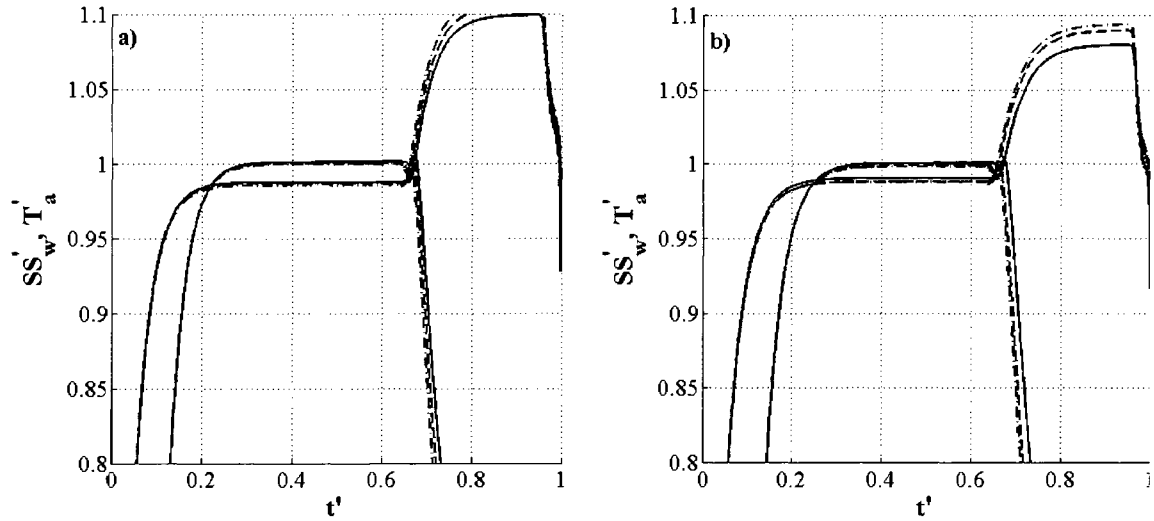


Figure 5.9. Same as Figure 5.7, but for $P = 500$ mb at 10 lpm.

temperature in the residence time provided which in turn delays the relaxation to the steady-state SS_w profile. At -60°C , the lamina is spending only a small amount of time at steady-state growth conditions. Finally, lower velocities and higher diffusivities (i.e. lower operating pressures) both allow the lamina to relax more rapidly and increase the *relative* time such that the time spent at the steady-state SS_w approaches that of the time spent at the steady-state temperature.

5.3 Ideal Operation

Before proceeding to results regarding simulations of microphysical growth, a few preliminary remarks are necessary. For simulating cloud particle trajectories, condensation coefficients need to be specified. As discussed in sections 2.2 and 2.4, the range of literature values is large. There is likely no one set of unique values that accurately model the behavior of cloud particles in the CFDC. In the instrument, there is a considerable amount of uncertainty in important parameters which, while not affecting the crystal size at large SS_w , may impact our ability to detect the onset of nucleation. These uncertainties include the actual temperature of the ice surface, the importance of phoretic effects and the dimensions of the ice surface (the length and thickness).

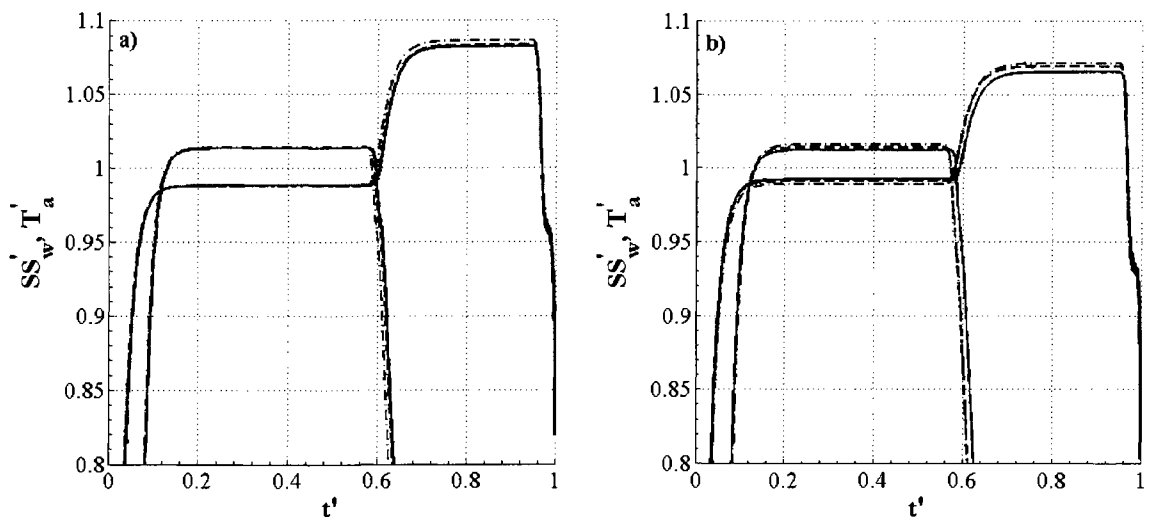


Figure 5.10. Same as Figure 5.7 for the $Q_t = 5$ lpm and $P = 500$ mb.

Both $\alpha_{c,w}$ and $\alpha_{c,i}$ will determine the final particle size, but, based on initial exploratory tests not shown, the choice of $\alpha_{c,w}$ is most critical. If this parameter is too small (< 0.1), freezing in the simulations is inhibited totally or delayed to the point that there is no time for crystal growth at any set of operating conditions, inconsistent with observations in Chapter 4. If it is too large (≈ 1), the onset of freezing would be detected at the conditions predicted by *Koop et al.* [2000] for all operating conditions, which is also inconsistent with observations. This parameter has a similar effect on the final size of the crystal (as does $\alpha_{c,i}$)— if too small, nucleation will be suppressed to such a late point in the trajectory that there is no time for crystal growth and the nucleated particles will be present but noticeably smaller. The upper bound of the estimate of the ice crystal condensation coefficient is nebulous as crystal sizes at higher SS_w often exceeded the measurement range of the CFDC-1H OPC. Based on the laboratory portion of this study, reasonable choices for condensation coefficients are 0.7 for liquid water and 0.4 for ice. These values are used throughout the rest of the study.

Given that the thermodynamic properties along the trajectory are time (position) dependent, the SS_w given below to describe the dominant mode of the final ice distribution are based on the analytical solution to the steady-state problem [*Rogers, 1988*]; this value provides a more relevant reference as the conditions are those that would be recorded by the CFDC data system. As stated in the previous

section, with the exception of the low pressure-high flow rate data set (10 lpm, 500 mb), the temperature tends to be slightly warmer and the saturation slightly higher in the growth region aerosol lamina than predicted by the analytical solution. For each simulation, thermodynamic data were collected along 10 trajectories released from the inlet. Each trajectory was fed into the microphysical model, and 100 particles were released at the start of each trajectory resulting in an aggregate of 1000 trajectories for each simulation.

The final crystal size reported is the group mean, calculated as

$$\overline{D_c} = \frac{\sum n_i D_i}{\sum n_i} \quad 5.5$$

which is simply the sum of the diameters resulting from nucleation at a particular point (D_i) in time weighted by the number nucleated at that point (n_i) divided by the total number nucleating. In most cases, the number nucleating is a significant fraction of the total population and the group mean is therefore a reasonable representation of the final crystal size.

Before proceeding to the results of the simulations, it is important to outline some expectations based on an understanding of the growth equations. First, the rate of growth at a fixed temperature will be approximately proportional to the amount of water mass available in the gas phase. The amount of water vapor available is expressed through the excess described by the saturation ratio (with respect to ice or

water depending on whether the growth is for a crystal or drop respectively). For a fixed saturation ratio, the mass of water available for growth at a colder temperature will be less than that available at warmer temperatures (Figure 2.3). This can be more concisely stated as: for a fixed temperature and pressure, the water vapor mixing ratio is proportional to the saturation ratio. Eqs. 2.4 and 2.5 can be rearranged such that:

$$S_w e_{s,w} = \frac{w_v p}{\epsilon} \quad 5.6$$

From Figure 2.3, variations in S_w (or S_i) result in more dramatic changes in the available water vapor mass at warmer temperatures. Therefore, at warmer operating conditions, changes in SS_w should result in larger changes in the cloud particle diameter.

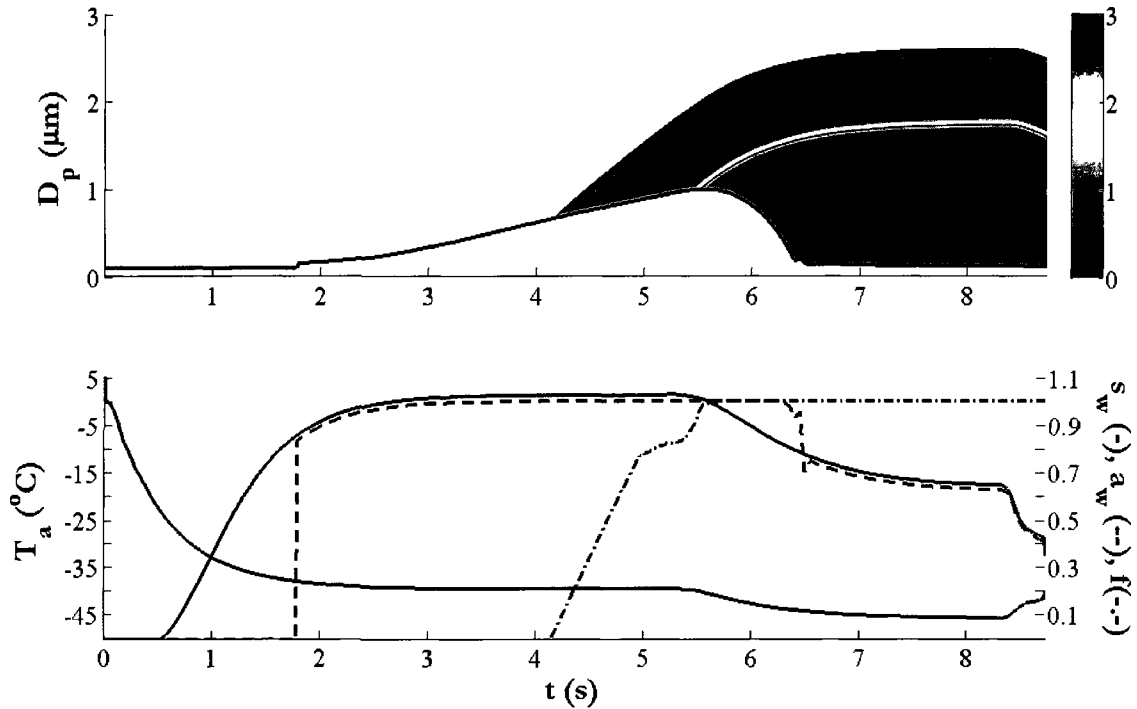


Figure 5.11. 100 nm particle trajectory released from the center node in the sample inlet for $SS_w = 1.64\%$ and $T_a \approx -40^{\circ}\text{C}$. Top panel shows the liquid drop and ice crystal growth while the bottom shows the temperature (left-hand ordinate) and the saturation ratio as well as the drop water activity and the fraction nucleating (right-hand ordinate).

5.3.1 Standard Operation

Figure 5.11 shows an example of a single trajectory for one set of conditions.

As in the bulk simulation, only 100 particles were released from the sample inlet.

The top plot shows both the haze drop growth (assuming no nucleation) with a color plot indicating the size (plotted on the ordinate) as well as the number nucleating (given by the color). The bottom plot shows the thermodynamic conditions as well as the drop water activity (a_w) and the fraction nucleating (f). The first thing to notice is the point of deliquescence; this is apparent by the point where the water activity

(dashed line in the lower panel) as well as the haze drop size (black curve in the upper panel) jumps in a discontinuous manner near 1.75 seconds. After deliquescence, both of these curves rise in a smooth, monotonic fashion as the droplet grows via diffusion. There is no freezing until shortly after 4 seconds. At this point, nucleation proceeds in an almost linear fashion as the probability of nucleation Eq. 2.33 is not sufficient at any time step to nucleate more than one particle during a single time step (generally less than 0.01 s). Around 4.8 seconds, nucleation slows almost to a halt as the number of available nuclei is depleted to the point where the probability of nucleation is not sufficient to allow nucleation to proceed in a single time step. Shortly after five seconds, the particle enters the evaporation region where the temperature and the saturation ratio begin to fall. However, the water activity remains near 1 after entering the evaporation region as the drop begins to evaporate; not until the drop approaches haze drop diameters does the water activity begin to fall toward the equilibrium values. Corresponding to the high water activity and the decrease in temperature is also a jump in the nucleation rate, thus driving the probability up sufficiently high allowing the remaining particles to nucleate immediately before the evaporation region.

Many of the features mentioned above are present in all of the simulations. In the case shown in Figure 5.11, the nucleation occurs over a relatively long period of time resulting in a wide distribution of ice crystal sizes, ranging from approximately

1.4 μm to 2.6 μm and a median value of approximately 2.2 μm along this trajectory. The high water activity homogeneous freezing threshold (0.989 for 100 nm particles) at the simulated temperature leads to this dispersion in the freezing curve; that is, although there is little difference between the equilibrium size and the kinetic size up to $a_w \approx 0.95$, there appears a divergence between the two values as the higher water activities begin to require more time to come to equilibrium.

The results for simulations at standard, laboratory operating conditions ($P = 850$ mb and $Q_t = 10$ lpm) are shown in Figure 5.12. The contour plots are produced by triangle-based linear interpolation to create a denser, smoother grid than that given by the conditions simulated (Chapter 3.2.1.3). The data for creating the plots are given in the appendix. It's important to note in these plots that white space indicates that there is no observation of freezing before the first simulated SS_w .

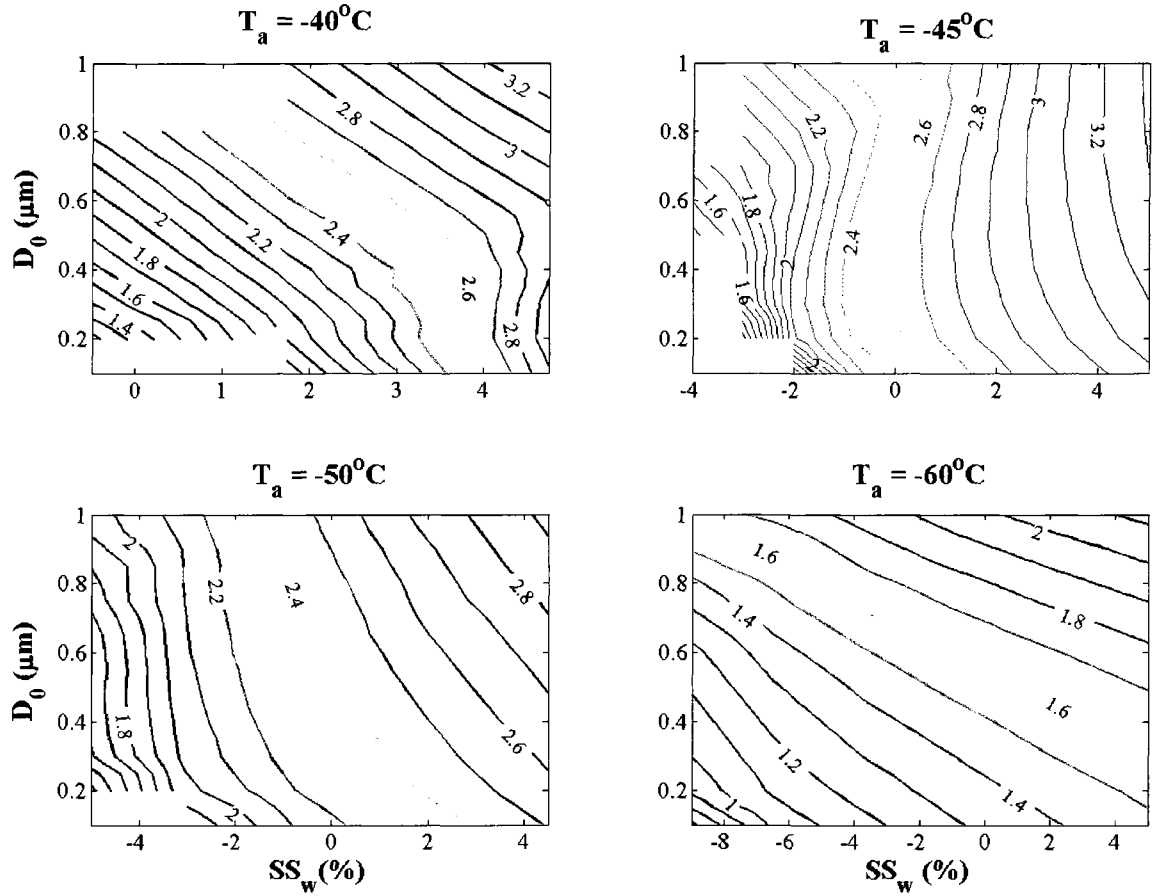


Figure 5.12. Final predicted crystal sizes (in microns) based on simulations as described above for $Q_t = 10$ lpm and $P = 850$ mb.

At -40°C , the first observation for $d_0 = 100$ nm comes in the simulation corresponding to $SS_w = 1.64SS\%$; this does not mean that freezing would not occur before this, but rather, there was no indication of freezing at the simulated conditions prior to this simulated SS_w ($SS_w = 0.52SS\%$ in this case). The impact of the high a_w threshold at -40°C can be seen in Figure 5.12. This figure indicates that this high threshold leads to 1) the dependence of the final crystal size on the initial diameter of the dry particle and 2) the apparent inhibition of freezing for the largest particles.

Based on Figure 5.12, the rate at which haze drops dilute plays an important role in the final mean crystal size as a function of the lamina SS_w and the initial dry diameter. The inability to observe nucleation until some point beyond water saturation for 100 nm particles may be due to the coarseness of the simulated saturations in the -40°C simulations. However, particles at the high end of the dry size spectrum should show evidence of freezing well before water saturation if the particles are in equilibrium with the environmental conditions. The lack of a signal below $SS_w = 1.5SS\%$ indicates that the larger particles are not diluting rapidly enough for nucleation to become significant. At higher SS_w , the final crystal sizes of the smaller particles exceed those near 500 nm. This suggests that the 200 nm particles are diluting more rapidly once onset conditions are reached and spending more time in an ice saturated environment than those at larger sizes.

At -45°C , the role of haze drop growth becomes more apparent. Once the SS_w has exceeded that required to freeze haze drops of all dry sizes, there is little difference in size between those particles with the smallest and largest initial dry diameters. At the coldest temperatures, the availability of water vapor mass becomes a more important issue. In these cases, the crystal growth rate varies little with SS_w and the maximum change in the final mean crystal size is approximately $1\ \mu\text{m}$ at -50°C and $< 1\ \mu\text{m}$ at -60°C across the entire modeled SS_w spectrum for a single dry diameter. Growth at these temperatures is dominated strictly by the initial dry

diameter. In this simulation, crystal diameters change by a maximum of 600 nm over a change of almost 15% in $SS_w SS$. Further, simulations indicate that at -60°C the observation of freezing (based on the $2\ \mu\text{m}$ OPC threshold) is possible only for very large SS_w and only for large initial dry diameters using a $2\ \mu\text{m}$ cutpoint for observation.

Given the short residence times in the growth region for the 10 lpm total flow at 850 mb case, experimental results will be particularly sensitive to residence time perturbations. Changes in the length of the ice surface or the total flow rate can have a significant impact on the observed onset of nucleation. With this in mind, the experimental results from the previous chapter at these operating conditions are remarkably consistent with the simulation results. As stated in the previous chapter, the observation is only mildly dependent on the MCA channel used to discern ice crystals; this finding is in line with the simulations discussed above (i.e. in the simulations, there is no evidence of small crystal growth at lower $SS_w SS$). Deviations between the modeled and observed freezing onsets are small and well within the limits of the measurement uncertainty in the SS_w (ranging from approximately 3% at -40°C to almost 4% at -50°C).

5.3.2 The Effect of Water Vapor Diffusion: Operation at Low Pressure

The following simulations were run at 500 mb. In some cases, this pressure is reached naturally through the operational platform (i.e. aircraft); 500 mb may be

representative of the atmospheric pressure encountered above 6 km. In other cases, pressure may be lowered mechanically via the use of an orifice or some other type of device which generates a pressure drop as it was in the experiments described in the previous section.

However the operational pressure is maintained, it is not entirely possible to decouple the effect on the final ice crystal sizes of increased diffusivity from that of increased residence time. In Eq. 3.1, the second term on the right hand side represents the buoyant force associated with the density gradient generated by the temperature difference between the warm and cold wall. This buoyant term tends to skew the peak in the velocity profile toward the cold wall, generating higher velocities than those estimated assuming a parabolic profile. Decreases in the pressure result in decreases in air density across the gap. This in turn tends to flatten the velocity profile and results in lower peak velocities, thereby increasing residence times in the growth region. At 10 lpm and 850 mb, the residence time of a particle in the chamber is approximately 8 s. In contrast, the residence time of a particle at that same flow rate but 500 mb is approximately 10 s, with most of that additional time spent in the growth region.

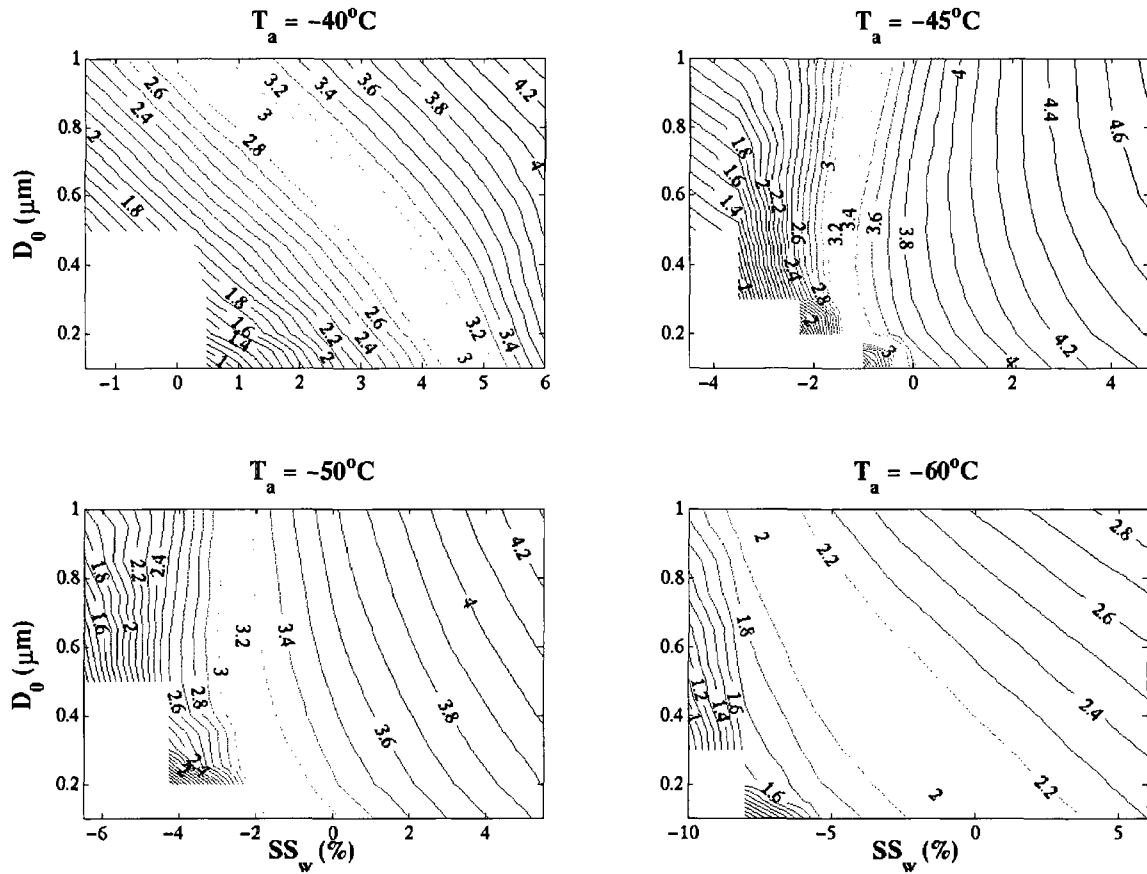


Figure 5.13. Final predicted crystal sizes (in microns) based on simulations as described above for $Q_t = 10$ lpm and $P = 850$ mb.

As in Figure 5.12, Figure 5.13 shows contours of the final crystal diameter as a function of the initial dry particle size and the steady-state SS_w for the four temperatures investigated. The data used to generate these contour plots may be found in the appendices. By reducing the pressure, simulated crystals appear to grow to a detectable size ($> 2\mu\text{m}$) for a wider range of conditions than at 850 mb. Also, at this pressure the final crystal size trends more strongly with SS_w than at 850 mb.

Figure 4.6 suggests major deviations between the laboratory-based observation of the onset of freezing and the simulated results (in the laboratory experiments, water saturation was required for observation of freezing for the entire range of sampled dry sizes and temperatures); however, as discussed in the previous chapter, freezing was observed at a lower sizing threshold than is captured by Figure 4.6 in most of the experiments (though not all). Although crystals did not immediately grow to sizes suggested by the simulations at 500 mb, the onset conditions at which ice crystal growth was observed at lower sizes in the experiments is more in line with the onset conditions captured by the simulations.

5.3.3 Increasing Particle Residence Time

Figure 5.14 shows the results from simulations in which $Q_t = 5$ lpm and $P = 500$ mb. The data used in constructing these plots are given in the appendix. From Figure 5.13 the predicted onset of nucleation is immediately observable. The results continue the trend discussed in the previous sections. At -40°C , there is now sufficient time in the growth region such that the smallest particles have time to dilute and nucleate early in the trajectory, growing to larger sizes than those with larger initial dry diameters. Growth as a function of the saturation is still small at the

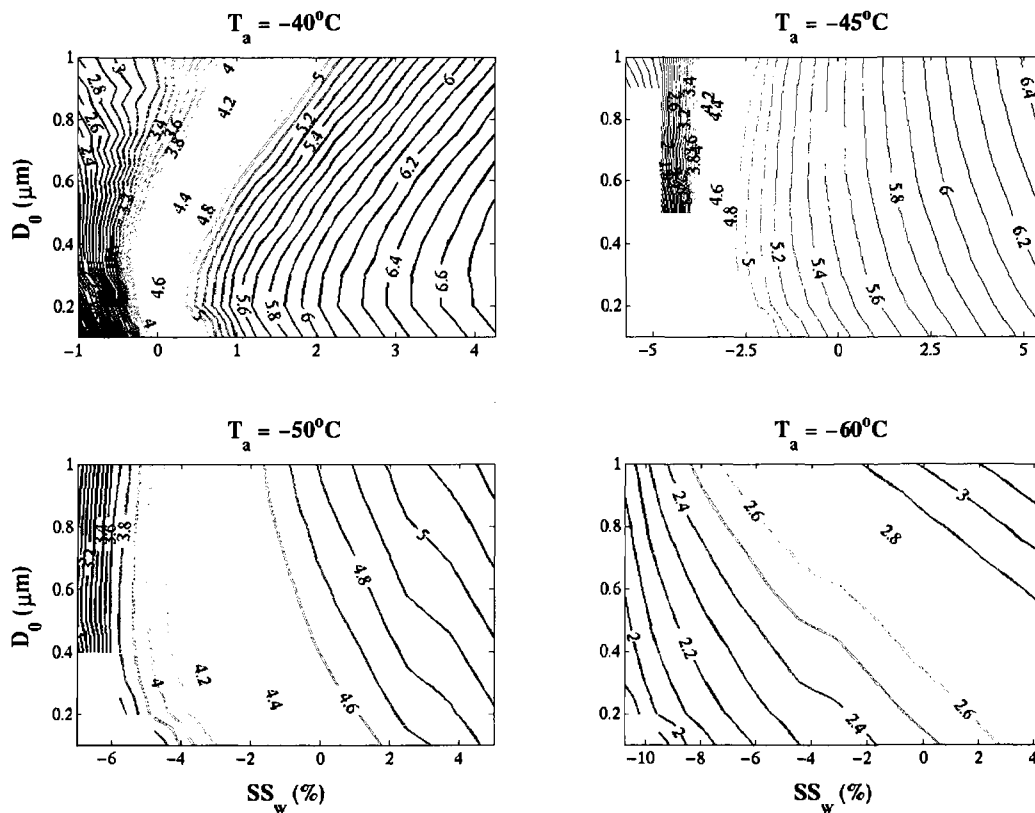


Figure 5.14. Final predicted crystal sizes (in microns) based on simulations as described above for $Q_t = 5$ lpm and $P = 500$ mb.

lower temperatures.

While laboratory observations at these conditions are more in line with these results, Figure 4.6 suggests that at low temperatures the larger particles (300 nm) are still having trouble diluting. This results in a noticeable deviation from the predicted onset at -50°C for the 300 nm particles in Figure 4.6. This feature does not seem to be accurately captured in these simulations.

5.4 Examination of Instrumental Non-idealities

Depending on the condition of the refrigeration system which cools the walls of the CFDC or the assumptions of the rate of heat transfer along the walls, there are a variety of thermal profiles that can be either hypothesized or have been directly observed in experiments. Temperature gradients along the walls have been observed in several different measurement settings. During INSPECT-II [Richardson *et al.*, 2007], depending on the operational conditions, the inner wall gradient was as high as 5 K along the length of the wall. These temperature gradients are typically due to incomplete charging of the refrigeration system. Oscillatory behavior of the wall temperatures along the length of the chamber might be expected if heating occurs between the refrigeration coils.

In any case, perturbations to the temperature profile have the potential to produce behavior that is difficult to predict by altering the values of the pertinent

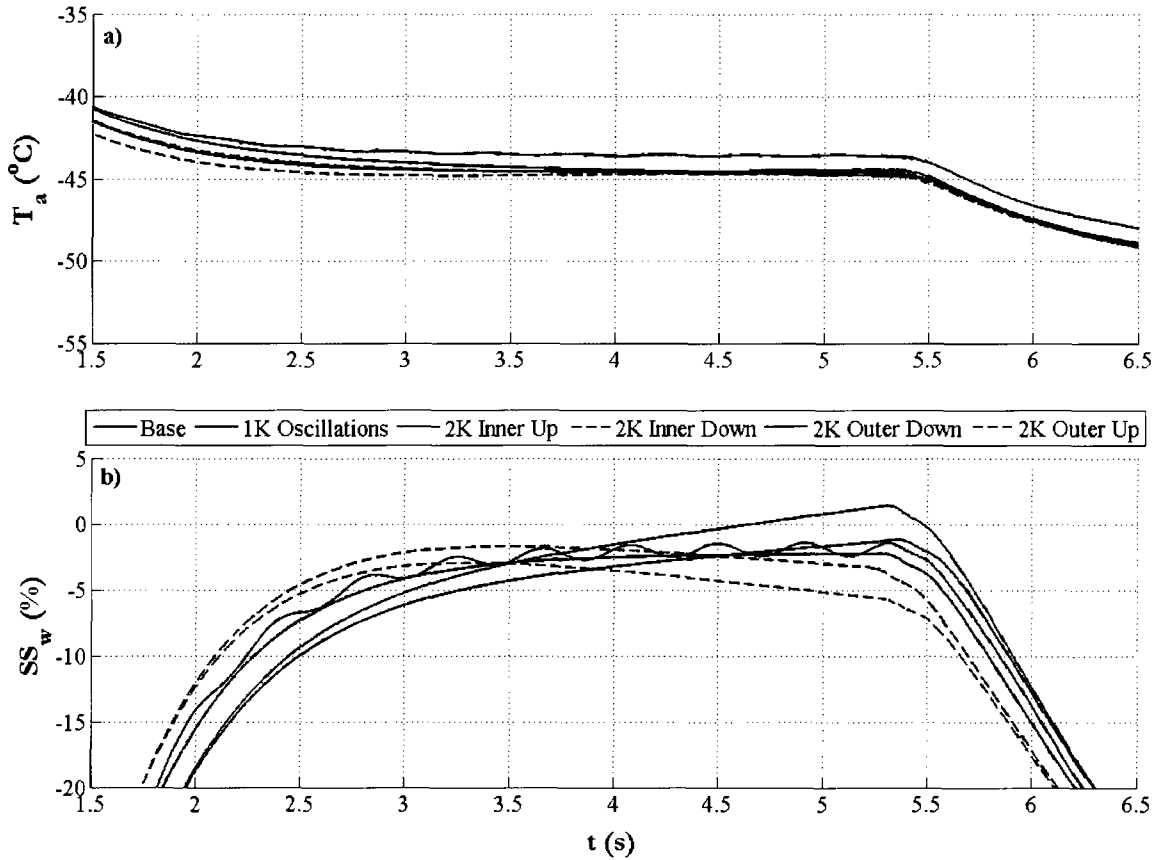


Figure 5.15. a) Temperature and b) supersaturation with respect to water for target conditions of $T_a = -45^{\circ}\text{C}$ and $SS_w = 3.15\%$ ($Q_t = 10$ lpm and $P = 850$ mb) and for the ideal simulation (i.e. no wall temperature perturbations) and the five perturbation cases simulated. In each case, the trajectory is that of the particle released from the 5th (center) node of the modeled sample inlet.

thermodynamic variables within the lamina. These perturbations to the lamina values are typically not as simple as changing the values within the steady-state region. Rather, they have the potential to alter the point at which the steady values (as in the ideal case) are reached as well as the total length of time the aerosol resides within the growth region of the chamber.

Perturbations modeled here were applied to the operating conditions of 10 lpm and 850 mb. Figure 5.15 shows the complex behavior of the thermodynamic variables in the aerosol lamina attributable to the different temperature perturbations. These plots show the temperature and supersaturation with respect to water along the path of a particle released from the center-most node (5th) of the sample inlet in the model domain. Gradients of opposite sign will have similar effects on the two walls. The behavior of the oscillatory profile is unique to the position of the oscillations on both walls (as is the case here). The thermodynamic profiles at other temperatures are similar to those shown in Figure 5.15. However, the ability of a trajectory to reach the target conditions in the growth region will determine the influence of the perturbation on the target conditions (i.e. at -60°C the 2 K inner down and outer up perturbations will show more pronounced tilts in their respective SS_w profiles).

Both the upward pointing outer wall gradient and the downward pointing inner wall gradient have the effect of enhancing SS_w relative to the base case at the upstream point of the growth region. Because the gradient on the outer wall is confined to a shorter region by the collar and evaporation region, the enhancement in SS_w will be confined primarily to the portion of the growth region in which the SS_w is still developing, thus limiting the impact of this perturbation. Peak SS_w will be smaller than those associated with the opposite gradient on the inner wall and dissipate more rapidly. In the case of the downward pointing outer wall gradient,

peak saturations will be considerably higher than the ideal case as the highest temperatures are realized in the downstream portion of the growth region, a region in which the temperature and SS_w profiles are already well developed in the ideal case. In this case, SS_w is greater than the ideal case in the second half of the growth region. The upward pointing inner wall gradient has a similar, but more muted response. Because the perturbation is spread along the inner wall, the ideal steady-state SS_w will be reached toward the end of the growth region and peak at significantly lower values.

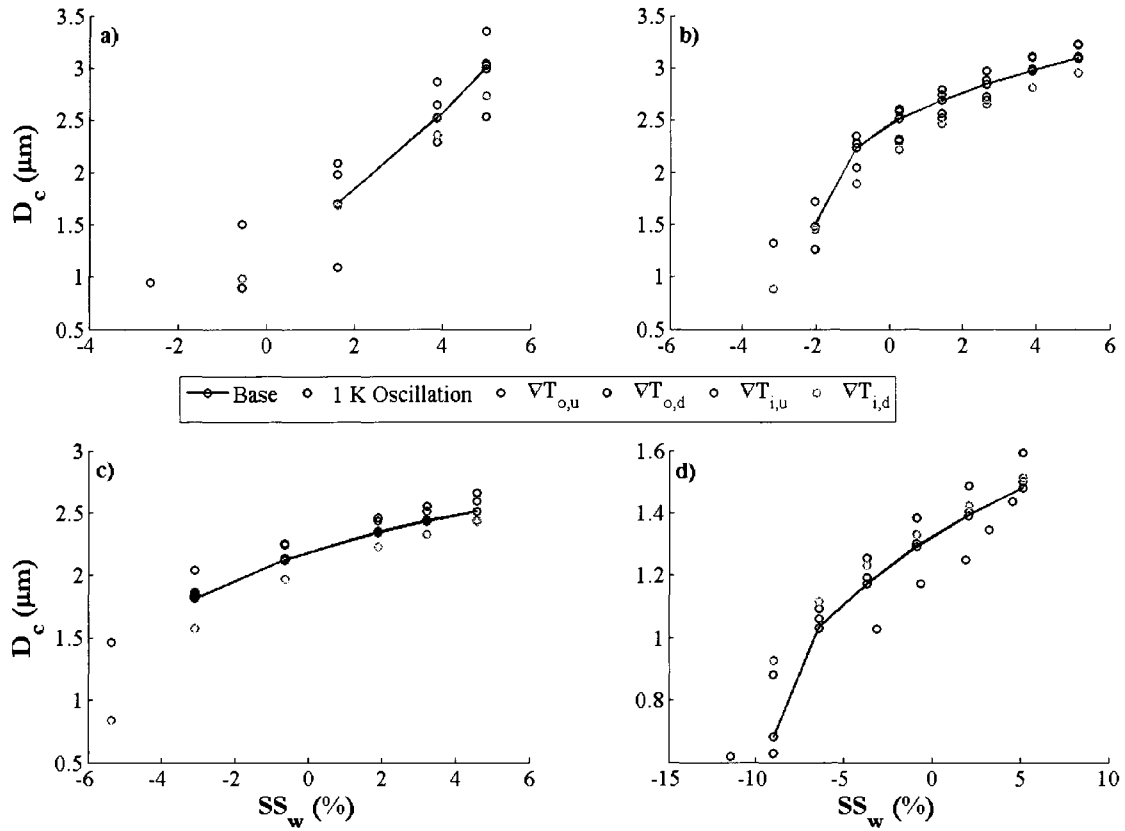


Figure 5.16. Final crystal size for an initial dry diameter of 100 nm given wall temperature perturbations at a) -40°C , b) -45°C , c) -50°C , and d) -60°C . ∇T refers to the 2 K wall gradient for which subscript o refers to the outer wall while i refers to the inner wall and subscript d refers to a downward pointing gradient (temperatures increase down along the wall) and u refers to an upward pointing gradient.

For most of these cases, the temperature in the lamina for the different perturbations is not significantly different from the base case (although complete relaxation to the ideal steady-state value depends on the perturbation). The exception is the oscillatory case where the perturbations align such that both the SS_w and the temperature are elevated throughout the growth region, creating a periodic

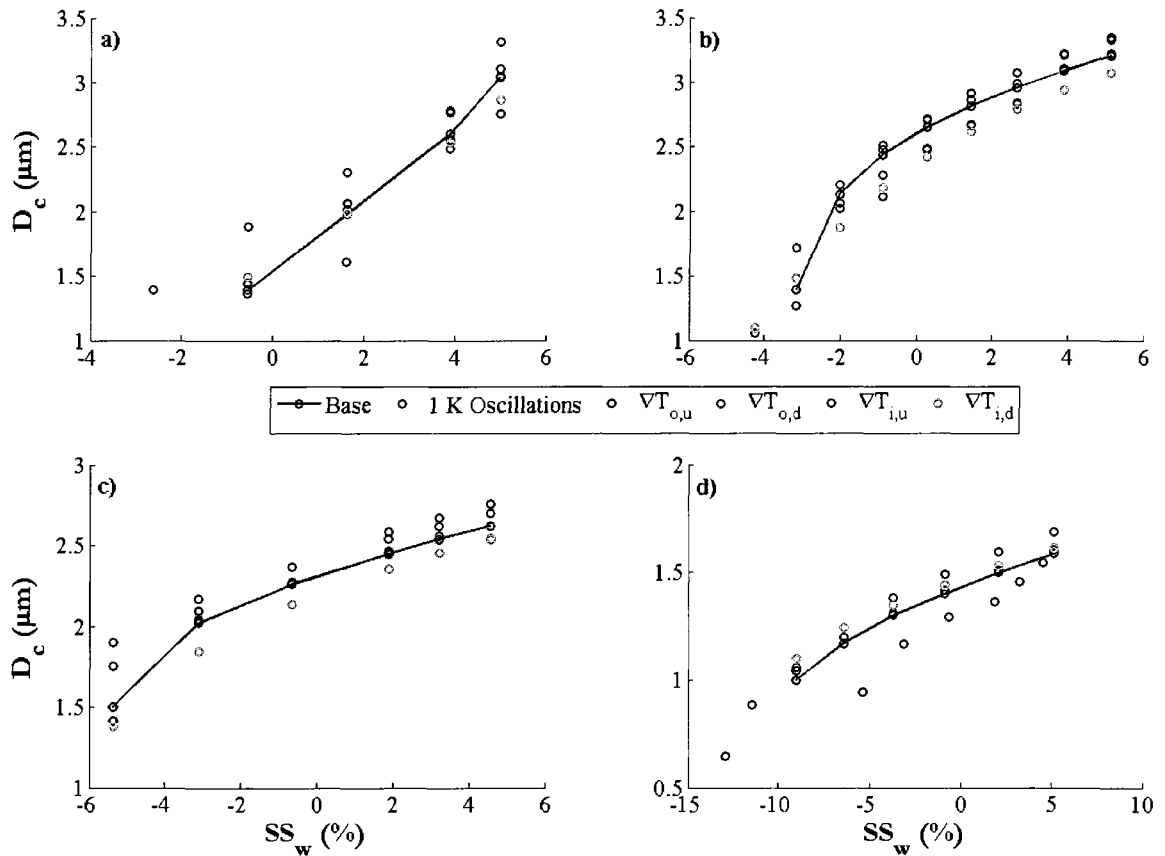


Figure 5.17. Same as in Figure 5.16 but for an initial dry diameter of 300 nm.

oscillation in the lamina SS_w and a small but still visible oscillation in the lamina temperature.

Comparison of the impact of the different perturbations on the final crystal size is shown in Figure 5.16 for an initial dry diameter of 100 nm and Figure 5.17 for 300 nm. The response of the cloud particles in the simulations is, based on the foregoing analysis of the thermodynamic profiles, as expected. The impact of the upward pointing gradient on the outer wall is generally to inhibit the onset of freezing within the chamber, either such that freezing occurs but crystal growth is

impaired or that freezing itself is suppressed. Aside from the 100 nm case at -40°C , the oscillations have little impact on the development of crystal formation in these simulations, a statement that holds true for the rest of the initial dry diameter conditions (not shown). Similarly, the inner upper gradient ($\nabla T_{i,u}$) seems to have only a limited impact on the final size (slightly larger than that given in the base case) and no real impact on the initial SS_w at which freezing is observed, except in the -45°C case (Figure 5.16(b) and Figure 5.17(b)) where the observed onset of freezing is delayed. The most dramatic change in the freezing characteristics is attributable to the downward pointing gradient on the outer wall ($\nabla T_{o,d}$). While the crystal size in the perturbed simulation and that for the base case are not significantly different where nucleation has occurred, this perturbation tends to result in particles freezing earlier than in the base case.

Given the conditions under which these wall perturbation simulations were run, the resulting differences in the onset of freezing and final crystal size are relatively minor. The response of the aerosol to these perturbations is complex and weakly size and temperature dependent, so it is difficult to extrapolate these results to a different set of operating conditions. However, it is likely that perturbations that result in higher saturations than the ideal case will consistently produce onset SS_w lower than that predicted by *Koop et al.* [2000] for the ideal case. At operating conditions producing longer residence times (lower pressure and/or smaller flow

rates), aerosol will reside longer in these regions of elevated $SS_w SS$ resulting in significantly higher nucleation rates and thus higher probabilities of nucleation (Eq. 2.33).

5.5 Summary of Results from the Computational Study

This portion of the study attempted to build on the results from the previous chapter using numerical modeling and provide insight into how the fluid dynamics and energy and mass transport drive cloud particle growth in the CFDC-1H. Using a CFD model accounting for conduction through portions of the chamber in indirect contact with the ambient (cabin) environment, several interesting features were uncovered. First, a moist bubble near the collar forms in all simulations. The bubble is generated by the interaction between the cooling, hydrophilic collar and the warm, moist air at the trailing edge of the growth region. At the core of the bubble, $SS_w SS$ can reach as high as 80 to 90%, according to simulations. Displacements of the lamina from the predicted position might significantly perturb cloud particle development in this region.

Several dynamic features appear in the simulations that have the potential to disturb the lamina. In the region where the sheath flows converge with the sample flow, a region of free shear, boundary layer separation seems to occur near the outer edge of the inner inlet blade generating a region of mild recirculation. This separation appears to be heavily influenced by temperature gradients and can be

ameliorated by reducing pressure or increasing the inner wall temperature in this region. Additionally, a vortex develops within the outlet region. The vortex is driven by a warm inner wall on the outer outlet cone (warmed via conduction) interacting with the cool air entering from the evaporation region. Results from experiments thus far do not indicate any dispersion of the lamina associated with the first feature. Given the location of the vortex, it is likely that it will have no significant impact on the final cloud particle size and at most may result in particle loss if particles do come into contact with this vortex (an interaction that the simulations do not bear out).

The trajectories in the steady-state region compare favorably with the analytic solution given in *Rogers* [1988]. Although not discussed, the lamina position predicted from the analytic equations roughly coincides with the lamina in the simulation. Small deviations in the thermodynamic variables are attributable to a convective component not captured by the analytic solution. In any case, the deviations are well within the experimental uncertainty of the technique. Simulations indicate multiple benefits from decreases in the flow rate and pressure. Not only does the trajectory reside longer in the portion of the chamber preceding the evaporation region (generally, 60% of the particle residence time in the chamber is spent in this region, regardless of the operating conditions), but the saturation and temperature profiles initially relax more rapidly to the steady-state SS_w and T_a in the growth region.

Finally, CFD simulations coupled with a microphysical model indicate that dilution of haze drops (a non-equilibrium effect) is a major factor in the ability of the CFDC-1H to observe freezing at warmer cirrus regime temperatures. At temperatures below -50°C , the availability of water vapor begins to limit cloud particle growth. At higher temperatures, changes in SS_w can have an impact on the final crystal size while at lower temperatures the final size is dominated by residence time in the growth region rather than the $SS_w SS$. At low temperatures, there is little change in the final crystal size with $SS_w SS$ once the particle has frozen. All-in-all, the simulations agreed reasonably well with the experimental data collected in the previous chapter. Additional simulations with the microphysical model demonstrated that, for most cases, perturbations to the wall temperature profiles have a limited effect on the ability of the CFDC-1H to observe freezing. One gradient in particular (a downward pointing gradient along the outer wall), however, has the potential to alter the thermodynamic profile such that the observation of freezing is well before that predicted using the parameterization of *Koop et al.* [2000]. Thus far, the simulations and the laboratory data from the previous chapter suggest that the CFDC-1H should be a reasonable tool for measuring freezing to temperatures as low as -50°C .

6 MEASUREMENT OF THE FREEZING BEHAVIOR OF AN AMBIENT AEROSOL

Although *Koop et al.* [2000] provide a parameterization of homogeneous freezing that describes the freezing onset conditions for a wide array of aqueous solutions, it is clear that atmospheric particles can be considerably more complex than the compounds examined in that study. Due to a variety of production mechanisms, atmospheric particulate matter may be both internally and externally mixed [*Finlayson-Pitts and Pitts*, 1999]. This variability in the chemical composition impacts the water uptake behavior of the ambient aerosol and therefore the freezing activity of the particles. The impact of this variability on the freezing properties of a real aerosol has never been directly measured. However, using the observed water uptake properties of ambient particles at a variety of locations, it is possible to hypothesize the effect of chemical composition on the freezing onset conditions. Figure 6.1 shows the predicted onset SS_w at three temperatures as a function of size and hygroscopicity as indicated by κ (Eq. 3.30). Based on a review of ambient aerosol hygroscopicity, *Andreae and Rosenfeld* [2008] suggest that the behavior of remote

continental aerosol may be broadly represented by $\kappa=0.3\pm0.1$ and that of marine aerosol may be represented by $\kappa = 0.7 \pm 0.2$. Figure 6.1 suggests that the difference in hygroscopicity represented by this range of κ results in only small differences in the freezing onset SS_w as a function of size and temperature, except for particles with $d_0 < 100$ nm. For particles larger than 100 nm, Figure 6.1 suggests that the difference in the onset SS_w is well within the uncertainty of the CFDC-1H measurements.

The objective of the following portion of this study was to examine the freezing onset conditions of a size-selected, ambient aerosol and compare the results to both the predicted values and those freezing onset conditions measured for ammonium sulfate. The measurements of the freezing onset conditions of a monodisperse subsample of the ambient aerosol can be directly compared to those of monodisperse ammonium sulfate previously measured (Chapter 4) to determine if

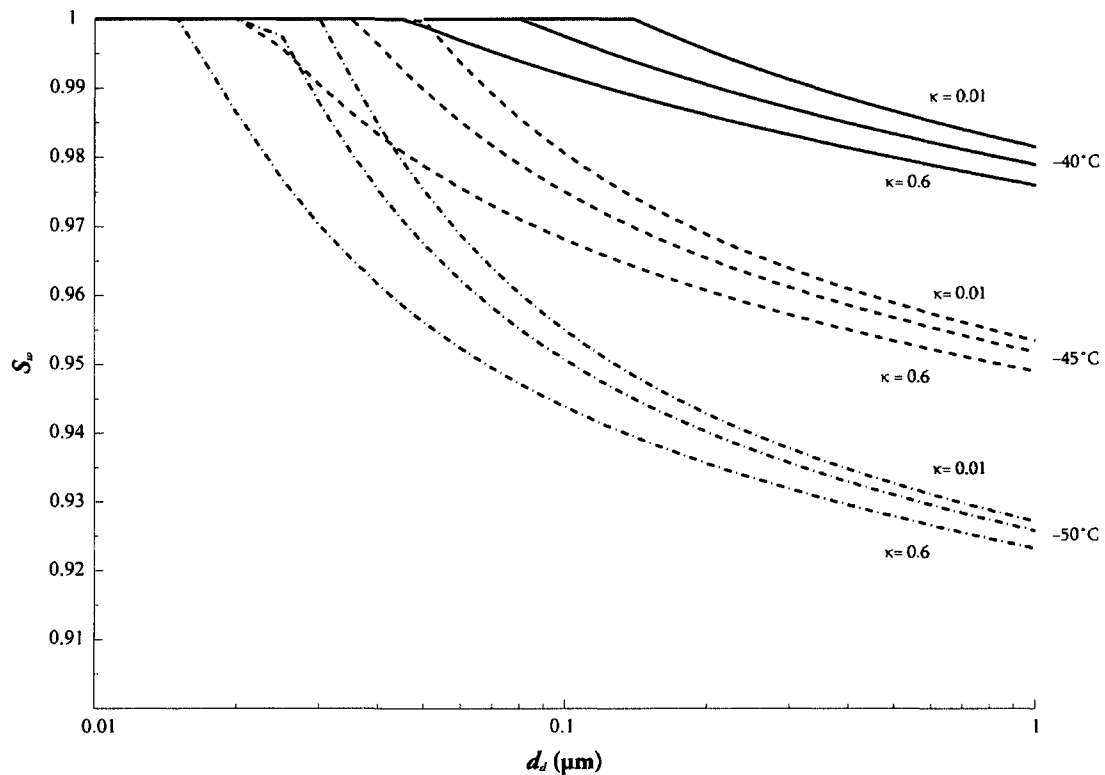


Figure 6.1. Curves indicate the freezing onset S_w as a function of size and κ (0.6, 0.1, and 0.01) for three different temperatures (calculated for the equilibrium diameter at the given T , S_w pair, $f_{HF} = 0.001$ and $\Delta t = 3$ s). Ammonium sulfate is assumed to have a $\kappa \approx 0.6$ [Petters and Kreidenweis, 2007], a value similar to that proposed for modeling marine aerosol ($\kappa = 0.7 \pm 0.2$) by Andreae and Rosenfeld [2008] based on a review of CCN activation studies. In the same review, Andreae and Rosenfeld have also proposed $\kappa = 0.3 \pm 0.1$ for modeling continental aerosol.

there was an observable difference. However, based on the parameterization of *Koop et al.* [2000], it is expected that any difference between the freezing onset SS_w of the ambient particles will not be significantly different from that of the ammonium sulfate for a given temperature. The hygroscopicity and mixing state of the aerosol were monitored using two different measurements of the water uptake behavior of the ambient aerosol: an HTDMA and a CCNc. The HTDMA provides size dependent measures of the hygroscopicity of particles in the subsaturated ($S_w > 1.5$) regime while the CCNc provides a measure of the bulk hygroscopicity in the supersaturated regime ($S_w > 1$) for the aerosol with $d_0 < 390 < 390$ nm.

The chemical composition of collected ice crystal residuals was examined using TEM/EDS. This provides further insight into the chemical nature of the particles serving as homogeneous freezing nuclei and can be compared with water uptake measurements to determine the relationship between the chemical nature of the ambient aerosol expressed through the hygroscopicity and that inferred from the elemental composition provided by TEM analysis.

In this portion of the study, the freezing properties of the ambient aerosol were measured on selected days over a two week period. During this period, construction was actively ongoing approximately 100 m south of the sample inlet.

6.1 Measurements from 30 June 2008

The first set of measurements took place on 30 June 2008. During the period coinciding with all measurements (11:00 to 16:30; all times are in Mountain Standard Time), the conditions were warm (i.e., mean ambient temperature approximately 304 K) and dry ($RH_w \approx 15.5\%$) with light winds (2.4 m/s) from the southeast (meteorological data from this measurement period are taken from the Christman Field Weather Station and archived at http://www.atmos.colostate.edu/wx/fcc/fccwx_current.php). The HTDMA operated from 11:00 to 14:00 while CFDC-1H data were collected from approximately 13:00 to 16:00 (Figure 6.2(a); HTDMA sampling period is denoted by a light grey box while the CFDC sampling periods are denoted by dark grey boxes). The HTDMA scanned S_w at two different dry, mobility diameters (100 nm and 300 nm). At both sizes, the wet size distribution (that measured by the second DMA in Figure 3.10) was monomodal. Growth factor (gf) measurements indicate continuous water uptake for $S_w \geq 0.2$ with no significant difference in the measured gf between the two initial dry sizes (all HTDMA data are available in the appendix). Measured κ 's using the HTDMA were near 0.1 for both sizes (0.13 ± 0.02 and 0.1 ± 0.01 for 100 nm and 300 nm particles respectively) and are in reasonable agreement with the CCN derived κ (with a median value of 0.157 and 25th and 75th percentiles of 0.154 and 0.166 respectively; statistics are calculated based on the points given in Figure 6.2(a) and exclude the

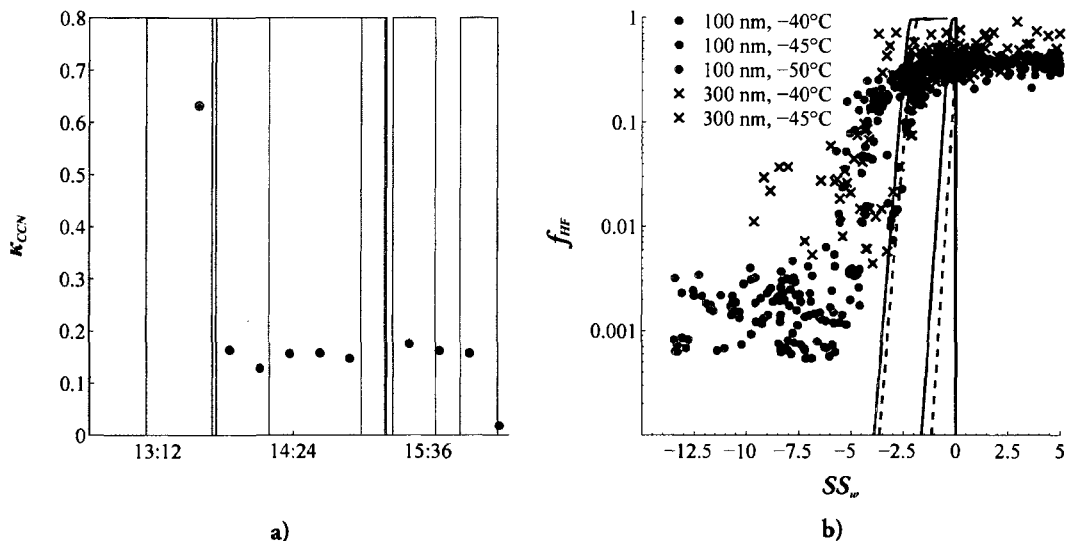


Figure 6.2. Data collected from 30 June 2008 experiments. a) CCN derived κ as a function of time. Shaded areas indicate where HTDMA (light grey) and CFDC-1H (dark grey) measurements were made. The HTDMA derived κ values were 0.13 ± 0.02 for 100 nm particles and 0.1 ± 0.01 for 300 nm particles. The red filled circle with $\kappa \approx 0.6$ indicates an ammonium sulfate calibration point. b) Freezing activation curves for size-selected, ambient aerosol. Predicted freezing curves based on the *Koop et al.*[2000] parameterization are shown as solid lines (100 nm particles) and dashed lines (300 nm particles). Calculations were made for $\kappa \approx 0.15$ and $\Delta t = 3$ s.

calibration period indicated by $\kappa \approx 0.6$). CCN data for the measurement periods discussed in this section are available in the appendix.

Figure 6.2(b) shows the fraction freezing (f_{HF}) as a function of SS_w . Note that the maximum fraction of the incoming aerosol freezing is approximately 0.4 to 0.5, consistent with observations on other days during this study as well as observations of fractions freezing during the ammonium sulfate experiments described in Chapter 4 (curves not shown). Recalibration of the total flow controller at the start of this experimental period shows a bias in the total flow measurement of approximately +0.17 slpm (no similar bias was detected for the sheath flow controller). For all

experiments hereafter, the total flow rate was adjusted upward by 0.17 slpm to achieve the desired total flow rate (5 lpm at the chamber conditions). This adjustment results in an overestimation of the total sample volume and an underestimation of the measured concentration that is not accounted for in these plots, which in turn results in an upward adjustment of the fraction nucleating by approximately 0.2 to 0.3 and has no impact on the conclusions of this study. The remaining fraction not accounted for may be the result of depositional losses in the chamber and sampling lines.

As with the ammonium sulfate experiments (see Figure 4.1 for example), Figure 6.2(b) shows a rapid activation from the baseline concentrations at low SS_w to “full activation” at higher SS_w ($\Delta SS_w \approx 1\%$). Freezing onset conditions (as calculated in Chapter 4 and given in Table 6.2 at the end of the chapter) are consistent with the onset conditions for size-selected ammonium sulfate and indicate a bias in the calculated SS_w of approximately 1.5% to 2.5% from that predicted by the *Koop et al.* [2000] parameterization across the lamina temperature range in these experiments.

6.2 Measurements from 1 July 2008

As on the previous day, conditions on 1 July were warm (mean temperature of 300 K during the sampling period shown in Figure 6.3(a)) and relatively dry ($RH_w \approx 25\%$) with light winds (≈ 2.7 m/s) out of the southeast. However, while 30 June was mostly sunny, 1 July was marked by broken cloud cover with measureable precipitation near 12:00.

Measurements of the CCN-derived hygroscopicity and freezing activity are shown in Figure 6.3. No HTDMA data are available for this day. The median κ for the CCN measurements during this period is 0.163 with 0.08 and 0.166 for the 25th and 75th percentiles. The low 25th percentile value is attributable to the single outlier near the beginning of the period ($\kappa \rightarrow 0$). The $\kappa = 0$ measurement is consistent with

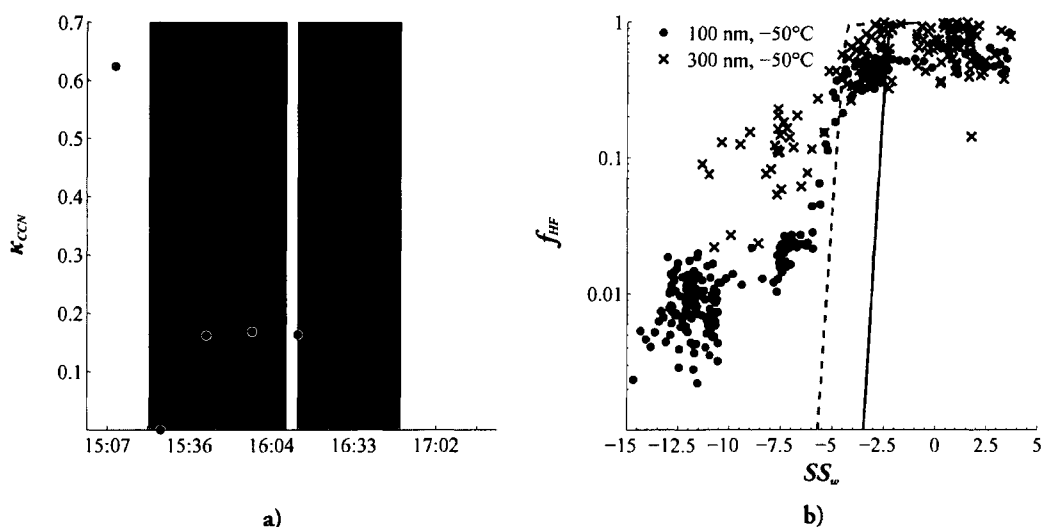


Figure 6.3. Same as Figure 6.2 but for data collected on 1 July 2008. No HTDMA data are available for this day.

measurements of CCN activity for the 4 hours prior to the CFDC measurements (not shown). The CCN activation curves associated with these low κ values show a considerable amount of dispersion (high β ; Equation 3.35) and exhibit no dominant activation mode. This behavior inhibits our ability to obtain meaningful insights into the aerosol hygroscopicity. However, for the bulk of the experiment coinciding with CFDC-1H measurements, the calculated CCN-derived κ is in line with values of κ calculated on the previous day.

Concentrations of particles larger than $2\ \mu\text{m}$ measured at -50°C and low SS_w by the CFDC-1H (Figure 6.3(b)) are slightly elevated over the previous day. On this day, these concentrations were between 0.2 and $0.3\ \text{scm}^{-3}$ while during other measurement periods they were $< 0.1\ \text{scm}^{-3}$ at $SS_w < -6\%$. The elevated baseline concentrations and complexity of the CCN activation curves throughout the day suggest the influence of insoluble material which may result in higher concentrations of heterogeneous ice nuclei. However, the lack of periodic filter measurements to assess background (measurements for which the sample flow is diverted through a filter) prevents us from drawing any definite conclusions regarding the presence of heterogeneous IN. The freezing onset SS_w of freezing is consistent with the ammonium sulfate experiments and with measurements conducted the previous day.

6.3 Measurements from 3 July 2008

On 2 July 2008, light precipitation was measured at Christman Field associated with the passage of a cold front, based on archived surface data available from <http://weather.unysis.com>. The passage of the front resulted in mean temperatures on 3 July 2008 cooler than the previous two days (294 K) and elevated relative humidities ($RH_w \approx 56\%$). Winds were light (2.7 m/s) and out of the east. The HTDMA measured hygroscopicities in the latter portion of the day (Figure 6.4(a)), but κ 's are available only to $S_w \approx 0.8$.

This day represents the only day for which the growth factors measured by the

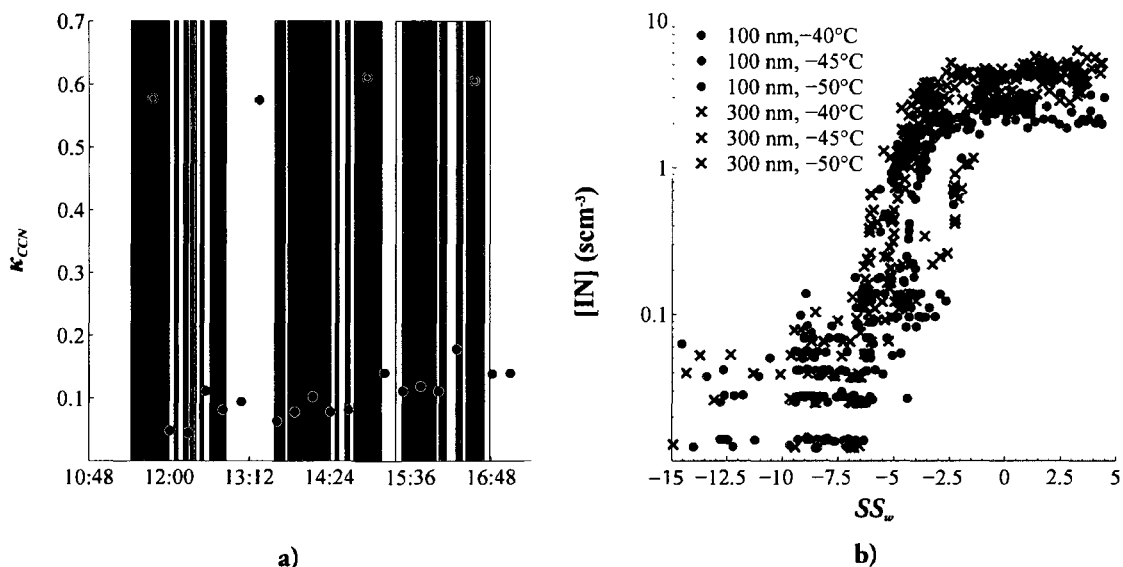


Figure 6.4. Same as Figure 6.2 but for data collected on 3 July 2008. No valid [CN] data were collected that day, so only standard freezing nuclei ([IN]) concentrations are given. The HTDMA derived κ values are 0.16 and 0.26 for 100 nm and 300 nm particles respectively. No confidence intervals are given for the HTDMA measurements as there was only a single measurement at $S_w \geq 0.8$ for each diameter.

HTDMA varied significantly between the two sizes. At $S_w \approx 0.82S$, the gf 's are 1.18 and 1.28 for 100 nm and 250 nm particles respectively. The corresponding κ 's for these two values are 0.16 (100 nm) and 0.26 (250 nm). As with the measurements on 30 June 2008, particles exhibit continuous water uptake for $S_w \geq 0.2$. The CCNc derived κ 's display a slight temporal trend with κ increasing throughout the day. κ 's derived from CCN data were initially below 0.1 and increased to approximately 0.15 by the end of the day. Despite the initial low κ values, the CCN activation curves for this day all transition smoothly from 0 fraction activated to 1 with the heterogeneity parameter β only slightly greater (approximately 0.3 for these measurements) than the ammonium sulfate calibration values (approximately 0.1 throughout the entire study) indicating that the aerosol is not homogeneous but there is no dominant mode in the CCN activity. Unfortunately, the CCN method does not produce κ as a function of diameter and therefore is not able to corroborate the disparate measures of κ obtained using the HTDMA.

Figure 6.4(b) shows the freezing activation curves – limited [CN] data are available for this day so the freezing curves are shown in terms of absolute measured concentrations. As with the ammonium sulfate experiments, the change in SS_w from the baseline concentrations to full activation was small ($\sim 1\%$). However, similar to 1 July 2008, the -40°C and -45°C data show some evidence of elevated concentrations of

particles with diameters larger than 2 μm prior to the onset of apparent homogeneous freezing.

This day (3 July 2008) represents the first of two days on which TEM grids were collected for analysis of the composition of ice crystal residuals. The target particle number for collection was between 10^3 and 10^4 . Aside from blanks, the period over which sample collection for TEM analysis occurred was variable and based on the concentration of particles sampled (i.e. as concentrations of 300 nm particles were smaller, a larger collection time was required than that for 100 nm particles); generally, this period was less than 3 minutes. Both samples were collected while operating at $SS_w \geq 5\%$. The high SS_w was used to encourage ice crystals to grow to a size large enough for collection on the TEM grids. This method is insufficient to determine the composition as a function of the fraction freezing given the rapid transition between baseline and full activation of the sampled aerosol. At this SS_w , it is expected that the chemical composition should resemble that of the ambient aerosol (not observed on this day).

On this day, eight grids were collected, two of which were blanks. Of these grids, RJ Lee analyzed three – one blank and two samples at -45°C (100 nm and 300 nm size-selected particles). The only blank analyzed from this day showed signs of contamination associated with a residue - areas where the residue is present show signs of particle loading while residue free areas are also particle free. Grids are

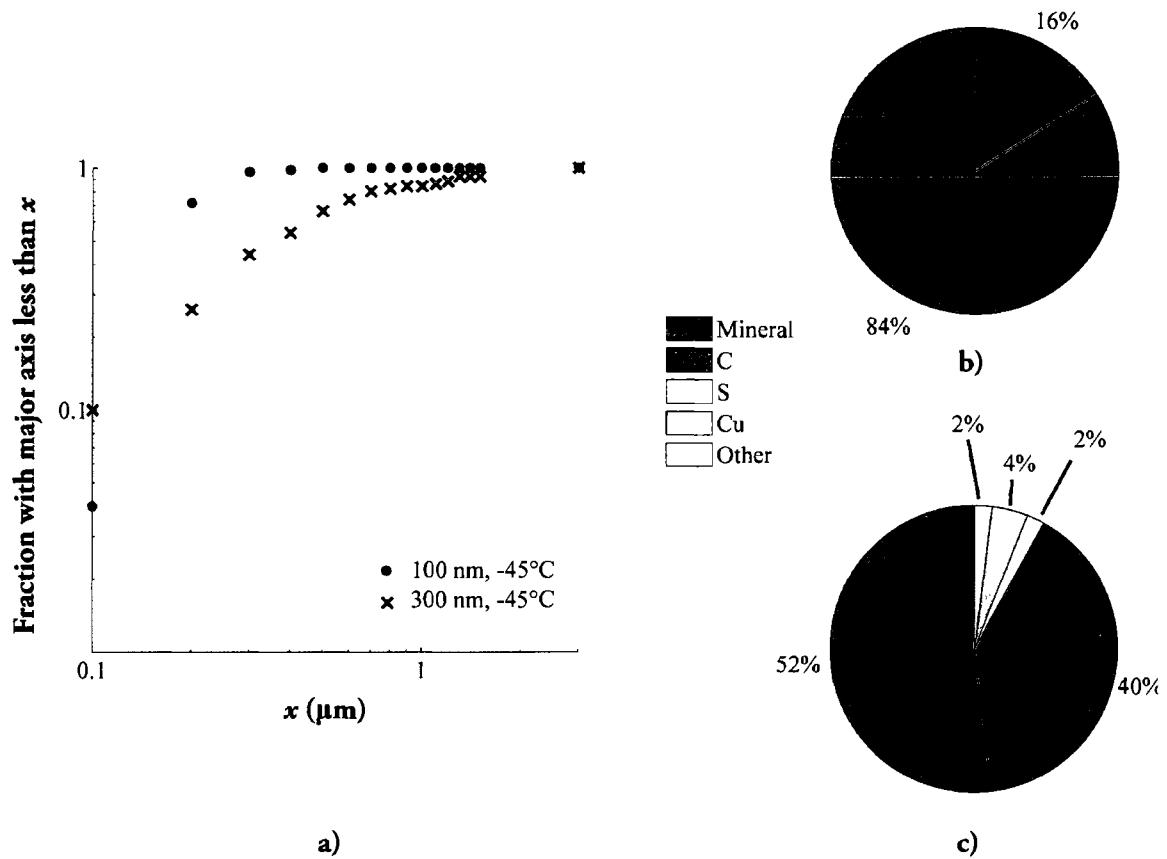


Figure 6.5. Results from TEM analysis for 3 July 2008. a) Characterization of particle size as a function of the major axis length. b) Chemical analysis of the 100 nm particles analyzed. c) Chemical analysis of the 300 nm particles analyzed.

affixed to the impactor stage using a double sided tape. It is inferred from the description of the blank analyzed by RJ Lee that the sample side came into contact with the tape, thus contaminating the blank. The dominant elements associated with particles analyzed in the residue were potassium and chloride. These elements were not observed on any of the other grids analyzed by RJ Lee.

Fifty particles were analyzed on each grid. For these samples, the chemical composition of the particles can be broken down into five broad categories with

composition dominated by 1) elements of soil or industrial origin, such as Si, Mg, and Al, 2) carbon, 3) sulfur, 4) copper, and 5) a mixture of the first three. The most frequently detected categories were the mineral type with carbon dominated particles making up the second most abundant type. Particles with copper as the dominant element were few and tended to be large. They are believed to be associated with deterioration of the CFDC wall coating which improves the wettability.

The complex shapes of the particles analyzed inhibit a clear correlation between the dimensions observed on the grid and a mobility diameter. As discussed in Chapter 3.3, ambient particles are often externally mixed and contain a variety of shapes that are difficult to capture with a single shape factor (Eq. 3.34). In addition, the morphological analysis conducted by RJ Lee in this work is restricted to observation of particles as viewed from above the filter allowing characterization of only two of the dimensions. Finally, particles may fragment on impact or volatile portions may vaporize in the beam preventing observation of the whole particles on which ice may have formed. However, Figure 6.5(a) shows that the major axis of the 100 nm particles is well defined by the mobility diameter – over 70% of the particles have a major dimension between approximately 100 and 200 nm. In contrast, the distribution of the major axis dimension for the 300 nm particles is broad, partially the result of the presence of large, multiply charged particles (see Chapter 3.3), but

also attributable to the difficulties of ascribing a volume equivalent diameter to the observed dimensions.

Figure 6.5(b) and (c) show the distribution of particle types for the two samples collected and analyzed from this day. For both initial dry sizes, the chemical composition is dominated by mineral type elements and carbon containing species. The composition of the 300 nm sample is almost evenly split between those two dominant types.

6.4 Measurements from 9 July 2008

The final measurement period of this study was conducted on 9 July 2008. During the sampling period, skies were mostly clear and conditions were warm (303

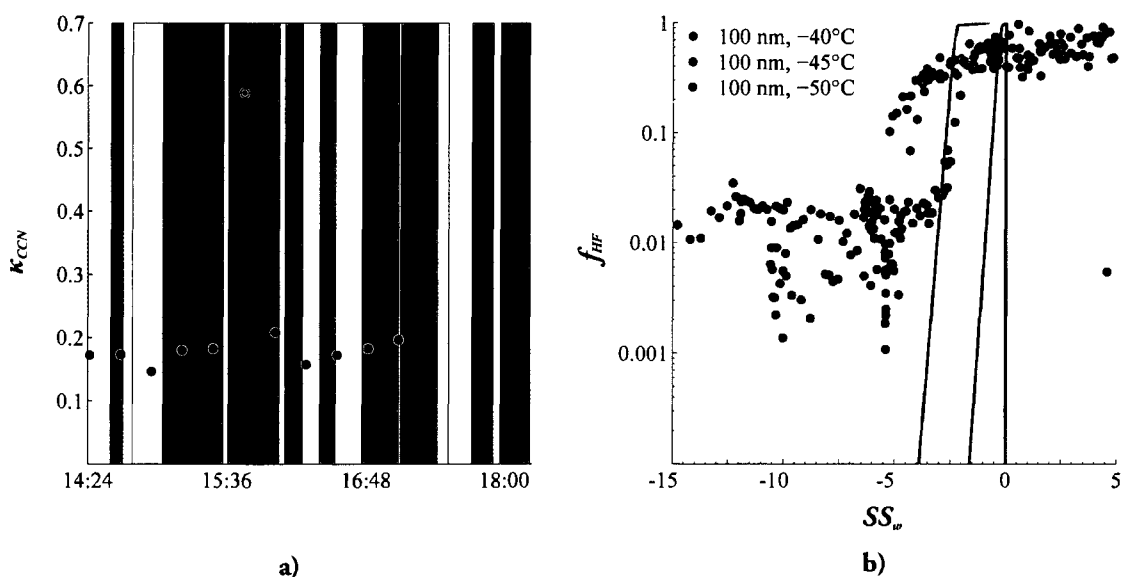


Figure 6.6. Same as Figure 6.2 but for 9 July 2008. HTDMA measured κ 's are 0.23 ± 0.04 and 0.19 ± 0.04 for 100 nm and 300 nm particles respectively.

K), dry ($RH_w \approx 21\%$) and the winds were light (3.5 m/s) and out of the southeast. HTDMA and CCNc measurements are available for most of the sampling period. In addition, six TEM grids (two of which were blank) were collected for analysis of the ice crystal residuals by RJ Lee.

Figure 6.6(a) shows κ values as a function of time inferred from CCN measurements. The median value for κ using the CCN technique was 0.177 while the 25th and 75th percentiles were 0.172 and 0.182 respectively. These values are in reasonable agreement with the HTDMA measurements which exhibit continuous water uptake and no significant difference in κ at the two different sizes, 100 nm (0.23 ± 0.04 and 0.19 ± 0.04).

Freezing activation curves are shown in Figure 6.6(b) (size-selected, 100 nm particles only) and Figure 6.7 (no size-selection and size-selected, 100 nm particles). The size-selected, 100 nm particles show the same offset from the prediction of the onset SS_w as a function of T by *Koop et al.* [2000] that the previous days show. Baseline concentrations of observed particles larger than 2 μm at low SS_w are approximately 0.2 scm^{-3} at -40°C and $\leq 0.1 \text{ scm}^{-3}$ at the colder temperatures. As with the previous day, the lack of filter measurements inhibits our ability to draw any conclusions regarding the high baseline concentrations.

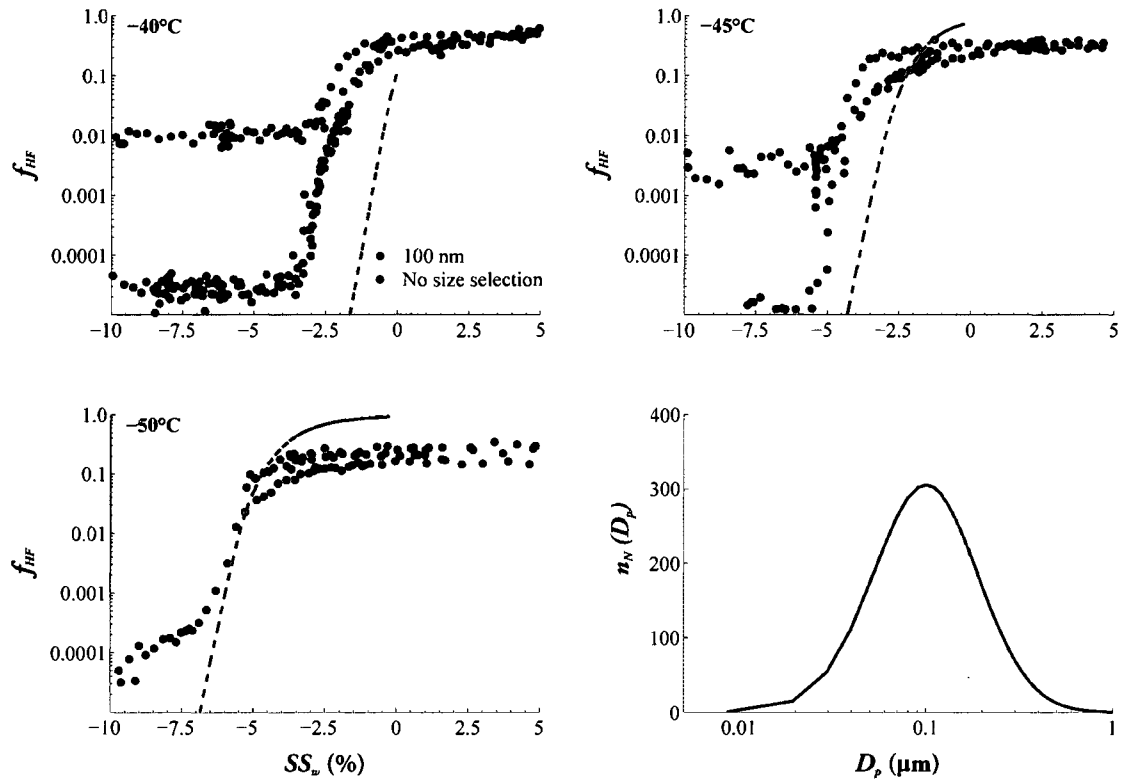


Figure 6.7. Results of homogeneous freezing experiments at the three different temperatures for 9 July 2008. The dashed black line in each panel shows the fraction freezing for a lognormally distributed aerosol with a count mean diameter of 150 nm and a geometric standard deviation of 2.0. The aerosol are assumed to have a κ of 0.1, a value near that measured on this day.

While the transition from the baseline concentration to full activation was rapid with size-selected aerosol, the freezing activation curves of the full distribution of particles from onset to full activation spanned a larger range in SS_w (Figure 6.7). At -40°C , approximately 1% of the particles freeze prior to $SS_w = -2.5\%$ and approximately 10% of the population are freezing somewhere before -1% . It is not clear that all particles have frozen before the highest SS_w is reached. Results are similar for the -45°C case. At -50°C , the final fraction freezing is significantly below

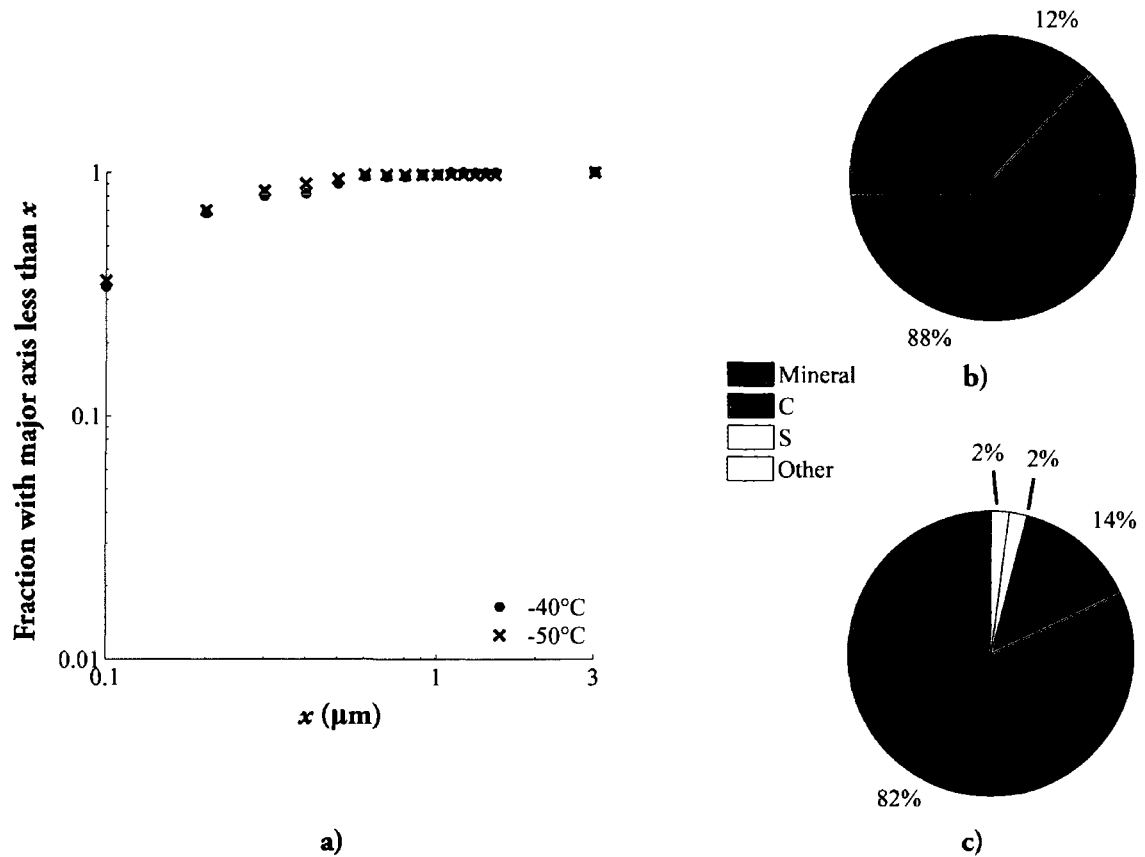


Figure 6.8. Results from analysis of two TEM grids collected on 9 July 2008. For these experiments, the whole ambient aerosol population was sampled. The samples were collected at two different processing temperatures (-40°C and -50°C). The SS_w 's for collection were -2% at -40°C and 3% at -50°C . a) Cumulative distribution of the length of the major particle axis. b) Chemical composition of particles sampled at -40°C . c) Chemical composition of particles sampled at -50°C

the two warmer cases; while approximately 30% of the 100 nm population of particles have frozen by $SS_w = 5\%$, the fraction freezing plateaus near 15% at $SS_w \approx -2.5\%$ for the full distribution of particles.

The analyzed blank collected on 9 July was particle free. Figure 6.8 shows the results of the analysis of two TEM grids collected during this sampling period. The grids were collected with no size-selection at two different temperatures, -40°C and -

50°C, and RJ Lee scientists indicated that the loadings were light to moderate. The SS_w 's during the collection were -2% at -40°C and 3% at -50°C. In contrast to the size-selected samples for which $\leq 10\%$ of the particles had a major axis dimension < 100 nm, over 30% of the analyzed particles at both temperatures had a major axis dimension less than 100 nm (Figure 6.8(a)). The TEM elemental analysis (Figure 6.8(b) and (c)) indicates that particle composition was dominated by mineral type elements with carbon containing species being the second most abundant type, similar to the results from 3 July 2008.

6.5 Discussion

A summary of the water uptake data is given in Table 6.1 along with an overview of the CFDC and TEM measurements. Both the HTDMA and CCNc measurements were in reasonable agreement with κ values ranging from approximately 0.1 to 0.2 throughout this portion of the study, κ values representative of a moderately hygroscopic organic species [Petters and Kreidenweis, 2007].

Table 6.1. Summary of data collected as described above. κ 's given for the HTDMA are provided with the 95% confidence interval for measurements at $S_w \geq 0.8$. No measurements are available on 1 July 2008. CCN derived κ 's are given as the median value (top) and the 25th and 75th percentiles (bottom in parentheses). CFDC sampling conditions and the sampled particles sizes in nm are given in the 6th column while the sampling temperature and particle sizes collected for TEM analysis are given in the 7th column. In both of these columns, all indicates a sample in which no size selection was made.

Date	κ_{HTDMA}		κ_{CCN}	CFDC	TEM
	100	250/300			
30 June	0.13±0.02	0.10±0.008	0.157 (0.152,0.163)	-40°C: 100, 300 -45°C: 100, 300 -50°C: 100	N/A
1 July	N/A	N/A	0.163 (0.08, 0.166)	-50°C: 100, 300	N/A
3 July	0.163	0.257	0.107 (0.081, 0.138)	-40°C: 100, 300 -45°C: 100, 300 -50°C: 100, 300	-45°C: 100 and 300 nm
9 July	0.23±0.04	0.19±0.04	0.177 (0.172, 0.178)	-40°C: 100, all -45°C: 100, all -50°C: 100, all	-40°C: all -50°C: all

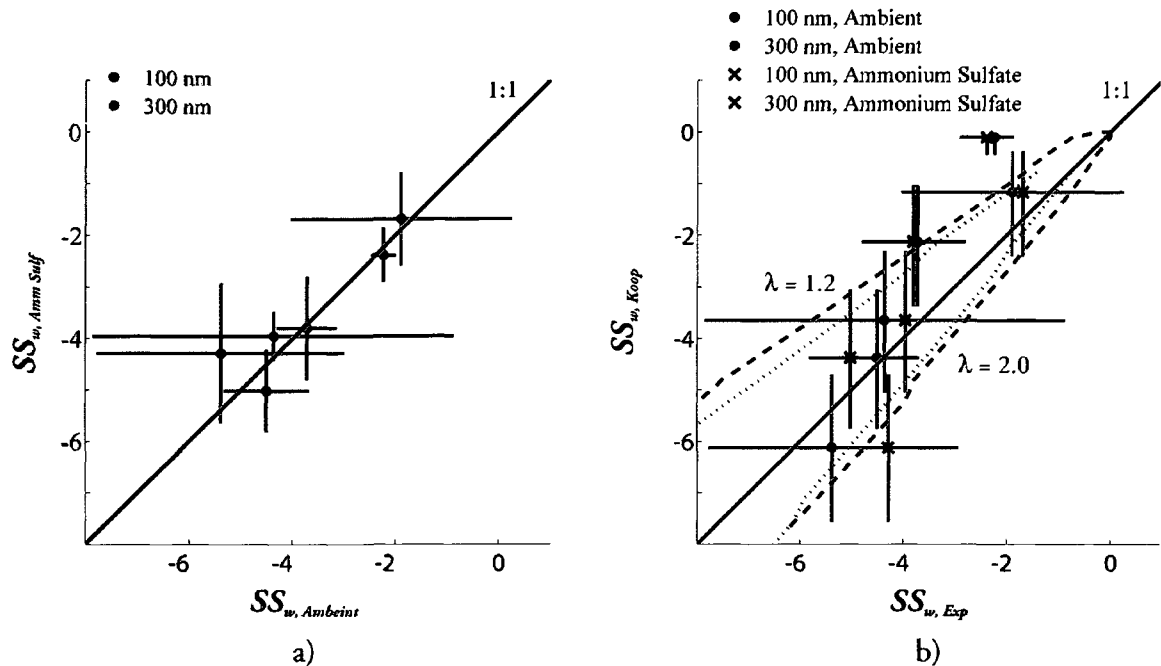


Figure 6.9. a) Size-selected ammonium sulfate onset SS_w plotted against size-selected ambient data for the three different T_a (-40°C , -45°C , and -50°C) and two different particles sizes. b) Koop *et al.* [2000] predicted onset SS_w for size-selected particles plotted against the measured SS_w at three different T_a (-40°C , -45°C and -50°C). The predicted values are based on a $\Delta t = 3$ s, $f_{HF} = 0.001$ and $\kappa \approx 0.15$. Dashed (100 nm) and dotted (300 nm) lines show comparisons of the predicted SS_w using the freezing parameterization described in DeMott *et al.* [1997] for $\lambda = 2.0$ and 1.2 with that given by Koop *et al.* Bars on experimental data show the confidence interval for the measurement. Bars on Koop *et al.* values show calculated $\Delta a_w \pm 0.15$.

Regardless of size, all HTDMA measurements exhibit continuous water uptake with no clear deliquescent transition. This has been observed in previous studies and is often associated with the hypothesized presence of organics [Dick *et al.*, 2000; Prenni *et al.*, 2001a]. The measured gf 's span the definition of less hygroscopic and more hygroscopic aerosol given in Swietlicki *et al.* [2008] and are consistent with previous studies where the air mass sampled was representative of an urban, polluted one [Aklilu *et al.*, 2006; Gysel *et al.*, 2007].

Figure 6.9(a) shows the freezing onset conditions of the size-selected ammonium sulfate plotted against the onset conditions obtained for the size-selected ambient aerosol (onset freezing conditions for the size-selected ambient aerosol are determined using the methodology outlined in the introduction to Chapter 4 and are given in Table 6.2). Despite the discrepancy in the predicted onset freezing conditions calculated using the parameterization of *Koop et al.* [2000] and the measured freezing onset conditions of ammonium sulfate, Figure 6.9 shows that the expected similarity between the onset SS_w for ammonium sulfate and that of the size-selected ambient aerosol expressed in Figure 6.1 is indeed observed.

Figure 6.9(b) plots the *Koop et al.* [2000] prediction of freezing onset (with $\Delta a_w \pm 0.015$ calculations for the error bars, a value that captures the scatter in the data used to construct the parameterization) versus both the size-selected ambient and ammonium sulfate freezing onset data. In this figure, the *Koop et al.* prediction is also plotted against the prediction of freezing using the melting point depression parameterization described in *DeMott et al.* [1997] for two different values of λ . This plot highlights the uncertainty in the inferred measurement conditions (SS_w and T_a) and indicates that the 100 nm freezing onset SS_w at -40°C is similar to that predicted for T_a near -45°C or for larger particles (the temperature of the measurements is readily identified by the onset SS_w predicted by the *Koop et al.* parameterization, with onset $SS_{w,Koop}$ decreasing with decreasing T_a). At all temperatures, the freezing

onset SS_w for 300 nm, ambient particles observed by the CFDC-1H is captured by the *Koop et al.* parameterization within the uncertainty of the parameterization and the measurement. While the *Koop et al.* parameterization seems to capture the onset SS_w for the ammonium sulfate at the two warmer temperatures, the observed onset SS_w at -50°C begins to deviate from this parameterization such that it requires significantly higher SS_w than that predicted. As the observation of the onset of homogeneous freezing of the ambient and the ammonium sulfate particles are the same within the statistical uncertainty of the respective measurements, this is likely due to instrumental limitations for the observation of freezing onset under these operating conditions.

Table 6.2. Freezing onset conditions from all ambient aerosol experiments

D_p (nm)	T_{target} (°C)	T_o (°C)	SS_w (%)	$\overline{SS_w}$	S_{SS_w}	$\overline{T_a}$	S_{T_a}
100	-40	-40.75	-2.33	-2.23 ± 0.24	3.00	-40.44 ± 0.7	0.52
		-40.28	-2.15				
		-40.26	-2.19				
	-45	-46.07	-3.46	-3.72 ± 0.58	3.3	-45.75 ± 0.69	0.52
		-45.63	-3.80				
		-45.55	-3.89				
	-50	-50.43	-4.32	-4.5 ± 0.82	3.6	-50.61 ± 0.32	0.55
		-50.43	-4.58				
		-50.80	-5.16				
-50.75		-3.93					
300	-40	-40.63	-1.72	-1.68 ± 2.15	3.06	-40.62 ± 0.2	0.51
		-40.60	-2.06				
	-45	-45.15	-4.08	-3.95 ± 3.5	3.28	-45.25 ± 1.2	0.52
		-45.34	-4.63				
	-50	-50.53	-5.19	-5.38 ± 2.39	3.58	-50.56 ± 0.46	0.51
		-50.60	-5.56				

Unlike the size-selected measurements, the ambient aerosol with no size selection freezes over a wide range of SS_w (Figure 6.7). Much of this range in SS_w can be modeled using the *Koop et al.* [2000] parameterization of homogeneous freezing (as shown by the predicted freezing lines in Figure 6.7), indicating that size plays the dominant role in how particles freeze. This implies that assessing the chemical composition as a function of the fraction of particles freezing with no information regarding the ice crystal residual size is difficult as the difference in composition may

be a result of the different aerosol formation mechanisms [*Finlayson-Pitts and Pitts, 1999*].

As particles were collected at SS_w 's where a majority of the sampled particles were activating, it is expected that the chemical composition of the ice crystal residuals should resemble that of the ambient population. Although no measurements of the composition were conducted in conjunction with this campaign, measurements of the chemical composition of particles from previous years along the Front Range indicate an aerosol of very different composition. Bulk chemical analysis from an EPA air quality system site in Denver (<http://www.epa.gov/ttn/airs/airsaqs/index.htm>) suggests that aerosol composition during late summer is dominated by carbon-based compounds (approximately 40 to 60% by mass) with nitrates and sulfates making up another 30%. These values are similar to those found at an IMPROVE site in the northern Colorado Rockies for a similar time of year [*Malm et al., 2004*]. In contrast, the dominant elements observed on the analyzed grids were associated with soil and industrial sources (Figure 6.5 and Figure 6.7) regardless of particle size. While nitrates are expected to vaporize in the electron beam, sulfur associated with sulfates is observable [*Li et al., 2003*]. The overwhelmingly dominant presence of mineral-type elements in the particles analyzed suggests that particles freezing homogeneously were not efficiently transmitted through the outlet of the CFDC-1H at sizes reasonable for collection by

impaction. It is possible that homogeneously formed crystals may evaporate rapidly enough such that their aerodynamic size is insufficient for them to be collected via impaction. This evaporation would be exacerbated by the low flow rates used in this study and would bias collection toward particles that nucleate most readily via heterogeneous processes, thus explaining the predominance of mineral-related elements in all samples and the bias toward larger sizes in the 300 nm selected samples.

Comparison of concentrations observed on the grids and those counted by the CFDC-1H OPC should also provide some insight. Scientists at RJ Lee described the particle loadings as “light to moderate”, where light was defined as on the order of 1 particle per grid opening, and moderate was on the order of 10 per grid opening. For a 3 mm, 200 mesh grid with 50% of the grid area being open, this translates to about 500 particles on the grid for “light” loading (assuming even particle distribution on the grid surface) to about 5000 particles for “moderate” loading. During experiments, particle counts above 2 μm were typically ≥ 5000 for the TEM sampling period and 3×10^4 and 1×10^5 for the samples with no size selection. The numbers suggest that there is possibly an order of magnitude difference between the counts of particles over 2 μm and the number of particles captured on the grid, greater if the particle distribution is not even across the entire grid surface. Although not conclusive, this

further supports the conclusion that the particles captured by the grid represented only a subset of the total number of particles freezing in the experiment.

7 CONCLUSIONS AND RECOMMENDATIONS

7.1 Summary and Conclusions

Due to their ubiquity, high clouds play an important role in the Earth's radiative budget. Perturbations to the distribution of these clouds and their microphysical properties can have important implications for future climate. With this in mind, a significant effort has been exerted in recent years to determine the conditions under which these clouds form particularly via laboratory studies using aerosol with well characterized physiochemical properties. From these efforts, *Koop et al.* [2000] produced a parameterization of the homogeneous freezing process which is widely used to validate laboratory results and to model cloud formation at low temperature in GCMs. However, the applicability of this parameterization to an aerosol of unknown composition has not previously been determined for atmospheric samples. The CSU CFDC is an instrument that has the potential to make direct measurements of the ice nucleation properties of ambient particles *in-situ*. Initially developed for the study of heterogeneous nucleation in the laboratory, the CFDC was

redesigned in the late 1990's to operate on an aircraft platform at low temperatures. Since the redesign, the CFDC has been operated in the field at cirrus conditions with limited success.

This dissertation discusses numerical and laboratory studies prompted by a more recent redesign of the chamber (referred to as the CFDC-1H). The performance of the CFDC-1H was first studied in the laboratory by measuring the onset freezing conditions of ammonium sulfate at a variety of operating conditions. Ammonium sulfate was chosen as the freezing properties of this deliquesced solute have been studied extensively and are well constrained. At standard operating conditions (10 lpm, 850 mb) the observed freezing onset SS_w for the temperature range studied (-40°C to -50°C) for both 100 nm and 300 nm particles deviated little from water saturation, but deviated significantly from those predicted by the *Koop et al.* parameterization of homogeneous freezing. We concluded that there are operational limits to the detection of the freezing onset conditions at these temperatures related to the limited residence time for crystal nucleation and growth. At lower pressure (500 mb), despite the expectation of improved performance due to enhanced diffusivity and increased particle residence times that would permit nucleated crystals to more readily grow to detectable sizes, the results were quantitatively similar. However, there did appear to be some activity at lower sizes in the OPC spectrum at conditions more in line with those predicted by the parameterization leading to an

inference that ice was simply nucleating too late in the growth period in the CFDC to achieve detection. At a lower flow rate (5 lpm) and therefore increased particle residence time in the growth region, the performance improved significantly with measured onset conditions matching the predicted within the uncertainty of the measurement.

Computational fluid dynamics (CFD) simulations and an offline microphysical model were used to understand the reasons for the observed discrepancies between the measured and predicted homogeneous freezing onset conditions. In addition, the simulations allowed investigation of the CFDC-1H operation at a temperature representative of the upper troposphere not accessible in the current refrigeration configuration (-60°C). Also, five different wall boundary conditions were investigated to determine the impact of thermal non-idealities on onset freezing conditions and crystal growth in the CFDC.

The CFD simulations revealed several features of the flow that might impact the distribution of the particles in the chamber as well as affect the final crystal size. At the inlet, boundary layer separation driven by fluid density gradients on the inner portion of the chamber resulted in distortion of the streamlines and a region of recirculation near the inner inlet blade. In the outlet region, conduction through the outer portion of the base which is not actively temperature controlled results in a warming of the outer region of the flow and thus generates a region of recirculation

that confines the flow toward the inner portion of the chamber. At the collar, the interaction of a cooling, hydrophobic boundary with water vapor diffusing from the upstream edge is generating a “moist bubble”; that is, a region of anomalously high S_w . The saturations reach as high as 1.8 or 1.9 in the middle of the bubble. The simulations indicate that the aerosol lamina is not interacting with these features and the rapid transition from background concentrations to $\approx 100\%$ freezing in the nucleation signal appears to support this. However, the presence of these features should be considered when adjustments are made to the sheath to total flow ratio which controls the width and position of the lamina. The CFD simulations also indicated that the analytic solution proposed in *Rogers* [1988] for the steady-state thermodynamic conditions is a reasonable approximation for the conditions experienced by the particles in the growth region. However, the operating conditions (flow rate and pressure) have a significant impact on the amount of time the particles reside at these conditions, and our simulations confirmed that limited residence time is the primary reason that observations of the freezing onset deviate from those predicted by *Koop et al.* [2000].

Thermodynamic conditions along particle trajectories were extracted from the CFD simulations and used as inputs in a microphysical model. Despite large uncertainties in the thermodynamics of supercooled water and the accommodation coefficients used in the diffusional growth equations, the results for the ideal

simulations (i.e., no wall temperature perturbation) agreed with the laboratory results within the uncertainty of the measurement. However, the simulations could not account for the low SS_w measured at -40°C for both particle sizes, suggesting a bias in the observed SS_w . The particle response to changes in SS_w became progressively smaller with changes in temperatures due to the change in the water mass available for growth – i.e., the change in the mean crystal size as a function of SS_w was larger at warmer temperatures. Based on simulations, perturbations to the wall temperatures have little effect on nucleation and crystal growth with the exception of the 2 K, downward gradient along the length of the outer wall. This perturbation consistently resulted in lower freezing onset SS_w 's at a single temperature than the other perturbed simulations.

The final portion of the study was intended to test the applicability of a laboratory-based parameterization of homogeneous freezing to an ambient aerosol. An HTDMA and CCNc measured the water uptake properties of the ambient aerosol. The water uptake measurements provided some insight into the mixing state and chemical composition of the ambient aerosol which have the potential to impact the observed freezing onset conditions. The water uptake measurements were in reasonable agreement with κ values varying between 0.1 and 0.2 for the CFDC measurement periods. These values showed that the aerosol was significantly less hygroscopic than ammonium sulfate and may be representative of a continental

aerosol as defined by *Andreae and Rosenfeld* [2008]. However, calculations of the predicted onset freezing conditions using these hygroscopicity values indicated that the onset SS_w determined in the CFDC would not be measurably different from that of ammonium sulfate. The CFDC-1H was operated at 5 lpm and ambient pressure (~ 850 mb) in this portion of the study. As hypothesized, size-selected measurements of the freezing onset conditions compared favorably with the results of size selected ammonium sulfate particles in the previous portion of the study, indicating that the presence of insoluble components has a limited effect on these onset conditions; an effect which is not discernable by this technique. Freezing curves for the total aerosol population compared similarly with the prediction by the homogeneous freezing parameterization of *Koop et al.* [2000] indicating that size plays an important role in the freezing activity of ambient aerosol. This is the first reported direct experimental evidence for the validity of the present understanding of homogeneous freezing and the ability to detect it compared to heterogeneous ice nucleation on an ambient aerosol population.

Particles acting as freezing nuclei for $SS_w > 0 > 0$ were collected downstream of the CFDC-1H for analysis via TEM coupled with EDS. Analysis indicated that the collected aerosol was dominated by mineral-like elements (Si, Mg, Al). The composition was not consistent with measured κ 's which suggested the presence of some inorganic or organic hygroscopic material. The results indicate that smaller

crystals formed in the CFDC and detected by the OPC may evaporate before reaching the impactor. Although variations of this technique have been used successfully before, it is apparent that further investigation is needed in order to optimize this method of collection and analyses at these operating conditions.

Overall, the simulations predict and laboratory experiments indicate that the CFDC-1H should be able to capture the onset of homogeneous freezing down to -50°C (within the uncertainty of the measurement) using a modified set of operating conditions (i.e. conditions that result in higher growth region residence times, such as low flow rates), demonstrating that the CFDC-1H can be used as an important tool in the study of cold clouds. It will be difficult for any technique utilized *in-situ* to overcome uncertainties in the measurement of RH_w such that small differences in the freezing onset conditions that may be associated with hygroscopicity or heterogeneous ice nucleation close to the homogenous freezing limit may be detected. Careful consideration of the experimental approach will be required to capture these small deviations in onset conditions. However, considering that ice crystals in cirrus clouds represent only a small fraction of the total number of particles [cf. *Kärcher and Stöm, 2003; Ström et al., 1997*], an instrument such as the CFDC is a vital tool in determining the [IN] which may activate in strong preference to homogeneous freezing (i.e., outside the uncertainty of the measured RH_w).

Although not explicitly studied, kinetic limitations on individual particle nucleation and growth have the potential to also impact measurements of heterogeneous IN. This is particularly true for particles that serve as immersion or condensation freezing nuclei, for which some dilution would be required for activation [DeMott, 2002]. However, for more active IN such as pristine dusts there should be no kinetic limitation that would inhibit the ability of the CFDC-1H to detect their presence. This has been demonstrated in both the INSPECT-I [DeMott *et al.*, 2003] and INSPECT-II [Richardson *et al.*, 2007] campaigns and more rigorously in unpublished laboratory studies.

7.2 Recommendations

This study led to a number of suggestions for future work. Foremost among these is further characterization of the instrument at low pressure. Numerical simulations indicate that there should be significant benefits of operation at low pressure – peak velocities approach those of parabolic flow thus increasing particle residence time within the chamber and increased diffusivity should translate to more rapid cloud particle growth. However, these expectations were not entirely borne out in the laboratory experiments. In these measurements, the pressure was controlled via an orifice located immediately upstream of the CFDC. A pump downstream of the orifice pulled flow to maintain a fixed pressure. For choked flow (i.e., chamber $P \leq 450$ mb), the excess flow exceeded the CFDC sample flow. Using this system,

particle transmission approached zero. A method for controlling the inlet pressure should be developed which allows for operation of the CFDC at low pressure while maintaining high particle transmission efficiencies. *Lee et al.* [1995] discuss a variety of designs for pressure reducers and *Bahreini et al.* [2008] demonstrate the implementation of one of these designs for use with the Aerodyne Aerosol Mass Spectrometer.

The low pressure experiments also emphasized the need for a system to discern crystal formation that is not reliant on the optical size. The detector should discriminate based on the phase of the particle rather than the size. Currently, efforts are under way to integrate a variant of the small ice detector [SID, *Kaye et al.*, 2008] with the laboratory version of the CFDC. This detector allows the imaging of high-resolution spatial scattering patterns of ice crystals down to $\sim 1 \mu\text{m}$ at a high acquisition rate ($\sim 20 \text{ s}^{-1}$). The scattering patterns for drops and crystals are distinctly different and readily discernable. At the present moment, the current detector is bulky and requires a separate data acquisition system, facts which limit the current design to use in a laboratory setting only. Future research should result in a detector adaptable to the current CFDC-1H rack design with an integrated data acquisition system.

Attempts to collect crystal residuals on a TEM grid for offline analysis via impaction exposed some shortcomings of the technique as applied. This technique

has been used successfully when sampling at warmer temperatures and higher flow rates. However, in these cold temperature experiments, evaporation of small crystals may have been occurring. The need to maintain an environment closer to that produced in the evaporation region of the CFDC to limit crystal evaporation downstream of the CFDC increases with decreasing temperature as particle growth becomes restricted at lower temperatures. Ideally, the downstream temperature should be maintained near the cold wall temperature. Some exploratory tests using a simple cooling system and known freezing nuclei (such as ammonium sulfate) should provide sufficient information on an upper temperature limit. Extending the model domain in the simulations described previously could also provide rapid feedback on how evaporation rates are affected by temperature.

Collection of ice crystal residuals for TEM analysis has several shortcomings: it is labor intensive, provides no immediate feedback on the chemical composition, is prone to contamination associated with the handling of the grids and more volatile species (such as nitrate and occasionally sulfates) are vaporized in the electron beam. The CFDC has been successfully operated with single particle mass spectrometers measuring the chemical composition of ice crystal residuals in two different campaigns [*Cziczo et al.*, 2003; *Richardson et al.*, 2007], although the transmission efficiency between the CFDC outlet and the mass spectrometer inlet was low. Using this method, we were able to obtain the chemical composition as a function of the

fraction freezing. In addition, species such as nitrate and sulfate that may volatilize in the electron beam are observable by single particle mass spectrometry. Continued development on the interface between the CFDC-1H and a mass spectrometer will improve our ability to successfully make more complete, real-time measurements of the chemical composition of freezing nuclei.

Finally, the results from the limited field study imply that, from a cold cloud modeling standpoint, particles may be divided into two classes, hygroscopic and insoluble; the mixing of less hygroscopic components with more hygroscopic components leads to limited changes in the onset homogeneous freezing conditions of the more hygroscopic components. It is clear that these results need further confirmation as the aerosol at ground level in an urban setting is not necessarily representative of the aerosol at higher altitudes. Field campaigns either at high altitude sites with access to the free troposphere such as Storm Peak Laboratory [*Borys and Wetzel, 1997*] or aircraft-based are necessary to provide validation of these results. In addition, the location of an ammonium sulfate calibration system in the rack would provide periodic feedback on the performance of the system and constraints on the thermodynamic variables inferred from the measurements.

Appendix A: Simulated Crystal Size Distributions

The following tables give the results for the mean crystal size (Eq. 5.5) at the given operating conditions. For each simulation, $\alpha_{c,w} = 0.7$ and $\alpha_{c,i} = 0.4$. The SS_w given is that calculated via the analytical solution (Eq. 3.2 close to locate the lamina and Eqs. 3.4 and 3.5 for the vapor pressure and temperature respectively). For all simulations, the total to sample flow rate ratio is 10:1.

A.1 The Base Case

The base case represents the standard protocol for laboratory operation of the CFDC. In each of these simulations, $Q_t = 10$ lpm and $P = 850$ mb.

Table A.1. Results of base case simulations at $T_a = -40^\circ\text{C}$

d_0 (nm)	SS_w (%)			
	-0.52	1.64	3.90	4.99
100	-	1.69	2.52	2.99
200	1.16	1.86	2.61	3.06
300	1.38	1.98	2.60	3.03
400	1.56	2.11	2.60	2.97
500	1.71	2.24	2.66	2.9
600	1.84	2.36	2.77	2.95
700	1.97	2.48	2.87	3.04
800	2.12	2.58	2.98	3.14
900	-	2.68	3.08	3.23
1000	-	2.77	3.18	3.33

Table A.2. Results of base case simulations at $T_a = -45^\circ\text{C}$

d_0 (nm)	SS_w (%)								
	-4.24	-3.15	-2.03	-0.89	0.26	1.44	2.65	3.89	5.15
100	-	-	1.48	2.23	2.51	2.69	2.84	2.97	3.09
200	-	1.01	2.07	2.40	2.62	2.78	2.92	3.05	3.17
300	-	1.39	2.13	2.44	2.65	2.82	2.96	3.09	3.21
400	-	1.47	2.11	2.44	2.66	2.84	2.99	3.12	3.25
500	1.32	1.55	2.05	2.42	2.66	2.85	3.00	3.14	3.28
600	1.46	1.67	1.99	2.37	2.64	2.84	3.01	3.16	3.30
700	1.60	1.78	1.98	2.31	2.60	2.83	3.01	3.17	3.32
800	-	1.89	2.08	2.27	2.56	2.80	3.01	3.18	3.33
900	-	2.00	2.19	2.34	2.52	2.77	2.99	3.17	3.34
1000	-	2.12	2.29	2.44	2.58	2.75	2.97	3.17	3.34

Table A.3. Results of base case simulations at $T_a = -50^\circ\text{C}$

SS_w (%)	-5.36	-3.11	-0.65	1.90	3.22	4.56
d_0 (nm)						
100	-	1.81	2.12	2.34	2.43	2.51
200	1.25	1.96	2.21	2.41	2.49	2.58
300	1.50	2.02	2.26	2.45	2.54	2.62
400	1.55	2.04	2.30	2.49	2.58	2.67
500	1.55	2.06	2.33	2.53	2.62	2.71
600	1.54	2.08	2.36	2.57	2.66	2.75
700	1.60	2.09	2.38	2.61	2.70	2.80
800	1.70	2.10	2.41	2.64	2.75	2.84
900	1.81	2.10	2.44	2.68	2.79	2.89
1000	1.92	2.14	2.47	2.73	2.83	2.93

Table A.4. Results of base case simulations at $T_a = -60^\circ\text{C}$.

SS_w (%)	-9.01	-6.43	-3.73	-0.90	2.05	5.14
D_0 (nm)						
100	0.68	1.03	1.17	1.29	1.39	1.48
200	0.93	1.12	1.24	1.35	1.44	1.53
300	1.00	1.17	1.30	1.40	1.50	1.59
400	1.05	1.23	1.36	1.46	1.56	1.65
500	1.11	1.29	1.42	1.53	1.62	1.71
600	1.17	1.36	1.49	1.60	1.69	1.78
700	1.27	1.44	1.57	1.68	1.77	1.86
800	1.38	1.52	1.66	1.76	1.86	1.95
900	1.51	1.61	1.75	1.86	1.95	2.04
1000	1.65	1.73	1.84	1.95	2.05	2.13

A.2 Low Pressure

In each of the following simulations, $Q_t = 10$ lpm and $P = 500$ mb.

Table A.5. Results of low pressure simulations at $T_a = -40^\circ\text{C}$

d_0 (nm)	SS_w (%)				
	-1.66	0.47	2.67	4.96	6.07
100	-	0.73	2.07	3.07	3.63
200	-	1.25	2.28	3.21	3.76
300	-	1.58	2.47	3.32	3.84
400	-	1.84	2.64	3.42	3.89
500	1.30	2.07	2.81	3.53	3.94
600	1.50	2.29	2.98	3.64	3.99
700	1.73	2.48	3.14	3.77	4.06
800	1.94	2.67	3.29	3.90	4.16
900	2.14	2.85	3.45	4.03	4.27
1000	2.33	3.02	3.59	4.16	4.39

Table A.6. Results of low pressure simulations at $T_a = -45^\circ\text{C}$

SS_w (%)	-4.60	-3.50	-2.38	-1.23	-0.07	1.07	2.29	3.53	4.75
d_0 (nm)									
100	-	-	-	1.63	3.55	3.82	4.03	4.20	4.32
200	-	-	1.15	3.35	3.73	3.94	4.13	4.29	4.41
300	-	0.76	2.20	3.45	3.79	4.00	4.19	4.35	4.47
400	-	1.02	2.52	3.48	3.82	4.04	4.23	4.40	4.53
500	1.06	1.26	2.58	3.46	3.83	4.06	4.27	4.44	4.57
600	1.24	1.47	2.55	3.42	3.82	4.08	4.29	4.48	4.62
700	1.44	1.68	2.48	3.35	3.80	4.08	4.31	4.50	4.65
800	1.64	1.86	2.43	3.27	3.76	4.08	4.32	4.53	4.68
900	1.84	2.05	2.41	3.18	3.71	4.06	4.32	4.54	4.71
1000	2.02	2.22	2.45	3.09	3.65	4.04	4.32	4.55	4.73

Table A.7. Results of low pressure simulations at $T_a = -50^\circ\text{C}$

SS_w (%)	-6.68	-4.40	-2.11	0.37	2.96	4.30	5.66
d_0 (nm)							
100	-	-	2.93	3.33	3.60	3.72	3.84
200	-	1.08	3.11	3.43	3.68	3.80	3.92
300	-	2.15	3.18	3.48	3.74	3.86	3.97
400	-	2.47	3.22	3.53	3.79	3.91	4.03
500	0.98	2.55	3.25	3.57	3.84	3.96	4.08
600	1.14	2.56	3.27	3.61	3.89	4.01	4.13
700	1.32	2.53	3.29	3.65	3.93	4.06	4.18
800	1.50	2.48	3.30	3.68	3.97	4.10	4.23
900	1.68	2.43	3.31	3.71	4.01	4.15	4.28
1000	1.85	2.39	3.32	3.74	4.05	4.19	4.33

Table A.8. Results of low pressure simulations at $T_a = -60^\circ\text{C}$

SS_w (%)	-10.53	-8.07	-5.46	-2.73	0.13	3.10	6.21
d_0 (nm)							
100	-	0.72	1.70	1.88	2.03	2.17	2.31
200	-	1.55	1.79	1.95	2.10	2.23	2.37
300	0.53	1.63	1.85	2.01	2.15	2.29	2.42
400	0.71	1.68	1.90	2.06	2.21	2.34	2.48
500	0.90	1.73	1.96	2.12	2.27	2.41	2.54
600	1.06	1.77	2.01	2.18	2.33	2.47	2.60
700	1.21	1.82	2.07	2.25	2.40	2.54	2.67
800	1.36	1.87	2.13	2.32	2.47	2.61	2.74
900	1.51	1.92	2.20	2.39	2.54	2.68	2.82
1000	1.66	1.98	2.27	2.46	2.62	2.76	2.89

A.3 Low Flow Rate

In the following simulations, $Q_t = 5$ lpm and $P = 500$ mb.

Table A.9. Results of low flow rate simulations at $T_a = -40^\circ\text{C}$

SS_w (%)	-1.04	0.01	1.09	2.19	3.30	4.44
d_0 (nm)						
100	0.19	4.19	5.52	6.08	6.44	6.74
200	1.08	4.67	5.66	6.17	6.53	6.82
300	1.76	4.62	5.61	6.15	6.53	6.84
400	1.94	4.43	5.48	6.07	6.49	6.83
500	1.95	4.17	5.29	5.95	6.42	6.79
600	2.02	3.87	5.07	5.80	6.32	6.72
700	2.21	3.57	4.82	5.62	6.19	6.63
800	2.41	3.32	4.56	5.43	6.04	6.52
900	2.61	3.18	4.31	5.21	5.88	6.40
1000	2.79	3.23	4.08	5.00	5.70	6.26

Table A.10. Results of low flow rate simulations at $T_a = -45^\circ\text{C}$

SS_w (%)	-4.76	-3.69	-2.60	-1.48	-0.34	0.82	2.00	3.21	4.45	5.71
d_0 (nm)										
100	-	-	4.54	5.05	5.29	5.48	5.64	5.80	5.04	5.16
200	-	4.06	4.89	5.18	5.38	5.56	5.72	5.87	5.09	5.21
300	-	4.38	4.95	5.22	5.43	5.61	5.77	5.93	5.12	5.25
400	-	4.45	4.97	5.25	5.46	5.64	5.81	5.97	5.15	5.28
500	0.86	4.42	4.96	5.26	5.48	5.67	5.85	6.01	5.17	5.30
600	1.42	4.36	4.94	5.25	5.50	5.70	5.88	6.05	5.19	5.32
700	1.65	4.28	4.90	5.24	5.50	5.71	5.90	6.08	5.20	5.34
800	1.82	4.17	4.85	5.22	5.50	5.72	5.92	6.11	5.20	5.35
900	1.93	4.05	4.79	5.20	5.49	5.73	5.94	6.13	5.20	5.36
1000	2.02	3.91	4.71	5.16	5.48	5.73	5.95	6.15	5.20	5.36

Table A.11. Results of low flow rate simulations at $T_a = -50^\circ\text{C}$

SS_w (%)	-7.1	-5.98	-4.84	-3.68	-2.49	-1.28	-0.04	1.22	2.51	3.81	5.16
d_0 (nm)											
100	-	-	3.68	4.00	4.17	4.32	4.45	4.55	4.67	4.73	4.85
200	-	3.58	3.92	4.11	4.25	4.39	4.51	4.61	4.73	4.79	4.90
300	-	3.71	3.98	4.15	4.30	4.43	4.56	4.66	4.78	4.83	4.95
400	2.75	3.75	4.01	4.19	4.34	4.47	4.60	4.70	4.82	4.88	4.99
500	2.94	3.76	4.03	4.21	4.37	4.51	4.64	4.74	4.87	4.92	5.04
600	2.94	3.75	4.04	4.23	4.40	4.54	4.67	4.78	4.91	4.97	5.08
700	2.87	3.73	4.04	4.25	4.42	4.57	4.71	4.82	4.95	5.01	5.13
800	2.82	3.71	4.04	4.26	4.44	4.60	4.74	4.86	4.99	5.05	5.17
900	2.77	3.67	4.03	4.27	4.46	4.63	4.78	4.90	5.03	5.10	5.22
1000	2.71	3.63	4.02	4.28	4.48	4.65	4.81	4.93	5.07	5.14	5.26

Table A.12. Results of low flow rate simulations at $T_a = -60^\circ\text{C}$

SS_w (%)	-4.60	-3.50	-2.38	-1.23	-0.07	1.07	2.29	3.53	4.75
d_0 (nm)									
100	-	-	-	1.63	3.55	3.82	4.03	4.20	4.32
200	-	-	1.15	3.35	3.73	3.94	4.13	4.29	4.41
300	-	0.76	2.20	3.45	3.79	4.00	4.19	4.35	4.47
400	-	1.02	2.52	3.48	3.82	4.04	4.23	4.40	4.53
500	1.06	1.26	2.58	3.46	3.83	4.06	4.27	4.44	4.57
600	1.24	1.47	2.55	3.42	3.82	4.08	4.29	4.48	4.62
700	1.44	1.68	2.48	3.35	3.80	4.08	4.31	4.50	4.65
800	1.64	1.86	2.43	3.27	3.76	4.08	4.32	4.53	4.68
900	1.84	2.05	2.41	3.18	3.71	4.06	4.32	4.54	4.71
1000	2.02	2.22	2.45	3.09	3.65	4.04	4.32	4.55	4.73

A.4 Ice Crystal Distributions for the Perturbed Boundary Conditions

The following results are from the simulations of the perturbed boundary conditions. The operating conditions are the same as those given for the base case ($Q_t = 10$ lpm, $P = 850$ mb). In each case, the walls in the growth region are perturbed as described below.

A.4.1 Outer Wall Downward Gradient

The following distributions were generated for simulations in which a 2 K gradient was applied along the outer wall of the growth region with the temperature increasing down along the wall.

Table A.13. Results of the outer wall downward gradient simulations for $T_a = -40^\circ\text{C}$

SS_w (%)	-2.61	-0.52	1.64	3.90
d_0 (nm)				
100	0.94	1.50	2.08	2.64
200	1.21	1.72	2.22	2.74
300	1.39	1.88	2.31	2.78
400	1.53	2.02	2.42	2.82
500	1.66	2.15	2.53	2.90
600	1.80	2.27	2.64	3.00
700	1.93	2.37	2.75	3.10
800	-	2.47	2.86	3.20
900	-	2.57	2.96	3.29
1000	-	2.65	3.06	3.39

Table A.14. Results of the outer wall downward gradient simulations for $T_a = -45^\circ\text{C}$

SS_w (%)	-4.24	-3.15	-2.03	-0.89	0.26	1.44	2.65	3.89	5.15
d_0 (nm)									
100	-	1.32	1.72	2.05	2.31	2.52	2.69	2.98	3.11
200	-	1.62	1.95	2.22	2.44	2.63	2.79	3.06	3.18
300	1.06	1.71	2.02	2.28	2.49	2.67	2.83	3.10	3.22
400	1.20	1.75	2.05	2.30	2.51	2.69	2.86	3.14	3.26
500	1.33	1.78	2.06	2.31	2.53	2.71	2.87	3.16	3.29
600	1.48	1.82	2.07	2.32	2.53	2.72	2.89	3.18	3.31
700	-	1.92	2.08	2.32	2.53	2.73	2.90	3.20	3.34
800	-	2.03	2.17	2.33	2.54	2.73	2.91	3.22	3.36
900	-	2.13	2.27	2.40	2.55	2.74	2.92	3.24	3.38
1000	-	2.22	2.37	2.50	2.62	2.76	2.93	3.25	3.40

Table A.15. Results of the outer wall downward gradient simulations for $T_a = -50^\circ\text{C}$

SS_w (%)	-7.60	-5.36	-3.11	-0.65	1.90	3.22	4.56
d_0 (nm)							
100	0.81	1.45	1.86	2.14	2.35	2.44	2.43
200	1.15	1.67	1.99	2.23	2.42	2.51	2.49
300	1.28	1.75	2.04	2.28	2.47	2.56	2.54
400	1.35	1.79	2.08	2.31	2.51	2.60	2.58
500	1.40	1.83	2.11	2.35	2.55	2.64	2.63
600	1.47	1.86	2.14	2.38	2.59	2.68	2.67
700	1.57	1.89	2.18	2.42	2.63	2.72	2.72
800	1.67	1.93	2.21	2.46	2.67	2.77	2.76
900	1.78	2.00	2.25	2.50	2.71	2.81	2.81
1000	1.90	2.11	2.30	2.55	2.76	2.86	2.87

Table A.16. Results of the outer wall downward gradient simulations for $T_a = -60^\circ\text{C}$

SS_w (%)	-12.91	-11.43	-9.01	-6.43	-3.73	-0.90	2.05	5.14
d_0 (nm)								
100	-	0.62	0.88	1.06	1.19	1.30	1.40	1.50
200	-	0.80	0.99	1.14	1.26	1.36	1.46	1.55
300	0.65	0.88	1.06	1.20	1.31	1.42	1.51	1.60
400	0.77	0.96	1.12	1.26	1.37	1.48	1.57	1.66
500	-	1.04	1.19	1.33	1.44	1.54	1.64	1.72
600	-	1.13	1.27	1.40	1.51	1.61	1.71	1.80
700	-	1.24	1.36	1.48	1.60	1.70	1.79	1.87
800	-	1.36	1.46	1.58	1.68	1.78	1.87	1.96
900	-	1.50	1.58	1.67	1.78	1.88	1.97	2.05
1000	-	-	1.70	1.78	1.88	1.98	2.06	2.15

A.4.2 Outer Wall Upward Gradient

The following distributions were generated for simulations in which a 2 K gradient was applied along the outer wall of the growth region with the lowest temperature at the bottom of the wall with the temperature increasing up along the wall.

Table A.17. Results of the outer wall upward gradient simulations for $T_a = -40^\circ\text{C}$

SS_w (%)	1.64	3.90	4.99
d_0 (nm)			
100	1.09	2.52	3.04
200	1.41	2.58	3.10
300	1.61	2.48	3.05
400	1.77	2.39	2.93
500	1.91	2.45	2.79
600	2.04	2.56	2.77
700	2.15	2.66	2.86
800	2.26	2.77	2.96
900	2.38	2.87	3.06
1000	2.51	2.97	3.16

Table A.18. Results of the outer wall upward gradient simulations for $T_a = -45^\circ\text{C}$

SS_w (%)	-0.89	0.26	1.44	2.65	3.89	5.15
d_0 (nm)						
100	-	2.30	2.56	2.72	2.98	3.10
200	2.09	2.45	2.65	2.80	3.06	3.17
300	2.11	2.48	2.68	2.84	3.10	3.22
400	-	2.44	2.68	2.86	3.14	3.25
500	1.36	2.32	2.66	2.86	3.16	3.28
600	1.52	2.08	2.60	2.85	3.17	3.31
700	1.66	1.90	2.48	2.81	3.18	3.33
800	1.80	2.01	2.31	2.73	3.18	3.34
900	1.95	2.12	2.31	2.61	3.16	3.34
1000	-	2.22	2.41	2.57	3.12	3.32

Table A.19. Results of the outer wall upward gradient simulations for $T_a = -50^\circ\text{C}$

d_0 (nm)	SS_w (%)				
	-3.11	-0.65	1.90	3.22	4.56
100	1.83	2.14	2.34	2.42	2.51
200	1.98	2.22	2.40	2.49	2.57
300	2.03	2.27	2.45	2.54	2.62
400	2.05	2.30	2.49	2.58	2.66
500	2.06	2.33	2.53	2.62	2.71
600	2.05	2.36	2.57	2.66	2.75
700	2.00	2.38	2.61	2.70	2.79
800	1.89	2.40	2.64	2.75	2.84
900	1.89	2.41	2.68	2.79	2.88
1000	1.99	2.40	2.71	2.83	2.93

Table A.20. Results of the outer wall upward gradient simulations for $T_a = -60^\circ\text{C}$

d_0 (nm)	SS_w (%)					
	-9.01	-6.43	-3.73	-0.90	2.05	5.14
100	-	1.03	1.17	1.25	1.34	1.43
200	0.88	1.11	1.24	1.31	1.40	1.49
300	0.94	1.17	1.29	1.36	1.46	1.54
400	0.95	1.22	1.35	1.42	1.52	1.60
500	0.91	1.28	1.42	1.49	1.58	1.67
600	-	1.34	1.49	1.57	1.66	1.75
700	-	1.39	1.56	1.65	1.74	1.83
800	-	1.44	1.64	1.73	1.83	1.91
900	-	1.55	1.72	1.82	1.92	2.01
1000	-	1.68	1.80	1.92	2.02	2.10

A.4.3 Inner Wall Downward Gradient

The following distributions were generated for simulations in which a 2 K gradient was applied along the inner wall of the growth region with the temperature increasing down along the wall.

Table A.21. Results of the inner wall downward gradient simulations for $T_a = -40^\circ\text{C}$

d_0 (nm)	SS_w (%)		
	-0.52	1.64	3.90
100	0.98	1.68	2.36
200	1.30	1.87	2.48
300	1.49	1.99	2.53
400	1.65	2.12	2.57
500	1.78	2.25	2.65
600	1.90	2.37	2.75
700	2.01	2.49	2.86
800	2.14	2.60	2.97
900	2.28	2.70	3.07
1000	-	2.80	3.17

Table A.22. Results of the inner wall downward gradient simulations for $T_a = -45^\circ\text{C}$

SS_w (%)	-4.24	-3.15	-2.03	-0.89	0.26	1.44	2.65	3.89	5.15
d_0 (nm)									
100	-	0.88	1.45	1.89	2.22	2.46	2.65	2.81	2.95
200	0.92	1.34	1.78	2.11	2.37	2.58	2.75	2.89	3.03
300	1.10	1.48	1.88	2.18	2.42	2.62	2.79	2.94	3.07
400	1.25	1.56	1.92	2.21	2.45	2.64	2.81	2.97	3.11
500	1.39	1.61	1.94	2.22	2.46	2.66	2.83	2.99	3.13
600	1.51	1.72	1.95	2.23	2.47	2.67	2.85	3.01	3.16
700	1.64	1.83	1.99	2.23	2.47	2.68	2.86	3.03	3.18
800	1.78	1.94	2.10	2.25	2.48	2.69	2.87	3.04	3.20
900	-	2.04	2.21	2.35	2.49	2.70	2.89	3.06	3.22
1000	-	2.14	2.31	2.45	2.58	2.72	2.91	3.08	3.24

Table A.23. Results of the inner wall downward gradient simulations for $T_a = -50^\circ\text{C}$

SS_w (%)	-5.36	-3.11	-0.65	1.90	3.22	4.56
d_0 (nm)						
100	0.83	1.57	1.97	2.22	2.33	2.43
200	1.24	1.77	2.08	2.31	2.40	2.50
300	1.38	1.84	2.14	2.36	2.45	2.54
400	1.46	1.89	2.18	2.40	2.49	2.59
500	1.51	1.92	2.21	2.43	2.53	2.63
600	1.56	1.95	2.24	2.47	2.57	2.67
700	1.63	1.99	2.27	2.51	2.61	2.71
800	1.73	2.02	2.31	2.55	2.66	2.76
900	1.83	2.07	2.36	2.59	2.70	2.80
1000	1.94	2.14	2.40	2.64	2.75	2.85

Table A.24. Results of the inner wall downward gradient simulations for $T_a = -60^\circ\text{C}$

d_0 (nm)	SS_w (%)					
	-9.01	-6.43	-3.73	-0.90	2.05	5.14
100	0.93	1.12	1.23	1.33	1.42	1.51
200	1.05	1.19	1.29	1.39	1.48	1.56
300	1.10	1.24	1.35	1.44	1.53	1.62
400	1.15	1.30	1.41	1.50	1.59	1.68
500	1.19	1.36	1.47	1.57	1.66	1.74
600	1.22	1.42	1.54	1.64	1.73	1.81
700	1.27	1.50	1.62	1.72	1.81	1.89
800	1.38	1.56	1.70	1.81	1.90	1.98
900	1.51	1.63	1.79	1.90	1.99	2.07
1000	1.65	1.74	1.87	1.99	2.08	2.17

A.4.4 Inner Wall Upward Gradient

The following distributions were generated for simulations in which a 2 K gradient was applied along the inner wall of the growth region with the temperature increasing up along the wall.

Table A.25. Results of the inner wall upward gradient simulations for $T_a = -40^\circ\text{C}$

d_0 (nm)	SS_w (%)		
	-0.52	1.64	3.90
100	-	1.97	2.85
200	1.13	2.01	2.88
300	1.36	2.01	2.77
400	1.54	2.14	2.66
500	1.69	2.27	2.71
600	1.84	2.38	2.81
700	1.98	2.49	2.91
800	2.14	2.59	3.01
900	-	2.68	3.10
1000	-	2.77	3.20

Table A.26. Results of the inner wall upward gradient simulations for $T_a = -45^\circ\text{C}$

d_0 (nm)	SS_w (%)						
	-2.03	-0.89	0.26	1.44	2.65	3.89	5.15
100	-	2.35	2.58	2.74	2.88	3.11	3.21
200	2.19	2.49	2.68	2.82	2.95	3.18	3.28
300	2.20	2.51	2.71	2.86	2.99	3.22	3.33
400	1.85	2.49	2.71	2.88	3.02	3.26	3.37
500	1.50	2.41	2.70	2.88	3.04	3.29	3.41
600	1.63	2.22	2.65	2.87	3.04	3.31	3.44
700	1.75	1.99	2.53	2.83	3.03	3.33	3.46
800	1.87	2.07	2.36	2.74	2.99	3.34	3.48
900	1.99	2.18	2.35	2.61	2.92	3.33	3.48
1000	2.12	2.28	2.45	2.59	2.83	3.30	3.48

Table A.27. Results of the inner wall upward gradient simulations for $T_a = -50^\circ\text{C}$

d_0 (nm)	SS_w (%)	-5.36	-3.11	-0.65	1.90	3.22	4.56
100	-	2.03	2.25	2.43	2.51	2.59	
200	1.84	2.13	2.32	2.49	2.57	2.65	
300	1.90	2.17	2.37	2.54	2.62	2.70	
400	1.90	2.20	2.41	2.58	2.66	2.74	
500	1.82	2.22	2.44	2.62	2.70	2.78	
600	1.64	2.24	2.48	2.66	2.75	2.83	
700	1.58	2.24	2.50	2.70	2.79	2.88	
800	1.69	2.23	2.53	2.74	2.84	2.92	
900	1.80	2.19	2.56	2.78	2.88	2.97	
1000	1.92	2.16	2.57	2.82	2.92	3.02	

Table A.28. Results of the inner wall upward gradient simulations for $T_a = -60^\circ\text{C}$

d_0 (nm)	SS_w (%)	-9.01	-6.43	-3.73	-0.90	2.05	5.14
100	0.93	1.12	1.23	1.33	1.42	1.51	
200	1.05	1.19	1.29	1.39	1.48	1.56	
300	1.10	1.24	1.35	1.44	1.53	1.62	
400	1.15	1.30	1.41	1.50	1.59	1.68	
500	1.19	1.36	1.47	1.57	1.66	1.74	
600	1.22	1.42	1.54	1.64	1.73	1.81	
700	1.27	1.50	1.62	1.72	1.81	1.89	
800	1.38	1.56	1.70	1.81	1.90	1.98	
900	1.51	1.63	1.79	1.90	1.99	2.07	
1000	1.65	1.74	1.87	1.99	2.08	2.17	

A.4.5 Oscillating Growth Region Temperatures

The following distributions were generated in simulations for which the temperature oscillated along the length of both walls, the oscillation being 2 K with a period equal to the twice the distance between the refrigeration coils.

Table A.29. Results of the oscillating temperature profile simulations for $T_a = -40^\circ\text{C}$

SS_w (%)	-0.52	1.64	3.90	4.99
d_0 (nm)				
100	0.89	1.69	2.29	2.53
200	1.22	1.90	2.42	2.65
300	1.44	2.06	2.55	2.76
400	1.62	2.20	2.67	2.86
500	1.78	2.34	2.78	2.97
600	1.93	2.46	2.89	3.07
700	2.08	2.57	3.00	3.17
800	2.25	2.68	3.10	3.27
900	-	2.78	3.21	3.37
1000	-	2.87	3.31	3.47

Table A.30. Results of the oscillating temperature profile simulations for $T_a = -45^\circ\text{C}$

SS_w (%)	-4.24	-3.15	-2.03	-0.89	0.26	1.44	2.65	3.89	5.15
d_0 (nm)									
100	-	-	1.26	2.27	2.60	2.79	2.97	3.10	3.23
200	-	1.03	2.02	2.44	2.70	2.88	3.04	3.18	3.30
300	-	1.27	2.06	2.48	2.72	2.91	3.07	3.21	3.35
400	1.20	1.44	2.01	2.45	2.72	2.92	3.09	3.24	3.37
500	1.35	1.58	1.94	2.39	2.69	2.92	3.10	3.25	3.40
600	1.50	1.71	1.92	2.31	2.64	2.89	3.09	3.26	3.41
700	1.65	1.83	2.03	2.25	2.58	2.85	3.08	3.26	3.42
800	-	1.94	2.14	2.31	2.53	2.80	3.05	3.25	3.42
900	-	2.07	2.25	2.41	2.56	2.77	3.01	3.23	3.41
1000	-	2.20	2.35	2.52	2.66	2.80	2.99	3.20	3.40

Table A.31. Results of the oscillating temperature profile simulations for $T_a = -50^\circ\text{C}$

SS_w (%)	-5.36	-3.11	-0.65	1.90	3.22	4.56
d_0 (nm)						
100	-	1.85	2.24	2.45	2.55	2.66
200	1.03	2.05	2.33	2.53	2.62	2.72
300	1.41	2.10	2.37	2.58	2.67	2.76
400	1.49	2.13	2.41	2.62	2.72	2.81
500	1.50	2.14	2.43	2.66	2.75	2.85
600	1.53	2.15	2.46	2.69	2.79	2.89
700	1.64	2.15	2.48	2.72	2.83	2.93
800	1.75	2.14	2.50	2.76	2.87	2.97
900	1.85	2.14	2.52	2.79	2.90	3.01
1000	1.97	2.20	2.54	2.82	2.94	3.05

Table A.32. Results of the oscillating temperature profile simulations for $T_a = -60^\circ\text{C}$

SS_w (%)	-9.01	-6.43	-3.73	-0.90	2.05	5.14
d_0 (nm)						
100	0.63	1.09	1.25	1.38	1.48	1.59
200	0.97	1.19	1.33	1.44	1.54	1.64
300	1.05	1.24	1.38	1.49	1.60	1.69
400	1.09	1.30	1.43	1.55	1.65	1.75
500	1.14	1.35	1.50	1.61	1.71	1.81
600	1.20	1.42	1.56	1.68	1.78	1.88
700	1.29	1.48	1.63	1.75	1.85	1.95
800	1.41	1.56	1.71	1.83	1.94	2.03
900	1.53	1.64	1.79	1.92	2.02	2.12
1000	1.67	1.76	1.88	2.01	2.11	2.21

Appendix B: HTDMA Data

Tabulated values of the data returned from the HTDMA. Given in each of the tables are the measured RH_w (the uncertainty in which is $\pm 2\%$), the calculated gf (uncertainty in which is ± 0.02), the derived κ , and the calculated a_w .

Table B.1. Measured HTDMA data for particles having a 100 nm mobility diameter.

	t	RH_w (%)	gf	κ	a_w
30-Jun	11:11:04	19.21	1.00	0.03	0.19
	12:03:52	41.91	1.02	0.07	0.41
	12:24:16	51.93	1.03	0.09	0.51
	12:40:16	61.50	1.04	0.09	0.60
	13:11:28	80.55	1.15	0.14	0.79
	13:26:16	85.52	1.17	0.12	0.83
	13:41:16	90.01	1.25	0.13	0.88
	14:40:54	33.87	1.01	0.09	0.33
	15:13:28	50.87	1.03	0.09	0.50
3-Jul	11:30:50	19.55	1.01	0.08	0.19
	15:23:26	43.13	1.03	0.14	0.42
	15:47:36	52.33	1.04	0.13	0.51
	16:05:28	62.34	1.07	0.15	0.61
	16:22:52	72.32	1.11	0.16	0.71
	16:40:04	82.17	1.18	0.16	0.80
9-Jul	14:47:57	20.74	1.00	-	-
	15:11:21	41.44	1.02	0.10	0.41
	15:30:09	51.75	1.04	0.12	0.51
	15:47:57	61.79	1.06	0.12	0.60

t	RH_w (%)	gf	κ	a_w
16:05:09	72.08	1.11	0.15	0.70
16:22:21	82.13	1.21	0.19	0.80
16:38:57	87.05	1.29	0.21	0.85
16:54:21	90.40	1.37	0.22	0.88
17:09:21	92.22	1.48	0.26	0.89
17:24:08	92.23	1.48	0.27	0.89

Table B.2 Measured HTDMA data for particles having a 300 nm (30 June) or 250 nm mobility diameter.

	t	RH_w (%)	gf	κ	a_w
30-Jun	11:17:30	18.94	0.99	0.03	-
	12:13:28	41.87	1.01	0.03	0.42
	12:30:54	51.99	1.01	0.03	0.52
	12:46:54	61.46	1.02	0.05	0.61
	13:02:30	70.93	1.06	0.07	0.70
	13:18:06	80.48	1.11	0.10	0.80
	13:32:54	85.44	1.17	0.11	0.85
	13:47:54	89.98	1.22	0.10	0.89
	14:01:12	91.77	1.27	0.11	0.91
3-Jul	11:38:07	19.55	1.00	0.01	-
	15:37:30	43.01	1.03	0.11	0.43
	15:55:06	52.50	1.06	0.18	0.52
	16:12:58	62.41	1.08	0.16	0.62
	16:30:22	72.31	1.17	0.24	0.72
	16:47:34	82.17	1.28	0.26	0.81
9-Jul	14:55:14	20.68	0.99	0.02	-
	15:18:51	41.68	1.01	0.04	0.41
	15:37:39	51.82	1.03	0.08	0.51
	15:55:27	62.14	1.05	0.10	0.62
	16:12:39	72.18	1.09	0.11	0.72
	16:29:51	82.20	1.18	0.14	0.81
	16:46:27	87.15	1.26	0.16	0.86
	17:01:51	90.31	1.37	0.19	0.89
	17:16:51	92.22	1.48	0.22	0.91
17:31:25	91.90	1.45	0.21	0.91	

Appendix C: CCN Data

C.1 Tabulated CCN Data

Below are given the values (both direct and inferred) of the CCN measurements. ΔT is the temperature gradient used to generate the supersaturation, s_{crit} is the critical supersaturation derived from the ammonium sulfate calibrations, D_{50} is the critical diameter and κ and β represent the CCN derived hygroscopicity and heterogeneity parameters. All calculations were performed as described in Chapter 3.3.2.1. The red entries represent the ammonium sulfate calibrations. Only those measurements which coincided with CFDC measurements of homogeneous freezing are shown below.

Table C.1. CCNc measurements from 30 June.

Time	ΔT	s_{crit}	D_{50}	κ	B
13:34:00	10.57	0.56	0.041	0.632	0.094
13:50:00	12.66	0.67	0.057	0.163	0.251
14:06:00	5.71	0.31	0.103	0.128	0.303
14:22:00	8.49	0.45	0.075	0.156	0.213
14:38:00	10.57	0.56	0.065	0.157	0.205
14:54:00	12.66	0.67	0.059	0.147	0.224
15:26:00	5.71	0.31	0.093	0.175	0.205
15:42:00	8.49	0.45	0.074	0.162	0.251
15:58:00	10.57	0.56	0.065	0.157	0.199
16:14:00	12.66	0.67	0.114	0.018	1.113
16:30:00	5.71	0.31	0.099	0.145	0.265

Table C.2. CCNc measurements from 1 July.

Time	ΔT	s_{crit}	D_{50}	κ	β
15:10	10.57	0.69	0.036	0.624	0.077
15:26	12.66	0.82	0.33	0	1.919
15:42	5.71	0.38	0.084	0.162	0.218
15:58	8.49	0.55	0.064	0.169	0.326
16:14	10.57	0.69	0.056	0.163	0.212

Table C.3. CCNc measurements from 3 July.

Time	ΔT	s_{crit}	D_{50}	κ	β
11:45	8.49	0.55	0.043	0.577	0.118
12:01	10.57	0.69	0.083	0.048	0.488
12:17	12.66	0.83	0.075	0.044	0.554
12:33	5.71	0.36	0.098	0.111	0.314
12:49	8.49	0.55	0.082	0.081	0.333
13:05	10.57	0.69	0.067	0.094	0.358
13:21	10.57	0.69	0.037	0.574	0.098
13:37	12.66	0.83	0.067	0.063	0.425
13:53	5.71	0.36	0.11	0.078	0.35
14:09	8.49	0.55	0.076	0.102	0.281
14:25	10.57	0.69	0.071	0.078	0.336
14:41	12.66	0.83	0.062	0.081	0.32
14:57	12.66	0.83	0.032	0.611	0.103
15:13	5.71	0.36	0.091	0.14	0.227
15:29	8.49	0.55	0.074	0.111	0.303
15:45	10.57	0.69	0.062	0.119	0.216
16:01	12.66	0.83	0.056	0.111	0.277
16:17	5.71	0.36	0.084	0.178	0.163
16:33	5.71	0.36	0.056	0.605	0.089
16:49	8.49	0.55	0.069	0.138	0.293

Table C.4. CCNc measurements from 9 July.

Time	ΔT	s_{crit}	D_{50}	κ	β
14:25	10.57	0.65	0.057	0.172	0.095
14:41	12.66	0.77	0.051	0.173	0.096
14:57	5.71	0.38	0.086	0.146	0.136
15:13	8.49	0.54	0.064	0.18	0.109
15:29	10.57	0.65	0.056	0.182	0.092
15:45	10.57	0.65	0.038	0.589	0.105
16:01	12.66	0.77	0.048	0.208	0.107
16:17	5.71	0.38	0.084	0.157	0.125
16:33	8.49	0.54	0.065	0.172	0.094
16:49	10.57	0.65	0.056	0.182	0.112
17:05	12.66	0.77	0.049	0.196	0.103

C.2 CCN Activation Curves

The CCN activation curves are shown below where the ordinate represents the fraction nucleating (as represented by the dots) or the fraction of the population of particles having the diameter plotted on the abscissa. In each case, a sigmoidal curve is fitted to the measured CCN activation fraction. The plots with the fitted curve and the measured activated fraction in red represent the ammonium sulfate calibration points.

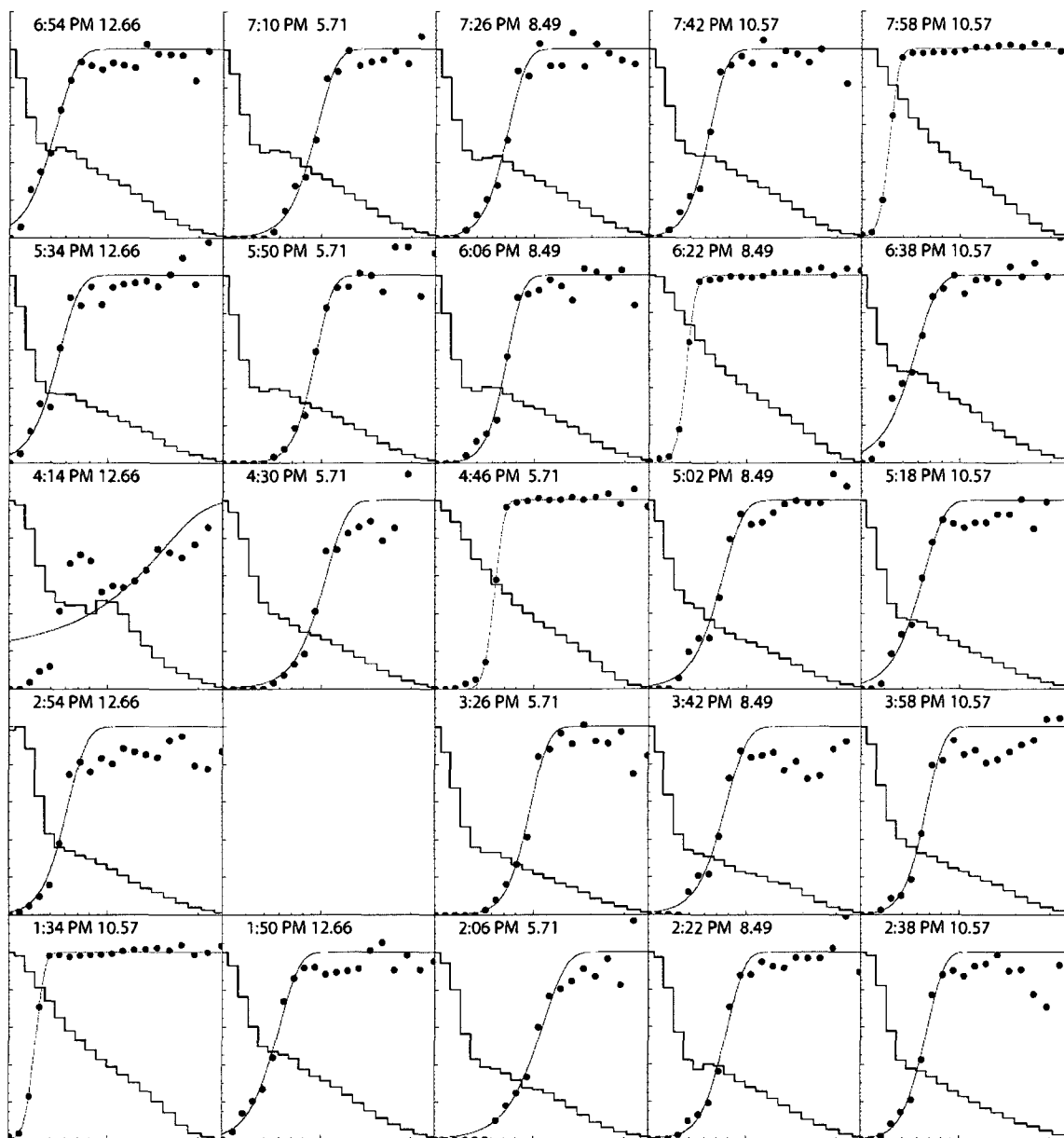


Figure C.1. CCN activation curves and size distributions of particles less than 400 nm measured by the CCNc's in-rack SMPS from 30 June 2008. The time of collection and the temperature gradient are given in the upper left hand corner of each plot.

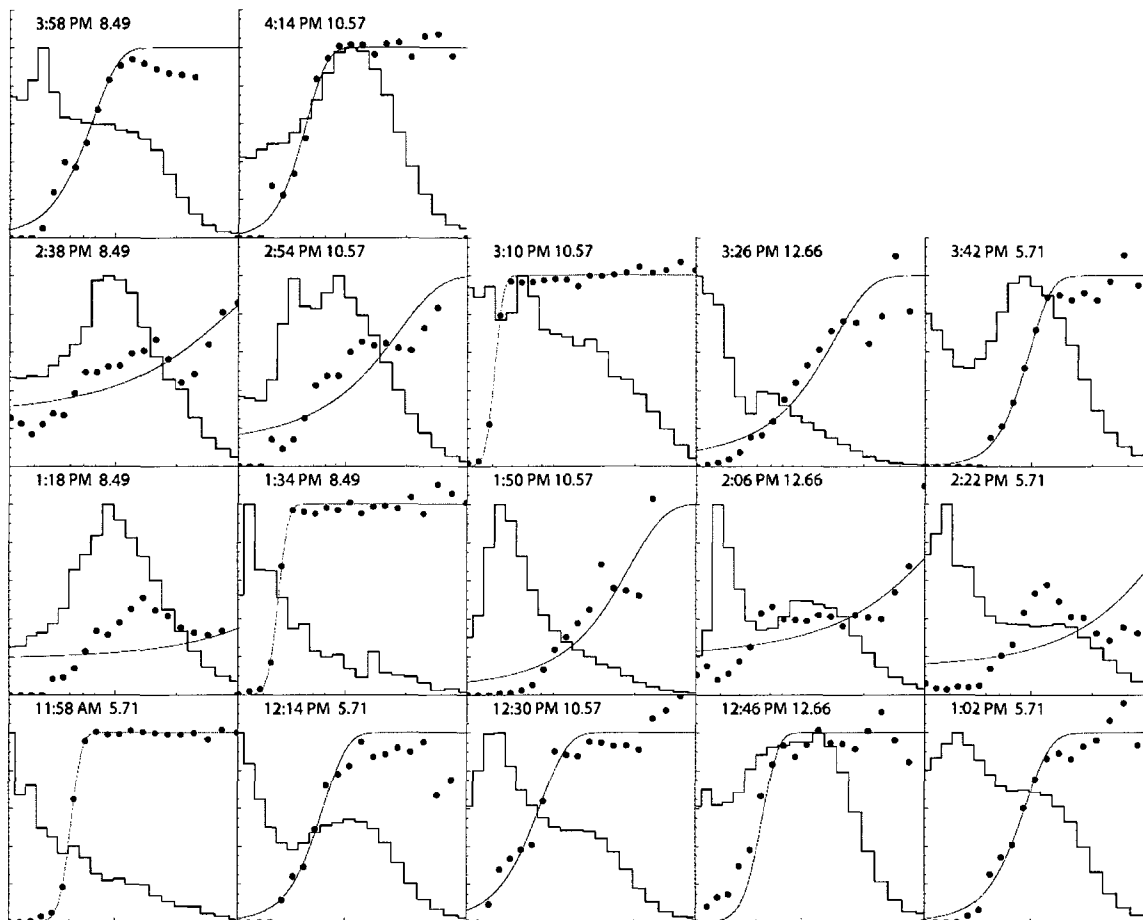


Figure C.2. CCN activation curves for 1 July 2008.

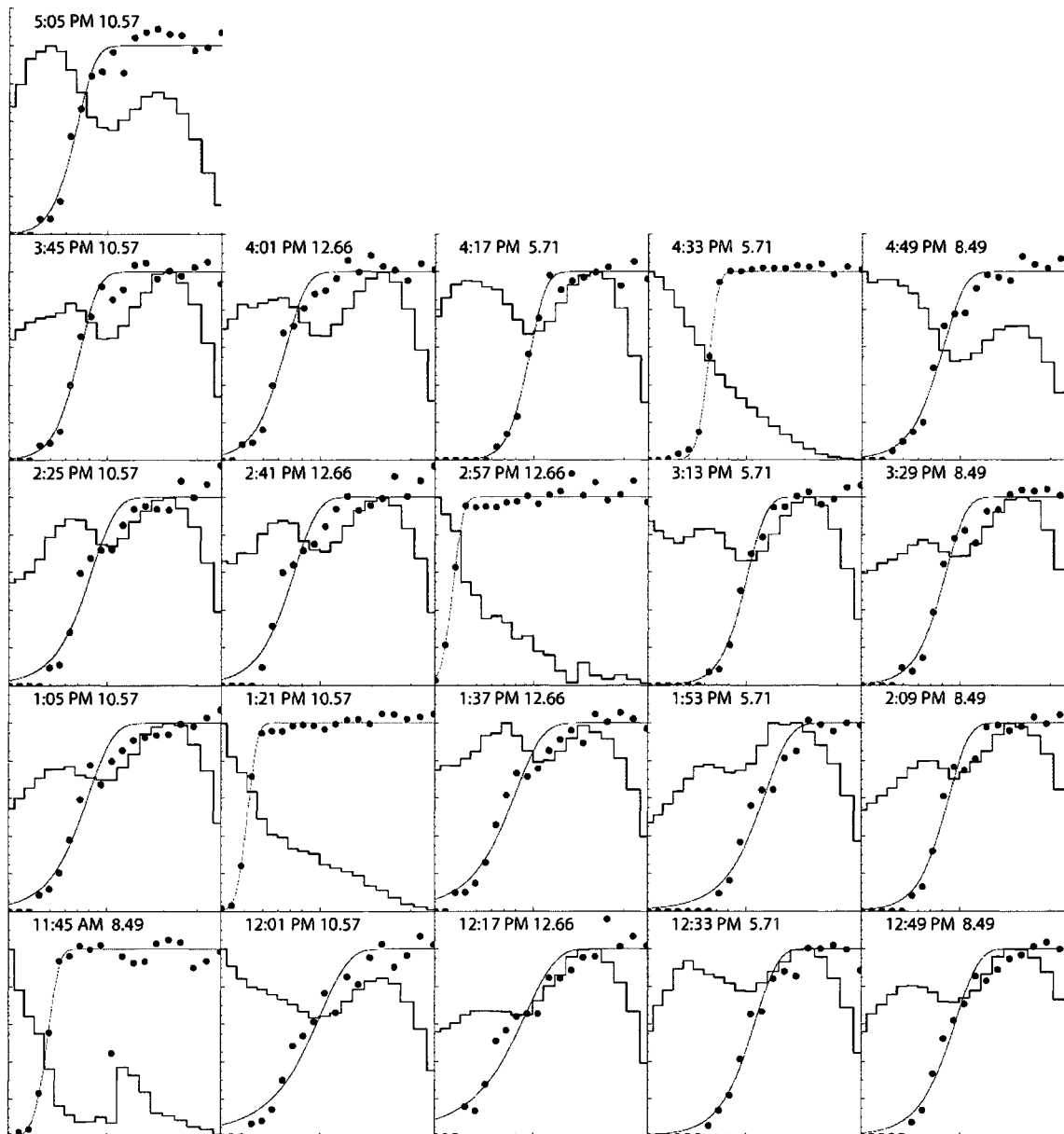


Figure C.3. CCN activation curves for 3 July 2008.

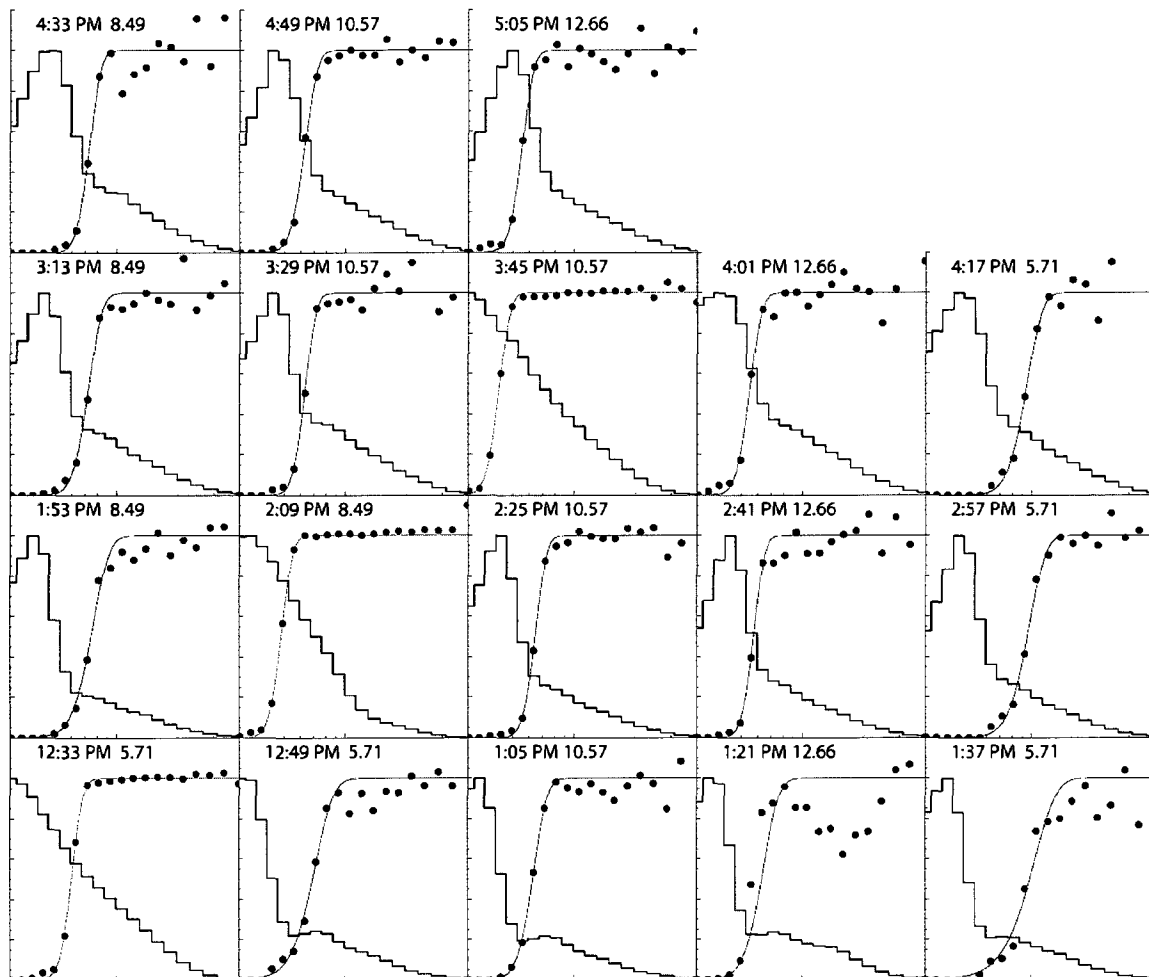


Figure C.4. CCN activation curves for 9 July 2008.

REFERENCES

- Abbatt, J. P. D., S. Benz, D. J. Cziczo, Z. Kanji, U. Lohmann, and O. Mohler (2006), Solid ammonium sulfate aerosols as ice nuclei: A pathway for cirrus cloud formation, *Science*, *313*(5794), 1770-1773.
- Aklilu, Y., M. Mozurkewich, A. J. Prenni, S. M. Kreidenweis, M. R. Alfarra, J. D. Allan, K. Anlauf, J. Brook, W. R. Leitch, S. Sharma, H. Boudries, and D. R. Worsnop (2006), Hygroscopicity of particles at two rural, urban influenced sites during Pacific 2001: Comparison with estimates of water uptake from particle composition, *Atmos. Environ.*, *40*(15), 2650-2661, doi: 10.1016/j.atmosenv.2005.11.063.
- Anderson Jr., J. D. (1995), *Computational Fluid Dynamics: The Basics with Applications*, McGraw-Hill, Inc., New York.
- Andreae, M. O., and D. Rosenfeld (2008), Aerosol-cloud-precipitation interactions. Part 1. The nature and sources of cloud-active aerosols, *Earth-Science Reviews*, *89*(1-2), 13-41, doi: 10.1016/j.earscirev.2008.03.001.
- Archuleta, C. M., P. J. DeMott, and S. M. Kreidenweis (2005), Ice nucleation by surrogates for atmospheric mineral dust and mineral dust/sulfate particles at cirrus temperatures, *Atmos. Chem. Phys.*, *5*, 2617-2634.
- Bahreini, R., E. J. Dunlea, B. M. Matthew, C. Simons, K. S. Docherty, P. F. DeCarlo, J. L. Jimenez, C. A. Brock, and A. M. Middlebrook (2008), Design and operation of a pressure-controlled inlet for airborne sampling with an aerodynamic aerosol lens, *Aerosol Sci. Technol.*, *42*(6), 465-471, doi: 10.1080/02786820802178514.
- Bartell, L. S. (1997), On possible interpretations of the anomalous properties of supercooled water, *J. Phys. Chem. B*, *101*(38), 7573-7583, doi: 10.1021/jp971411d.
- Batchelor, G. K. (1967), *An Introduction to Fluid Dynamics*, 615 pp., Cambridge University Press, London.

- Berglund, R. N., and B. Y. H. Liu (1973), Generation of monodisperse aerosol standards, *Environ. Sci. Technol.*, *7*(2), 147-153, doi: 10.1021/es60074a001.
- Bertram, A. K., T. Koop, L. T. Molina, and M. J. Molina (2000), Ice formation in $(\text{NH}_4)_2\text{SO}_4\text{-H}_2\text{O}$ particles, *J. Phys. Chem. A*, *104*(3), 584-588, doi: 10.1021/jp9931197.
- Borys, R. D., and M. A. Wetzel (1997), Storm Peak Laboratory: A research, teaching, and service facility for the atmospheric sciences, *Bull. Amer. Meteor. Soc.*, *78*(10), 2115-2123, doi: 10.1175/1520-0477(1997)078<2115:SPLART>2.0.CO;2.
- Boulama, K., and N. Galanis (2004), Analytical solution for fully developed mixed convection between parallel vertical plates with heat and mass transfer, *Journal of Heat Transfer*, *126*(3), 381-388, doi: 10.1115/1.1737774.
- Braban, C. F., J. P. D. Abbatt, and D. J. Cziczo (2001), Deliquescence of ammonium sulfate particles at sub-eutectic temperatures, *Geophys. Res. Lett.*, *28*(20), 3879-3882.
- Brechtel, F. J., and S. M. Kreidenweis (2000), Predicting particle critical supersaturation from hygroscopic growth measurements in the humidified TDMA. part I: Theory and sensitivity studies, *J. Atmos. Sci.*, *57*(12), 1854-1871, doi: 10.1175/1520-0469(2000)057<1854:PPCSFH>2.0.CO;2.
- Brown, D. E., S. M. George, C. Huang, E. K. L. Wong, K. B. Rider, R. S. Smith, and B. D. Kay (1996), H_2O condensation coefficient and refractive index for vapor-deposited ice from molecular beam and optical interference measurements, *J. Phys. Chem. A*, *100*, 4988-1995.
- Buck, A. L. (1981), New equations for computing vapor-pressure and enhancement factor, *J. Appl. Meteor.*, *20*(12), 1527-1532, doi: 10.1175/1520-0450(1981)020<1527:NEFCVP>2.0.CO;2.
- Carrico, C. M., M. D. Petters, S. M. Kreidenweis, J. L. Collett, Jr., G. Engling, and W. C. Malm (2008), Aerosol hygroscopicity and cloud droplet activation of extracts of filters from biomass burning experiments, *J. Geophys. Res.*, *113*(D8), D08206, doi: 10.1029/2007JD009274.
- Chen, Y. L., P. J. DeMott, S. M. Kreidenweis, D. C. Rogers, and D. E. Sherman (2000), Ice formation by sulfate and sulfuric acid aerosol particles under upper-tropospheric conditions, *J. Atmos. Sci.*, *57*(22), 3752-3766, doi: 10.1175/1520-0469(2000)057<3752:IFBSAS>2.0.CO;2.
- Chuang, P. Y., R. J. Charlson, and J. H. Seinfeld (1997), Kinetic limitations on droplet formation in clouds, *Nature*, *390*, 594-596.
- Clegg, S. L., P. Brimblecombe, and A. S. Wexler (1998), Thermodynamic model of the system $\text{H}^+\text{-NH}_4^+\text{-SO}_4^{2-}\text{-NO}_3^-\text{-H}_2\text{O}$ at tropospheric temperatures, *J. Phys. Chem. A*, *102*, 2137-2154.

- Cziczo, D. J., and J. P. D. Abbatt (1999), Deliquescence, efflorescence, and supercooling of ammonium sulfate aerosols at low temperature: Implications for cirrus cloud formation and aerosol phase in the atmosphere, *J. Geophys. Res. Atmos.*, *104*(D11), 13781-13790.
- Cziczo, D. J., P. J. DeMott, C. Brock, P. K. Hudson, B. Jesse, S. M. Kreidenweis, A. J. Prenni, J. Schreiner, D. S. Thomson, and D. M. Murphy (2003), A method for single particle mass spectrometry of ice nuclei, *Aerosol Sci. Technol.*, *37*(5), 460-470, doi: 10.1080/02786820390112687.
- Cziczo, D. J., P. J. DeMott, S. D. Brooks, A. J. Prenni, D. S. Thomson, D. Baumgardner, J. C. Wilson, S. M. Kreidenweis, and D. M. Murphy (2004a), Observations of organic species and atmospheric ice formation, *Geophys. Res. Lett.*, *31*(12).
- Cziczo, D. J., D. M. Murphy, P. K. Hudson, and D. S. Thomson (2004b), Single particle measurements of the chemical composition of cirrus ice residue during CRYSTAL-FACE, *J. Geophys. Res.*, *109*, D04201, doi: 10.1029/2003JD004032.
- Davidovits, P., C. E. Kolb, L. R. Williams, J. T. Jayne, and D. R. Worsnop (2006), Mass accommodation and chemical reactions at gas-liquid interfaces, *Chem. Rev.*, *106*(4), 1323-1354, doi: 10.1021/cr040366k.
- DeMott, P. J., M. P. Meyers, and W. R. Cotton (1994), Parameterization and impact of ice initiation processes relevant to numerical-model simulations of cirrus clouds, *J. Atmos. Sci.*, *51*(1), 77-90, doi: 10.1175/1520-0469(1994)051<0077:PAIOII>2.0.CO;2.
- DeMott, P. J., D. C. Rogers, and S. M. Kreidenweis (1997), The susceptibility of ice formation in upper tropospheric clouds to insoluble aerosol components, *J. Geophys. Res.-Atmos.*, *102*(D16), 19575-19584.
- DeMott, P. J., S. M. Kreidenweis, and D. C. Rogers (2001), Airborne measurements of tropospheric ice-nucleating aerosol particles in the Arctic spring, *J. Geophys. Res.*, *106*(D14), 15045, doi: 10.1029/2000JD900790.
- DeMott, P. J. (2002), Laboratory Studies of Cirrus Cloud Processes, in *Cirrus*, edited by D. K. Lynch, et al., New York.
- DeMott, P. J., D. J. Cziczo, A. J. Prenni, D. M. Murphy, S. M. Kreidenweis, D. S. Thomson, R. Borys, and D. C. Rogers (2003), Measurements of the concentration and composition of nuclei for cirrus formation, *Proc. Natl. Acad. Sci.*, *100*(25), 14655-14660, doi: 10.1073/pnas.2532677100.
- Dick, W. D., P. Saxena, and P. H. McMurry (2000), Estimation of water uptake by organic compounds in submicron aerosols measured during the Southeastern Aerosol and Visibility Study, *J. Geophys. Res.-Atmos.*, *105*(D1), 1471-1479.

- Doser, D. I., K. D. Crain, M. R. Baker, V. Kreinovich, and M. C. Gerstenberger (1998), Estimating uncertainties for geophysical tomography, *Reliable Computing*, *4*, 241-268.
- Finlayson-Pitts, B. J., and J. N. Pitts, Jr. (1999), *Chemistry of the Upper and Lower Atmosphere: Theory, Experiments and Applications*, New York.
- FLUENT, Inc. (2003), *FLUENT 6.3 User's Guide*, Lebanon, NH.
- Fortin, T. J., J. E. Shilling, and M. A. Tolbert (2002), Infrared spectroscopic study of the low-temperature phase behavior of ammonium sulfate, *J. Geophys. Res.-Atmos.*, *107*(D10), doi: 10.1029/2001jd000677.
- Fukuta, N., and L. A. Walter (1970), Kinetics of hydrometeor growth from a vapor-spherical model, *J. Atmos. Sci.*, *27*(8), 1160, doi: 10.1175/1520-0469(1970)027<1160:KOHGFA>2.0.CO;2.
- Fukuta, N., and M. N. Myers (2007), Simultaneous measurement of condensation and thermal accommodation coefficients for cloud droplet growth in due consideration of a new moving surface-boundary effect, *J. Atmos. Sci.*, *64*, 955-968, doi: 10.1175/JAS3834.1.
- Gershenson, M., P. Davidovits, L. R. Williams, Q. A. Shi, J. T. Jayne, C. E. Kolb, and D. R. Worsnop (2004), Uptake of (H₂O)-O-17(g) and D₂O(g) by aqueous sulfuric acid droplets, *J. Phys. Chem. A*, *108*(9), 1567-1573, doi: 10.1021/jp0364021.
- Gierens, K. (2003), On the transition between heterogeneous and homogeneous freezing, *Atmos. Chem. Phys.*, *3*, 437-446.
- Gierens, K. M., M. Monier, and J. F. Gayet (2003), The deposition coefficient and its role for cirrus clouds, *J. Geophys. Res.-Atmos.*, *108*(D2), 4069-4073, doi: 10.1029/2001jd001558.
- Goff, J. A., and S. Gratch (1946), Low-pressure properties of water from -160 to 212 °F, paper presented at 52nd Annual Meeting of the American Society of Heating and Ventilating Engineers, New York.
- Gunn, R. (1956), The ratio of the positive and negative light ion conductivities within a neutral aerosol space, *Journal of Colloid Science*, *11*(6), 661-696.
- Gysel, M., J. Crosier, D. O. Topping, J. D. Whitehead, K. N. Bower, M. J. Cubison, P. I. Williams, M. J. Flynn, G. B. McFiggans, and H. Coe (2007), Closure study between chemical composition and hygroscopic growth of aerosol particles during TORCH2, *Atmos. Chem. Phys.*, *7*, 6131-6144.
- Haag, W., B. Kärcher, J. Ström, A. Minikin, U. Lohmann, J. Ovarlez, and A. Stohl (2003), Freezing thresholds and cirrus cloud formation mechanisms inferred from in situ measurements of relative humidity, *Atmos. Chem. Phys.*, *3*, 1791-1806.

- Hagen, D. E., R. J. Anderson, and J. L. Kassner (1981), Homogeneous condensation - freezing nucleation rate measurements for small water droplets in an expansion cloud chamber, *J. Atmos. Sci.*, *38*(6), 1236-1243, doi: 10.1175/1520-0469(1981)038<1236:HCNRMF>2.0.CO;2.
- Hall, W. D., and H. R. Pruppacher (1976), Survival of ice particles falling from cirrus clouds in subsaturated air, *J. Atmos. Sci.*, *33*(10), 1995-2006.
- Hartmann, D. L. (1994), *Global Physical Climatology*, Academic Press, San Diego.
- Haynes, D. R., N. J. Tro, and S. M. George (1992), Condensation and evaporation of H₂O on ice surfaces, *J. Phys. Chem.*, *96*(21), 8502-8509.
- Hinds, W. C. (1999), *Aerosol Technology: Properties, Behavior, and Measurement of Airborne Particles*, New York.
- Hung, H.-M., and S. T. Martin (2001), Apparent freezing temperatures modeled for several experimental apparatus, *J. Geophys. Res.*, *106*(D17), 20739-20394.
- Jakubczyk, D., M. Zientara, K. Kolwas, and M. Kolwas (2007), Temperature dependence of evaporation coefficient for water measured in droplets in nitrogen under atmospheric pressure, *J. Atmos. Sci.*, *64*(3), 996-1004, doi: 10.1175/JAS3860.1.
- Jensen, E. J., J. B. Smith, L. Pfister, J. V. Pittman, E. M. Weinstock, D. S. Sayres, R. L. Herman, R. F. Troy, K. Rosenlof, T. L. Thompson, A. M. Fridlind, P. K. Hudson, D. J. Cziczo, A. J. Heymsfield, C. Schmitt, and J. C. Wilson (2005), Ice supersaturations exceeding 100% at the cold tropical tropopause: Implications for cirrus formation and dehydration, *Atmos. Chem. Phys.*, *5*, 851-862.
- Kärcher, B., and J. Stöm (2003), The roles of dynamical variability and aerosols in cirrus cloud formation, *Atmos. Chem. Phys.*, *3*, 823-838.
- Kärcher, B. (2004), Cirrus clouds in the tropical tropopause layer: Role of heterogeneous ice nuclei, *Geophys. Res. Lett.*, *31*, L12101, doi: 10.1029/2004GL019774.
- Kay, J. E., and R. Wood (2008), Timescale analysis of aerosol sensitivity during homogeneous freezing and implications for upper tropospheric water vapor budgets, *Geophys. Res. Lett.*, *35*(L10809), doi: 10.1029/2007GL032628.
- Kaye, P. H., E. Hirst, R. S. Greenaway, Z. Ulanowski, E. Hesse, P. J. DeMott, C. Saunders, and P. Connolly (2008), Classifying atmospheric ice crystals by spatial light scattering, *Optics Letters*, *33*(13), 1545-1547, doi: 10.1364/OL.33.001545.
- Khalizov, A. F., M. E. Earle, W. J. W. Johnson, G. D. Stublely, and J. J. Sloan (2006a), Development and characterization of a laminar aerosol flow tube, *Rev. Sci. Instr.*, *77*(3), doi: 10.1063/1.2175958.

- Khalizov, A. F., M. E. Earle, W. J. W. Johnson, G. D. Stubbley, and J. J. Sloan (2006b), Modeling of flow dynamics in laminar aerosol flow tubes, *J. Aerosol. Sci.*, *37*(10), 1174-1187, doi: 10.1016/j.jaerosci.2005.11.008
- Khvorostyanov, V. I., and J. A. Curry (2004), Thermodynamic theory of freezing and melting of water and aqueous solutions, *J. Phys. Chem. A*, *108*(50), 11073-11085, doi: 10.1021/jp048099+.
- Knutson, E. O., and K. T. Whitby (1975), Aerosol classification by electric mobility: Apparatus, theory and applications, *J. Aerosol. Sci.*, *6*, 443-451.
- Koop, T., B. Luo, A. Tsias, and T. Peter (2000), Water activity as the determinant for homogeneous ice nucleation in aqueous solutions, *Nature*, *406*(10), 611-614, doi: 10.1038/35020537.
- Kreidenweis, S. M., Y. Chen, D. C. Rogers, and P. J. DeMott (1998), Isolating and identifying atmospheric ice-nucleating aerosols: a new technique, *Atmos. Res.*, *46*(3-4), 263-278.
- Kristovich, D. A. R., G. S. Young, J. Verlinde, P. J. Sousounis, P. Mourad, D. Lenschow, R. M. Rauber, M. K. Ramamurthy, B. F. Jewett, K. Beard, E. Cutrim, P. J. DeMott, E. W. Eloranta, M. R. Hjelmfelt, S. M. Kreidenweis, J. Martin, J. Moore, H. T. Ochs, D. C. Rogers, J. Scala, G. Tripoli, and J. Young (2000), The Lake-Induced Convection Experiment and the Snowband Dynamics Project, *Bull. Amer. Meteor. Soc.*, *81*(3), 519-542, doi: 10.1175/1520-0477(2000)081<0519:TLCEAT>2.3.CO;2.
- Kulmala, M., and P. E. Wagner (2001), Mass accommodation and uptake coefficients - a quantitative comparison, *J. Aerosol. Sci.*, *32*, 833-841.
- Laaksonen, A., T. Vesala, M. Kulmala, P. M. Winkler, and P. E. Wagner (2005), Commentary on cloud modelling and the mass accommodation coefficient of water, *Atmos. Chem. Phys.*, *5*, 461-464.
- Lee, J. K., K. L. Rubow, D. Y. H. Pui, and B. Y. H. Liu (1995), Comparative study of pressure reducers for aerosol sampling from high-purity gases, *Aerosol Sci. Technol.*, *23*(4), 481-490.
- Li, J., J. R. Anderson, and P. R. Buseck (2003), TEM study of aerosol particles from clean and polluted marine boundary layers over the North Atlantic, *J. Geophys. Res. - Atmos.*, *108*(D6), doi: 10.1029/2002jd002106.
- Li, Y. Q., P. Davidovits, Q. Shi, J. T. Jayne, C. E. Kolb, and D. R. Worsnop (2001), Mass and thermal accommodation coefficients of H₂O(g) on liquid water as a function of temperature, *J. Phys. Chem. A*, *105*(47), 10627-10634, doi: 10.1021/jp012758q.
- Libbrecht, K. G. (2003), Growth rates of the principal facets of ice between -10°C and -40°C, *J. Cryst. Growth*, *247*, 530-540.

- Lin, H., K. J. Noone, J. Strom, and A. J. Heymsfield (1998), Small ice crystals in cirrus clouds: A model study and comparison with in situ observations, *J. Atmos. Sci.*, *55*(11), 1928-1939, doi: 10.1175/1520-0469(1998)055<1928:SICICC>2.0.CO;2.
- Liu, B. Y. H., and D. Y. H. Pui (1974), Equilibrium bipolar charge-distribution of aerosols, *Journal Of Colloid And Interface Science*, *49*(2), 305-312.
- Magee, N., A. M. Moyle, and D. Lamb (2006), Experimental determination of the deposition coefficient of small cirrus-like ice crystals near -50C, *Geophys. Res. Lett.*, *33*(L17), doi: 10.1029/2006GL026665.
- Malm, W. C., B. A. Schichtel, M. L. Pitchford, L. L. Ashbaugh, and R. A. Eldred (2004), Spatial and monthly trends in speciated fine particle concentration in the United States, *J. Geophys. Res.-Atmos.*, *109*(D3), -, doi: 10.1029/2003jd003739.
- Mangold, A., R. Wagner, H. Saathoff, U. Schurath, C. Giesemann, V. Ebert, M. Kramer, and O. Mohler (2005), Experimental investigation of ice nucleation by different types of aerosols in the aerosol chamber AIDA: implications to microphysics of cirrus clouds, *Meteorologische Zeitschrift*, *14*(4), 485-497.
- Martin, S. T. (2000), Phase transitions of aqueous atmospheric particles, *Chem. Rev.*, *100*(9), 3403-3453, doi: 10.1021/cr990034t
- Mozurkewich, M. (1986), Aerosol growth and the condensation coefficient for water: A review, *Aerosol Sci. Technol.*, *5*(2), 223-236, doi: 10.1080/02786828608959089.
- Murphy, D. M., and T. Koop (2005), Review of the vapour pressures of ice and supercooled water for atmospheric applications, *Quart. J. R. Met. Soc.*, *131*(608), 1539.
- Noone, K. B., K. J. Noone, J. Heintzenberg, J. Strom, and J. A. Ogren (1993), In-situ observations of cirrus cloud microphysical properties using the counterflow virtual impactor, *J. Atmos. Oceanic Technol.*, *10*(3), 294-303, doi: 10.1175/1520-0426(1993)010<0294:ISOOCC>2.0.CO;2.
- Onasch, T. B., R. L. Siefert, S. D. Brooks, A. J. Prenni, B. Murray, M. A. Wilson, and M. A. Tolbert (1999), Infrared spectroscopic study of the deliquescence and efflorescence of ammonium sulfate aerosol as a function of temperature, *J. Geophys. Res.*, *104*(D17), 21317.
- Pauling, L. (1970), *General Chemistry*, New York.
- Petters, M. D., and S. M. Kreidenweis (2007), A single parameter representation of hygroscopic growth and cloud condensation nuclei activity, *Atmos. Chem. Phys.*, *7*, 1961-1971.
- Petters, M. D., A. J. Prenni, S. M. Kreidenweis, and P. J. DeMott (2007), On measuring the critical diameter of cloud condensation nuclei using mobility selected aerosol, *Aerosol Sci. Technol.*, *41*(10), 907-913, doi: 10.1080/02786820701557214.

- Pitzer, K. S., and G. Mayorga (1973), Thermodynamics of Electrolytes .2. Activity and Osmotic Coefficients for Strong Electrolytes with One or Both Ions Univalent, *J. Phys. Chem.*, *77*(19), 2300-2308.
- Pratte, P., H. v. d. Bergh, and M. J. Rossi (2006), The kinetics of H₂O vapor condensation and evaporation on different types of ice in the range 130-210 K, *J. Phys. Chem. A*, *110*(9), 3042-3058, doi: 10.1021/jp053974s.
- Prenni, A. J., P. J. DeMott, S. M. Kreidenweis, D. E. Sherman, L. M. Russell, and Y. Ming (2001a), The effects of low molecular weight dicarboxylic acids on cloud formation, *J. Phys. Chem. A*, *105*(50), 11240-11248.
- Prenni, A. J., M. E. Wise, S. D. Brooks, and M. A. Tolbert (2001b), Ice nucleation in sulfuric acid and ammonium sulfate particles, *J. Geophys. Res.-Atmos.*, *106*(D3), 3037-3044.
- Prenni, A. J., P. J. DeMott, C. Twohy, M. R. Poellot, S. M. Kreidenweis, D. C. Rogers, S. D. Brooks, M. S. Richardson, and A. J. Heymsfield (2007a), Examinations of ice formation processes in Florida cumuli using ice nuclei measurements of anvil ice crystal particle residues, *J. Geophys. Res.-Atmos.*, *112*(D10), doi: 10.1029/2006JD007549.
- Prenni, A. J., M. D. Petters, S. M. Kreidenweis, P. J. DeMott, and P. J. Ziemann (2007b), Cloud droplet activation of secondary organic aerosol, *J. Geophys. Res.-Atmos.*, *112*(D10), doi: 10.1029/2006jd007963.
- Prodi, F., G. Santachiara, and C. Cornetti (2002), Measurements of diffusiophoretic velocities of aerosol particles in the transition region, *J. Aerosol. Sci.*, *33*(1), 181-188.
- Pruppacher, H. R. (1995), A new look at homogeneous ice nucleation in supercooled water drops, *J. Atmos. Sci.*, *52*(11), 1924-1933, doi: 10.1175/1520-0469(1995)052<1924:ANLAHI>2.0.CO;2.
- Pruppacher, H. R., and J. D. Klett (1997), *Microphysics of Clouds and Precipitation*, 2nd ed., Kluwer Academic Publishers, Boston.
- Rader, D. J., and P. H. McMurry (1986), Application of the tandem differential mobility analyzer to studies of droplet growth or evaporation, *J. Aerosol. Sci.*, *17*(5), 771-787.
- Rasmussen, D. H. (1982), Thermodynamics and nucleation phenomena - a set of experimental-observations, *J. Cryst. Growth*, *56*(1), 56-66.
- Ren, C., and A. R. MacKenzie (2005), Cirrus parametrization and the role of ice nuclei, *Quart. J. R. Met. Soc.*, *131*, 1585-1605, doi: 10.1256/qj.04.126.
- Richardson, M. S., P. J. DeMott, D. Cziczo, J. Jimenez, E. Dunlea, A. J. Prenni, S. Y. Brooks, S. M. Kreidenweis, J. Snider, M. Petters, D. Murphy, R. Borys, and C. McDade

(2004), Investigations of the Physical and Chemical Properties of Free Tropospheric Ice Nuclei, in *AGU Fall Meeting*, edited, San Francisco.

Richardson, M. S., P. J. DeMott, S. M. Kreidenweis, D. J. Cziczo, E. J. Dunlea, J. L. Jimenez, D. S. Thomson, L. L. Ashbaugh, R. D. Borys, D. L. Westphal, G. S. Casuccio, and T. L. Lersch (2007), Measurements of heterogeneous ice nuclei in the western United States in springtime and their relation to aerosol characteristics, *J. Geophys. Res.*, *112*(D2), D02209, doi: 10.1029/2006JD007500.

Roberts, G. C., and A. Nenes (2005), A continuous-flow streamwise thermal-gradient CCN chamber for atmospheric measurements, *Aerosol Sci. Technol.*, *39*, 206-221, doi: 10.1080/027868290913988.

Rogers, D. C. (1988), Development of a continuous flow thermal gradient diffusion chamber for ice nucleation studies, *Atmos. Res.*, *22*, 149-181.

Rogers, D. C. (1994), Detecting ice nuclei with a continuous flow diffusion chamber—some exploratory tests of instrument response, *J. Atmos. Oceanic Technol.*, *11*(4), 1042-1047, doi: 10.1175/1520-0426(1994)011<1042:DINWAC>2.0.CO;2.

Rogers, D. C., P. J. DeMott, S. M. Kreidenweis, and Y. L. Chen (1998), Measurements of ice nucleating aerosols during SUCCESS, *Geophys. Res. Lett.*, *25*(9), 1383-1386.

Rogers, D. C., P. J. DeMott, S. M. Kreidenweis, and Y. L. Chen (2001), A continuous-flow diffusion chamber for airborne measurements of ice nuclei, *J. Atmos. Oceanic Technol.*, *18*(5), 725-741, doi: 10.1175/1520-0426.

Rogers, D. C., D. Straub, and P. J. DeMott (2004), Computational Fluid Dynamics Study of an Ice Nucleation Chamber, in *14th International Conference on Clouds and Precipitation - IAMAS-ICCP 2004*, edited, Bologna, Italy.

Sadtchenko, V., M. Brindza, M. Chonde, B. Palmore, and R. Eom (2004), The vaporization rate of ice at temperatures near its melting point, *J. Chem. Phys.*, *121*(23), 11980-11992, doi: 10.1063/1.1817820.

Sassen, K., and G. C. Dodd (1988), Homogeneous nucleation rate for highly supercooled cirrus cloud droplets, *J. Atmos. Sci.*, *45*(8), 1357-1369, doi: 10.1175/1520-0469(1988)045<1357:HNRFHS>2.0.CO;2.

Sassen, K., and G. C. Dodd (1989), Haze particle nucleation simulations in cirrus clouds, and applications for numerical and lidar studies, *J. Atmos. Sci.*, *46*(19), 3005-3014, doi: 10.1175/1520-0469(1989)046<3005:HPNSIC>2.0.CO;2.

Schaefer, V. J. (1946), The production of ice crystals in a cloud of supercooled water droplets, *Science*, *104*(2707), 457-459.

Schaefer, V. J. (1952), Formation of ice crystals in ordinary and nuclei-free air, *Industrial and Engineering Chemistry*, *44*(6), 1300-1304.

- Seifert, M., J. Strom, R. Krejci, A. Minikin, A. Petzold, J. F. Gayet, U. Schumann, and J. Ovarlez (2003), In-situ observations of aerosol particles remaining from evaporated cirrus crystals: Comparing clean and polluted air masses, *Atmos. Chem. Phys.*, *3*, 1037-1049.
- Seinfeld, J. H., and S. N. Pandis (1998), *Atmospheric Chemistry and Physics: From Air Pollution to Climate Change*, John Wiley & Sons, Inc., New York.
- Shampine, L. F. (1986), Some practical Runge-Kutta formulas, *Mathematics Of Computation*, *46*(173), 135-150.
- Shaw, R. A., and D. Lamb (1999), Experimental determination of the thermal accommodation and condensation coefficients of water, *J. Chem. Phys.*, *111*(23), 10659-10663
- Starr, F. W., C. A. Angell, and H. E. Stanley (2003), Prediction of entropy and dynamic properties of water below the homogeneous nucleation temperature, *Physica A*, *323*, 51-66, doi: 10.1016/S0378-4371(03)00012-8.
- Stetzer, O., B. Baschek, F. Luond, and U. Lohmann (2008), The Zurich Ice Nucleation Chamber (ZINC) - A new instrument to investigate atmospheric ice formation, *Aerosol Sci. Technol.*, *42*(1), 64-74, doi: 10.1080/02786820701787944.
- Stratmann, F., A. Kiselev, S. Wurzler, M. Wendisch, J. Heintzenberg, R. J. Charlson, K. Diehl, H. Wex, and S. Schmidt (2004), Laboratory studies and numerical simulations of cloud droplet formation under realistic supersaturation conditions, *J. Atmos. Oceanic Technol.*, *21*, 876-887, doi: 10.1175/1520-0426(2004)021<0876:LSANSO>2.0.CO;2.
- Straub, D., D. C. Rogers, A. J. Prenni, and P. J. DeMott (2004), Flow Dynamics and Particle Trajectories in an Ice Nucleation Chamber, in *AAAR: 23rd Annual Conference*, edited, Atlanta, GA.
- Ström, J., B. Strauss, T. Anderson, F. Schröder, J. Heintzenberg, and P. Wendling (1997), In situ observations of the microphysical properties of young cirrus clouds, *J. Atmos. Sci.*, *54*(21), 2542-2553, doi: 10.1175/1520-0469(1997)054<2542:ISOOTM>2.0.CO;2.
- Ström, J., M. Seifert, B. Kärcher, J. Ovarlez, A. Minikin, J. F. Gayet, R. Krejci, A. Petzold, F. Auriol, W. Haag, R. Busen, U. Schumann, and H. C. Hansson (2003), Cirrus cloud occurrence as function of ambient relative humidity: a comparison of observations obtained during the INCA experiment, *Atmos. Chem. Phys.*, *3*, 1807-1816.
- Sutherland, W. (1893), The viscosity of gases and molecular force, *Philosophical Magazine*, *36*, 507-531.

Sweet, J. N., E. P. Roth, and M. Moss (1987), Thermal conductivity of Inconel 718 and 304 stainless steel, *International Journal of Thermophysics*, *8*(5), 593-606.

Swietlicki, E., H. C. Hansson, K. Hameri, B. Svenningsson, A. Massling, G. McFiggans, P. H. McMurry, T. Petaja, P. Tunved, M. Gysel, D. Topping, E. Weingartner, U. Baltensperger, J. Rissler, A. Wiedensohler, and M. Kulmala (2008), Hygroscopic properties of submicrometer atmospheric aerosol particles measured with H-TDMA instruments in various environments - a review, *Tellus Series B-Chemical and Physical Meteorology*, *60*(3), 432-469, doi: 10.1111/j.1600-0889.2008.00350.x.

Tabazadeh, A., and O. B. Toon (1998), The role of ammoniated aerosols in cirrus cloud nucleation, *Geophys. Res. Lett.*, *25*(9), 1379-1382.

Tang, I. N., and H. R. Munkelwitz (1994), Water activities, densities, and refractive indices of aqueous sulfates and sodium nitrate droplets of atmospheric importance, *J. Geophys. Res.*, *99*(D9).

Twohy, C. H., and M. R. Poellot (2005), Chemical characteristics of ice residual nuclei in anvil cirrus clouds: evidence for homogeneous and heterogeneous ice formation, *Atmos. Chem. Phys.*, *5*, 2289-2297.

Vieceli, J., M. Roeselova, and D. J. Tobias (2004), Accommodation coefficients for water vapor at the air/water interface, *Chem. Phys. Lett.*, *393*, 249-255, doi: 10.1016/j.cplett.2004.06.038.

Voigtländer, J., F. Stratmann, D. Niedermeier, H. Wex, and A. Kiselev (2007), Mass accommodation coefficient of water: A combined computational fluid dynamics and experimental data analysis, *J. Geophys. Res.*, *112*(D20), doi: 10.1029/2007JD008604.

Wexler, A. (1976), Vapor-Pressure Formulation For Water In Range 0 To 100 Degreesc - Revision, *Journal of Research of the National Bureau of Standards Section A-Physics And Chemistry*, *80*(5-6), 775-785.

Wexler, A. (1977), Vapor Pressure Formulation For Ice, *Journal of Research of the National Bureau Of Standards Section A-Physics And Chemistry*, *81*(1), 5-20.

Wiedensohler, A. (1988), An approximation of the bipolar charge-distribution for particles in the sub-micron range, *J. Aerosol. Sci.*, *19*(3), 387-389.

Winkler, P. M., A. Vrtala, P. E. Wagner, M. Kulmala, K. E. J. Lehtinen, and T. Vesala (2004), Mass and thermal accommodation during gas-liquid condensation of water, *Phys. Rev. Lett.*, *93*(7).

Wise, M. E., R. M. Garland, and M. A. Tolbert (2004), Ice nucleation in internally mixed ammonium sulfate/dicarboxylic acid particles, *J. Geophys. Res.*, *109*, D06212, doi: 10.1029/2001GL014289.

Wylie, D. P., and W. P. Menzel (1999), Eight years of high cloud statistics using HIRS, *J. Climate*, *12*(1), 170-184.

Xu, J., D. Imre, R. McGraw, and I. Tang (1998), Ammonium sulfate: Equilibrium and metastability phase diagrams from 40 to -50 degrees C, *J. Phys. Chem. B*, *102*(38), 7462-7469.

Zhou, J. C., E. Swietlicki, H. C. Hansson, and P. Artaxo (2002), Submicrometer aerosol particle size distribution and hygroscopic growth measured in the Amazon rain forest during the wet season, *J. Geophys. Res.*, *107*(D20), 8055, doi: 10.1029/2000JD000203

Zientara, M., D. Jakubczyk, K. Kolwas, and M. Kolwas (2008), Temperature dependence of the evaporation coefficient of water in air and nitrogen under atmospheric pressure: Study in water droplets, *J. Phys. Chem. A*, *112*, 5152-5158, doi: 10.1021/jp7114324.